Wrocław University of Technology
Centre of Advanced Materials and Nanotechnology

Materials Science
Poland

Workshop on Functional Materials
FMA 2004
Athens, Greece, *23-26* September 2005

Guest Editors:
Nikos Guskos, Janusz Typek

Vol.23 • No. 4 • 2005

Oficyna Wydawnicza Politechniki Wrocławskiej

Materials Science is an interdisciplinary journal devoted to experimental and theoretical research into the synthesis, structure, properties and applications of materials.

Among the materials of interest are:

- glasses and ceramics
- sol-gel materials
- photoactive materials (including materials for nonlinear optics)
- laser materials
- photonic crystals
- semiconductor micro- and nanostructures
- piezo-, pyro- and ferroelectric materials
- high-T_c, superconductors
- magnetic materials
- molecular materials (including polymers) for use in electronics and photonics
- novel solid phases
- other novel and unconventional materials

The broad spectrum of the areas of interest reflects the interdisciplinary nature of materials research. Papers covering the modelling of materials, their synthesis and characterisation, physicochemical aspects of their fabrication, properties and applications are welcome. In addition to regular papers, the journal features issues containing conference papers, as well as special issues on key topics in materials science.

Materials Science is published under the auspices of the Centre of Advanced Materials and Nanotechnology of the Wrocław University of Technology, in collaboration with the Institute of Low Temperatures and Structural Research of the Polish Academy of Sciences and the Wroclaw University of Economics.

All accepted papers are placed on the Web page of the journal and are available at the address:
http://MaterialsScience.pwr.wroc.pl

The Journal is supported by the State Committee for Scientific Research

Printed in Poland

Drukarnia Oficyny Wydawniczej Politechniki Wrocławskiej
Zam. nr 3/2006.

CONTENTS

J. T. Devreese, Contributions of George J. Papadopoulos 851
H. Pfnür, V. Zielasek, Ch. Tegenkamp, T. Block, Z. Kallassy, Geometrical and electronic properties of ultra thin epitaxial metal nanowires on flat and vicinal Si surfaces 861
A. Modinos, N. Stefanou, Photonic crystals: a novel class of functional materials 877
A. Bezkrovnyi, N. Guskos, J. Typek, N.Yu. Ryabova, M. Bosacka, A. Blonska-Tabero, M. Kurzawa, I. Rychlowska-Himmel, G. Zolnierkiewicz, Neutron diffraction study of $Mn_3Fe_4V_6O_{24}$ 883
I. A. Hadjiagapiou, A. Malakis, S.S. Martinos, Inverse-range-parameter dependence of gas-liquid nucleation in a Yukawa fluid. A density functional approach 891
T. Bodziony, N. Guskos, A. Biedunkiewicz, J. Typek, R. Wróbel, M. Maryniak, Characterization and EPR studies of TiC and TiN ceramics at room temperature 899
L. Licea-Jiménez, R W. Rychwalski, Novel nanocomposites using carbon nanotubes and melamine-formaldehyde 909
R.J. Kaleńczuk, M. Lewicki, Preparation and characterization of nanocarbons for hydrogen storage 915
N. Guskos, J. Typek, G. Zolnierkiewicz, A. Blonska-Tabera, M. Kurzawa, M. Bosacka, Magnetic resonance study of $M_3Fe_4V_6O_{24}$ (M = Mg, Zn, Mn, Cu, Co) compounds 923
J. Typek, J. Kostrzewa, N. Guskos, Synthesis and ESR study of $(Tb_xY_{1-x})_2Cu_20_5$ solid solutions 929
U. Narkiewicz, I. Kucharewicz, W. Arabczyk, S. Lenart, Carturisation of nanocrystalline iron with ethylene 939
A. C. Malakis, I. A. Hadjiagapiou, S. S. Martinos, N. G. Fytas, Finite-size analysis via the critical energy-subspace method in the Ising models 947
N. Guskos, J. Typek, G. J. Papadopoulos, M. Maryniak, K. Aidinis, The linewidths and integrated intensities of the d-d transitions in photoacoustic spectra of polyamine copper(II) complexes 955
R. Z. Rogowski, The kinetics of nucleation in inhomogeneous media based on the classical Avrami model 961
N. Guskos, J. Typek, M. Maryniak, Z. Roslaniec, D. Petridis, M. Kwiatkowska, FMR study of γ-Fe_20_3 magnetic nanoparticles in a multiblock poly(ether-ester) copolymer matrix 971
V. V. Novikov, K.W. Wojciechowski, O.A. Komkova, T. Thiel, Anomalous relaxation in dielectrics. Equations with fractional derivatives 977
G. E. Zardas, P.H. Yannakopoulos, Ch.I. Symeonides, O. Csabay, P. C. Euthymiou. Persistent photoconductivity in a InP:Fe single layer structure at room temperature 985
G. Bergmański, M. Białoskórski, M. Rychcik-Leyk, J. Rybicki, Structure recognition in MD-simulated materials. A case study of $B0_3$ triangles in borate glasses 989
N. Guskos, J. Typek, M. Maryniak, U. Narkiewicz, I. Kucharewicz, R. Wróbel, FMR study of agglomerated nanoparticles in a Fe_3C/C system 1001
S. P. Kruchinin, V.F. Klepikov, V.E. Novikov, D.S. Kruchinin, Nonlinear current oscillations in the fractal Josephson junction 1009
Z. Czech, R. Milker, Development trends in pressure-sensitive adhesive systems 1015
I. E. Lipiński, J. Kuriata, Some implications of the nonlinear properties of SASD crystals 1023
N. Guskos, D.G. Paschalidis, J. Majszczyk, J. Typek, M. Maryniak. Photoacoustic study of a new neodymium(III) hydrazone complex 1029
B. Padlyak, J. Kornatowski, G. Zadrożna, K. Fabisiak, A. Gutszej EPR study of chromium centres in CrAPO-5 molecular sieves 1035
J. Typek, E. Filipek, M. Maryniak, N. Guskos, Magnetic resonance study of $SbV0_5$ thermal decomposition products 1047
T. Bodziony, N. Guskos, J. Typek, Z. Roslaniec, U. Narkiewicz, M. Kwiatkowska, M. Maryniak, Temperature dependence of the FMR spectra of Fe_30_4 and Fe_3C nanoparticle magnetic systems in copolymer matrices 1055

Materials Science-Poland, Vol. 23, No. 4, 2005

Contributions of George J. Papadopoulos*

J. T. DEVREESE**

TFVS, Departement Fysica, Universiteit Antwerpen, B-2610 Antwerpen, Belgium

eiTT/COBRA, Departement Natuurkunde, Technische Universiteit Eindhoven
P.O. Bus 513, 5600 MB Eindhoven, The Netherlands

I review some of the scientific work of George Papadopoulos. The main emphasis is on his works on path integrals and their applications. The review is closed by an excursus on polaron physics, where the path-integral approach has been proven to be the method of excellence.

Key words: quantum dynamics; path-integral method; Dirac electron; magnetic field; polarons

1. Preface

Discussions with George Papadopoulos, more often than not, ended up with reflections on Thales, Pythagoras, Plato, Aristotle, Archimedes… (Fig. 1). I therefore cannot resist the temptation to illustrate my present review of some of George's work with references to Ancient Greece. I had the pleasure to interact with George over longer periods. On this occasion, I wish George many new creative achievements in the coming period.

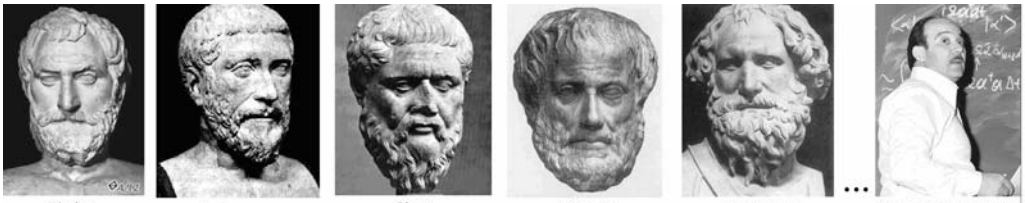

Fig. 1. Prolonging the timeline of theoretical studies from Ancient Greece

*Opening lecture, Workshop on Functional Materials, Athens, Greece, 23 September, 2004.

**E-mail: jozef.devreese@ua.ac.be

2. Path integrals and their applications

Path integrals and their applications in quantum, statistical and solid state physics have been the subject of the book [1], co-authored by George Papadopoulos. Among the original contributions by George, his excursions on quantum dynamics and path integrals must be mentioned. The path integral for the partition function, which determines the free energy, is calculated over closed paths. See Figure 2 for an example of an (intricate-) closed path.

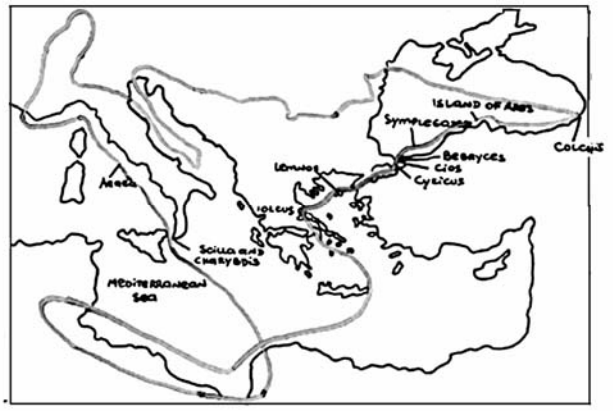

Fig. 2. *Beginning with thee, O Phoebus, I will recount the famous deeds of men of old, who, at the behest of King Pelias, down through the mouth of Pontus and between the Cyanean rocks, sped well-benched Argo in quest of the golden fleece*. (Apollonius Rhodius, Argonautica) (map from http://lukio.vimpeli.fi/italia/argoviag.htm)

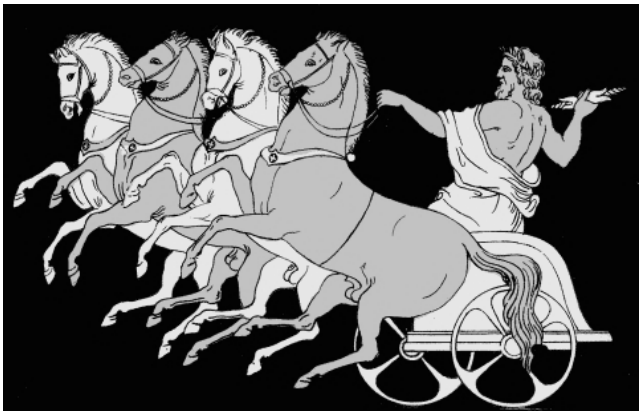

Fig. 3. *And therein were fashioned two chariots, racing, and the one in front Pelops was guiding, as he shook the reins, and with him was Hippodameia at his side, and in pursuit Myrtilus urged his steeds, and with him Oenomaus had grasped his couched spear, but fell as the axle swerved and broke in the nave, while he was eager to pierce the back of Pelops.* (Apollonius Rhodius, Argonautica) (The Chariot of Zeus, from *Stories from the Greek Tragedians* by Alfred Church, 1879. http://en.wikipedia.org/wiki/Image: The Chariot of Zeus, Project Gutenberg eText 14994.png)

He treated the quantum dynamics of dissipative Lagrangians, proposed a systematic approach for the derivation of the path-integral propagator for a constrained particle described by a dissipative Lagrangian [3]. In Figure 3, an early illustration of the effect of dissipation is presented. As friction heated the axle of Oenomaus' chariot, the wax linchpins melted, and when the wheels eventually fell off, the whole chariot broke apart.

Further, George developed a path integral description of an electron gas in a random potential [4] and analyzed functional integrals with applications in polymer physics and in the study of spin-Bose systems.

Feynman's path-integral method had already been successful in tackling many quantum-mechanical problems. Although, in principle, there was nothing to prevent the application of the method to obtain a formal expression for the propagator of the Dirac equation, in practice a variety of mathematical difficulties had prevented direct actual calculations. In 1976 George co-authored a paper [5] in which the propagator for a free fermion and for a fermion in a magnetic field was directly derived in the path-integral formalism. The propagator for a Dirac electron in a constant magnetic field was indirectly obtained by evaluating a world-line (space-time path) integral. The corresponding spectrum was then extracted from an auxiliary propagator.

3. A spectrum of scientific activities

The works of George span a broad spectrum of his fruitful scientific activities. Problems of relativistic physics remained one of George's key interests over his scientific career. He and his co-authors provided a useful approximation to treat the Dirac equation with a confining scalar potential and a fourth component of the vector potential of rectangular shape [6]. They also demonstrated the analytic advantages of those potentials [7]. Figure 4 shows Prometheus subjected to a "confining potential".

Several works of George and his co-workers deal with the interaction of light with matter. He analyzed the interaction of radiation with atoms [8], light-scattering properties of linear polymers, energy exchange between parametric modes in a nonlinear optical medium, the energetics of a system consisting of radiation and a two-level atom in an ideal resonant cavity [9], the amplitude and phase of the acoustic effect.

Another field of his research interests is in the physics of tunneling, where he provided important ingredients for the understanding of time-dependent quantum tunneling via crossover processes [10] and of photon induced tunneling oscillations in a double quantum well [11].

George and his co-authors also extensively applied fundamental theoretical approaches to problems of materials physics. For example, they characterized polycrystalline polyamine copper dinitrate complexes [12] and iron oxide pigments: hematite, goethite and magnetite [13] using photoacoustic, EPR and electrical conductivity investigations.

Fig. 4. *Thou firmament of God, and swift-winged winds,*
Ye springs of rivers, and of ocean waves
That smile innumerous! Mother of us all,
O Earth, and Sun's all-seeing eye, behold,
*I pray, what I, a God, from Gods endur*e.
(*Aeschylus, Prometheus Bound*, http://www.bartleby.com/8/4/1.html)
(Picture by P. P. Rubens, from http://www.artprints-on-demand.co.uk/noframes/rubens/prometheus.htm)

4. Polarons

The polaron concept is of interest, not only because it describes the particular physical properties of an electron in polar crystals and ionic semiconductors, but also because it is an interesting field-theoretical model consisting of a fermion interacting with a scalar boson field.

A conduction electron (or hole) together with its self-induced polarization in a polar crystal forms a quasiparticle, which is called a polaron [14–17]. Properties of polarons have attracted increasing attention due to their relevance to physics of conjugated polymers, colossal magnetoresistance perovskites, high-T_c superconductors, layered MgB_2 superconductors, fullerenes, quasi-1D conductors, semiconductor nanostructures.

A conduction electron repels the negative ions and attracts the positive ions (Fig. 5). A self-induced potential arises, which acts back on the electron and modifies its physical properties. The polaron coupling constant was introduced by Fröhlich [16]:

$$\alpha = \frac{e^2}{\hbar}\sqrt{\frac{m_b}{2\hbar\omega_{\mathrm{LO}}}}\left(\frac{1}{\varepsilon_\infty}-\frac{1}{\varepsilon_0}\right)$$

where ω_{LO} is the long-wavelength frequency of a longitudinal optical (LO) phonon; ε_∞ and ε_0 are, respectively, the electronic and the static dielectric constants of the polar crystal, m_b is the electron (hole) band mass.

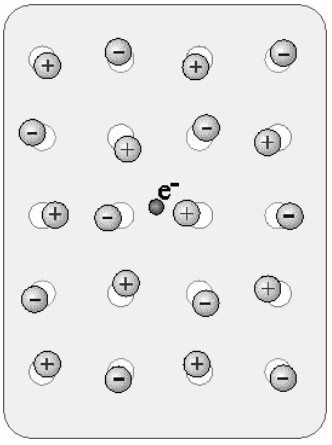

Fig. 5. An artist's view of a polaron (from Ref. [18])

Feynman's all-coupling path-integral treatment [19, 20] is based on his suggestion to formulate the polaron problem in the Lagrangian form of quantum mechanics and then to eliminate the phonon field from the propagator. As a result, the polaron problem is formulated [19] as an equivalent one-particle problem in which the interaction, non-local in time or "retarded", is between the electron and itself:

$$\langle 0,\beta|0,0\rangle = \int D\mathbf{r}(\tau)\exp\left[-\frac{1}{2}\int_0^\beta \dot{\mathbf{r}}^2 d\tau + \frac{\alpha}{2^{3/2}}\int_0^\beta\int_0^\beta \frac{e^{-|\tau-\sigma|}}{\left[\mathbf{r}(\tau)-\mathbf{r}(\sigma)\right]}\,d\tau d\sigma\right]$$

with $\beta = 1/(k_{\mathrm{B}}T)$.

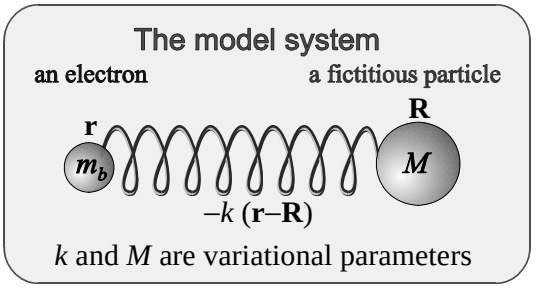

Fig. 6. The Feynman model system for a variational study of the polaron

Feynman introduced a variational principle for path integrals to study the polaron. He simulated the interaction between the electron and the polarization modes by a harmonic interaction between a hypothetical particle and the electron (Fig. 6).

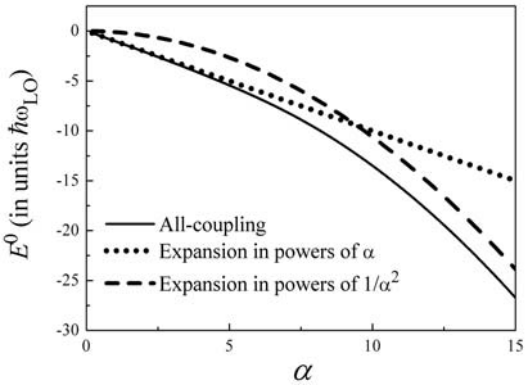

Fig. 7. Feynman-polaron energy as a function of α: the all-coupling theory

Applying the variational principle for path integrals resulted in an upper bound for the polaron self-energy at all α, which at weak and strong coupling gave quite accurate limits (see Fig. 7). Feynman obtained a smooth interpolation between weak and strong coupling for the ground-state energy. Over the years, the Feynman polaron model remained in many respects the most successful approach to this problem.

At zero temperature and in the weak-coupling limit, the optical absorption is due to the elementary polaron scattering process, schematically shown in Fig. 8. An incoming photon is absorbed by a polaron. The polaron emits a phonon during the absorption process and takes recoil energy from the incident light.

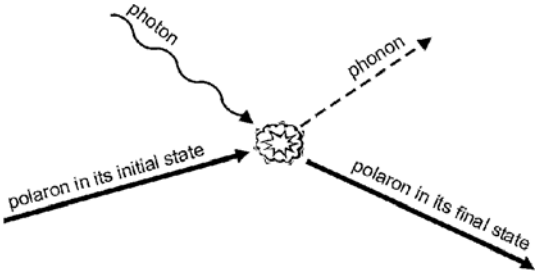

Fig. 8. Elementary polaron scattering process (from Ref. [21], © 2003 by the American Institute of Physics)

In the weak-coupling limit ($\alpha << 1$), the polaron absorption coefficient at zero temperature can be expressed in terms of elementary functions in two limiting cases [23, 24]:

- at high densities

$$\Gamma(\omega) = \frac{1}{\varepsilon_0 nc} \frac{2^{1/2} N^{2/3} \alpha}{(3\pi^2)^{1/3}} \frac{e^2}{(\hbar m_b \omega_{LO})^{1/2}} \frac{\omega\text{-}1}{\omega^3} \Theta(\omega\text{-}1)$$

- and at low densities

$$\Gamma(\omega) = \frac{1}{\varepsilon_0 nc} \frac{2Ne^2\alpha}{3m_b\omega_{\mathrm{LO}}} \frac{(\omega-1)^{1/2}}{\omega^3}$$

where ω is the frequency of the incident light represented in units of ω_{LO}.

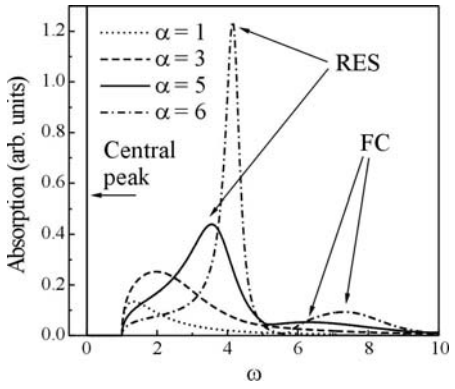

Fig. 9. Polaron optical absorption spectra at zero temperature, calculated within the path integral method [24, 25] for various values of α. A δ-like central peak is schematically shown by a vertical line (from Ref. [21], © 2003 by the American Institute of Physics)

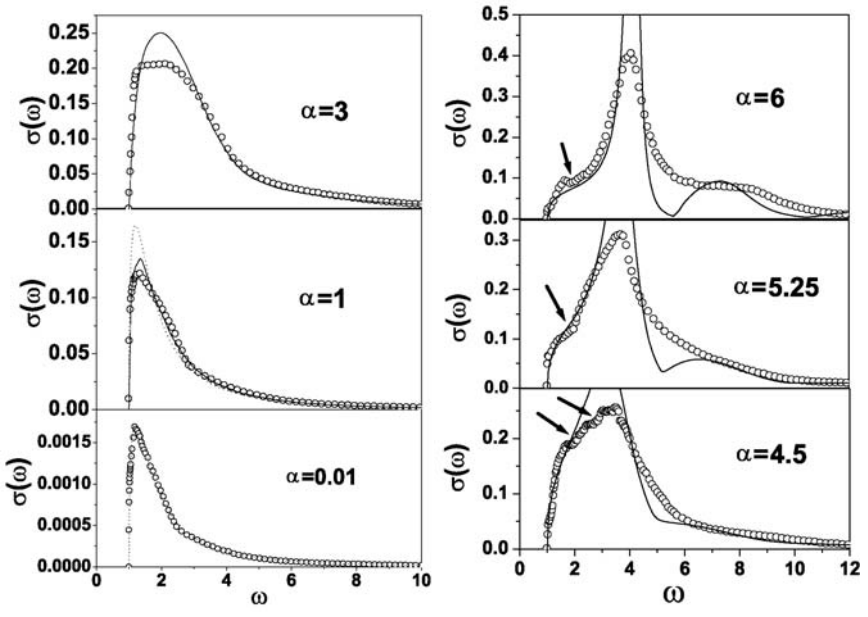

Fig. 10. Left-hand panel: Optical conductivity spectra for the weak-coupling regime (open circles) compared to the second-order perturbation theory (dotted lines) and arbitrary-coupling path-integral theory [24] (solid lines). Right-hand panel: Optical conductivity spectra for the intermediate coupling regime (open circles) compared to the arbitrary-coupling path-integral theory (DSG [24]), (solid lines). Arrows point to the anomalies in absorption spectra arising at the two- and three-phonon thresholds (from. Ref. [26], © 2003 by the American Physical Society)

The optical absorption of single large polarons at arbitrary coupling has been derived using the path-integral method [24, 25] (Fig. 9). At larger coupling, $\alpha \geq 5.9$, the polaron can undergo transitions toward a relatively stable internal excited state called the "relaxed excited state" (RES). The RES peak in the spectrum also has a phonon sideband, which is related to a Franck–Condon- (FC)-type transition. For α ranging from ~4 to ~7, the RES peak is very intense compared with the FC peak.

Calculations of the optical conductivity for the Fröhlich polaron performed within the diagrammatic Quantum Monte Carlo method [26] (Fig. 10), fully confirm the results of the path-integral variational approach [24] at $\alpha \leq 3$. In the intermediate coupling regime $3 < \alpha < 6$, the low-energy behaviour and the position of the maximum of the optical conductivity spectrum of Ref. [26] follow well the prediction of Ref. [24]. There are the following qualitative differences between the two approaches in the intermediate and strong coupling regime: in Ref. [26], the dominant peak broadens and the second peak does not develop, giving instead rise to a flat shoulder in the optical conductivity spectrum at $\alpha = 6$. This behaviour can be attributed to the optical processes with participation of two or more phonons. The RES peaks calculated in [24, 25] tend to become too narrow as α increases. The nature of the excited states of a polaron needs further study.

References

[1] *Path Integrals and Their Applications in Quantum, Statistical and Solid State Physics*, G.J. Papadopoulos, J.T. Devreese (Eds.), Plenum Press, New York,1978.

[2] SOULI S., *Greek Mithology*, Michalis Toubis S.A., Athens, 1995.

[3] PAPADOPOULOS G.J., J. Phys. A-Math. Nucl. Gen., 7 (1974), 209.

[4] PAPADOPOULOS G.J., Phys. Rev. D, 11 (1975), 2870.

[5] PAPADOPOULOS G.J., DEVREESE J.T., Phys. Rev. D, 13 (1976), 2227.

[6] GRYPEOS M.E., KOUTROULOS C.G., PAPADOPOULOS G.J., Phys. Rev. A, 50 (1994), 29.

[7] PAPADOPOULOS G.J., KOUTROULOS C.G., GRYPEOS M.E., Int. J. Theor. Phys., 39 (2000), 455.

[8] PAPADOPOULOS G.J., J. Phys. A-Math. Gen., 13 (1980), 1423.

[9] PAPADOPOULOS G.J., Phys. Rev. A 37 (1988), 2482.

[10] PAPADOPOULOS G.J., J. Phys. A-Math. and Gen. 23 (1990), 935.

[11] PAPADOPOULOS G.J., MELAS P., Foundations of Physics, 31 (2001), 165.

[12] GUSKOS N., PAPADOPOULOS G.J., LIKODIMOS V., MAJSZCZYK J., TYPEK J., WABIA M., GRECH E., DZIEMBOWSKA T., PERKOWSKA A., AIDINIS K., J. Appl. Phys., 90 (2001), 1436.

[13] GUSKOS N., PAPADOPOULOS G.J., LIKODIMOS V., PATAPIS S., YARMIS D., PRZEPIERA A., PRZEPIERA K., MAJSZCZYK J., TYPEK J., WABIA M., AIDINIS K.,, DRAZEK Z., Mat. Res. Bull., 37 (2002), 1051.

[14] LANDAU L.D., Phys. Z. Sowjetunion, 3 (1933), 664.

[15] PEKAR S.I., U*ntersuchungen über die Elektronentheorie der Kristalle*, Akademie, Berlin, 1954.

[16] FRÖHLICH H., Adv. Phys. 3 (1954), 325.

[17] ALEXANDROV A.S., MOTT N., *Polarons and bipolarons*, World Scientific, Singapore, 1996.

[18] DEVREESE J.T.L., *Moles agitat mentem*. Ontwikkelingen in de fysika van de vaste stof. Rede uitgesproken bij de aanvaarding van het ambt van buitengewoon hoogleraar in de fysica van de vaste stof, in het bijzonder de theorie van de vaste stof, bij de Afdeling der Technische Natuurkunde aan de Technische Hogeschool Eindhoven, March 9, 1979.

[19] FEYNMAN R.P., Phys. Rev., 97 (1955), 660.

[20] FEYNMAN R.P., HELLWARTH R.W., IDDINGS C.K., PLATZMAN P.M., Phys. Rev. 127 (1962), 1004.
[21] DEVREESE J.T., *Polarons*, [in:] *Lectures on the Physics of Highly Correlated Electron System*s VII, A. Avella and F. Mancini (Eds.). Conference Proceeding 678, AIP, Melville, 2003, pp. 3–56.
[22] GUREVICH V.L., LANG I.G., FIRSOV YU.A., Sov. Phys.– Sol. St., 4 (1962), 918.
[23] DEVREESE J., HUYBRECHTS W., LEMMENS L., Phys. Stat. Sol. (b), 48 (1971), 77.
[24] DEVREESE J., DE SITTER J.AND GOOVAERTS M., Phys. Rev. B, 5 (1972), 2367.
[25] DEVREESE J.T., *Internal Structure of Free Fröhlich Polarons, Optical Absorption and Cyclotron Resonance*, [in:] *Polarons in Ionic Crystals and Polar Semiconductors*, North-Holland, Amsterdam, 1972, pp. 83–159.
[26] MISHCHENKO A.S., NAGAOSA N., PROKOF'EV N.V., SAKAMOTO A., SVISTUNOV B.V., Phys. Rev. Lett., 91 (2003), 236401.

Received 7 December 2004
Revised 7 June 2005

Materials Science-Poland, Vol. 23, No. 4, 2005

Geometrical and electronic properties of ultra thin epitaxial metal nanowires on flat and vicinal Si surfaces

H. PFNÜR*, V. ZIELASEK, CH. TEGENKAMP, T. BLOCK, Z. KALLASSY

Institut für Festkörperphysik, Universität Hannover, Appelstr. 2, D-30167 Hannover, Germany

The study of metallic low-dimensional nanoscale systems requires the generation of ultra-small structures. We demonstrate the feasibility of the formation of metallic wires of arbitrary shape with a lateral width below 10 nm and a thickness from one to several monolayers using a combination of electron beam lithography in ultra-high vacuum and tunnelling microscopy. These methods can be easily combined with surfaces structured by self-organization. As an example, a system consisting of Pb on Si(557) is discussed. It exhibits quasi one-dimensional conduction properties already with one Pb monolayer, which undergoes a temperature-driven structural phase transition, switching the system between high and low conductance anisotropy.

Key words: *low-dimensional nanoscale system; metal epitaxy; nanowires; silver; silicon; electron-beam lithography; tunnelling microscopy; surface conductivity*

1. Introduction

One- or two-dimensional electronic systems are very interesting physical objects, since due to electron confinement, increased electron correlation [1] leads to strong deviations from the Fermi liquid, and in 1D to the formation of a Luttinger liquid [2, 3]. Particularly in one-dimensional systems the enhanced interaction is accompanied by instabilities. Interactions between the lattice, charge, and spin cause the formation of charge and spin density waves lowering the energy and leading to metal –insulator transitions in the electronic transport properties of such systems [1, 4].

Already for ideal systems it is clear that the electronic properties of low -dimensional systems are intimately related to their geometric structure. In real and very small one- or two-dimensional systems, this problem is modified by the fact that they must be supported by or embedded into a substrate material or stabilized by other means. Thus their realizations are always approximate and use either strongly anisot-

*Corresponding author, e-mail: pfnuer@fkp.uni-hannover.de

ropic crystals [5, 6] and polymers [7] or supporting surfaces [8]. Adsorbed layers, which partly form chain structures on substrates like Si(111) [8, 9], are alternative realizations that come closer to atomic chains, and allow precise access to the geometric and electronic properties of quasi one-dimensional systems.

These examples illustrate that realizations of quasi one-dimensional systems are of high interest. In the present paper, we explore two possibilities of realizations. The first is using the top-down approach, i.e. it is an extension of conventional electron beam lithography, which has the potential to provide one-dimensional structures of arbitrary shape. The limit of one-dimensionality, however, is not yet reached at present. We report on our first results of combining electron beam lithography with epitaxy of silver on silicon for the generation of epitaxial metal nanowires on an insulating support. In order to avoid surface contamination induced by the lithographical processes, we employ an *in situ* nanolithography technique for silicon surfaces, developed by Ichikawa and his group, which takes place entirely in ultra-high vacuum. It is demonstrated that this nanolithography technique, in combination with low -temperature silver epitaxy, may generate ultra thin continuous epitaxial metal nanowires with the width below 20 nm.

In the second part of this paper, a further and quite intriguing example of a bottom-up approach, i.e. the self-organized generation of strongly anisotropic metallic nanostructures in the Pb/Si(557) system, is discussed. The Si(557) surface as a substrate already has a striped wire-like structure with the alternation of (111) and (112) oriented micro-facets, which seems to be almost unchanged by the adsorption of lead. Thus, electronic and geometrical properties can be well compared with those obtained on a flat Si(111) substrate, for which magnetoconductance and correlation with geometric properties have been recently studied extensively [10–13]. The (557) surface is able to superimpose its symmetry onto the adsorbed Pb layer, which, after appropriate treatment, forms chain structures, so that transitions between one- and two-dimensional behaviour can be studied with this system. Even after Pb adsorption, the Fermi level is pinned close to a mid-gap position [14], so that the underlying Si interface is always depleted of charge, irrespective of doping. Here we present temperature-dependent macroscopic DC conductivity measurements in the coverage range between submonolayers up to several layers of Pb obtained after different steps of annealing.

2. Experimental

UHV-lithography experiments were carried out in ultrahigh vacuum (base pressure below 3×10^{8} Pa) in a combined scanning electron microscope (SEM) – scanning tunnelling microscope (STM) system (JEOL SPM 4500 SX). Both microscopes are confocal and can be operated simultaneously at variable sample temperatures in the range 60–900 K. While the electron gun (1–25 keV) provides an SEM resolution of 4 nm, an eucentric tilting mechanism of the sample stage renders it possible to vary the an-

gle of incidence of the electron beam between 0 and 30º (Fig. 1). At glancing incidence, microprobe reflection high-energy electron diffraction (μRHEED) may be used to check the crystallinity of the generated structures. Any diffraction spot may be chosen as an input signal for scanning reflection electron micrographs (SREM). An additional electron energy analyser was used for the Auger electron spectroscopy

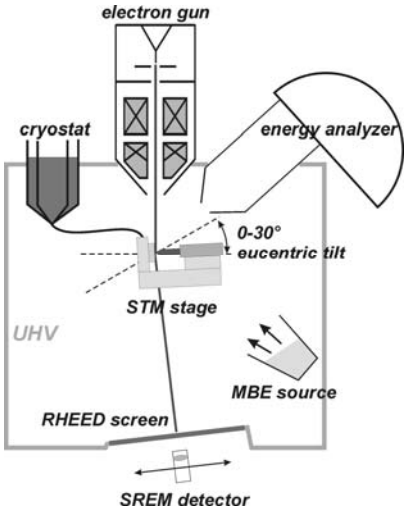

Fig. 1. Schematic drawing of the SEM-STM. This setup also allows scanning Auger microscopy (SAM), electron diffraction at sample areas of the beam diameter (RHEED), and scanning microscopy with the reflected electrons (SREM). Sample temperature can be varied in the range 60–900 K during measurements

(AES) and scanning Auger electron microscopy (SAM). The Si(111) substrate samples, sized 0.3×1.5×7 mm^3, were cut from wafers of high resistivity (>1000 Ω·cm). The substrate surfaces were prepared by repeated flash heating to 1400 K by direct current while keeping the ambient pressure below 1×10^{-7} Pa. To oxidize the surface, the sample temperature was raised to 943 K for 10 min after oxygen (99.999%) was introduced into the chamber at a pressure of 2×10^{-4} Pa. It has been demonstrated that a complete layer of oxide 0.3 nm thick is formed under these conditions [15–17]. Surface quality and contamination were monitored by STM, RHEED, and AES. Silver was evaporated from a well-outgassed Knudsen cell. The deposition rate was determined using a quartz microbalance calibrated via STM measurements. For calibration, Ag was deposited in submonolayer amounts onto the substrate held at the temperature of 700 K. The areal fraction of Si(111) ($\sqrt{3}\times\sqrt{3}$)R30°–Ag regions was determined and the Ag coverage calculated, assuming the density of 1 Ag atom per Si atom of the topmost layer (7.83×10^{14} cm^{-2}) in the ($\sqrt{3}\times\sqrt{3}$)-reconstructed regions, according to the HCT model [18].

Experiments with Pb on Si(557) were carried out again under ultra-high vacuum conditions in two separate vacuum chambers, set up for conductivity measurements at variable temperatures down to 3.5 K (apparatus A), and for tunnelling microscopy at variable temperatures down to 40 K (apparatus B). In both chambers, the average morphology was controlled by low energy electron diffraction (LEED), and the cleanliness of the Si surfaces by STM and by Auger spectroscopy (AES). The Si(557)

substrates (Crystec, Berlin) were chemically cleaned ex-situ. Atomically clean Si(557) surfaces were obtained by removing the native oxide by evaporation of Si at a surface temperature of 1170 K instead of using high temperatures [19]. The Pb coverage was calibrated by conductivity measurements of thick Pb films grown on Si(111) substrates at 20 K [11] within the accuracy of 5% of a monolayer (ML).

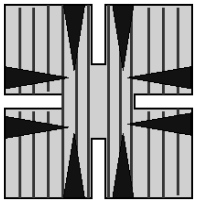

Fig. 2. Schematic of Si(557) samples prepared for DC conductance measurements via the eight $TiSi_2$ contact pads (marked by dark triangles). The lines indicate the stripe structure along the $[1\bar{1}0]$ direction

In our experiments, an extended four-point probe technique was used to conduct measurements (Fig. 2). The sample had eight pre-deposited macroscopic $TiSi_2$ contacts with a thickness of approximately 50 nm, which were separated pairwise by slits machined into the samples as shown in Figure 2. The separation between equivalent contacts was approximately 10 mm. Details about experimental procedures, thickness calibration, etc. can be found in ref. [20].

3. UHV electron beam lithography

3.1. Generation of Si(111)/Si oxide templates

The lithographical process used in order to form clean silicon windows within an oxide mask is shown in Figure 3, and has been described in detail by Ichikawa and

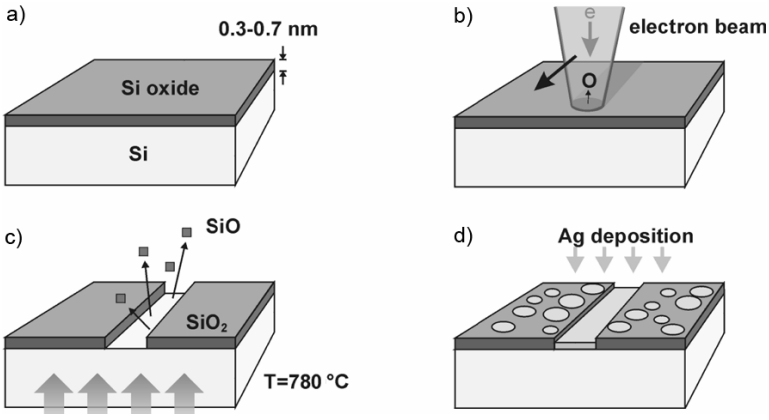

Fig. 3. E-beam lithography in UHV for the generation of silver nanostructures on silicon: a) thin thermal oxide on Si, b) electron-induced oxygen desorption in selected areas, c) void formation in the oxide via thermal desorption of SiO, d) Ag deposition leading to cluster formation in oxide areas and epitaxial Ag layers in the Si window

co-workers [21, 22]. An oxidized Si sample is irradiated with the electron beam of the SEM, thus partially reducing the SiO_2. Heating the sample to temperatures below the desorption temperature of SiO_2 leads to electron-beam induced selective thermal decomposition and the desorption of substoichiometric oxide. The width of the silicon windows depends on the primary electron dose and on the duration of subsequent heating. The total electron dose has to be optimised in order to obtain continuous Si windows while maintaining a good lateral resolution, as the plume of secondary electrons damages the oxide around the focus of the primary electron beam. In our experiments, the sample surface was irradiated at an angle of ca. 10° with respect to the surface plane, with a total surface electron dose of 100–200 C/cm^2 and an electron energy of 25 keV. After electron irradiation, the surface was heated up to 780 °C for 10–30 s. Besides the desorption of SiO, the etching of SiO_2 by bared Si leads to the decomposition of the oxide [17], which is seen by the continuous propagation of the oxide boundary and widening of the Si windows during prolonged heating. STM has demonstrated that the Si surface in the window areas is atomically clean.

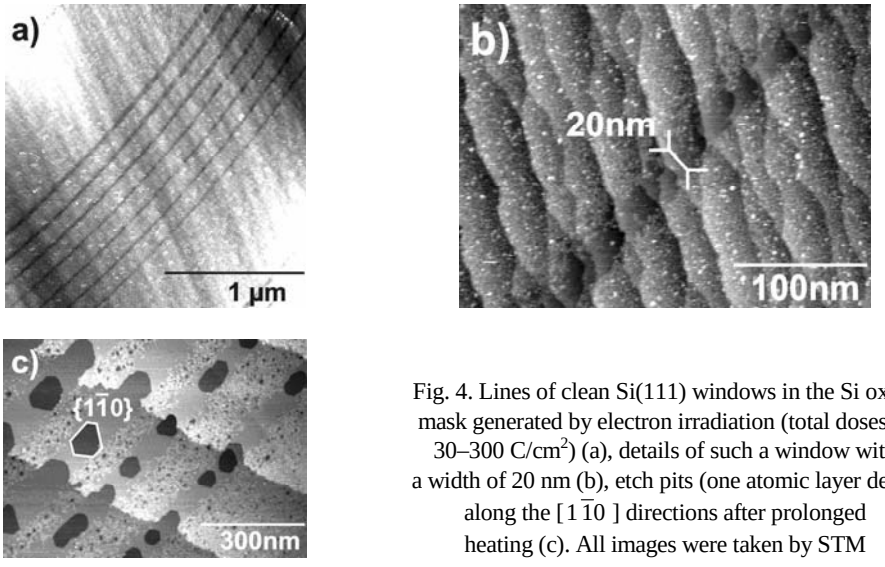

Fig. 4. Lines of clean Si(111) windows in the Si oxide mask generated by electron irradiation (total doses of 30–300 C/cm^2) (a), details of such a window with a width of 20 nm (b), etch pits (one atomic layer deep) along the [1 $\bar{1}$0] directions after prolonged heating (c). All images were taken by STM

Figure 4 shows line-shaped Si(111) windows, which were generated as templates for silver nanowires. With electron doses and the subsequent heating procedure optimised, the windows are continuous over a distance of several micrometers (Fig. 4a). We have generated the windows as narrow as 7 nm, while windows with the width of 20 nm as shown in Figure 4b are achieved regularly, also on substrates with a high step density, where the boundaries between oxide and windows often appear less sharp than on large single terraces. Figure 4c shows the result of prolonged heating after electron irradiation. The consumption of silicon from the bared areas during the decomposition of the oxide is evident by etch pits, which form especially at atomic steps, but also on flat Si(111) terraces in the window areas. The etch pits are one

atomic layer deep and their borders are probably aligned along the $[1\bar{1}0]$ directions, as observed, e.g., for Si(111) etching by water [23].

3.2. Ag epitaxy

The deposition of silver is the next step in the lithographical process. On bare silicon surfaces, silver grows epitaxially without forming silicides, making silver an ideal candidate for insulated metal nanostructures on silicon with a well-defined interface between metal and substrate. Silver on Si(111) exhibits a variety of growth modes. At room temperature, silver grows on Si(111) in the Stranski–Krastanov mode [24]. For silver deposition at low temperatures (<170 K) and various annealing procedures, however, a variety of metastable structures have been reported as a result of limited kinetics. STM studies have shown that silver grows layer by layer and is atomically flat at a sample temperature of 100 K [25].

Layer by layer growth has also been observed for deposition at 150–170 K [26]. With an increasing amount of the deposited material, interconnected islands, flat islands on top of a rough wetting layer, and continuous Ag layers have been observed when the surfaces were annealed to room temperature after deposition [27]. For the flat islands, preferred island heights have been identified. While the reason for the occurrence of different preferred heights in seemingly similar experiments (2 ML [26, 27, 28] and 6 ML [29]) has not been clarified yet, these magic heights are ascribed to the contribution of electron confinement within the metal layer to its free energy [28]. Spot profile analysis of LEED has shown that the continuous films consist of atomically flat grains, forming a small-angle (6°) rotational mosaic [30]. Grain diameters in the range 1.5–9.5 nm have been observed, depending on the substrate temperature during deposition and annealing.

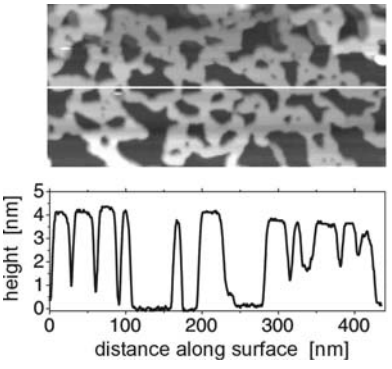

Fig. 5. STM of 10 ML of Ag on homogeneous Si(111) deposited at 130 K and annealed to room temperature. A percolated network of flat Ag islands is seen. Bottom: the line scan shows the narrow range of island heights around 4 nm

As an example from own measurements, Figure 5 shows an STM image of 10 ML Ag on a Si(111) substrate with a low step density and wide terraces in the range of 100 nm. The silver layer was deposited at 130 K and annealed to room temperature. Instead of a continuous Ag layer, we find a percolated network of islands, obviously

aligned along the low index directions of the substrate lattice (the STM image in Figure 5 is not corrected for thermal drift). The islands all have about the same height of 4 nm, with a variation of not more than ±15%, as shown by the line scan in Figure 5.

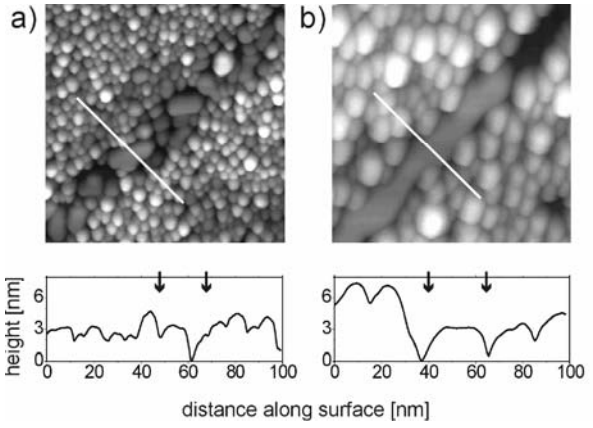

Fig. 6. STM images (size 150×150 nm^2) of 7 ML Ag deposited at 130 K on an Si(111) window in an oxide mask and annealed to a) 300 K and b) 700 K. Line scans along the white lines are shown below the STM image; 3 nm high Ag islands are seen in the window areas (borders of the window areas are marked by arrows). Sample bias –8 V, tunnelling current – 45 pA

Such a percolated network of islands of uniform height in a line-shaped Si window within an oxide mask would make a perfect nanowire. Figure 6a shows 7 ML Ag deposited on a Si(111)/Si oxide template at 130 K and annealed to room temperature. On the oxide area, spherical Ag nanoclusters have formed. The low surface free energy of the oxide surface inhibits the metal to wet the oxide. In the line-shaped Si(111) window, separate flat epitaxial islands with diameters in the range of 10–20 nm are detected. Obviously the growth mode in the narrow Si(111) window differs from that on bare Si(111), either due to defects such as nucleation sites or due to additional kinetic limitations. Apparently there is no significant transport of silver from the oxide area to the silicon window and vice versa. All material hitting the oxide area is consumed by the clusters. When the diffusion of silver atoms is restricted to the line-shaped Si(111) window, any coarsening of islands may be hindered.

Figure 6b shows the result of annealing 7 ML Ag deposited at 130 K on a line-shaped Si(111)/Si oxide template up to about 700 K. Comparison with Figure 6a reveals that the clusters on the oxide have coarsened. They still appear to be spherical in shape, indicating that they are not interconnected. Within the Si(111) window, a single elongated island has formed. The line scan depicted underneath the STM image reveals that the island is about 3 nm high, has a flat top, and is separated from the adjacent clusters in the oxide area.

Such nanowire sections have been observed with a total length up to 250 nm in our STM experiments. Figure 7 shows two nanowire sections with the width of 15–25 nm in adjacent Si(111) windows. The disturbances visible in the STM image are due to tip

changes, presumably induced by the detachment or attachment of silver atoms. Figure 7 also shows two islands in an 80 nm wide Si(111) window. Their lateral shape

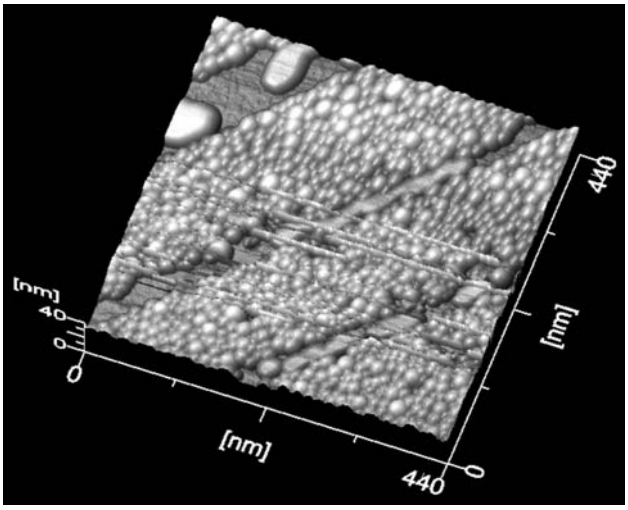

Fig. 7. A demonstration of wire-shaped Ag islands on an Si(111)/Si oxide mask in a narrow Si window (20 nm wide), and of 2D Ag islands in the wider window (80 nm)

appears as round as it is expected for silver deposition on bare silicon. Obviously, the tendency to form elongated nanowire sections is promoted by narrow Si windows. The role of the interface between the Si window and the oxide for Ag diffusion and the nucleation of Ag islands have not been investigated yet.

3.3. Ag wetting layer

Besides the 3 nm high nanowire sections, the Ag wetting layer in the Si(111) windows may be regarded as a metal nanowire in its own right. A surface state conductance in the range of $(5–10)\times10^{-5}\,\Omega^{-1}$ has been reported [31]. The $(\sqrt{3}\times\sqrt{3})R30^{\circ}$-Ag surface has a metallic surface state band as demonstrated by the observation of standing electron waves [32] and a two-dimensional plasmon [33]. It is particularly interesting, since, in contrast to the nanowire sections shown above, the wetting layer is limited in length only by the size of the Si(111) window. It is generated by annealing silver on Si(111) up to 700 K or by depositing at that temperature, and is composed of $(\sqrt{3}\times\sqrt{3})R30^{\circ}$-Ag domains [34].

Figure 8 shows the wetting layer formation in line-shaped Si(111) windows within an oxide mask. While only 0.5 ML Ag was deposited on the surface (deposition temperature 790 K, rate 0.13 ML/min) the window area is completely covered by the wetting layer, indicating Ag diffusion from the oxide to the window area. Pits due to

an Ag-induced surface reconstruction as well as islands of an additional layer can be seen in the window areas. The observed height differences within the windows always correspond to multiples of the Si(111) bilayer thickness. This observation indicates that the Si substrate is completely covered by the wetting layer, because the height difference between (7×7) and adjacent ($(\sqrt{3}\times\sqrt{3})$-Ag terraces would clearly differ from the Si bilayer thickness.

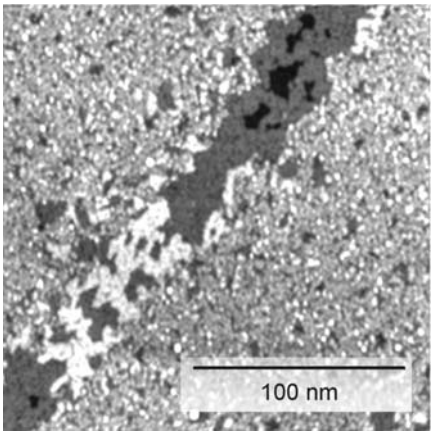

Fig. 8. STM image of 0.5 ML Ag deposited on a Si(111)/Si oxide template at 790 K at the rate of 0.13 ML/min. Due to migration from the surrounding oxide film, the Si window is covered by a continuous Ag wetting layer. In some parts (bright areas), a second Ag layer starts to grow

Concluding this section, we have shown that ultra thin crystalline metal nanostructures with characteristic lateral dimensions of much less than 20 nm can be generated on an insulating support using a combination of electron beam lithography in ultra-high vacuum and Ag epitaxy on Si(111). Details of the morphology of the metal deposit depend partly on the lateral constriction imposed by the oxide mask. Various thicknesses can be exploited starting with the wetting monolayer. Arbitrary shapes have not been tested explicitly yet, but seem to be easily feasible.

4. Conductance of Pb on Si(557) in the monolayer regime

In the Pb/Si(557) system, we start with a macroscopic measurement (distance between contacts was 10 mm, as already mentioned) of conductance on Si(557) samples that were prepared as described in the experimental section. For Pb layers evaporated onto the Si(557) samples at low temperature (below 25 K), the onset of measurable Pb-induced conductance was found to be close to 0.6 ML (ML given with respect to the density of Si surface atoms). Annealing to temperatures up to 600 K leads to an increase in conductance (except at coverages close to the percolation threshold, at which no effect was detected) and to the reversibility of conductance as a function of temperature. It is characterized by a weak anisotropy, with conductance normal to the steps being smaller by typically a factor of 1.5 than that perpendicular to them.

4.1. Conductance of an anisotropic Pb monolayer

This behaviour of a weak anisotropy and a gradual increase in conductance as a function of temperature is changed drastically by an annealing step to 640 K. The curves obtained after this high-temperature annealing step are now dominated by an abrupt change at the temperature of 78 K, separating a high-temperature region with small conductance anisotropy (ratio 1.5) from the low-temperature region characterized by high anisotropy (ratio 30–60). At temperatures below 78 K, a stepwise increase of $\sigma_{\parallel}$ by typically a factor of 3 is observed, whereas $\sigma_{\perp}$ drops sharply by a factor of 2–10. This final step of annealing obviously induces two effects. The monolayer undergoes an ordering process that is strongly activated, so that it occurs only during annealing to temperatures close to desorption. The alternative that a mixing of Si and Pb atoms in the first layers takes place, so that a surface silicide is formed, is unlikely judging by the STM data presented below.

The switching of conductance from low to high anisotropy was found to be independent of the initial Pb coverage, Θ_{ini}, after the high-temperature annealing step to 640 K, if it exceeded 1 ML. An example, with Θ_{ini} = 4 ML and annealing to 640 K, is shown in Figure 9. The vapour pressure of bulk Pb at 640 K is 7×10^{-7} mbar [35]. This means that after annealing for several minutes all multilayers of Pb must have been desorbed, directly explaining the insensitivity of the conductance results to the initial coverage in the multilayer range after the high-temperature annealing step. The fact that conductance can be switched, driven by temperature, from high to low anisotropy is therefore a property of the monolayer of Pb and/or of the conductance channels induced by the Pb monolayer on the Si(557) surface. The assumption of monolayer coverage is fully compatible with the STM results described below. As seen there, atomic wire-like structures are formed after this high-temperature annealing step, which are responsible for the anisotropy of the conductance observed at low temperature.

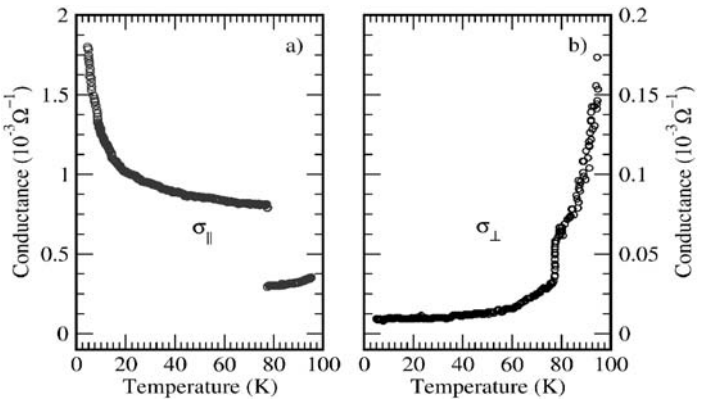

Fig. 9. DC conductance as a function of temperature after the adsorption of 4 ML and annealing to 640 K, measured along the [112] ($\sigma_{\perp}$) and [110] direction ($\sigma_{\parallel}$)

For the "optimal" conductance curves after annealing, i.e. those obtained with initial Pb coverages of 3ML or more, $\sigma_{\parallel}$ below T_c can be well described by $\sigma_{\parallel} = A + B \times T^{-n}$, with n close to 1 (see Fig. 10). This decrease of $\sigma_{\parallel}$ as a function of temperature contrasts with the increase above the jump at 78 K, indicating thermally activated behaviour above this threshold. $\sigma_{\perp}$, on the other hand, is thermally activated in both temperature regimes. Whereas for $\sigma_{\perp}$ defects may play some role as mentioned, the optimal conductance values of $\sigma_{\parallel}$ did not vary between different samples, and neither the abrupt changes seen in the conductance at 78 K nor the temperature dependence of $\sigma_{\parallel}$ below 78 K can be explained by defects. While we cannot expect that a surface is free of defects like point defects or steps, at least on the atomic scale, such defects cannot act as effective scatterers along Pb chains.

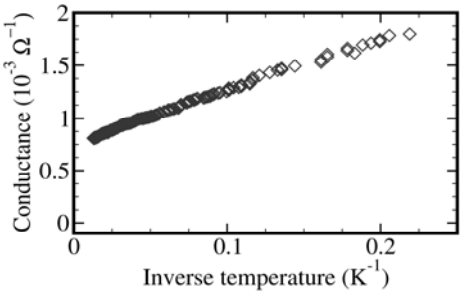

Fig. 10. Conductance curve $\sigma_{\parallel}$ from Fig. 9 below 78 K plotted versus $1/T$

This property changes when the coverage is so small that only very few chains are left, which form a conducting channel between the contacts of our experimental setup. Here there is a high probability for more extended defects that can only be surmounted by thermal activation. This scenario seems to be valid at a Pb concentration of 0.8 ML and lower. The observed jump in conductance at T_c and the increase of $\sigma_{\parallel}$ as a function of temperature below T_c is compatible with the assumption of sections of isolated chains separated by gaps, which can still be surpassed by thermal activation.

4.2. Conductance and geometrical properties

The clean Si(557) surface (not shown) corresponds closely to that shown in Ref. [36]. These results are supported by LEED, which shows the characteristic 7×7 reconstruction of (111) facets [37, 38] and the known 2×1 reconstruction of Si(112) surfaces [39]. Microscopically, the (111) facets are separated by 3-fold steps. The typical terrace lengths that can be obtained on our samples are around 200 nm. Neighbouring (111) terraces are separated by steps that correspond to steps of 6 and 9 atomic heights. Kinks in the step edges can also be seen. In any case, these extended line defects remain on the atomic level. Even with a low density of terraces, many thousand steps intersect the path between two contacts in our experimental setup.

As judged from a large series of adsorption experiments and various annealing steps, adsorbed Pb leaves the terrace structure of the Si(557) sample unaltered. After

the adsorption of Pb at low temperatures and annealing for 15 minutes at 640 K, STM reveals the characteristic chain structure shown in Figure 11, with an average spacing between the chains of 14 Å. This chain structure is found only after the high-temperature annealing step, whereas a more irregular bumpy hill-and-valley structure is found at lower annealing temperatures. The chain structure is destroyed by annealing at 650 to 660 K. Thus there is a close correlation between the chain structure observed here and the strongly anisotropic conductance behaviour found below 78 K at one monolayer coverage. The surface shown in Figure 11 is completely covered with Pb, and all chain structures are Pb-induced.

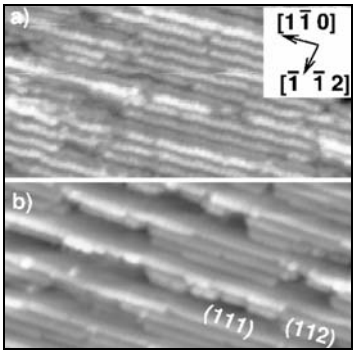

Fig. 11. STM images (40 ×20 nm^2) of the chains after the adsorption of 10 ML Pb/Si(557) and annealing to 640 K. The temperatures of measurement were a) 40 K and b) 100 K

It seems that two different kinds of chains on the surface can be discriminated, which may be attributed to chain formation on the two facets. As judged from chains ending at small clean 7×7 islands, the bright chains must be located on the (111) facets or at the edge between the two facets, whereas the other chains must be on the (112) facets. The step-step distance there is around 10 Å on the clean surface, i.e. it is significantly smaller than the Pb–Pb chain separation. This enlarged chain distance can be caused by effective lateral repulsion between wires, so that they are not located at equivalent positions on each mini-terrace, supporting the assumption of coupled chains. As an alternative, step separations on the original (112) facets, induced by Pb and high-temperature annealing, could be enlarged at the expense of the extension of the (111) facet. If this rearrangement of the local step structure is necessary, it would explain the necessity for high-temperature annealing. In any case, it is obvious that each Pb wire consists of more than one atomic chain in order to accommodate a Pb concentration of approximately 1 ML. Even at a temperature of 40 K these chains contain a lot of defects that limit the typical undistorted length of a chain to 30–100 nm, with the bright chains containing typically less defects than the others. Whereas the chain separation has a well-defined value, the stacking sequence normal to the chains seems to follow the local variation of facet sizes, so that it is not long range ordered.

The abrupt changes observed at T_c = 78 K are directly correlated with an intriguing structural phase transition that does not change the chain structure itself, as seen in Figure 11a, b (the images there were taken at 40 K and 100 K, respectively, i.e. below and above the phase transition). The effects associated with the phase transi-

tion, however, are most clearly visible in one-dimensional Fourier transformations along and perpendicular to the chain structures. The results are shown in the top part of Figure 12 for a typical single scan. Averages over an area of 40×40 nm^2 are shown in a log scale in panels a) and b) of this figure.

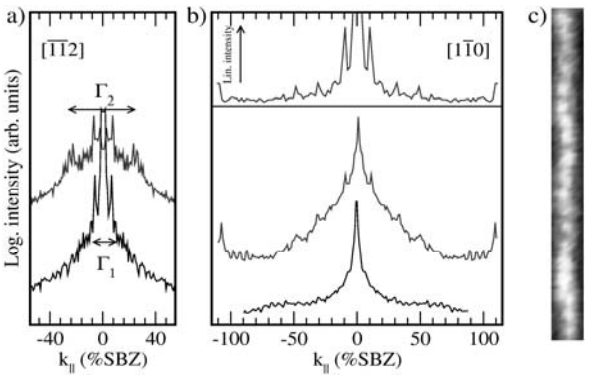

Fig. 12. Fourier transformations of line scans from STM pictures at 100 K (lower curves) and at 40 K for the direction perpendicular (a) and parallel (b) to the steps. The top graph of b) shows the Fourier transform of a single atomic chain in a linear scale. Such a chain is shown in c) in real space.

In the direction normal to the chains (left part of Fig. 12), for both temperatures, a clearly enhanced Fourier component Γ_1 is seen, which corresponds to an average hill and valley spacing of 57 Å, i.e., to the periodicity of the clean Si(557) surface. For T = 40 K an additional, but considerably broader component Γ_2 is seen, which corresponds to the 14 Å spacing of the Pb wires.

Parallel to the chain structure the Fourier transforms calculated from 40 K STM images show, in contrast to those of STM images taken 100 K, an additional periodicity with a fundamental wavelength of 10 times the next neighbour separation of Si, along with higher harmonics. The peak at 110% SBZ corresponds to the nearest -neighbour spacing of Pb with approximately the bulk Pb lattice constant. Little correlation of this periodicity between different chains was found. The modulation of the chains is weak, as is obvious from Figures 11 and 12. It cannot be induced by missing Pb atoms, as seen, e.g., for the case of Ga on Si(112) [40], but rather by a modulation of the local position of adatoms, most likely due to the misfit between Si and Pb lattice constants. Since the lattice constant of Si is 9% larger than the lattice constant of Pb, registry between the ideal Si and Pb lattices is obtained every ten Si atoms, which agrees well with the ten-fold periodicity found.

Approaching T_c from higher temperatures, it seems to be the locking of the chains into the high order commensurate superperiodicity, coupled with a regular separation between the Pb induced chains, that causes the switching from low to high anisotropy and into a highly conducting state along the chains with a “metallic”-like temperature dependence.

Electrical conduction in this system occurs in the partially filled band of Si surface states, which is modified by the adsorbed Pb chains that impose their symmetry and their periodicity onto this band. As judged from the low electrical conductivity in the $[1\bar{1}0]$ direction in the low temperature regime and its temperature dependence, coupling is rather weak between the chains, and the electrons close to E_F are preferably localized within one chain. Along the chains, the 10-fold periodicity imposes a mesoscopic modulation that effectively backfolds the band structure of the unmodulated chains. Thus the effective Fermi wavelength λ_F cannot be smaller than twice the modulation period, but may be even much longer. The corresponding effective increase of λ_F can rationalize why these electrons are quite unsusceptible to local defects on the atomic scale along the chains. Although defects are present, they do not lead to the localization of the conducting electrons along the wires down to temperatures of 4 K.

Passing the phase transition, the conductance normal to the Pb chains drops sharply, but here the activated temperature behaviour seen above the phase transition remains also at temperatures below. This strong anisotropy means a strongly enhanced localization of the electrons in the direction normal to the wires, which is destroyed at higher temperatures when the spatial correlation between the wires is lost. We note that above the phase transition both $\sigma_\parallel$ and $\sigma_\perp$ return to activated behaviour, i.e., to an increased sensitivity to local defects. This fits qualitatively to the model of a much shorter effective λ_F in both directions in the high-temperature phase than at low temperatures.

The conductance behaviour in the highly anisotropic state may be a candidate for Luttinger liquid behaviour in coupled chains [41]. Since we observe quasi one-dimensional conductivity down to 4 K, the energy scales for two-dimensional coupling are extremely small (of the order of a few kelvin or even less) compared to standard quasi one-dimensional conductors [42]. This suggests that we have found a system with almost ideal one-dimensional conductive properties. On the other hand, the quantitative properties deviate clearly from predictions for DC conductance in a Luttinger liquid, even in the presence of defects [43], since a rather high background must be subtracted from the data in order to obtain a simple power law. The meaning of the (still one-dimensional) “background” conductance must remain open at this point. Significant coupling between the chains must also exist, as indicated by the nonzero value of $\sigma_\perp$ and its increase as a function of temperature [42, 44]. Whether defects such as additional steps are important for these deviations cannot be answered at the moment.

Summarizing, our results show that quasi-metallic quasi one-dimensional conductance with extremely high values of conductance can be obtained with only one monolayer of Pb that forms a chain structure on Si(557). Conductance can be switched from low to high anisotropy by an order-disorder phase transition with a mesoscopic modulation period. Thus, and in strong contrast to the metal-insulator transitions seen in most systems when temperature is decreased, we observe transi-

tions from a quasi one-dimensional metal at low temperature to an insulator (with temperature-activated behaviour) at high temperature parallel to the Pb chains, and an insulator–metal transition in the direction normal to the Pb chains.

Both sets of experiments described in this paper emphasize the power of ultimate nanostructuring for gaining new insight into the physics of low-dimensional systems. Especially the role of defects must be clarified in further experimental studies on a very small scale, so that individual defects and their influence on conductance can be directly detected. Such experiments seem to be feasible with such nanoscale techniques.

References

[1] VOIT J., Rep. Prog. Phys., 58 (1995), 977.
[2] LUTTINGER J.M., Phys. Rev., 119 (1960), 1153.
[3] HALDANE F.D., J. Phys. C. Solid State Phys., 14 (1981), 2585.
[4] PEIERLS R.E., *Quantum theory of solids*, Clarendon, Oxford, 1955.
[5] JEROME D., Chemica Scripta, 17 (1981), 13.
[6] CLAESSEN R., SING M., SCHWINGENSCHLÖGL U., BLAHA P., DRESSEL M., JACOBSEN C.S., Phys. Rev. Lett., 88 (2002), 096402.
[7] ROTH S., GRAUPNER W., Synthetic Metals, 57 (1993), 3623.
[8] HIMPSEL F.J., ALTMANN K.N., BENNEWITZ R., CRAIN J.N., KIRAKOSIAN A., LIN J.-L., MCCHESNEY J.L, J. Phys. C, 13 (2001), 11097.
[9] TANIKAWA T., MATSUDA I., KANAGAWA T., HASEGAWA S., Phys. Rev. Lett., 93 (2004), 016801.
[10] PETKOVA A., WOLLSCHLÄGER J., GÜNTER H.-L., HENZLER M., Surf. Sci., 482–485 (2000), 922.
[11] PFENNIGSTORF O., PETKOVA A., GÜNTER H.-L, HENZLER M., Phys. Rev. B, 65 (2002), 045412.
[12] VILFAN I., HENZLER M., PFENNIGSTORF O., PFNÜR H., Phys. Rev. B, 66 (2002), 241306.
[13] VILFAN I., PFNÜR H., Eur. Phys. J. B, 36 (2003), 281.
[14] RICCI D.A., MILLER T., CIANG T.-C., Phys. Rev. Lett., 93 (2004), 136801.
[15] WATANABE H., KATO K., UDA T., FUJITA K., ICHIKAWA M., KAWAMURA T., TERAKURA K., Phys. Rev. Lett. 80 (1998), 345.
[16] MATSUDO T., OHTA T., YASUDA T., NISHIZAWA M., MIYATA N., YAMASAKI S., SHKLYAEV A.A., ICHIKAWA M., Appl. Phys., 91 (2002), 3637.
[17] MIYATA N., WATANABE H., ICHIKAWA M., Phys. Rev. Lett., 84 (2000), 1043.
[18] KATAYAMA M., WILLIAMS R., KATO M., NOMURA E., AONO M., Phys. Rev. Lett., 66 (1991), 2762.
[19] CZUBANOWSKI M., TEGENKAMP C., PFNÜR H., Appl. Phys. Lett., 84 (2004), 350.
[20] TEGENKAMP C., KALLASSY Z., GÜNTER H.-L., ZIELASEK V., PFNÜR H., Eur. Phys. J. B, 43 (2005) 557.
[21] MARUNO S., FUJITA S., WATANABE H., ICHIKAWA M., J. Appl. Phys., 82 (1997), 639.
[22] FUJITA S., MARUNO S., WATANABE H., ICHIKAWA M., J. Vac. Sci. Technol. B, 16 (1998), 2817.
[23] PIETSCH G., KÖHLER U., HENZLER M., Chem. Phys. Lett., 197 (1992), 346.
[24] LOENEN E.V., IWAMI M., TROMP R., VAN DER VEEN J., Surf. Sci., 137 (1984), 1.
[25] MEYER G., REIDER K.-H., Appl. Phys. Lett., 64 (1994), 3560.
[26] KIMBERLIN K., RUTTER G., NAGLE L., ROOS K., M.TRINGIDES, Surf. Interface Anal., 35 (2003), 1069.
[27] JIANG C.-S., YU H., SHIH C.-K., EBERT P., Surf. Sci., 518 (2002), 63.
[28] GAVIOLI L., KIMBERLIN K., TRINGIDES M., WENDELKEN J., ZHANG Z., Phys. Rev. Lett., 82 (1999), 129.
[29] HUANG L., CHEY S.J., WEAVER J., Surf. Sci., 416 (1998), L1101.
[30] MORESCO F., ROCCA M., HILDEBRANDT T., HENZLER M., Surf. Sci., 463 (2000), 22.
[31] JIANG C.-S., HASEGAWA S., INO S., Phys. Rev. B, 54 (1996), 10389.
[32] SATO N., TAKEDA S., NAGAO T., HASEGAWA S., Phys. Rev. B, 59 (1999), 2035.

[33] NAGAO T., HILDEBRANDT T., HENZLER M., HASEGAWA S., Phys. Rev. Lett., 86 (2001), 5747.
[34] WAN K., LIN A., NOGAMI J., Phys. Rev. B, 47 (1993), 13700.
[35] *Vacuum Physics and Technology*, Vol. 14, *Methods in Experimental Physics*, G.L. Weissler (Ed.), Academic Press, New York, 1979.
[36] KIRAKOSIAN A., BENNEWITZ R., CRAIN J.N., FAUSTER TH., LIN J.-L., PETROVYKH D.Y., HIMPSEL F.J., Appl. Phys. Lett., 79 (2001), 1608.
[37] HOQUE E., PETKOVA A., HENZLER M., Surf. Sci., 515 (2002), 312.
[38] HENZLER M., ZHACHUK R., Thin Solid Films, 428 (2003), 129.
[39] WANG X.-S., WEINBERG W.H., Surf. Sci., 314 (1994), 71.
[40] BASKI A.A., ERWIN S.C., WHITMAN L.J., Surf. Sci., 423 (1999), L265.
[41] BIERMANN S., GEORGES A., GIAMARCHI T., LICHTENSTEIN A. [in:] *Strongly Correlated Fermions and Bosons in Low Dimensional Disordered Systems*, I.V. Lerner, B.L. Althsuler, V.I. Falko, T. Giamarchi (Eds.), Kluwer, Dordrecht, 2002, p. 81.
[42] DRESSEL M., PETUKHOV K., SALAMEH B., ZORNAZA P., GIAMARCHI T., Phys. Rev. B, 71 (2005), 075104.
[43] GIAMARCHI T., SCHULZ H., Phys. Rev. B, 37 (1998), 325.
[44] GEORGES A., GIAMARCHI T., SANDLER N., Phys. Rev. B, 61 (2000), 16393.

Received 23 September 2004
Revised 16 November 2004

Materials Science-Poland, Vol. 23, No. 4, 2005

Photonic crystals: a novel class of functional materials

A. MODINOS[1], N. STEFANOU[2*]

[1]Department of Physics, National Technical University of Athens,
Zografou Campus, GR-157 80 Athens, Greece

[2]University of Athens, Section of Solid State Physics, Panepistimioupolis,
GR-157 84 Athens, Greece

Photonic crystals are inhomogeneous materials whose dielectric properties vary periodically in space on a macroscopic scale. These materials have novel and interesting properties concerning both basic physics and technological applications. After a brief description of the main properties of photonic crystals, we present some specific applications related to wave guiding and Anderson localization of light due to stacking faults in these crystals.

Key words: *photonic crystals; optical wave guide; Anderson localization*

1. Introduction

Photonic crystals are composite materials whose dielectric properties vary periodically in space on a macroscopic scale [1–3]. For example, a photonic crystal may consist of non-overlapping dielectric or metallic spheres arranged periodically in a host medium with a different dielectric function. When the diameters of the spheres and the lattice constant are of the same order as the wavelength of light, we cannot describe the optical properties of the composite medium using an effective-medium approximation (this approximation holds when the wavelength of light is much larger than the lattice constant). Therefore, for a given photonic crystal (and a given lattice constant) we expect to see qualitatively new phenomena – different from those observed in a homogeneous medium – at sufficiently high frequencies of the electromagnetic (EM) field and when the wavelength of the EM waves is about the same or smaller than the lattice constant. At these frequencies, one expects to find phenomena that can be derived from the multiple scattering of light (we shall use the term light to stand for any EM wave in what follows) by a multitude of scatterers in the medium.

* Corresponding author, e-mail: nstefan@cc.uoa.gr

Having in mind a photonic crystal of non-overlapping spheres in a host medium, we can state the basic problem related to the modes of propagation of light in the infinite crystal as follows. At a given frequency ω the wave scattered from a particular sphere of the crystal is generated by the wave incident on this sphere, which consists of the waves scattered by all other spheres in the crystal. Naturally, this leads to a homogeneous system of equations (essentially the Maxwell equations in some form), which may or may not have physical solutions at the given frequency, i.e. solutions remaining finite everywhere in the infinite crystal. It turns out, as expected, that these physical solutions are of the Bloch wave type, familiar from solid state physics. There, the Bloch waves are solutions of the Schrödinger field the electron sees in a periodic array of atoms. In the present case, the Bloch waves are EM waves in the composite medium under consideration. It turns out that there are regions of frequency over which propagating modes of the EM field cannot exist in the composite medium (an appropriate photonic crystal), in the same way that electron states cannot have energies in the gaps of the energy band structure of a crystalline solid.

2. A photonic crystal with an absolute gap

In Figure 1, we show an example of a frequency band structure of a three-dimensional photonic crystal, which exhibits an absolute frequency gap. It consists of non-overlapping spheres with a dielectric constant ε_s = 12.96 in air (ε = 1). The spheres are arranged as in a diamond crystal with a lattice constant a. We view the

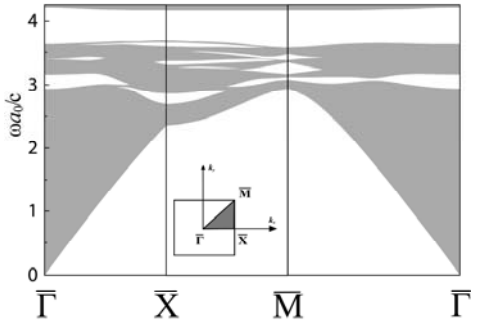

Fig. 1. Projection of the frequency band structure of a crystal consisting of dielectric spheres (ε_s = 12.96, S/a_0 = 0.25), arranged as in the structure of diamond in air (ε = 1), onto the SBZ of the (001) surface (shown in the inset)

crystal as a stack of layers parallel to the xy plane. The periodicity of the layers parallel to this plane is described by a two-dimensional square lattice defined by the primitive vectors $\mathbf{a}_1 = a_0(1,0,0)$ and $\mathbf{a}_2 = a_0(0,1,0)$, where $a_0 = a\sqrt{2}/2$ is the distance between second nearest neighbours in the diamond structure. A basis of two spheres with a radius of $S = a_0/4$, centred at (0,0,0) and $a_0(1/2,0,\sqrt{2}/4)$, defines the two planes of spheres of a layer. The (n+1)th layer along the z axis is obtained from the nth layer by a simple translation, de-

scribed by the primitive vector $\mathbf{a}_3 = a_0(1/2,1/2,\sqrt{2}/2)$. What Figure 1 actually shows, is the projection of the frequency band structure onto the surface Brillouin zone (SBZ) of the (001) surface of this crystal, in particular along the symmetry directions of the SBZ. For any value of $\mathbf{k}_\parallel$ (the reduced wave vector parallel to the (001) surface), the figure shows the regions of frequency over which at least one propagating mode of the EM field exists in the crystal (shaded regions) and those regions (gaps) where no such modes exist (blank regions). It is clear that an absolute frequency gap exists between $\omega a_0/c = 3.68$ and $\omega a_0/c = 4.16$ (c is the velocity of light in vacuum). We verified that this is indeed true by calculating the band structure at a sufficient number of $\mathbf{k}_\parallel$ points within the SBZ, using a layer multiple-scattering computer code [4, 5]. Over the region of an absolute frequency gap, there can be no propagating wave in the crystal in any direction of propagation, and a slab of the material (sufficiently thick) behaves like a perfect mirror for the light at all incidence angles. The technological applications of this property of photonic band gaps in the construction of useful devices in optoelectronics can be far-reaching. For example, a wave guide with walls made of such a material is an obvious possibility, and a lot of progress has already been made in this direction, especially in relation to two-dimensional wave guides [6].

3. Coupled resonator optical wave guides

A different type of wave guide, intrinsic to photonic crystals, which has come to be known as the coupled cavity wave guide (CCW) or coupled resonator optical wave guide (CROW), was suggested by us in 1998 [7] and, independently, by Yariv et al. a year later [8]. Imagine a photonic crystal with an absolute frequency gap, such as the one described in Figure 1. If we replace one of the spheres by a slightly different one

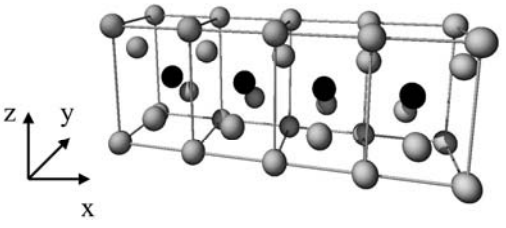

Fig. 2. A diamond structure of spheres. A linear chain of defect spheres (black spheres) is introduced along the [110] direction, which is taken as the x axis

(a defect sphere), we obtain a localized state of the EM field within and about this sphere at a frequency within the gap. In reality, one obtains a degenerate state, but for the sake of simplicity we shall assume that we have just one non-degenerate state. If a photon of this frequency is somehow generated within this sphere, it will stay there for ever in the absence of absorption. Now imagine a periodic chain of such spheres along a straight line, as shown in Figure 2. There is bound to be some coupling between these spheres (a hopping interaction). This leads to a one-dimensional narrow band of states, with a width depending on the strength of the coupling between the spheres. Light can now propagate along the chain with a (group) velocity much

smaller than that in a homogeneous medium. This velocity can be, to some degree, adjusted to suit a number of purposes. It is also interesting to note that, under certain conditions, the chain can consist of a number of sections joining at angles, and light will still flow through it without being reflected at the corners, which is indeed remarkable and potentially very useful in the design of integrated optoelectronic systems. There is presently a lot of activity related to CCWs [9–16], and hopefully there will be interesting applications, too.

4. Anderson localization of light

We would like to close this short review with a brief reference to a quite different problem, which shows the richness of photonic crystals as an area of research. We have established that a random introduction of stacking faults in a slab of an inverted-opal photonic crystal leads to Anderson localization of light (localization due to disorder) over certain frequency regions around the absolute frequency gap [17, 18]. We show this by calculating the transmission coefficient of light incident on a slab of the material as a function of the thickness D of the slab. When Anderson localization occurs, the ensemble-averaged logarithm of the transmittance of the slab $\langle \ln T \rangle$ diminishes with thickness as $\langle \ln T \rangle = -2D/l$, which allows us to determine the localization length l at various frequencies of the incident light. Hopefully such systems can be built in the laboratory [19, 20] in which case the possibility arises to directly compare theory and experiment at a quantitative level, something that is indeed quite rare in studies of Anderson localization phenomena.

References

[1] JOANNOPOULOS J.D., MEADE R.D., WINN J.N., Photonic *Crystals: Molding the Flow of Light*, Princeton University Press, Princeton, NJ, 1995.
[2] *Photonic Crystals and Light Localization in the 21st Century*, C.M. Soukoulis (Ed.), Kluwer, Dordrecht, 2001.
[3] SAKODA K., Optical Properties of Photonic Crystals, Springer-Verlag, Berlin, 2001.
[4] STEFANOU N., YANNOPAPAS V., MODINOS A., Comput. Phys. Commun., 113 (1998), 49.
[5] STEFANOU N., YANNOPAPAS V., MODINOS A., Comput. Phys. Commun., 132 (2000), 189.
[6] JOHNSON S.G., JOANNOPOULOS J.D., *Photonic Crystals: The Road from Theory to Practice*, Kluwer, Dordrecht, 2002.
[7] STEFANOU N., MODINOS A., Phys. Rev. B, 57 (1998), 12127.
[8] YARIV A., XU Y., LEE R. K., SCHERER A., Opt. Lett., 24 (1999), 711.
[9] BAYINDIR M., TEMELKURAN B., OZBAY E., Phys. Rev. Lett., 84 (2000), 2140.
[10] OLIVIER S., SMITH C., RATTIER M., BENISTY H., WEISBUCH C., KRAUSS T., HOUDRE R., OESTERLE U., Opt. Lett., 26 (2001), 1019.
[11] MOOKHERJEA S., YARIV A., Phys. Rev. E, 65 (2002), 056601.
[12] MOOKHERJEA S., YARIV A., Phys. Rev. E, 66 (2002), 046610.
[13] SOLTANI M., ADIBI A., XU Y., LEE R.K., Opt. Lett., 28 (2003), 1978.
[14] HAPP T.D., KAMP M., FORCHEL A., GENTNER J.-L., GOLDSTEIN L., Appl. Phys. Lett., 82 (2003), 4.

[15] MALKOVA N., GOPALAN V., J. Opt. Soc. Am. B, 21 (2004), 1679.
[16] YANIK M.F., FAN S., Phys. Rev. Lett., 92 (2004), 083901.
[17] YANNOPAPAS V., STEFANOU N., MODINOS A., Phys. Rev. Lett., 86 (2001), 4811.
[18] YANNOPAPAS V., STEFANOU N., MODINOS A., Phys. Rev. B, 68 (2003), 193205.
[19] VLASOV YU.A., BO X.Z., STURM J.C., NORRIS D.J., Nature (London), 414 (2001), 289.
[20] HOOGENBOOM J.P., VAN LANGEN-SUURLING A.K., ROMIJN H., VAN BLAADEREN A., Phys. Rev. Lett., 90 (2003), 138301.

Received 10 December 2004
Revised 14 April 2005

Materials Science-Poland, Vol. 23, No. 4, 2005

Neutron diffraction study of $Mn_3Fe_4V_6O_{24}$

A. BEZKROVNYI[1], N. GUSKOS[2,3], J. TYPEK[3*], N.YU. RYABOVA[1], M. BOSACKA[4], A. BLONSKA-TABERO[4], M. KURZAWA[4], I. RYCHLOWSKA-HIMMEL[4], G. ZOLNIERKIEWICZ[3]

[1]Frank Laboratory of Neutron Physics, Joint Institute for Nuclear Research, 141980 Dubna, Russia

[2]Solid State Physics, Department of Physics, University of Athens, Panepistimiopolis, 15 784 Zografos, Athens, Greece

[3]Institute of Physics, Szczecin University of Technology, al. Piastów 17, 70-310 Szczecin, Poland

[4]Department of Inorganic and Analytical Chemistry, Szczecin University of Technology, al. Piastow 42, 71-065 Szczecin, Poland

$Mn_3Fe_4V_6O_{24}$ compound was prepared using the solid-state reaction method. The magnetic and crystal structural studies were carried out by using neutron diffraction methods at the temperatures of 10 and 290 K. Down to 10 K no long-range magnetic order was observed. Essential differences in the positions of metal ions were observed as compared to similar systems (β-$Cu_3Fe_4V_6O_{24}$ and $Zn_3Fe_4V_6O_{24}$) investigated by X-ray and neutron diffraction methods. In this system, a disordering process involving iron and manganese atoms in M(2), M(3), M(4) cation sites was found, which could be responsible for the significant differences in the physical properties observed for this type of compound.

Key words: neutron diffraction; crystal structure

1. Introduction

The knowledge of the crystallographic and magnetic structures of multi -component vanadate oxide compounds is very important for better understanding their interesting physical properties [1–6]. Neutron diffraction studies of $Zn_2FeV_3O_{11}$ and $Mg_2FeV_3O_{11}$ compounds have shown that iron(III) and zinc/magnesium ions are disordered in their corresponding sublattices, and that the distributions on octahedral and trigonal bipyramidal sites are non-statistical [3, 5]. The $M_2FeV_3O_{11}$ (M = Zn and Mg) compounds synthesized in the reaction of $FeVO_4$ with pyrovanadates $M_2V_2O_7$ exhibited disorder in cation sites [2, 3, 5]. Recently, $M_3Fe_4V_6O_{24}$ (M = Zn, Co(II),

* Corresponding author: e-mail: typjan@ps.pl

Mg, Mn) compounds have been obtained as the products of reactions between $FeVO_4$ and $M_2V_2O_8$. These compounds crystallize in the triclinic space group $P\bar{1}$ [1, 7–9]. X-ray analysis has not revealed any disorder among iron(III) and divalent (Zn, Co, Mg) ions in the compounds.

The aim of this paper is to report a study of the crystal and magnetic structures of $Mn_3Fe_4V_6O_{24}$ compound, which was prepared in reaction between the MnO, Fe_2O_3, and V_2O_5. Neutron diffraction was used, and special care was taken to search for possible disorder in the cation sites.

2. Experimental

A powder sample of $Mn_3Fe_4V_6O_{24}$ was synthesized by the solid-state reaction method from appropriate metal oxides. MnO, V_2O_5, and Fe_2O_3 powders where mixed in a 3:3:2 molar ratio, according to the following reaction:

$$3MnO + 3V_2O_5 + 2Fe_2O_3 \rightarrow Mn_3Fe_4V_6O_{24}$$

The powders were mixed, pressed into pellets, and calcinated in air at 600 °C for 24 h, at 700 °C for 24 h, and at 750 °C for 24 h (twice). After each heating stage, the sample was slowly cooled down to room temperature, ground, and analysed by the differential thermal analysis (DTA) and X-ray diffraction (XRD), until the formation of a single phase sample could be verified. The obtained compound crystallized in the triclinic space group $P\bar{1}$, forming a dark brown-coloured powder, with its melting point at 1163 K, as determined by DTA.

The crystal structure of the $Mn_3Fe_4V_6O_{24}$ was investigated by the neutron powder diffraction method using a high luminosity DN-2 time-of-flight powder diffractometer on a IBR-2 pulsed reactor at the FLNF Frank Laboratory of the Joint Institute of Nuclear Research (JINR) in Dubna, Russia. The neutron diffraction patterns were measured with a resolution determined by the width of the pulse from a neutron source, $\Delta d/d = 0.01$, with interplanar spacing d_{hkl} ranging from 1 to 20 Å. The diffraction patterns were collected by using approximately 10 g of the investigated sample, enclosed in a thin-walled aluminium cylindrical container 8 mm in diameter. The counting time was 15 h for each temperature. Diffraction patterns were obtained at 10 K and 290 K, and analysed by the program MRIA (Multi-Phase Rietveld Analysis) [10] using X-ray diffraction data for β-$Cu_3Fe_4(VO_4)_6$ as a starting model for Rietveld refinement [1, 11].

3. Results and discussion

Figure 1 shows the neutron diffraction spectra of different profiles obtained at 10 and 290 K for the $Mn_3Fe_4V_6O_{24}$ compound. The diffraction patterns did not show any

long-range magnetic ordered state at the investigated temperatures. Figure 2 presents a neutron diffraction spectrum of $Mn_3Fe_4V_6O_{24}$ and a simulated spectrum calculated by the program MRIA ($\chi^2 = 1.75$). A very good agreement was obtained between the experimental and calculated spectra.

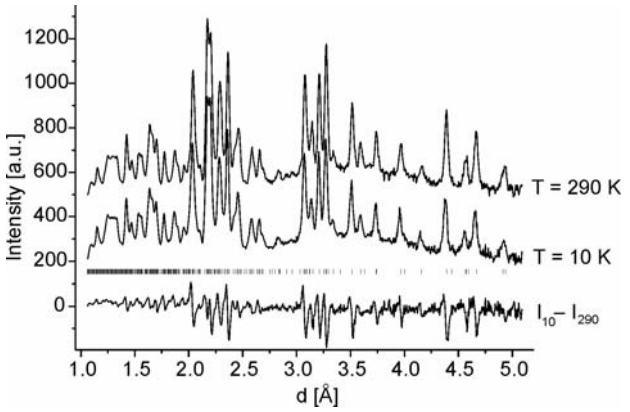

Fig. 1. Experimental neutron diffraction spectra of $Mn_3Fe_4V_6O_{24}$ obtained in the range of d_{hkl} up to 11 Å at 290 K, 10 K and the difference of their intensities

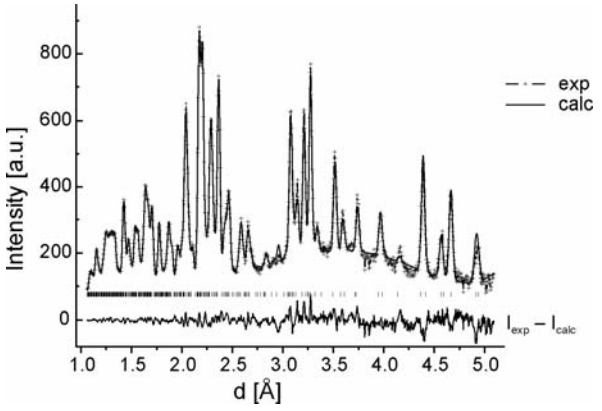

Fig. 2. Neutron diffraction spectrum of $Mn_3Fe_4V_6O_{24}$ and a simulated spectrum obtained by the MRIA program ($\chi^2 = 1.75$) at 290 K

$Mn_3Fe_4V_6O_{24}$ is a homeotype of β-$Cu_3Fe_4V_6O_{24}$ [11], since the structure is built from $M(1)O_6$ polyhedra, $M(2)O_5$ trigonal bipyramids, $M(3)O_6$ and $M(4)O_6$ octahedra, and isolated VO_4 tetrahedra. Fe_2O_{10} octahedral dimers alternate with $M(2)O_5$ bipyramids to form edge-sharing chains (Fe(1) and Fe(2) at the M(3) and M(4) positions, respectively). The $M(1)O_6$ octahedra are located between chains and share corners with both $M(2)O_5$ and Fe_2O_{10} units.

Figure 3 presents a projection of the structure along the [100] axis. M(1) ions are located within the [100] tunnels. The distance between M(1) ions is $d_{M(1)–M(1)} = 6.703$ Å in

the $Mn_3Fe_4(VO_4)_6$ compound. The $M(2)O_5$ bipyramid is connected with the $M(1)O_6$ polyhedron, with one Fe(1) octahedral dimer and one Fe(2) dimer through the O(11) atom, O(7)–O(6) edge, and O(4)–O(8) edge, respectively (Fig. 4).

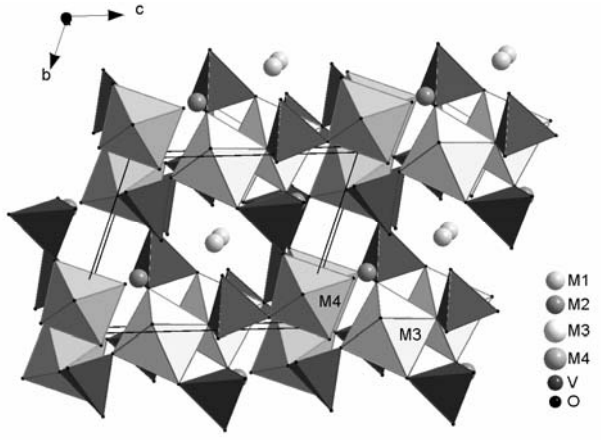

Fig. 3. Crystal structure of $Mn_3Fe_4V_6O_{24}$ viewed along the *a* axis.
See bottom of Table 2 for explanation of the symbols

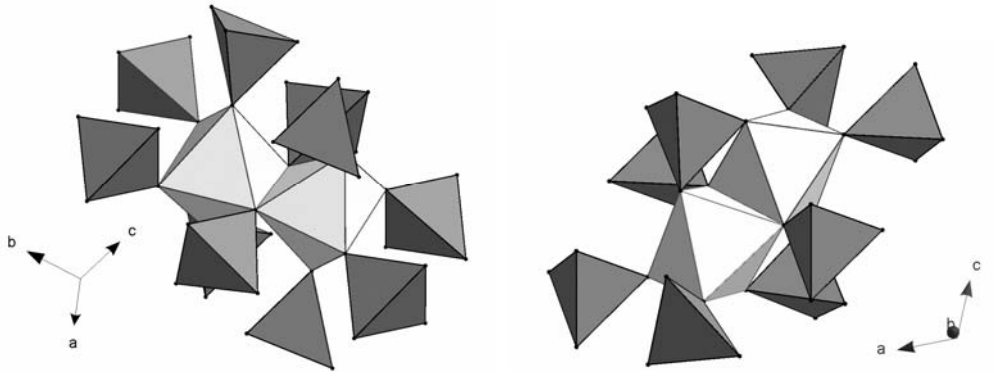

Fig. 4. Vanadium tetrahedral arrangement of the Fe1 (left) and Fe2 (right) dimers

Fe(1) and Fe(2) octahedra form edge-sharing dimeric clusters. Their environment of vanadium tetrahedra,VO_4, however, is different. $Fe(2)_2O_{10}$ octahedral dimers are surrounded by ten isolated VO_4 tetrahedra, each sharing one corner with the Fe(2) dimer, and therefore they form a $Fe(2)_2O_{10}$ unit. Only eight VO_4 tetrahedra build up a $Fe(1)_2O_{10}$ unit. They are linked to the Fe(1) dimer, since two $V(2)O_4$ share two vertices with the dimmer instead of one. The Fe(1)–Fe(1) distance $d_{Fe(1)–Fe(1)}$ = 3.330 Å is even longer than the Fe(2)–Fe(2) distance, $d_{Fe(2)–Fe(2)}$ = 3.148 Å, thus the difference $\Delta d = d_{Fe(1)–Fe(1)} - d_{Fe(2)–Fe(2)}$ = 0.182 Å. For the β-$Cu_3Fe_4V_6O_{24}$ compound, the above distances are [10]: $d_{Fe(1)–Fe(1)}$ = 3.095Å and $d_{Fe(2)–Fe(2)}$ = 3.152 Å, respectively, with a differences of *d* equal to –0.06 Å.

$V(1)O_4$ tetrahedra connect different Fe(1) dimers through their corners. $Fe(1)_2O_{10}$ units form chains parallel to the *a* axis (Fig. 5). $Fe(2)_2O_{10}$ units are linked to each other through $V(2)O_4$ and $V(3)O_4$ tetrahedra. They build up layers in the *ab* plane. The distance between neighbouring layers of $Fe(2)_2O_{10}$ units is equal to *c*.

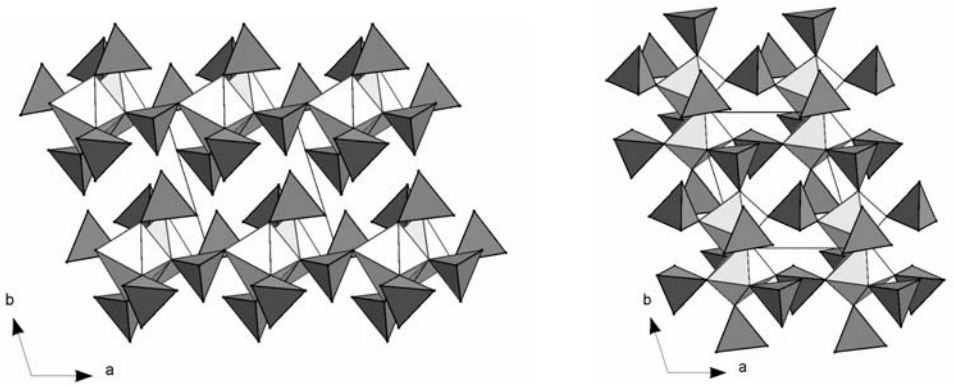

Fig. 5. Chains of $Fe(1)_2O_{10}$ units (left) and linked $Fe(2)_2O_{10}$ units in the *ab* plane (right)

Table 1. Crystallographic data for $Mn_3Fe_4V_6O_{24}$ obtained from neutron diffraction (at 10 K and 290 K) and XRD at room temperature. For comparison, similar data for $Zn_3Fe_4V_6O_{24}$ and β-$Cu_3Fe_4V_6O_{24}$ are given

Parameter	T = 290 K	T = 10 K	XRD [1]	$Zn_3Fe_4V_6O_{24}$ [7]	β-$Cu_3Fe_4V_6O_{24}$ [11]
System	triclinic				
Space group	*P*–1 (No. 2)				
fw	1077.84	1077.84	1077.84	1109.19	1103.66
a [Å]	6.7041(5)	6.7014(5)	6.703(2)	6.681(1)	6.600(3)
b [Å]	8.1487(7)	8.1410(7)	8.137(1)	8.021(2)	8.048(4)
c [Å]	9.8121(7)	9.8006(7)	9.801(2)	9.778(4)	9.759(5)
α [°]	105.51(1)	105.47(1)	105.56(1)	105.25(4)	106.08(3)
β [°]	105.54(1)	105.66(1)	105.58(2)	105.00(4)	103.72(3)
γ [°]	102.37(1)	102.41(1)	102.35(1)	102.20(4)	102.28(2)
V [Å^3]	473.4(1)	471.9(1)	471.9(2)	465.8	461.8
Z	1	1	1	1	1
d_{calc} [g/cm^3]	3.78	3.78	3.79	3.95	3.97
R_p	2.96	2.78	–	–	–
R_w	1.94	1.60	–	–	–
χ^2	1.70	1.60	–	–	–

$\chi^2 = \sum w(I_e - I_c)^2$; $R_w = [\sum w(I_e - I_c)^2/\sum wI_e^2]^{1/2}$; $R_p = \sum|I_e - I_c|/\sum|I_e|$.

$Mn_3Fe_4V_6O_{24}$ crystallizes in a triclinic system. The parameters of the unit cell determined from neutron diffraction (at both investigated temperatures, 10 K and 290 K)

and XRD analysis are presented in Table 1, together with literature data for the $Zn_3Fe_4V_6O_{24}$ and β-$Cu_3Fe_4V_6O_{24}$ compounds. The final refined atomic coordinates and the occupancy factors are shown in Table 2. The values of the unit cell parameters increase with increasing temperature, and some discrepancy is observed between the neutron diffraction and XRD data (Table 1). It is suggested that the analysis of the neutron diffraction data is more accurate. The three discussed compounds exhibit similar values of the crystal structure parameters.

Table 2. Atomic coordinates of $Mn_3Fe_4V_6O_{24}$ obtained from refined neutron diffraction data

Atom	Site	occupancy	T = 290 K			T = 10 K		
			x	y	z	x	y	z
M(1)	1g	1.0	0	1/2	1/2	0	1/2	1/2
M(2)	2i	2.0	0.791(8)	0.725(8)	0.232(5)	0.741(8)	0.674(7)	0.234(5)
M(3)	2i	2.0	0.375(1)	0.949(1)	0.6165(1)	0.377(1)	0.947(1)	0.616(1)
M(4)	2i	2.0	0.026(1)	0.199(1)	0.006(1)	0.035(2)	0.205(1)	0.011(1)
V(1)	2i	2.0	0.8960	0.9097	0.6673	0.8960	0.9097	0.6673
V(2)	2i	2.0	0.2221	0.6563	0.2708	0.2221	0.6563	0.2708
V(3)	2i	2.0	0.5988	0.2685	0.1275	0.5988	0.2685	0.1275
O(1)	2i	2.0	0.072(1)	0.053(1)	0.129(1)	0.071(1)	0.052(1)	0.130(1)
O(2)	2i	2.0	0.570(1)	0.148(1)	0.223(1)	0.572(1)	0.150(1)	0.223(1)
O(3)	2i	2.0	0.168(1)	0.437(1)	0.190(1)	0.167(1)	0.434(1)	0.190(1)
O(4)	2i	2.0	0.976(1)	0.270(1)	0.829(1)	0.976(1)	0.275(1)	0.831(1)
O(5)	2i	2.0	0.250(1)	0.789(1)	0.962(1)	0.253(1)	0.788(1)	0.966(1)
O(6)	2i	2.0	0.895(2)	0.966(1)	0.346(1)	0.889(2)	0.966(1)	0.345(1)
O(7)	2i	2.0	0.550(2)	0.253(1)	0.740(1)	0.540(2)	0.252(1)	0.739(1)
O(8)	2i	2.0	0.318(1)	0.231(1)	0.964(1)	0.316(1)	0.237(1)	0.965(1)
O(9)	2i	2.0	0.296(1)	–0.005(1)	0.394(1)	0.298(1)	–0.002(1)	0.392(1)
O(10)	2i	2.0	0.216(2)	0.694(1)	0.446(1)	0.215(2)	0.690(1)	0.441(1)
O(11)	2i	2.0	0.720(2)	0.485(2)	0.256(1)	0.724(2)	0.481(1)	0.254(1)
O(12)	2i	2.0	0.126(2)	0.299(1)	0.415(1)	0.132(2)	0.303(1)	0.419(1)

M(1) = Mn; M(2) = 1.60(2)Mn+0.40(2)Fe; M(3) = 0.08(2)Mn + 1.92(2)Fe; M(4) = 0.32(2)Mn + 1.68(2)Fe

The coordinates of vanadium, given in the Table 2, are taken from X-ray data for β-$Cu_3Fe_4V_6O_{24}$, since the vanadium position data are determined with a large uncertainty by the neutron diffraction method, due to the small scattering amplitude of vanadium.

The bond lengths and angles for the $Zn_3Fe_4V_6O_{24}$ compound at both investigated temperatures as well as the average values for the system β-$Cu_3Fe_4V_6O_{24}$ were calculated and compared [11]. The temperature dependences of the metal-oxygen bond lengths in $Mn_3Fe_4V_6O_{24}$ were calculated from the measurements at 290 K and 10 K, and the following values were obtained:

$$\Delta d_{1T} = \langle M(1)–O\rangle_{[4+2]}(290) – \langle M(1)–O\rangle_{[4+2]}(10) = 0.007 \text{ Å}$$

$$\Delta d_{2T} = \langle M(1)–O\rangle_{[4]}(290) – \langle M(1)–O\rangle_{[4]}(10) = 0 \text{ Å}$$

$$\Delta d_{3T} = \langle M(2)–O\rangle(290) – \langle M(2)–O(10)\rangle = –0.05 \text{ Å}$$

$$\Delta d_{4T} = \langle M(3)–O\rangle(290) – \langle M(3)–O\rangle(10) = –0.003 \text{ Å}$$

$$\Delta d_{5T} = \langle M(4)–O\rangle(290) – \langle M(4)–O\rangle(10) = 0 \text{ Å}$$

Thermal expansion is dominated by changes in distances involving M(2) positions. Bulk crystal unit cell parameters are changed between 10 K and 290 K in the following way: Δa_T = –0.001 Å, Δb_T = 0.003 Å, Δc_T = 0.006 Å, and the volume change ΔV_T = 0.7 Å^3. As can be seen, this thermal expansion is strongly anisotropic, being largest in the *c* direction and smallest in the *a* direction.

This neutron diffraction study of $Mn_3Fe_4V_6O_{24}$ powder has shown that the iron(III) and manganese(II) ions have a disordered structure, and that the distributions on the octahedral and trigonal bipyramidal sites are non-statistical. Some cations are disordered between octahedral iron and fivefold coordinated copper sites, and for the β-$Cu_3Fe_4V_6O_{24}$ compound this was detected by using Mossbauer spectroscopy [11]. X-ray diffraction analysis of the $Mn_3Fe_4V_6O_{24}$ system has shown that its iron atoms are not disordered with manganese atoms on any sites in this material. This is in contrast to our neutron diffraction study of this compound, because we have found a mixing of Mn and Fe ions at the M(2), M(3), and M(4) sites.

4. Conclusions

The $Mn_3Fe_4V_6O_{24}$ compound has been synthesized from MnO, V_2O_5, and Fe_2O_3. Neutron diffraction measurements were carried out at two selected temperatures – at room temperature and at 10 K. The analysis of the diffraction patterns has not shown any long-range magnetic order, and it produced better crystallographic results than those obtained from XRD analysis for the same system. The value of Δd (the difference between Fe(1)–Fe(1) and Fe(2)–Fe(2) distances) is equal to 0.182 Å for the $Mn_3Fe_4V_6O_{24}$ compound, being close to that for the isostructural β-$Cu_3Fe_4V_6O_{24}$ compound (–0.060 Å). We suggest that the coexistence of two different magnetic ions in these lattices could essentially influence these distances, which is especially evident in the case of the manganese(II) ion, whose magnetic momentum is greater than that of the copper(II) ion. The thermal expansion process in $Mn_3Fe_4V_6O_{24}$ has shown a strongly anisotropic character. The neutron diffraction method, in contrast to XRD, has revealed the existence of manganese and iron ion disorder at M(2), M(3), and M(4) sites in $Mn_3Fe_4V_6O_{24}$.

References

[1] WANG X., VANDER GRIEND D.A., STERN C.L., POEPPELMEIER K.R., Inorg. Chem., 39 (2000), 136.
[2] WANG X., VANDER GRIEND D.A., STERN C.L., POEPPELMEIER K.R., J. Alloys Comp., 298 (2000), 119.

[3] GUSKOS N., WABIA M., KURZAWA M., BEZKROVNYI A., LIKODIMOS V., TYPEK J., RYCHLOWSKA -HIMMEL I., BLONSKA-TABERO A., Radiat. Eff. Defects Solids, 158 (2003), 369.
[4] LIKODIMOS V., GUSKOS N., GLENIS S., SZYMCZAK R., BEZKROVNYI A., WABIA M., TYPEK J., GASIOREK G., KURZAWA M., RYCHLOWSKA-HIMMEL I., BLONSKA-TABERO A., Eur. Phys. J., B 38 (2004), 13.
[5] GUSKOS N., TYPEK J., BEZKROVNYI A., WABIA M., KURZAWA M., ANAGNOSTAKIS E.A., GASIOREK G., J. Alloys Comp., 377 (2004), 47.
[6] WANG X., PLESS J.D., VANDER GRIEND D.A., STAIR P.C., POEPPELMEIER K.R., HU Z., JORGENSEN J.D., J. Alloys Comp., 379 (2004), 87.
[7] KURZAWA M., BLONSKA-TABERO A., Mat. Res. Bull., 37 (2002), 849.
[8] KURZAWA M., BLONSKA-TABERO A., J. Therm. Anal. Cal., 77 (2004), 17.
[9] GUSKOS N., BEZKROVNYI A., TYPEK J., RYABOVA N.YU., BLONSKA-TABERO A., KURZAWA M., MARYNIAK M., J. Alloys Comp., 391 (2004), 20.
[10] ZLOKAZOV V.B., CHERNYSHEV V.V., J. Appl. Crystallogr., 25 (1992), 447.
[11] LAFONTAINE M.A., GRENECHE J.M., LALIGANT Y., FEREY G., J. Solid State Chem., 108 (1994), 1.

Received 23 September 2004
Revised 20 January 2005

Materials Science-Poland, Vol. 23, No. 4, 2005

Inverse-range-parameter dependence of gas–liquid nucleation in a Yukawa fluid A density functional approach

I. A. HADJIAGAPIOU*, A. MALAKIS, S. S. MARTINOS

Solid State Physics Section, Department of Physics, University of Athens, Panepistimiopolis, Zografos, Athens, GR 157-84

We studied the gas–liquid nucleation in Yukawa fluids by employing the density functional theory (DFT) and considering variable-range interaction forces between the particles of a one-component fluid. As a result, some interfacial quantities are sensitive in this kind of interaction (density profiles, principal tensors, mechanical surface tension and dividing radius), while some are not (pressure difference, density at the drop centre, equimolar surface tension).

Key words: *nucleation; density functional; Yukawa fluid; inverse-range-parameter; density profile*

1. Introduction

The nucleation process is one of the most universal phenomena found in various areas in physics, providing the mechanism for the onset of first-order transitions. A stable phase is formed in an otherwise homogeneous background of a metastable phase; such a process is the formation of a liquid drop inside a bulk vapour phase, wherein in a sufficiently supersaturated vapour phase spontaneous density fluctuations cause condensation, that is, they act as condensation nuclei (homogeneous nucleation) otherwise it is heterogeneous in the presence of a solid substrate. The gas –liquid nucleation has been subjected to intensive research because of its importance in atmospheric and industrial processes, thus considerable attention has been paid to the formulation of phenomenological theories to predict the nucleation rates from measurable quantities. A consistent theoretical description of nucleation should provide knowledge into the processes leading to the formation of the embryo-nucleus of the new phase as well as its size down to the very beginning two-particle clusters.

*Corresponding author, e-mail: ihatziag@phys.uoa.gr

The nucleation of a liquid drop from a bulk vapour phase was initially developed by Volmer, Farkas, Becker, Döring and Zeldovich, within the framework of thermodynamics, considering that even very small drops behave as macroscopic (classical nucleation theory CNT), thus having a well-defined radius and enclosing a bulk liquid phase of density corresponding to the exterior bulk vapour phase at the same temperature; also the respective surface tension is that of a planar dividing surface at equilibrium and the same temperature and the interface is narrow compared to the size of the nucleus. The free energy ΔG of cluster-formation in a supersaturated vapour consists of a bulk and a surface term, $\Delta G = -\Delta G_b + \Delta G_s$; the bulk term, ΔG_b, is due to the free energy gain of the condensing particles, while the surface term, ΔG_s, to the free energy loss because of the formation of the dividing interface of the cluster. Recent experimental results revealed that the conclusions of CNT are in error [1], especially in the case of small drops containing few particles; CNT underestimates the homogeneous nucleation rate, but accounts correctly for the main trends and provides a qualitative description. Its predictions however are to be taken with reservations, thus making necessary the reconsideration of this model. The initial attempt to correct CNT was the square gradient approximation (SGA), generalized by the density functional theory (DFT). The SGA was the first microscopic model; it was proposed by van der Waals and generalized by Cahn and Hilliard [2], according to which, the average density varies slowly over atomic distances and may not be valid away from the critical point. DFT is a rigorous statistical-mechanical approach in which the grand potential of a nonequilibrium inhomogeneous system being expressed as a functional of system's density and divided into intrinsic and extrinsic contributions, taking into account the interactions between particles, those with external fields and separating the various force fields into repulsive and attractive, the former ones are taken to be hard-sphere-like [3–5]. The equilibrium density of the inhomogeneous system extremizes the grand potential functional and results as a solution of a variational principle [3–5]. In the current research, the nucleation in a one-component system is studied via DFT for a Yukawa fluid, since it yields universal results that can serve as prototypes of various fluid systems and is computationally simpler.

2. Theory

The DFT of inhomogeneous fluids relies on a proper choice of the grand potential functional $\Omega_V(\rho(\boldsymbol{r}))$ [3–5]

$$\Omega_V\left(\rho(\vec{r})\right) = \int_V \left[f_{hs}\left(\rho(\vec{r})\right) + \frac{1}{2}\rho(\vec{r}) \int_V \rho(\vec{r}\,') \Phi_{FF}\left(\left|\vec{r} - \vec{r}\,'\right|\right) d\vec{r}\,' - \mu\rho(\vec{r}) \right] d\vec{r} \qquad (1)$$

in the absence of an external field; μ is the bulk vapour chemical potential and V the volume of the system. The term $f_{hs}\left(\rho(\vec{r})\right)$ is the Helmholtz free energy density of a uniform hard-sphere fluid at density $\rho(\vec{r})$, which accounts for the repulsive force

contribution; $\Phi_{FF}(\vec{r})$ is the attractive part of the pairwise potential between two fluid molecules $r = |\vec{r}|$ distant apart, which is chosen to be of the form

$$\Phi_{FF}(r) = -\frac{\alpha\lambda^3}{4\pi}\frac{e^{-\lambda r}}{\lambda r} \tag{2}$$

α and λ being constants; the latter is the inverse-range parameter, usually chosen as $\lambda d = 1$, where d is the hard-sphere diameter. The equilibrium density $\rho(\vec{r})$ of the inhomogeneous fluid is obtained by minimizing Eq. (1) through the variational principle

$$\frac{\partial \Omega_V\left[\rho(\vec{r})\right]}{\partial \rho(\vec{r})} = 0$$

yielding

$$\mu = \mu_{hs}\left(\rho(\vec{r})\right) + \int_V \rho(\vec{r}')\Phi_{FF}\left(|\vec{r} - \vec{r}'|\right)d\vec{r}' \tag{3}$$

where

$$\mu_{hs}\left(\rho(\vec{r})\right) = \frac{\partial f_{hs}\left(\rho(\vec{r})\right)}{\partial \rho(\vec{r})}$$

is the hard-sphere chemical potential.

For the sake of simplicity, all quantities are transformed to dimensionless units, $\mu^* \equiv \beta\mu$, $p^* \equiv \beta d^3 p$, $r^* \equiv \lambda r$, $\rho^* \equiv \rho d^3$, $\alpha^* \equiv \beta\alpha/d^3 = 11.102/T^*$; ($T^* = T/T_c$ where T_c is critical temperature) although the asterisks will be suppressed.

Substituting the attractive potential (Eq. (2)) into Eq. (3) and differentiating the resulting equation twice with respect to $u \equiv \lambda r$ yield

$$\mu''_{hs}\left(\rho(u)\right) + \frac{2}{u}\mu'_{hs}\left(\rho(u)\right) - \mu_{hs}\left(\rho(u)\right) + \mu = -\alpha\rho(u) \tag{4}$$

The prime denotes derivative with respect to u. In the limit $u \to 0$, the solution is less well-behaved, since at the origin $u = 0$ it is singular unless $\mu'_{hs}(u)$ vanishes in that limit

$$\lim_{u\to 0}\frac{\mu'_{hs}(u)}{u} = \lim_{u\to 0}\frac{\dfrac{d\mu'_{hs}(u)}{du}}{\dfrac{du}{du}} = \lim_{u\to 0}\mu''_{hs}(u) \tag{5}$$

according to de l'Hopital rule, therefore, in the neighbourhood of the origin, Eq. (4) becomes

$$\lim_{u\to 0}\mu''_{hs}(u)=\frac{1}{3}\left(\mu_{hs}(u)-\mu-\alpha\rho(u)\right) \tag{6}$$

Thus, the first boundary condition is $\mu'_{hs}(0)=0$. The other one is related to the behaviour of the solution at infinity as $u\to\infty$. As u gets larger, the contribution of the term $\left(2\mu'_{hs}(u)/u\right)$ becomes less significant and the behaviour of $\rho(u)$ is similar to that for a one-dimensional planar interface at the same temperature; hence, $\mu_{hs}(u)$ approaches the hard-sphere chemical potential of the bulk vapour phase $\mu_{hs}^{vs}\equiv\mu_{hs}(\rho_{vs})$ and $\mu'_{hs}(u)=0$ as $u\to\infty$.

The differential equation (4), with the boundary conditions

$$\mu'_{hs}(0)=0,\quad \mu_{hs}(\rho_{vs})=\mu_{hs}^{vs},\qquad \mu'_{hs}(\rho_{vs})=0$$

constitutes the problem under consideration, which will be solved numerically. The potential between two particles depends on the parameter λ, which is now considered to vary, control parameter. The spatial variable u transforms into $u\equiv\lambda r = (\lambda d)(r/d) = Lv$; v is the new spatial variable and L the new reduced inverse range parameter. As a result of this transformation, Eq. (4) becomes

$$\mu''_{hs}(v)+\frac{2}{v}\mu'_{hs}(v)+L^2\left(\mu-\mu_{hs}(v)\right)=-\alpha L^2\rho(v) \tag{7}$$

The calculation will be based on the Carnahan–Starling approximation for the hard spheres,

$$\beta p_{hs}(\rho)=\rho\frac{1+c+c^2-c^3}{(1-c)^3},\quad \beta\mu_{hs}(\rho)=\ln c+\frac{8c-9c^2+3c^3}{(1-c)^3} \tag{8}$$

where $c=\pi\rho d^3/6$, the packing fraction (called density for clarity); considering it as the dependent variable instead of $\mu_{hs}(v)$ or $\rho(v)$, Eq. (7) yields,

$$c''(v)=-\frac{2}{v}c'(v)-B_1(v)c'^2(v)-L^2\left(B_2(c)+B_3(c)c(v)\right) \tag{9a}$$

subject to the boundary conditions

$$c'(0)=0,\quad c(\infty)=c_{vs},\quad c'(\infty)=0$$

and

$$A_1(\eta)=\frac{\partial(\beta\mu_{hs})}{\partial\eta}=\frac{1}{\eta}+\frac{8-2\eta}{(1-\eta)^4},\quad A_2(\eta)=\frac{\partial A_1(\eta)}{\partial\eta}=-\frac{1}{\eta^2}+\frac{30-6\eta}{(1-\eta)^5} \tag{9b}$$

$$B_1(\eta)=\frac{A_2(\eta)}{A_1(\eta)},\qquad B_2(\eta)=\frac{\beta\mu-\beta\mu_{hs}(\eta)}{A_1(\eta)},\qquad B_3(\eta)=\frac{6\alpha\beta}{\pi A_1(\eta)} \tag{9c}$$

Because of the existence of the singularity at the origin, the solution is expanded in a power series about $v = 0$,

$$c(v) = q + \frac{v^2}{2!}c^{(2)}(0) + \frac{v^4}{4!}c^{(4)}(0) \quad \text{as } v \to 0 \tag{10}$$

where $q \equiv c(0)$ and

$$c^2(0) = -\frac{1}{3}\left[B_2(q) + qB_3(q)\right]$$

$$c^{(4)}(0) = -\frac{3}{5}\left\{2B_1(q)\left[c^{(2)}(0)\right]^2 + c^{(2)}(0)\left[\left(\frac{dB_2(c)}{dc}\right)_{v=0} + q\left(\frac{dB_3(c)}{dc}\right)_{v=0} + B_3(q)\right]\right\} \tag{11}$$

The interaction potential takes the form due to the transformation

$$\Phi_{FF}(L, v) = -\frac{\alpha_c L^3 \mathrm{e}^{-Lv}}{Lv}$$

$\alpha = 11.102 k_B T_c/4\pi$ and possesses a minimum at $Lv = 2$ as a function of L.

The surface tension $\gamma(R_\gamma;\Delta p)$, the work for the formation of the unit surface, in reduced units is

$$\gamma\left(R_\gamma;\Delta p\right) = \frac{1}{3\alpha L R_\gamma^2}\int_0^\infty \left(v\mu'_{hs}(v)\right)^2 dv + \frac{1}{3}LR_\gamma \Delta p \tag{12}$$

R_γ stands for the mechanical R_s or equimolar R_e dividing radii and Δp is the pressure difference

$$\Delta p = \int_{\text{inside}}^{\text{outside}} \frac{2}{\alpha L^2 v}\mu'^2_{hs}(v)\,dv = \frac{2\gamma_s}{R_s} \tag{13}$$

for the mechanical dividing surface [5].

Another important quantity is the nucleation work W for the formation of a nucleus, the difference between the grand potentials for the inhomogeneous and homogeneous systems

$$W = \Omega_V\left(\rho(\vec{r})\right) - \Omega_V\left(\rho_{VS}\right) = \Omega_V\left(\rho(\vec{r})\right) + p_B V$$

p_B the bulk pressure; taking into account (1)

$$W = \int_V \left\{\tfrac{1}{2}\rho(r)\left[\mu_{hs}(\rho) - \mu\right] - p_{hs}(\rho) + p_B\right\} d\vec{r}$$

3. Results and conclusions

In an inhomogeneous system, the common route followed for the study of its structure is in terms of temperature and bulk density, neglecting any other parameter that can affect it; such a parameter is the inverse range parameter L that changes the range of the intermolecular forces and affecting, in general, some of the system's parameters. The latter route is followed in the current case, the boundary value problem in hand is solved numerically by an iterative way; its solution provides the equilibrium density profile as a function of the radial distance from the centre of the drop, for specific values of the bulk vapour density c_{VS}, L and $T = 0.7$. From the numerical solution, it was found that $R_T(L) = R_T(L = 1)/L$, where $R_T(L)$ is the radial distance from the origin of the drop where $c(r,L)$ attains its bulk value c_{VS}, thus if $R_T(L = 1)$ is known [5], $R_T(L)$ can be calculated for any L for the same c_{VS}; the larger the L the smaller the $R_T(L)$, since on increasing L the attractive fluid/fluid interaction decreases, forming smaller drops, while the opposite is true on increasing L. Consequently, L and $R_T(L)$ cannot vary simultaneously.

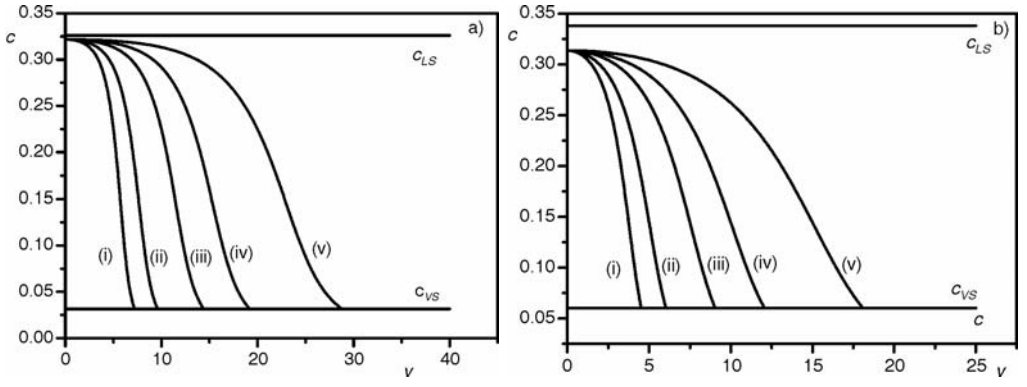

Fig. 1. Density profiles $c(v,L)$ vs. reduced distance v for various values of L : (i) 2.0, (ii) 1.5, (iii) 1.0, (iv) 0.75, (v) 0.5: a – c_{vs} = 0.03142 (ρ_{vs}= 0.06), b – c_{vs} = 0.06021 (ρ_{vs}= 0.115). The corresponding liquid densities, c_{Ls} = 0.326134 and c_{Ls} = 0.338244, respectively, at the same temperature are also indicated

The value of $R_T(L)$ can also be considered as an estimation of the physical radius of the drop without anticipating the structure of the enclosed fluid phase. For a specific value of c_{VS}, Eq. (9) was solved by considering L as independent variable assuming the values 0.5, 0.75, 1.0, 1.5, 2.0; the corresponding density profiles appear in Figures 1a, b for different bulk densities (c_{VS} = 0.0314159 (ρ_{VS} = 0.06) and c_{VS} = 0.0602139 (ρ_{VS} = 0.116); we observe that the structure of the density profile for any value of L is unaffected in comparison to that for $L = 1$, except that it is either broadened for $L < 1$ (larger radii) or shrunk for $L > 1$ (smaller radii). In addition, in Figure 1a, small supersaturation, the plots (iv) and (v) corresponding to smaller values of L possess a flat part close to the drop centre implying the existence of a homogeneous phase inside the drop with higher density than the corresponding c_{VS}.

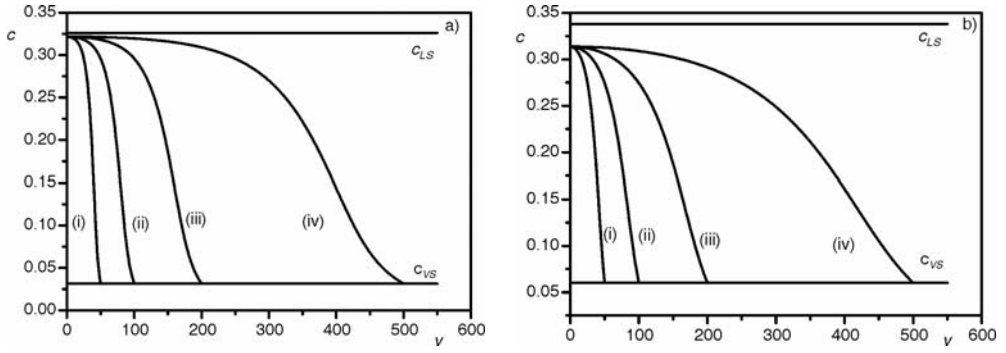

Fig. 2. Density profiles $c(v,L)$ vs. reduced distance v for various values of $R_T(L)$: (i) 50.0, (ii) 100.0, (iii) 200.0, (iv) 500.0: a) c_{vs} = 0.03142 (ρ_{vs}=0.06), b) c_{vs} = 0.06021 (ρ_{vs}=0.115). The corresponding liquid densities, c_{Ls} = 0.326134 and c_{Ls} = 0.338244, respectively, at the same temperature are also indicated

In order to make the broadening and shrinking of drops more obvious, $R_T(L)$ is now chosen as control parameter instead of L. The respective plots are given in Figures 2a, b. For small supersaturations, c_{VS} = 0.0314159 and high values of $R_T(L)$, the corresponding drop encompasses a liquid-like phase, evidenced by the straight line in Figure 2a (iii, iv), implying the existence of a homogeneous phase of constant density inside the drop while for smaller values of $R_T(L)$ the extent of the enclosed homogeneous phase is barely perceptible, thus Figure 2a (i, ii) are examples of highly inhomogeneous systems. However, for higher supesaturations, c_{VS} = 0.0602139 and higher values of $R_T(L)$, the extent of the homogeneous phase is much smaller than for the smaller supersaturations, Figure 2b. These examples indicate that a large drop cannot always enclose a homogeneous phase (a necessary ingredient of the Laplacian thermodynamics) for any value of c_{VS} but depends significantly on supersaturation.

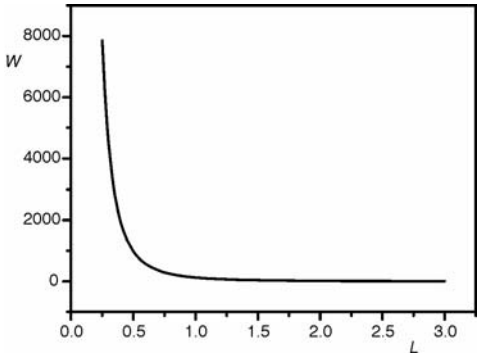

Fig. 3. The work of formation W *vs.* the scaled inverse-range parameter L

The work W for the formation of a nucleus in terms of L is shown in Figure 3, a decreasing function of L. For large values of L ($L >> 1$) the range of the fluid–fluid interactions is short, thus the formed clusters consist of a small number of particles

(small drops) and the required work is small although, ultimately, they cannot survive because of the strong hard sphere forces which dominate in short distances. On the contrary, for a small value of L (L <<1) the range of the fluid–fluid interactions is large, resulting in forming drops of large radii and the required work is larger. A similar behaviour is shown by the surface tension, the work for the formation of the unit surface. For a given value of the bulk vapour density, the quantities left unaffected on varying L are the density at drop centre, pressure difference Δp and the equimolar surface tension [5].

Concluding, the existence of a homogeneous phase inside a drop, whatever large it might be, is independent of L and depends only on supersaturation, since the attractive forces behave as a uniform background without affecting the structure of the system which is dominated only by the hard-sphere forces; the direct influence of L is to broad or shrink the density profile only. The effect of the attractive forces is to accommodate the particles of the interior phase into the available space without changing the structure.

Acknowledgements

This research was supported by the Special Account for Research Grants of the University of Athens under Grant Nos. 70/4/4071 and 70/4/4096.

References

[1] HUNG C.-H., KRASNOPOLER M.J., KATZ J.L., J. Chem. Phys., 90 (1989), 1856.
[2] CAHN J.W., HILLIARD J.E., J. Chem. Phys., 28 (1958), 258; J. Chem. Phys., 31 (1959), 688.
[3] EVANS R., Adv. Phys., 28 (1979), 143, [after:] D. Henderson (Ed.), *Fundamentals of Inhomogeneous Fluids*, Marcel Dekker, New York, 1992.
[4] DAVIS H.T., *Statistical Mechanics of Phases, Interfaces and Thin Films*, VCH, New York, 1996.
[5] HADJIAGAPIOU I., J. Phys. Condens. Matter, 6 (1994), 5303.

Received 23 September 2004
Revised 17 April 2005

Materials Science-Poland, Vol. 23, No. 4, 2005

Characterization and EPR studies of TiC and TiN ceramics at room temperature

T. BODZIONY[1], N. GUSKOS[1, 2], A. BIEDUNKIEWICZ[3], J. TYPEK[1*], R. WRÓBEL[4], M. MARYNIAK[1]

[1]Institute of Physics, Szczecin University of Technology, al. Piastów 17, 70-310 Szczecin, Poland

[2]Solid State Section, Department of Physics, University of Athens, Panepistimiopolis, 15 784 Zografos, Athens, Greece

[3]Institute of Material Engineering, Szczecin University of Technology, al. Piastów 19, 70-310 Szczecin, Poland

[4]Department of Chemical and Environment Engineering, Szczecin University of Technology, Pułaskiego 10, 70-322 Szczecin, Poland

Four samples, namely TiC/C, TiN/C, (TiC + Fe_xC_y + Fe)/C and TiN/amorphous carbon, have been prepared and investigated. In the former three samples titanium compounds were placed in a carbon matrix, while in the fourth one TiN was surrounded by an amorphous carbon. The samples have been characterized by XRD, SEM, and electron diffraction spectroscopy. The crystallite sizes and lattice parameters of TiC and TiN have been determined by the X-ray diffraction method. XRD measurements have shown that the lattice constants of nanosized samples were smaller than those of microsized samples. An essential influence of the carbon matrix during the crystallization process on the lattice parameters and grain size was observed. Electron paramagnetic resonance (EPR) measurements of the samples were carried out at room temperature. A narrow EPR absorption line has been recorded for the TiC/C, TiN/C, and TiN/amorphous carbon samples, whereas for the (TiC + Fe_xC_y + Fe)/C sample a ferromagnetic resonance spectrum, mainly of α-Fe and cementite Fe_3C, has been recorded. The narrow resonance EPR line is explained by carrier motion – free electrons in the case of the TiN/C sample and holes (carbon vacancies) in the case of TiC/C and TiN/amorphous carbon samples – which could lead to the creation of the pseudogap state in TiC_x or TiN_x compounds.

Key words: *EPR; titanium carbide; titanium nitride*

1. Introduction

Nanomaterials, due to their enhanced physical properties, are attractive for various applications. For example, titanium carbide (TiC) and titanium nitride (TiN) possess

*Corresponding author, e-mail: typjan@ps.pl

many useful properties: extreme hardness, high strength, resistance to heat, corrosion and wear, high resistance to chemical attack, high thermal stability, good electrical and thermal conductivity, interesting magnetic properties and, in the case of TiN – an attractive golden colour [1]. Nanometer-sized magnetic materials have attracted attention of many researchers because they exhibit such unusual chemical and physical properties as superparamagnetism and quantum tunnelling of magnetization [2]. Nanocrystalline TiC and TiN can be synthesized by several methods, such as synthesis in the gas phase, synthesis based on carbothermal reduction in vapour–solid or vapour–liquid phases, sol-gel methods and mechanical processing [1].

The electric and magnetic properties of nonporous carbon systems are expected to be similar to those of nanohorns and/or nanotubes, because the main part of nanoporous carbon systems and nanohorn and/or nanotube samples is a quasiamorphous net of randomly oriented graphene fragments a few nanometers in size [3]. Electron paramagnetic resonance is a powerful and sensitive method for characterizing paramagnetic centres and ions, e.g. $Ti^{3+,}$ and is useful in studying disordered titanium carbide or titanium nitrite materials, in which an undesirable but possible inclusion of impurities into the sample should be taken into account.

2. Experimental

A nonhydrolytic sol-gel process has been applied for the preparation of TiC and TiN nanocrystals [1]. In the present work, mixtures of polyacrylonitryle, dimethylformamide and titanium chlorides were used to form gels containing Ti–C bonds and being precursors for the synthesis of titanium carbide as well as titanium nitride. The dispersed phase of the gel is formed by polymerising polyacrylonitryle crosslinked with titanium chlorides, which initially forms connections with the polymer chains as a result of intermolecular interactions and chemical bonds. Dimethylformamide acts as the dispersing agent in this system. All the operations and gel precursor preparations were carried out in a glove box under a protective atmosphere of argon using the Schlenk technique. The gel samples were heated in a furnace in inert and/or reactive atmospheres, depending on the desired products. The heating was carried out in a gas atmosphere, which contained argon and/or nitrogen, hydrogen and ammonia, under atmospheric pressure and in the temperature range of 293–1273 K. The reactions leading to the appearance of TiC and TiN phases proceeded at temperatures below 800 K. The parameters for manufacturing TiC and TiN phases with or without carbon as coatings and powders are subject to patenting procedure.

The following techniques were applied for sample characterization: scanning electron microscopy (JEOL JSM 6100), X-ray diffraction (PHILIPS X'PERT), transmission electron microscopy, and electron diffraction (JEOL JEM 1200EX). The obtained TiC/C and TiN powders, Ti–C coatings, and TiN/C pumice were additionally

characterized by microanalysis with wavelength dispersive and energy dispersive spectroscopy (IBEX System Noran Instruments and an Oxford ISIS 300).

EPR measurements were carried out with a conventional X-band (ν = 9.43 GHz) Bruker E 500 spectrometer, with 100 kHz magnetic field modulation. Prior to the measurements, the samples were magnetized by a steady magnetic field of 1.4 T to saturate any domain structure. All EPR measurements were performed at room temperature.

3. Results and discussion

Four ceramic samples, namely TiC/C, TiN/C, (TiC + Fe_xC_y + Fe)/C, and TiN/amorphous carbon have been prepared with sizes in the micrometer and nanometer scales. The titanium phases in three of them – TiC, TiN and (TiC + Fe_xC_y + Fe) – were surrounded by carbon (C), and by amorphous carbon in the fourth one (TiN). In comparison to the case of conventional high-temperature synthesis, we managed to lower the temperature of TiC and TiN synthesis, and achieved unique microstructural properties of the samples.

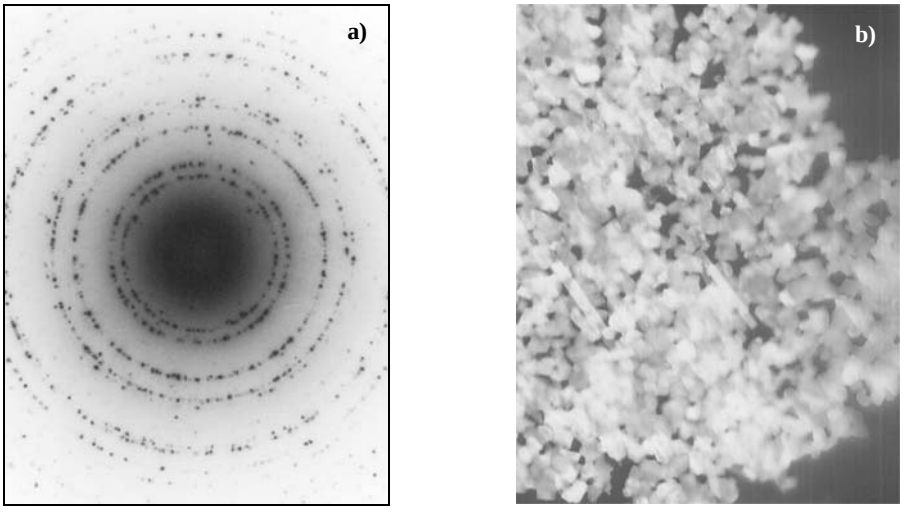

Fig. 1. TiC/C sample: electron diffraction pattern (a) and transmission electron micrograph (b)

The Transmission Electron Micrograph (TEM) and electron diffraction pattern of the TiC/C composite powder are presented in Figures 1a, b. Microscopic and microanalysis results suggest that the TiC phase is homogeneously dispersed in the carbon matrix. Figures 2a, b show the TEM image and electron diffraction pattern of the TiN/C composite powder. These TEM images show that the powder contains two crystalline phases: graphite and titanium carbide or titanium nitride, respectively. TEM investigations of the TiC/C and TiN/C particles showed that they formed with

an average size below 100 nm and 50 nm, respectively. Figures 3a, b show the TEM image and electron diffraction pattern of the TiN/amorphous carbon composite powder. The X-Ray powder diagrams of TiC/C (1), TiN/amorphous carbon (2), and TiN/C (3) are presented in Figure 4.

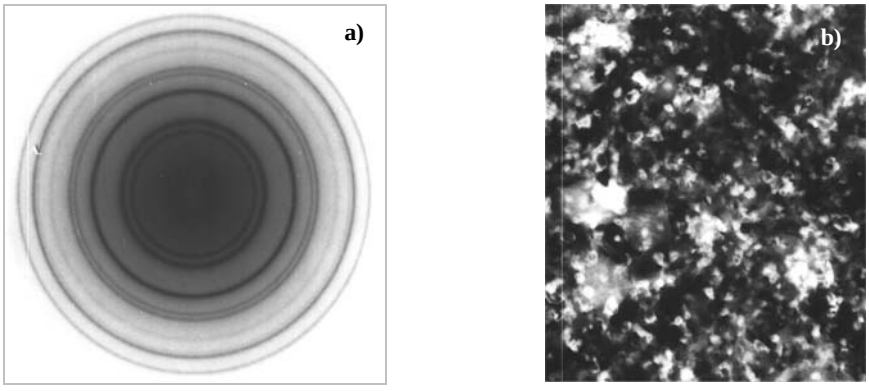

Fig. 2. TiN/C sample: electron diffraction pattern at room temperature (a) and transmission electron micrograph (b)

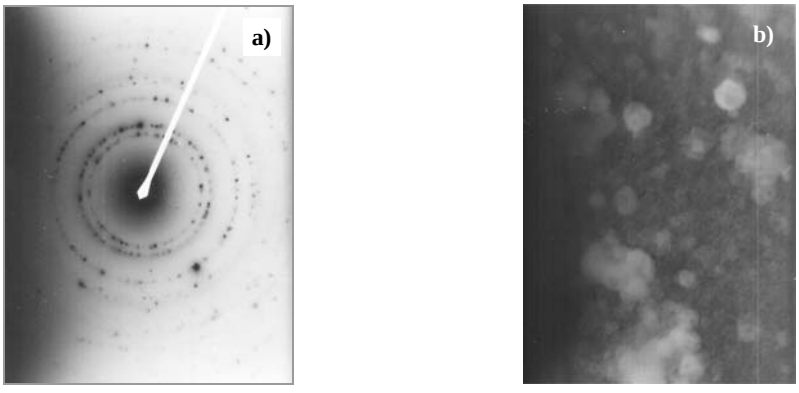

Fig. 3. TiN/amorphous carbon sample: electron diffraction pattern at room temperature (a) and transmission electron micrograph (b)

The lattice constants and crystallite sizes of the prepared composite powders have been determined using an X-ray diffraction method [4] and are shown in Table 1. The lattice constant of TiN is 0.4242 nm according to the 38-1420 ICDD (International Center of Diffraction Data) card. The lattice constant of TiN/amorphous carbon nanoparticles is practically the same as that from the ICDD card (only 0.1% less), while the lattice constant of TiN/C is significantly smaller (by about 1.1 %). The most important difference in the lattice constant was found for the TiC/C sample. The lattice constant of TiC is 0.4327 nm according to the 32-1383 ICDD card, and the lattice constant of TiC/C nanoparticles is 2.3 % smaller than for micrometer-sized TiC. Note

that the TiN/C and TiC/C samples, for which a significant difference in the lattice constant is observed, have small crystallite sizes. A comparison of the lattice parameters and grain sizes of TiN and TiC suggests an essential influence of the presence of the carbon matrix during the crystallization process.

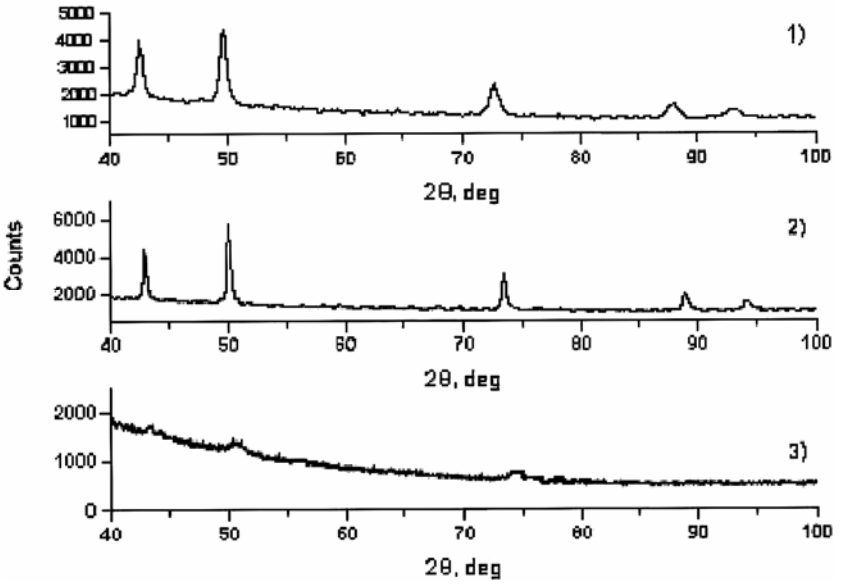

Fig. 4. XRD powder diagram of: 1 – TiC/C, 2 – TiN/amorphous carbon, 3 – TiN/C

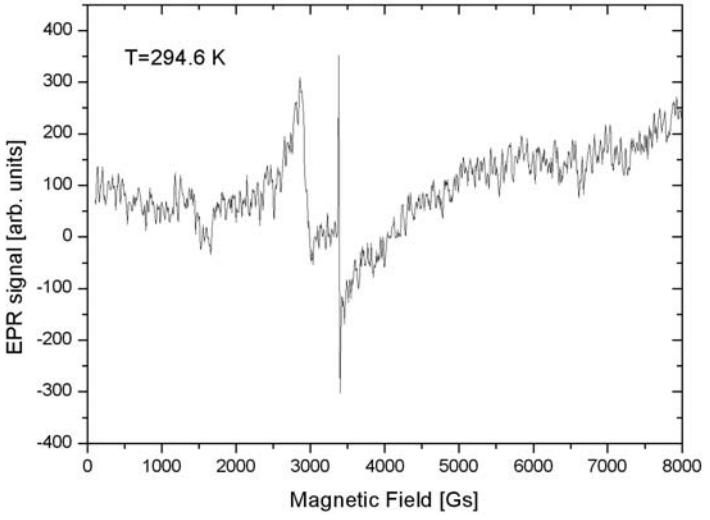

Fig. 5. The EPR spectrum of the TiC/C sample at room temperature

Table 1. The lattice constants of the TiN and TiC bulk compounds in the carbon matrix as compared to their values in the micrometer scale

Compound	Lattice constant [Å]	Lattice constant ratio [%]	Crystallite size [nm]
TiN/C	4.194(1)	–1.1	8.3(9)
	4.242 (ICDD)	Δa = 0.048 Å	>1000
TiN/amorphous carbon	4.238(1)	–0.1	55.1(8)
	4.242 (ICDD)	Δa = 0.004 Å	>1000
TiC/C	4.228(1)	–2.3	12.3(6)
	4.327 (ICDD)	Δa = 0.099 Å	>1000

Table 2. Values of the EPR parameters of TiN and TiC compounds in the carbon matrix

Compound	g	ΔB_{pp} [Gs]	Relative intensity
TiN/C	2.0025(3)	4.0(2)	1
TiN/amorphous carbon	1.9935(6)	82.0(5)	34
TiC/C	1.9959(3)	21.1(5)	2

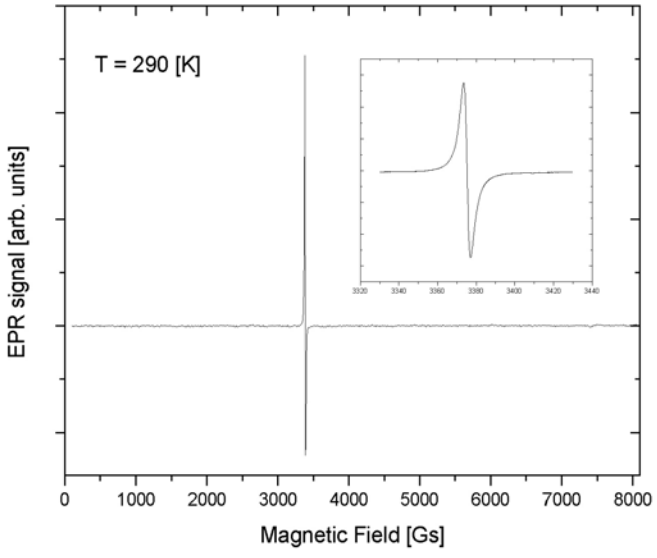

Fig. 6. The EPR spectrum of the TiN/C sample at room temperature. The inset in this picture shows the resonance line in an expanded magnetic field scale

Figure 5 shows the EPR spectrum of the TiC/C sample at room temperature. A sharp EPR line at a resonance field of B_{res} = 3385(9) Gs with a peak-to-peak linewidth of ΔB_{pp} = 21.0(5) Gs (see Table 2) can be observed. Another EPR line centered at B_{res} = 2924(9) Gs is also visible. The EPR spectrum of the TiN/C sample at room temperature is presented in Figure 6. A characteristic feature of this spectrum is

a very high and sharp needle-like resonance line cantered at B_{res} = 3375(9) Gs with a linewidth of ΔB_{pp} = 4.0(2) Gs (see Table 2). The inset in this picture shows this line in an extended scale. This EPR resonance line is almost symmetrical. Figure 7 shows the EPR spectrum of the TiN/amorphous carbon sample at T = 297 K. A relatively wide resonance signal is obtained with the resonance field of B_{res} = 3378(9) Gs and a peak-to-peak linewidth of ΔB_{pp} = 82.0(5) Gs (Table 2). The narrowest resonance line is seen for the TiN/C sample, above five times smaller than in the case of TiC/C. In the amorphous carbon matrix, this resonance line is observed with a much larger linewidth (Table 2).

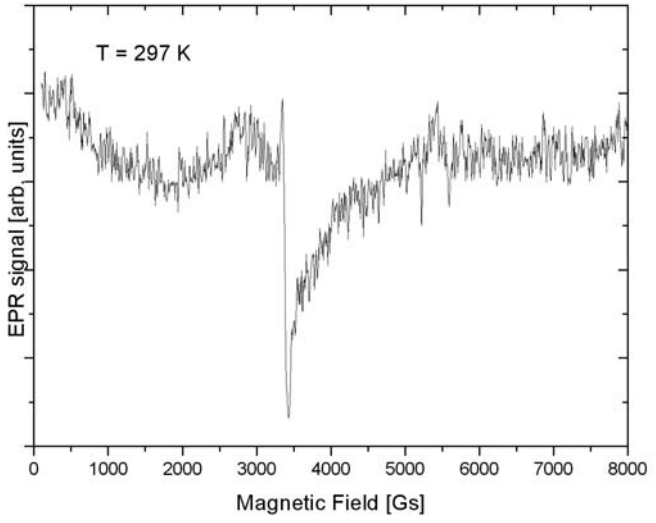

Fig. 7. The EPR spectrum of the TiN/amorphous carbon sample at room temperature

A resonance line with a different shape is presented in Figure 8, which shows the EPR spectrum of the (TiC + Fe_xC_y + Fe)/C sample at T = 307 K. In this figure, a very wide and strong EPR signal, shifted to low magnetic fields, is observed. Mossbauer spectroscopy for the (TiC + Fe_xC_y + Fe)/C sample has shown the presence of five forms of iron, mostly Fe^{3+}, α-Fe, and cementite (Fe_3C) [5]. We suggest that in ferro-magnetic resonance (FMR), the (TiC + Fe_xC_y + Fe)/C sample is observed, originating from α-Fe and cementite [6, 7].

A narrow EPR absorption line has been recorded for the three samples (TiC/C, TiN/C, TiN/amorphous carbon). In Table 2, the parameters of this signal – the g-parameter, peak-to-peak linewidth ΔB_{pp}, and integrated intensity – are presented for the three samples. The relative intensity is computed as a ratio of the EPR intensity of a given sample to the intensity of the weakest sample (TiN/C). It can be seen that the intensity of the TiC/C sample is two times larger, while the intensity of the TiN/amorphous carbon is 34 times larger than the intensity of the reference TiN/C sample. The g-parameter of TiN/C is almost equal to the g-value of free electrons

(2.0023), hence it appears that the narrow resonance line originates from free electrons. For TiN/amorphous carbon and TiC/C samples, the *g*-parameter is less than 2 and a resonance line is observed with a slightly asymmetric lineshape. In Ref. 8, the role of hole conductivity in EPR is stressed. We suggest that the narrow line in TiN/amorphous carbon and TiC/C samples is produced by hole movement [9], especially by the movement of carbon vacancies [10]. The conductance can include two types of current carrier movements: surface conductance across the percolating network of nanoclusters, and bulk conductance due to free carrier jumps through potential barriers at carbon cluster boundaries [8, 10].

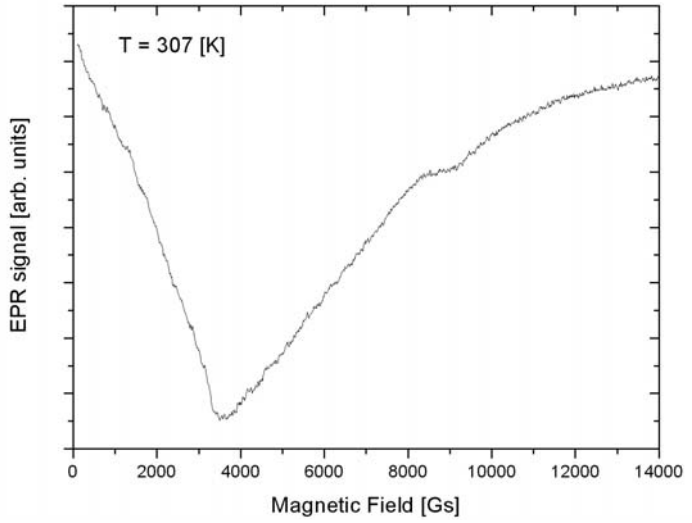

Fig. 8. The EPR spectrum of the (TiC + Fe_xC_y + Fe)/C sample at T = 307 K

For the TiC/C sample, an additional intense EPR line at higher resonance fields was recorded. It is suggested that this EPR spectrum could arise from complexes of Ti^{3+} ions [9]. The decrease in the lattice constants for nanometer-sized samples of crystallites could be the effect of titanium(III), and these ions could form centres of disorder, which might promote the semiconductor-metal transition at higher temperatures [11]. The shorter bonding between titanium(III) could bring about the disordered state more easily in the nanometer-sized TiC_x system than in titanium nitrites.

4. Conclusions

Four samples – TiC/C, TiN/C, (TiC + Fe_xC_y + Fe)/C, and TiN/amorphous carbon – have been prepared and investigated. These samples have been characterized by XRD, SEM, and electron diffraction spectroscopy. TiC and TiN crystallite sizes and lattice parameters have been determined by X-ray diffraction. XRD measurements

have shown that the lattice constants for nanometer-sized samples are smaller than for micrometer-sized ones. This fact is especially important for the physical properties (electrical and mechanical) of the TiC_x/C system. A comparison of the lattice parameters and grain sizes of TiN and TiC suggests an essential influence of the carbon matrix during crystallization process on their values. EPR measurements of the samples have been carried out at room temperature. Narrow EPR absorption lines were recorded for the TiC/C, TiN/C, and TiN/amorphous carbon samples, and essential differences were observed in the values of their EPR parameters. We suggest that the narrow resonance line originates from free electrons in the case of the TiN/C sample, and from hole movement (carbon vacancies) in the case of TiC/C and TiN/amorphous carbon samples, which could lead to the pseudogap in TiC_x or TiN_x compounds.

Acknowledgments

This work was partially supported by grant PBZ-KBN-095/TO8/2003.

References

[1] BIEDUNKIEWICZ A., Mater. Sci., 21 (2003), 445.
[2] TANGO T., HATSUTA T., MIYAJIMA K., KISHADA M., TASHIRO S., WAKABAYASHI K., J. Am. Ceram. Soc., 85 (2002), 2188.
[3] KYUTT R. N., SMORGONSKAYA E. A., DANISHEVSKII A. M., GORDEEV S. K., Solid State Phys. (in Russian), 41 (1999), 1359.
[4] BIEDUNKIEWICZ A., WROBEL R., submitted for publication in Mater. Sci.-Poland.
[5] Private communication, J. Suwalski, Institute for Nuclear Studies, Świerk, Poland.
[6] NARKIEWICZ U., GUSKOS N., ARABCZYK W., TYPEK J., BODZIONY T., KONICKI W., GASIOREK G., KUCHAREWICZ I., ANAGNOSTAKIS E.A., Carbon, 42 (2004), 1127.
[7] GUSKOS N., ANAGNOSTAKIS E. A., TYPEK J., GASIOREK G., BODZIONNY T., NARKIEWICZ U., ARABCZYK W., KONICKI W., Mol. Phys. Rep., 39 (2004), 58.
[8] SHANINA B. D. KONCHITIS A.A., KOLESNIK S.P., VEYNGER A.I., DANISHEVSKII A.M., POPOV V.V., GORDEEV S.V., GRECHINSKAYA A.V., Carbon, 41 (2003), 3027.
[9] VAN DOORSLAER S., SHANE J.J., STOLL S., SCHWEIGER A., KRANENBURG M., MEIER R.J., J. Organ. Chem., 634 (2001), 185.
[10] DYSON F.J., Phys. Rev., 98 (1955), 349.
[11] GUSKOS N., TYPEK J., BIEDUNKIEWICZ A., PATAPIS S., KARKAS K., MARYNIAK M., to be published in Rev. Adv. Mater. Sci. (2004).

Received 23 October 2004
Revised 24 February 2005

Materials Science-Poland, Vol. 23, No. 4, 2005

Novel nanocomposites using carbon nanotubes and melamine–formaldehyde

L. LICEA-JIMÉNEZ, R. W. RYCHWALSKI*

Department of Materials and Manufacturing Technology,
Chalmers University of Technology, SE-412 96 Göteborg, Sweden

The present work deals with a novel, ternary nanocomposite containing single-wall nanotubes (SWNTs), cellulose, and melamine-formaldehyde (MF). Thin sheets are assembled from α-cellulose papers, on which SWNT/MF has been deposited in liquid form, and next hot pressed without venting. The material is transparent/tinted. Dispersion/morphology was characterised by means of transmission electron microscopy (TEM) on ultramicrotome slices cut across a moulded sheet. Isolated thin bundles/nanotubes are found. They are oriented off the slice plane. TEM images of such cross-sections are presented. In-plane nanotubes are also present. The discussed SWNT/cellulose/MF nanocomposite is being developed towards multifunctional coatings.

Key words: *single-wall nanotube; melamine–formaldehyde; multifunctional coating nanocomposite*

1. Introduction

Discoveries in the field of cluster science, particularly in carbon species, are paving the way to new areas of materials science and new technologies. A carbon single-wall nanotube (SWNT) is formed by a hexagonal network of carbon atoms (graphene) rolled up seamlessly on a cylinder of radius R with various helicities. A multiwall nanotube (MWNT) is a collection of concentrically arranged SWNTs.

Advances in the production and purification of carbon nanotubes allow us to expect a simultaneous further price decrease and widening range of applications. Probably, the main application of nanotubes today is in polymeric matrix composites. Various polymeric matrices have been used by many researchers worldwide. Epoxy resins and poly(methyl methacrylate) (PMMA) have been frequently used [1]. Nanotube composites have been overviewed in several papers [2–8]. The relatively early stage of development, great expectations, and a bright future for nanotube composites have

*Corresponding author, e-mail: rodney.rychwalski@me.chalmers.se

been stated in the literature [9]. Carbon nanotube/melamine–formaldehyde (MF) composites have not been developed, in spite of the wide use of MF.

MF is a water-based amino resin with excellent mechanical, thermal, and coating properties, as well as appearance, and thus MF is extensively used for coating purposes. Processing characteristics are favourable. This resin offers a relatively short cycle time. Its disadvantage, however, is the release of water during production, thus there is a need of mould venting. Besides, formaldehyde is emitted, though this can be reduced with new low emission grades. In this work, we will adapt a non-vented hot pressing technique, used by us earlier, to prepare carbon fibre and carbon black filled MF [10, 11], and will prepare thin sheets of SWNT/cellulose/MF, with multifunctional coatings/laminates in mind.

2. Experimental

2.1. Materials

Madurit Mw 909 (50 wt. % solid content) from UCB (Denmark) and SWNT crude material from CarboLex (USA) were used. The supplied material contained approximately 50-70% of single-wall, closed-ended carbon nanotubes 1.4 nm in diameter (average value), produced by the arc discharge method, as given by the producer. In order to remove impurities (mainly amorphous carbon and catalyst particles), the crude material was purified by an oxidative process – the pristine material was refluxed in nitric acid under magnetic stirring at 110–120 °C for 24 h, followed by filtration through a 0.2 μm PTFE membrane filter, and washed with distilled water.

Purified carbon nanotubes were added to a 50 wt. % aqueous solution of MF. Two concentrations (0.5 and 1.5 wt. %) were used. Mild sonication was applied. The obtained dispersion was used as follows: 50 g/m^2 α-cellulose papers were impregnated with SWNT/MF, stacked and hot pressed at 150 °C and 4 MPa for 10 min. The use of cellulose was motivated by its two main functions: cellulose acts as an absorbing substrate, thus allowing hot pressing without venting, and cellulose practically removes the propensity of MF to microcracking.

2.2. TEM imaging

After the purification, single-wall nanotubes were characterised by transmission electron microscopy, using a Zeiss 912 Omega instrument. A small amount of SWNTs were dispersed in ethanol, sonicated for a few minutes, and then deposited on a copper grid coated with a holey carbon film.

SWNT/cellulose/MF samples were ultramicrotomed using a Reichert–Jung Ultracut E instrument. Slices 0.15 μm thick were cut with a diamond knife moving

across the sheet. Slices were studied to determine the degree of nanotube dispersion and other characteristics using a Zeiss 912 Omega instrument.

3. Results and discussion

The obtained composites were transparent and tinted, and were not microcracked. They are shown in Figure 1 where rather good transparency can be noticed (the print is visible through the nanocomposite layer).

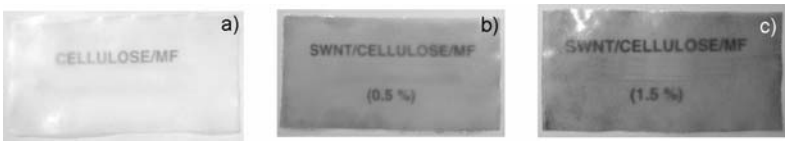

Fig. 1. SWNT/cellulose/MF composites: a) cellulose/MF (without nanotubes), b) SWNT/cellulose/MF with 0.5 wt. % nanotubes, c) SWNT/cellulose/MF with 1.5 wt. % nanotubes

A TEM image of purified single-wall carbon nanotubes is shown in Figure 2.

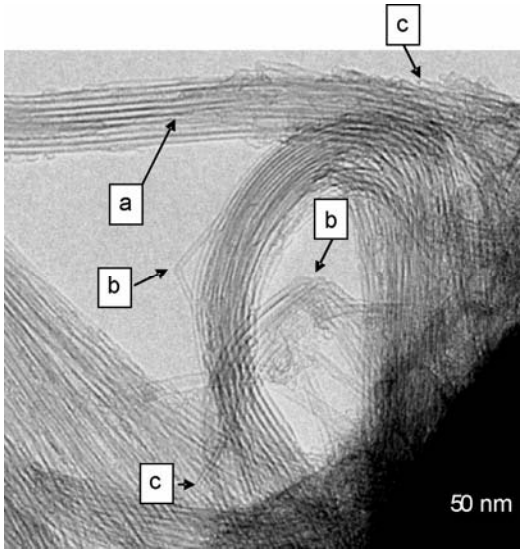

Fig. 2. TEM image of purified SWNTs: a) seemingly endless rope, b) isolated SWNT forming a knee, c) isolated SWNT end

Most of the carbon and catalyst impurities are removed. It can be seen that SWNTs are mainly entangled, forming seemingly endless ropes (arrow a), this type of nanotube architecture being typically mentioned in the literature. Also, isolated nanotubes are found (arrow b). For isolated nanotubes, or even for thin bundles, knees are

present (arrow b). Nanotube ends are found both when the nanotube is not aligned with a rope and when it is aligned (arrow c).

TEM images of the nanocomposite are shown in Fig. 3.

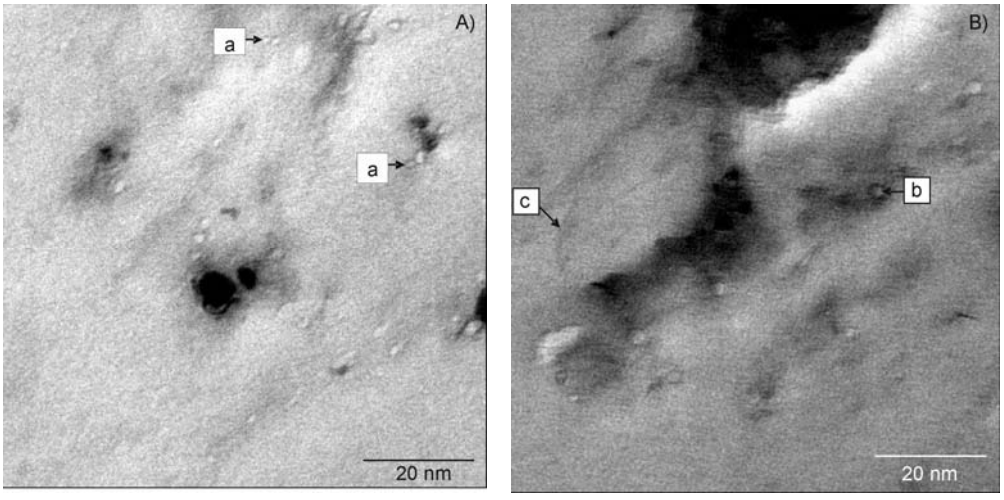

Fig. 3. TEM images of ultramicrotomed SWNT/cellulose/MF composite: A) pairs of off-plane nanotubes (arrow a) are seen. B) off-plane isolated nanotubes (arrow b) and in-plane nanotubes (arrow c) are seen

TEM imaging of this material is rather difficult. Nevertheless, in Figure 3 isolated nanotubes and occasionally pairs of nanotubes can be observed (arrows b and a, respectively). In Figure 3B, microdispersion is seen both for off-plane (refers to the slice) and in-plane nanotubes (arrows b and c, respectively). Interestingly, off-plane nanotubes occasionally assemble in thin bundles of two nanotubes (arrow a). Also, the ultramicrotome slices shown in Figure 3 contain cross-sectional images of nanotubes (arrows a and b). This behaviour can be contrasted with the well known behaviour published in literature, where nanotubes are aligned in the direction of the knife movement. We suggest that high matrix-nanotube interfacial shear strength and high shear strength of the matrix close to the nanotube play a role. Poor adhesion and low polymer strength would more likely cause a nanotube pull-out and the crack to deflect at the nanotube-matrix interface, both favouring nanotube alignment in the direction of the knife movement. The lighter shade inside the cross-sectional images suggests the nanotubes are un-filled. Areas of non-dispersed nanotubes are also present in the composite, as can be seen in Figure 3.

4. Conclusions

Ternary composites containing SWNTs, cellulose, and melamine-formaldehyde were prepared. Thin sheets were produced by hot pressing without venting of stacked

α-cellulose papers, on which liquid SWNT/MF was deposited by dipping. The obtained material is transparent and tinted. Ultramirotome slices cut across the sheet were possible to obtain. Dispersion characteristics and morphologies were tested by TEM, and TEM images of nanotubes are shown. TEM imaging of the present nanocomposite is rather difficult, nevertheless in-plane nanotubes (with respect to the slice), and off-plane thin bundles of two nanotubes and isolated nanotubes were possible to find. Their cross-sectional images are rather unusually contained in the TEM image. The latter behaviour, we suggest, is a result of high nanotube-matrix interfacial shear strength and high shear matrix strength in the vicinity of nanotubes. On the whole, nanotube concentration in the matrix was not uniform. Further work towards uniformity is needed in order to develop the material for multifunctional coatings.

Acknowledgements

The authors would like to thank Yiming Yao, Department of Materials Science and Engineering, Chalmers University of Technology for TEM imaging, Siw Kidman and Maud Langton, the Swedish Institute for Food and Biotechnology for ultramicrotomy, Perstorp AB for the α-cellulose papers, and UCB Company for the Madurit. The financial support of the National Council for Science and Technology, CONACYT (Mexico), the Swedish Foundation for International Cooperation in Research and Higher Education, STINT, and the Swedish Research Council, VR, are acknowledged.

References

[1] RYCHWALSKI R.W., MCQUEEN D.H., VOIGT B., LICEA-JIMÉNEZ L., PIC A., ROUXEL D., *New polymeric micro- and nanocomposites*, Symposium Materials-Energy Supply-Society and Environment, 13 December 2003, Chalmers University of Technology, Göteborg, Sweden.
[2] THOSTENSON E.T., REN Z., CHOU T.W., Comp. Sci. Technol., 61 (2001), 1899.
[3] LAU K.T. HUI D., Composites Part B: Engineering, 33 (2002), 263.
[4] NJUGUNA J., PIELICHOWSKI K., Adv. Eng. Mater., 5 (2003), 769.
[5] NJUGUNA J., PIELICHOWSKI K., Adv. Eng. Mater., 6 (2004), 204.
[6] ANDREWS R., WEISENBERGER M.C., Current Opinion Solid State Mater. Sci., 8 (2004), 31.
[7] BAUGHMAN R.H., ZHAKIDOV A.A., DE HEER W. A., Science, 297 (2002), 787.
[8] HARRIS P.J.F., Internat. Mater. Rev., 49 (2004), 31.
[9] Schaffer M. and Kinloch I.A., Comp. Sci. Technol., 64 (2004), 2281.
[10] VOIGT B., RYCHWALSKI, R.W., MCCARTHY D.M.C., DEN ADEL J.C., MARISSEN R., Polymer Composites, 24 (2003), 380.
[11] VOIGT B., ROUXEL D., MCQUEEN D.H., RYCHWALSKI R.W., Polymer Composites, 26 (2005), 144.

Received 23 September 2004
Revised 10 January 2005

Materials Science-Poland, Vol. 23, No. 4, 2005

Preparation and characterization of nanocarbons for hydrogen storage

R. J. KALEŃCZUK*

Centre for Knowledge Based Nanomaterials and Technologies KnowMatTech,
Department of Hydrogen Technologies and Nanomaterials,
Institute of Chemical and Environment Engineering,
Szczecin University of Technology, 70-310 Szczecin, Poland

Carbon nanomaterials have been pronounced as the most prospective material family for nanoelectronic applications, as well as materials for hydrogen storage. The catalytic methods we used for preparing different carbon nanoforms have been presented. During the study, a catalyst system composed of alkaline support and supported iron has been used. The effect of synthesis conditions and the carbon source material have been emphasised. The properties of the materials across the synthesis route have been studied by various instrumental techniques (i.e., ICP, SEM, FT-IR, low temperature nitrogen adsorption). The role of the catalyst is shown. Synthesized materials before as well as after the purification processes have been found to be very promising for hydrogen storage.

Key words: *hydrogen storage; carbon nanomaterial; nanomaterial synthesis*

1. Introduction

Carbon nanotubes (discovered by Iijima in 1991 [1]) have become some of the most thoroughly studied materials for technical applications. They are considered a very promising material for many new products (e.g., composite materials, catalyst materials, field emission materials). Furthermore, they show a great promise as storage media for hydrogen [2–4] and as such are of great interest to hydrogen-based economy. The hydrogen storage process of carbon nanotubes by themselves as well as of other carbonaceous nanomaterials has been extensively studied. The success of hydrogen storage within nanotubes will depend on a variety of parameters, including storage capacity and nanotube purity. To this end, the optimisation of the process

*Corresponding author, e-mail: rk@ps.pl

parameters for hydrogen storage and the quality of the prepared nanotube material are the key. To date, there are no methods [5–8] leading to the production of perfectly pure nanotubes. Most research has concentrated on the post-purification of the produced material from by-products like amorphous material, fullerenes, catalyst particles, and other carbon species [9–16]. Moreover, new methods enabling the mass production of storage materials should be studied. The carbon vapour deposition (CVD) method seems to be a solution (e.g. [17]), but in this case a suitable catalytic material is needed (mostly supported systems are used). The catalyst (the active agent as well as its support) should be removable after nanocarbons synthesis. In this work, an iron catalyst supported on calcium carbonate has been used.

2. Experimental

Carbon materials were synthesised by the decomposition of acetylene and methane in a tubular oven in the temperature range of 550–700 ºC. A monometallic salt of Fe(III) was applied as a catalyst. A calculated amount of $Fe(NO_3)_3 \cdot 9H_2O$ was dissolved in distilled water, and $CaCO_3$ was suspended in the solution. pH of the solution was held at about 7 by injecting ammonia water. The mixture was stirred for 30 minutes and then filtered. Material from filtration was dried at 105 ºC for 5 hours and calcinated for 1.5 hours under argon at 700 ºC. So prepared material was used in carbonaceous materials synthesis. As a blind probe, a sample of $CaCO_3$ with the same history was used.

The catalyst sample or blind probe was placed in a quartz boat, which was inserted in a quartz tube under argon flow (400 cm^3/min) for 2 h. Keeping a constant flow, the temperature was raised to the value assumed for the synthesis. After that, the composition of the gaseous mixture was changed. In the case of acetylene, it was introduced to reach 2 vol. % of C_2H_2 in the mixture. In the case of methane, the atmosphere was changed from Ar to CH_4. After 1 h (in the case of C_2H_2) or 24–120 h (in the case of CH_4), the gas flow was switched from hydrocarbon to argon and the boat was cooled down to room temperature. Iron loading was controlled by the ICP method (1% Fe wt.).

A two-step procedure similar to those described by us in [18] was used for purification. In the first step, amorphous carbon was burned off in oxygen at 500 ºC. In the next step, the catalyst was dispersed in a solution of diluted nitric acid for 20 h at 80 ºC, washed with distilled water, and dried at 105 ºC overnight. The morphology of the samples was studied by scanning electron microscopy (SEM), specific surface and pore size distribution by low temperature nitrogen adsorption, surface properties by infrared spectroscopy (FT-IR), phase composition by powder X-ray diffraction (XRD), and, finally, hydrogen storage capacity by volumetric methods [19].

3. Results and discussion

Figure 1 shows a SEM micrograph of a catalyst sample after the calcination step. In Figure 2, the product of synthesis under C_2H_2 at 750^{o}C is presented. At lower temperatures, the synthesis was ineffective. Figure 3 presents the surface of the samples after synthesis under methane for the syntheses lasting 27, 70, and 118 h. It can be observed that in the case of the shortest reaction time not all of the catalyst's surface is covered with a new material. On the other hand, there are no visible changes between the samples presented in Figs. 3b and c. No mass change was observed between the last two samples. The synthesis was probably concluded after 70 h.

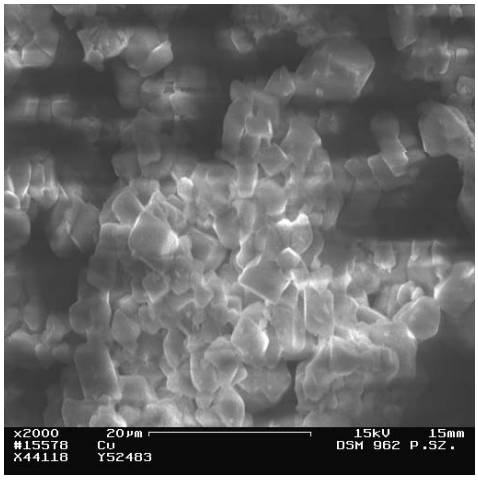

Fig. 1. The surface of the catalyst after calcination

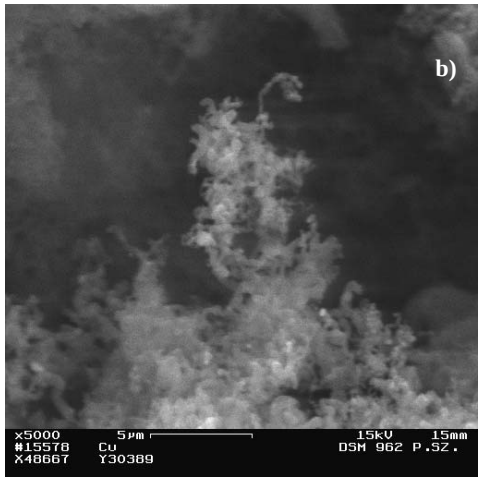

Fig. 2. The surface of the sample after synthesis (acetylene) at 750 ºC under magnifications: a) 2000, b) 20 000

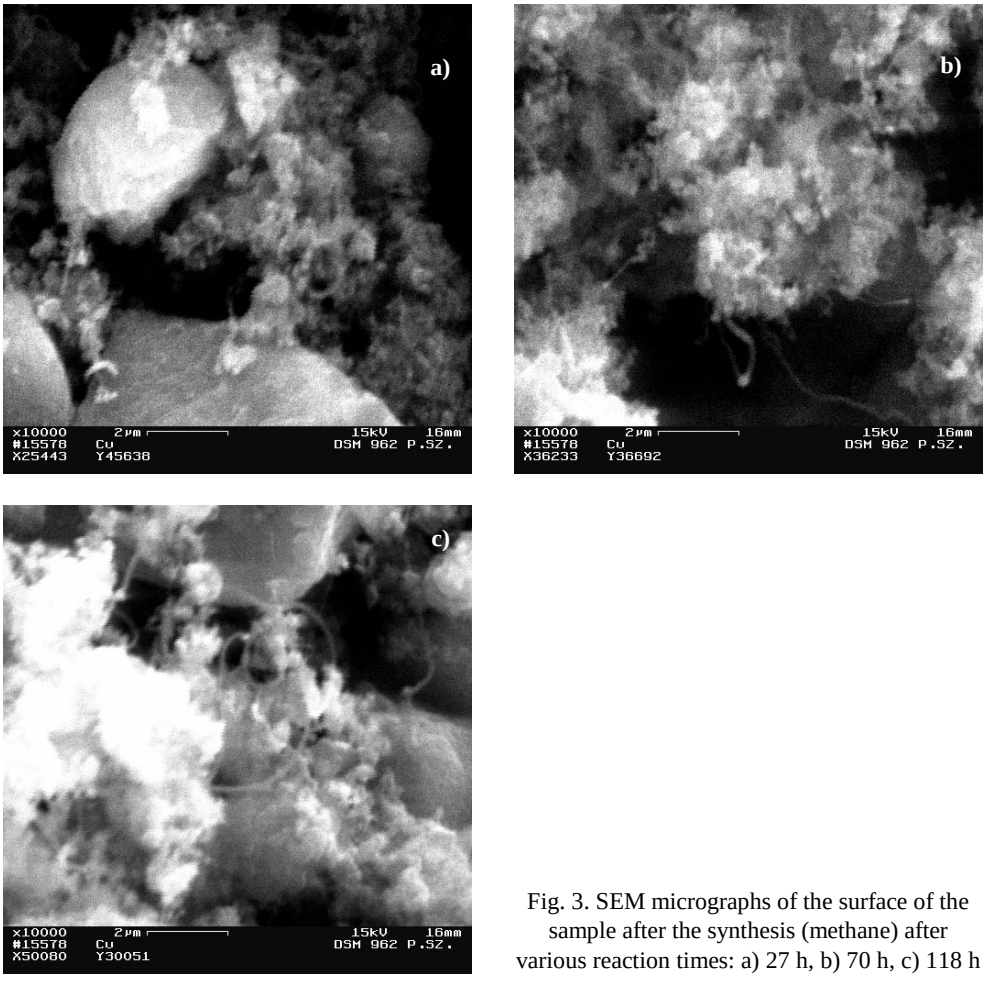

Fig. 3. SEM micrographs of the surface of the sample after the synthesis (methane) after various reaction times: a) 27 h, b) 70 h, c) 118 h

The forming of the nanomaterials was a catalytic process. In Figure 4, the pictures of the blind probe with no iron addition (support only, treated the same way as the catalyst) and of the catalyst surface are presented. It should be noted that in the case of the blind probe no new material occurs. Therefore it can be concluded that the process has a catalytic character. Now we will try to explain the phenomena following from Figure 3. Material synthesis was stopped because iron catalyst particles were blocked by new carbon materials.

In Figure 5, images of the synthesised materials after the purification procedure are presented. The material received with acetylene used as the carbon source (Fig. 5b) consists of fibres (tubes) with a larger diameter. Moreover, no catalyst material is observed. This was confirmed by ICP analysis: only traces of iron were found.

As follows from XRD measurements (not presented), the disintegration of $CaCO_3$ to CaO was concluded in the samples after synthesis at 750 ºC. The FT-IR method proved to be a very effective tool for studying the sample surface at different process

steps. In Figure 6, spectra of a samples before synthesis (after catalyst calcination) and after synthesis and the purification procedure are presented. As is visible, the spectrum of the purified sample is sharper, with no additives.

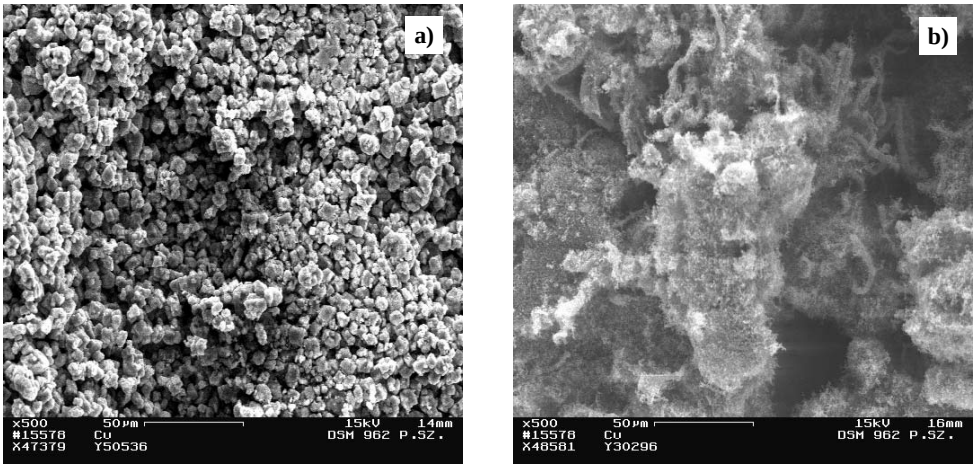

Fig. 4. Images of the surfaces of the sample after synthesis
on the blind probe (a) and on the catalyst (b), under the same magnification

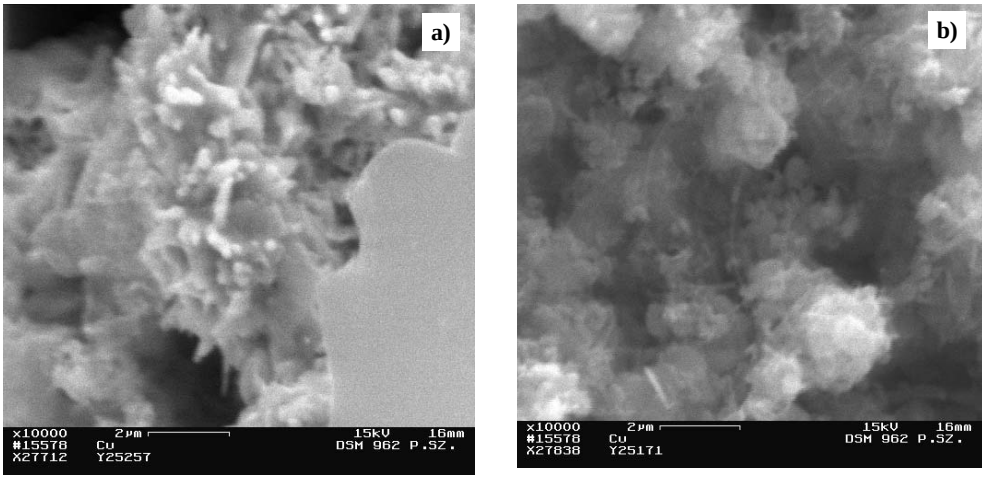

Fig. 5. Images of the surfaces of samples after the purification procedure: a) CH_4, b) C_2H_2)

The obtained samples, as follows from nitrogen adsorption measurements (not presented), differ in their specific surfaces, and pore size distributions. In samples after purification, a higher micropore content and a larger surface were found. This is due to the removal of amorphous carbon forms.

The prepared samples were used for studying hydrogen storage. Hydrogen loading ranges between 2 and 4 wt. %. When we compare these results to those already pre-

sented in previous studies, we see that hydrogen storage in carbon nanotubes is still questionable. Dillon et al. [20] concluded that pure single-walled carbon nanotubes

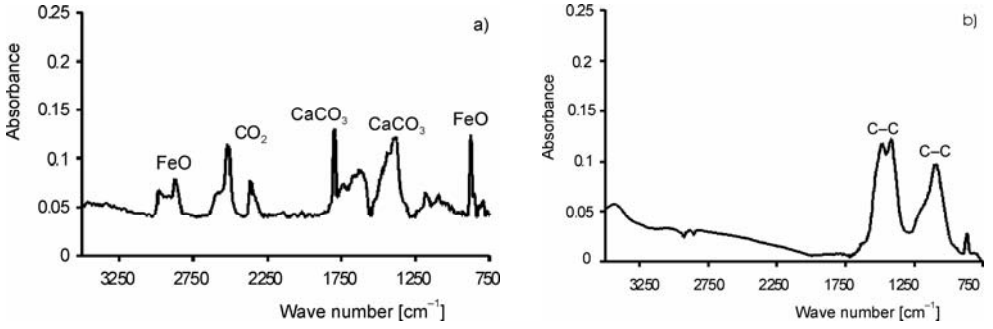

Fig. 6. FT-IR spectra for the studied samples:
a) the catalyst after calcination, b) the sample after synthesis and purification

(SWCNTs) are able to store 5–10 wt. % of H_2 (at 133 K and 0.04 MPa) that can be desorbed at room temperature. Chambers et al. [20] reported much higher storage capacities for carbon nanofibres – up to 67 wt. % at 25 ºC and 120 atm. Chen et al. [21] presented Li-doped multiCNTs (20 wt. % At 473–633 K and ambient pressure) and K-doped CNTs (14 wt. % at room temperature and ambient pressure). It is worth noting that Yang [22] pointed out that Chen's results should be treated as unreliable due to the presence of H_2O, and highlighted the difficulties that can be encountered in such studies.

4. Conclusions

The results presented here demonstrate that the described method can be used to prepare nanomaterials for the hydrogen storage but an optimisation of the synthesis parameters is needed.

Acknowledgements

This work was supported by the State Committee for Scientific Research in the framework of Scientific Project No. 4 T09B 059 25 (2003–2006). Also, the author wishes to thank MSc. students Ms. Mirosława Kamińska and Mr Marcin Feistner for their collaboration during the experimental work.

References

[1] IIJIMA S., Nature, 354 (1991), 56.
[2] LIU C., FAN Y.Y., LIU M., CONG H.T., CHENG H.M., DRESSELHAUS M.S., Science, 286 (1999), 1127.
[3] YE Y., AHN C.C., WITHAM C., FULZ B., LIU J.RINZLER A.G., COLBERT D., SMITH K.A., SMALLEY R.E., Appl. Phys. Lett., 74 (1999), 2307.
[4] SIMONYAN V.V., DIEP P., JOHNSON J.K., J. Chem. Phys., 111 (1999), 9778.

[5] GUO T., NIKOLAEV P., THESS A., COLBERT D.T., SMALLEY R.E., Chem. Phys. Lett., 243 (1995), 49.
[6] JOURNET C., MASER W.K., BARNIER P., LOISEAU A., Nature, 388 (1997), 756.
[7] NIKOLAEV P., BRONIKOWSKI M.J., BRADLEY R.K., ROHMUND F., COLBER D.T.T, SMITH K.A., SMALLEY R.E., Chem. Phys. Lett., 313 (1999), 91.
[8] CASSEL A., RAYMAKERS J., KONG J., DAI H., J. Phys. Chem., 103 (1999), 6484.
[9] RINZLER A.G., LIU J., DAI H., HUFFMAN C.B., RODRIGUEZ-MACIAS F., BOUL P.J., LU A.H., HEYMANN D., COLBERT D.T., LEE R.S., FISCHER J.E., RAO A.M., EKLUND P.C., SMALLEY R.E., Appl. Phys. A, 67 (1998), 29.
[10] HERNADI K., FONSECA A., NAGY J.B., BERNAERT D., RIGA J., LUCAS A., Synth. Met., 77 (1996), 31.
[11] DETLAFF-WEGLIKOWSKA U., ROTH S., [in:] H. Kuzmany, J. Fink, M. Mehring, S. Roth (Eds.), *Electronic Properties of Molecular Nanostructures*, AIP Conference Proceedings, 591 (2001), 171.
[12] CHIANG I.W., BRINSON B.E., SMALLEY R.E., MARGRAVE J.L., HAUGE R.H., J. Phys. B, 105 (2001), 1157.
[13] JEONG T., KIM W.-K., HAHN Y.-B., Chem. Phys. Lett., 344 (2001), 18.
[14] HERNADI K., SISKA A., THIEN-NGA L., FORRO L., KIRICSI I., Solid State Ionics, 203 (2001), 141.
[15] PARK Y.S., CHOI Y.C., KIM K.S., CHING D.-C., BAE D.J., AN K.H., LIM S.C., ZHU X.Y., LEE Y.H., Carbon, 39 (2001), 655.
[16] ZHANG M., YUDASAKA M., NIHEY F., IIJIMA S., Chem. Phys. Lett., 328 (2000), 350.
[17] COUTEAU E E., HERNADI K., SEO J.W., THIÊN-NGA, L., MIKÓ CS., GAÁL R., FORRÓ L., Chem. Phys. Lett., 378 (2003), 9.
[18] KALEŃCZUK R.J., BOROWIAK-PALEN E., Przemysł Chemiczny, 82 (2003), 149.
[19] KALEŃCZUK R.J., BOROWIAK-PALEŃ E., Polish J. Chem. Technol., 3 (2001), 6.
[20] DILLON A.C., JONES K.M., BEKKEDAHL T.A., KIANG C.H., BETHUNE D.S., HEBEN M.J., Nature, 386 (1997), 377.
[21] CHAMBERS A., PARK C., BAKER R.T.K., RODRIGUEZ N.M., J. Phys. Chem. B, 102 (1998), 4253.
[22] CHEN P., WU X., LIN M., TAN K.L., Science, 285 (1999), 91.

Received 23 September 2004
Revised 14 March 2005

Materials Science-Poland, Vol. 23, No. 4, 2005

Magnetic resonance study of $M_3Fe_4V_6O_{24}$ (M = Mg, Zn, Mn, Cu, Co) compounds

N. GUSKOS[1, 2], J. TYPEK[2*], G. ZOLNIERKIEWICZ[2], A. BLONSKA-TABERO[3], M. KURZAWA[3], M. BOSACKA[3]

[1]Solid State Section, Department of Physics, University of Athens, Panepistimiopolis, 15 784 Zografos, Athens, Greece

[2]Institute of Physics, Szczecin University of Technology, al. Piastów 17, 70-310 Szczecin, Poland

[3]Department of Inorganic and Analytical Chemistry, Szczecin University of Technology, al. Piastów 42, 71-065 Szczecin, Poland

Multicomponent vanadates, $M_3Fe_4V_6O_{24}$ (M = Mg(II), Mn(II), Zn(II), Co(II) and Cu(II)), have been synthesized by the solid-state reaction method using a stoichiometric mixture of MO, Fe_2O_3, and V_2O_5 oxides. They crystallize in the triclinic space group $P\bar{1}$ and have a complicated structure with two metal ion subsystems. Electron paramagnetic resonance (EPR) measurements have been performed at room temperature and an intense, almost symmetric EPR lines were recorded for all investigated samples except $Co_3Fe_4V_6O_{24}$. The integral intensity and linewidth of this line essentially depends on the kind of M(II) metal ion in the crystalline matrix. The EPR line intensity for the sample $Co_3Fe_4V_6O_{24}$ is over one order of magnitude smaller than for all other investigated compounds, and the position of its resonance line is shifted towards lower magnetic fields. The difference in linewidths and intensities are due to the various magnetic interactions between magnetic ions in the lattice, especially for systems containing two different magnetic ions.

Key words: *electron paramagnetic resonance; vanadate*

1. Introduction

Multicomponent vanadate oxide systems attract a particular interest due to their interesting physical properties, especially site disorder and frustration phenomena [1–7]. The temperature dependences of the magnetic susceptibilities and electron paramagnetic resonance (EPR) spectrum of the $Zn_2FeV_3O_{11}$ compound have shown an

*Corresponding author, e-mail: typjan@ps.pl

inherent magnetic inhomogeneity in the iron(III) subsystem [5]. XRD and neutron diffraction studies of $M_2FeV_3O_{11}$ (M = Zn(II), Mg(II)) compounds showed that iron(III) and metal(II) ions were disordered in their corresponding subsystems, and the distributions on the octahedral and trigonal bipyramidal sites were non-statistical [3, 4, 6]. Novel $M_3Fe_4V_6O_{24}$ (M = Zn(II), Co(II), Mg(II)) compounds have been obtained as a product of the reaction between $FeVO_4$ and $M_3V_2O_8$ (M = Zn(II), Co(II), Mg(II)) and have been found to crystallize in the triclinic space group $P\bar{1}$ [6, 8, 9]. Neutron diffraction studies of the $Zn_3Fe_4V_6O_{24}$ compound have not shown any disorder in its corresponding subsystem of iron(III) and metal(II) ions [11].

This work presents the results of EPR measurements of $M_3Fe_4V_6O_{24}$ (M = Mg(II), Mn(II), Zn(II), Co(II) and Cu(II)) compounds, prepared as a product of the reaction between MO, Fe_2O_3, and V_2O_5, and discusses the reasons for the observed differences in the resonance fields, linewidths and integrated intensities of their EPR spectra recorded at room temperature.

2. Experimental

Polycrystalline $M_3Fe_4V_6O_{24}$ samples were prepared by the solid-state reaction method using a stoichiometric mixture of MO, V_2O_5, and Fe_2O_3 oxides or appropriate hydroxycarbonates, according to the following reaction [8, 9]:

$$3MO + 3V_2O_5 + 2Fe_2O_3 \rightarrow M_3Fe_4V_6O_{24}$$

The reactants were mixed, pressed into pellets and calcinated in air at a temperature range of 560–900 °C in 20 h stages. After each heating stage, the samples were slowly cooled down to room temperature, ground, and analysed by differential thermal analysis (DTA) and X-ray diffraction (XRD). Heating was continued until the formation of a single-phase sample could be confirmed. The obtained compounds crystallize in the triclinic space group $P\bar{1}$, forming powders with a brown-olive colour, with a melting point in the range of 1100–1140 K. The $Zn_3Fe_4V_6O_{24}$ sample was prepared by two methods, differing in the starting reactants: the first method was based on the above described reaction, in the other the $FeVO_4$ and $Zn_3V_2O_8$ vanadates were synthesized separately and subsequently mixed according to the reaction:

$$4FeVO_4 + Zn_3V_2O_8 \rightarrow Zn_3Fe_4V_6O_{24}$$

The heating cycles were: 700 °C (24 h), 750 °C (24 h) and 800 °C (24h) [8].

EPR measurements were carried out with a conventional X-band (ν = 9.43 GHz) Bruker E 500 spectrometer, with 100 kHz magnetic field modulations. The samples, in the form of loose powder, containing about 30 mg of the material, were placed into 4 mm diameter quartz tubes.

3. Results and discussion

Table 1 presents the crystallographic parameters for the studied $M_3Fe_4V_6O_{24}$ compounds, and for comparison, also for an isomorphic $M_2FeV_3O_{11}$ system. The replacement of metal(II) ions in the structure introduces some differences in the crystallographic parameters.

Table 1. Structure parameters for the $M_2FeV_3O_{11}$ and $M_2Fe_4V_6O_{24}$ compounds

Compound	Crystallographic system	Lattice constants [nm]	Angles [°]	Z	Reference
$Mg_2FeV_3O_{11}$	triclinic	a = 0.64406(4) b = 0.68117(4) c = 1.01057(7)	α = 97.371(8) β = 103.458(8) γ = 101.504(7)	2	[4]
$Zn_2FeV_3O_{11}$	triclinic	a = 0.64538(5) b = 0.68393(4) c = 0.9988(1)	α = 97.556(9) β = 102.650(8) γ = 101.308(8)	2	[5]
$Mg_3Fe_4V_6O_{24}$	triclinic	a = 0.6678(5) b = 0.8027(4) c = 0.9759(7)	α =105.16(8) β = 104.95(9) γ = 101.91(9)	1	[8]
$Mn_3Fe_4V_6O_{24}$	triclinic	a = 0.67034(5) b = 0.81477(7) c = 0.9808(8)	α = 105.25(1) β = 105.54(1) γ = 102.37(1)	1	[2]
$Zn_3Fe_4V_6O_{24}$	triclinic	a = 0.66812(1) b = 0.8021(2) c = 0.9778(4)	α = 105.25(4) β = 105.00(4) γ = 102.20(4)	1	[8]
$Co_3Fe_4V_6O_{24}$	triclinic	a = 0.6685(2) b = 0.8003(5) c = 0.9764(8)	α = 105.30(9) β = 105.21(6) γ = 101.83(7)	1	[9]
$Cu_3Fe_4V_6O_{24}$	triclinic	a = 0.6600(3) b = 0.8048(4) c = 0.9759(5)	α = 106.08(3) β = 103.72(3) γ = 102.28(2)	1	[10]

The distances between magnetic iron(III) ions in the $M_3Fe_4V_6O_{24}$ compounds are given in Table 2. These values show a decreasing trend in both sublattices with iron(III) ions ($d_{Mg} > d_{Mn} > d_{Zn} > d_{Cu}$), while the differences $\Delta d = d_{Fe(1)–Fe(1)} - d_{Fe(2)–Fe(2)}$ are over twice as large for the sample with Mg(II) and almost the same for the other three compounds.

Table 2. The distances between magnetic ions in the $M_3Fe_4V_6O_{24}$ system

Compound	$d_{Fe(1)–Fe(1)}$ [nm]	$d_{Fe(2)–Fe(2)}$ [nm]	Δd [nm]	Reference
$Mg_3Fe_4V_6O_{24}$	0.3148	0.3330	–0.0182	
$Mn_3Fe_4V_6O_{24}$	0.3132	0.3212	–0.0080	[10]
$Zn_3Fe_4V_6O_{24}$	0.3117	0.3192	–0.0075	[11]
$Cu_3Fe_4V_6O_{24}$	0.3095	0.3152	–0.0057	[10]

Figure 1 shows the EPR spectra for all investigated $M_3Fe_4V_6O_{24}$ samples at room temperature. An intense, almost symmetric EPR line is recorded for all samples except for $Co_3Fe_4V_6O_{24}$. The lineshape of this EPR line has been fitted very well by using the Lorentzian-shape function. The obtained parameters of the EPR spectra for all six samples are given in Table 3. The resonance fields of five samples (excluding the sample with cobalt(II)) are basically the same, with $g = 2.00$, similarly as the EPR spectrum arising from the high spin ground state of the iron(III) ion. The peak-to-peak linewidth ΔH_{pp} and integrated intensity I, defined as the product of the signal amplitude and the square of the peak-to-peak linewidth, strongly depend on the kind of M(II) ion in the crystal matrix. An EPR study of the $M_2FeV_3O_{11}$ (M = Ni(II), Zn(II), Mg(II), Co(II)) system has shown that the coexistence of two different magnetic ions in the lattice (Ni(II)–Fe(III) or Co(II)–Fe(III)) induces the absence of an EPR signal in the high spin iron(III) ions [12]. For the $Co_2FeV_3O_{11}$ sample, no EPR signal was recorded, while for the $Ni_2FeV_3O_{11}$ compound the EPR spectrum was dominated by the exchange coupled vanadium(IV) ions [13]. The coexistence of magnetic iron(III) ions with nonmagnetic ions (Zn and Mg) in the above samples manifests itself in the EPR spectra through the variation of the integrated intensity (Table 3), while the disorder phenomena between magnetic and nonmagnetic ions take place. It has been suggested that the disorder processes of iron atoms with zinc atoms in the $Zn_2FeV_3O_{11}$ compound could be responsible for the significant differences observed in its physical properties, influenced by the method of sample preparation [2, 5, 6].

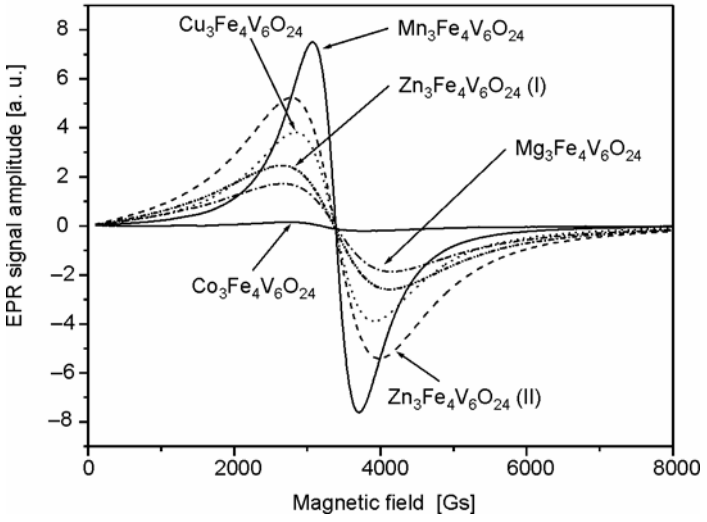

Fig. 1. The EPR spectra of all investigated samples at room temperature

Neutron diffraction of $Zn_2FeV_3O_{11}$ powder has shown that the iron(III) and zinc(II) ions are disordered in their corresponding sublattices, and that the distribution on the octahedral and the trigonal bipyramidal sites is non-statistical. A Mössbauer spectros-

copy study has found that some cations are disordered between the octahedral iron and the fivefold coordinated copper site in the β-$Cu_3Fe_4V_6O_{24}$ compound [10]. In contrast, neutron diffraction analysis of the $Zn_3Fe_4V_6O_{24}$ system has shown that iron atoms are not disordered with zinc atoms on any sites in this material [11]. The simultaneous existence of magnetic dimers and of triangular cationic topology around some sites has incited us to explore the magnetic behaviour and possible frustration effects in these compounds. For the polycrystalline β-$Cu_3Fe_4V_6O_{24}$, the inverse magnetic susceptibility varies linearly with temperature in the 250–20 K range and has a negative Curie–Weiss temperature Θ (–80 K), which indicates the presence of antiferromagnetic interactions in this substance [10].

Table 3. EPR parameters at room temperature for some compounds of the multicomponent vanadate oxide system

Compound	Linewidth ΔH_{pp} [kGs]	Resonance field		Integrated intensity I [a. u.]
		H_r [kGs]	g	
$Mg_3Fe_4V_6O_{24}$	1.498(5)	3.382(4)	1.999(1)	91.5
$Mn_3Fe_4V_6O_{24}$	0.636(5)	3.386(4)	1.997(1)	69.2
$Zn_3Fe_4V_6O_{24}$ (I)	1.524(5)	3.362(4)	2.010(1)	133.1
$Zn_3Fe_4V_6O_{24}$ (II)	1.204(5)	3.376(4)	2.002(1)	174.9
$Co_3Fe_4V_6O_{24}$	1.052(5)	3.193(4)	2.117(1)	4.5
$Cu_3Fe_4V_6O_{24}$	1.094(5)	3.373(4)	2.005(1)	104.6
$Mg_2FeV_3O_{11}$	1.527(5)	3.380(1)	2.000(1)	–
$Zn_2FeV_3O_{11}$	1.449(5)	3.375(1)	2.004(1)	–

For the $Co_3Fe_4V_6O_{24}$ compound, a weak EPR line, shifted towards lower magnetic fields, is observed. This could be the result of interaction between iron(III) ions and highly magnetic cobalt(II) ions. A similar trend was observed for other samples with two different magnetic ions (Mn(II) and Cu(II)), in which the linewidths and intensities are influenced (Table 3).

The differences in the parameters of the EPR spectra for two samples of $Zn_3Fe_4V_6O_{24}$ prepared using different thermal annealing processes could arise from the inherent disorder or from presumed oxygen deficiency. The effects of disorder processes, seen by the EPR spectroscopy, could not be recorded by neutron diffraction measurements.

4. Conclusions

$M_3Fe_4V_6O_{24}$ compounds were synthesized from appropriate oxides and EPR measurements have been carried out at room temperature. An analysis of the EPR spectra was done using Lorentzian-type functions. The observed differences in the crystallographic parameters of these compounds did not have a major influence on the

recorded EPR parameters. We observe that the coexistence of two different magnetic ions in the lattice has a strong influence on the EPR spectrum.

References

[1] RAMIREZ A.P., Annu. Rev. Mater. Sci., 24 (1994), 453.
[2] WANG X., GRIEND D.A., STERN C.L., POEPPELMEIER K.R., Inorg. Chem., 39 (2000), 136.
[3] WANG X., VAN DER GRIEND D.A., STERN CH.L., POEPPELMEIER K.R., J. Alloys Comp., 298 (2000), 119.
[4] GUSKOS N., WABIA M., KURZAWA M., BEZKROVNYI A., LIKODIMOS V., TYPEK J., RYCHLOWSKA -HIMMEL I., BLONSKA-TABERO A., Radiat. Eff. Defects Solids, 158 (2003), 369.
[5] LIKODIMOS V., GUSKOS N., GLENIS S., SZYMCZAK R., BEZKROVNYI A., WABIA M., TYPEK J., GASIOREK G., KURZAWA M., RYCHLOWSKA-HIMMEL I., BLONSKA-TABERO A., Eur. Phys. J., B 38 (2004), 13.
[6] GUSKOS N., TYPEK J., BEZKROVNYY A., WABIA M., KURZAWA M., ANAGNOSTAKIS E.A., GASIOREK G., J. Alloys Comp., 377 (2004), 47.
[7] RYCHLOWSKA-HIMMEL I., BLONSKA-TABERO A., J. Therm. Anal. Cal., 56 (1999), 205.
[8] KURZAWA M., BLONSKA-TABERO A., Mat. Res. Bull., 37 (2002), 849.
[9] KURZAWA M., BLONSKA-TABERO A., J. Therm. Anal. Cal., 77 (2004), 17.
[10] LAFONTAINE M.A., GRENECHE J.M., LALIGANT Y., FEREY G., J. Solid State Chem., 108 (1994), 1.
[11] GUSKOS N., BEZKROVNYI A., TYPEK J., RYABOVA N.YU., BLONSKA-TABERO A., KURZAWA M., MARYNIAK M., J. Alloys Comp., 391 (2005), 20.
[12] GUSKOS N., WABIA M., LIKODIMOS V., TYPEK J., KURZAWA M., BLONSKA-TABERO A., RYCHLOWSKA -HIMMEL I., Mol. Phys. Rep., 36 (2002), 27.
[13] LIKODIMOS V., GUSKOS N., TYPEK J., WABIA M., *NATO Science Series, II. Mathematics, Physics and Chemistry*, 67 (2002), 201.

Received 23 September 2004
Revised 23 March 2005

Materials Science-Poland, Vol. 23, No. 4, 2005

Synthesis and ESR study of $(Tb_xY_{1-x})_2Cu_2O_5$ solid solutions

J. TYPEK[1*], J. KOSTRZEWA[1], N. GUSKOS[1, 2]

[1]Institute of Physics, Szczecin University of Technology, al. Piastów 17, 70-310 Szczecin, Poland

[2]Solid State Section, Department of Physics, University of Athens, Panepistimiopolis, 15 784 Zografos, Athens, Greece

Polycrystalline samples of $(Tb_xY_{1-x})_2Cu_2O_5$, where x = 1.0, 0.75, 0.50, 0.38, 0.25, 0.125 and 0, were synthesized by the solid-state reaction technique. XRD measurements showed that the obtained samples are single-phase and belong to the orthorhombic space group $Pna2_1$. The observed linear change of the lattice parameters and unit cell volume with terbium concentration is in agreement with Vegard's law. A thermogravimetric study of the decomposition process of the obtained samples revealed small sample-dependent mass losses in the temperature range 1030–1050 °C, and a larger, intrinsic mass loss in the range 1100–1150 °C. The former are probably due to the $4\ CuO \rightarrow 2\ Cu_2O + O_2$ transformation, while the latter is related to the reaction $2Y_2Cu_2O_5 \rightarrow 4YCuO_2 + O_2$. The peak temperature of the main decomposition stage varies linearly with terbium concentration, which could be explained by an increasing distortion of coordination polyhedra around the copper ion, caused by the substitution of the larger Tb^{3+} cation. The ESR spectra of $(Tb_xY_{1-x})_2Cu_2O_5$ solid solutions showed a complicated structure due to the presence of various copper clusters (tetramers, trimers). Moreover, the ESR spectra were anisotropic in an external magnetic field, despite originating from powder samples.

Key words: *solid solutions; ESR; copper complexes*

1. Introduction

The discovery of high-temperature superconductivity in $RBa_2Cu_3O_7$ compounds (where R is a rare earth element) has greatly increased interest in other non-superconducting copper oxides. $R_2Cu_2O_5$ compounds with the orthorhombic space group $Pna2_1$ include a well known "blue phase", $Y_2Cu_2O_5$, often found as a common second phase in the synthesis of $YBa_2Cu_3O_7$. The family of the orthorhombic $R_2Cu_2O_5$ compounds includes those with rare-earth R^{3+} cations smaller then Gd, i.e. Tb, Dy, Ho, Y,

*Corresponding author, e-mail: typjan@ps.pl.

Er, Tm, Yb, as well as with Lu, In, and Sc [1–3]. The most characteristic feature of the $R_2Cu_2O_5$ crystallographic structure is the occurrence of zigzag copper chains along the *a*-axis (Fig. 1). There is a distorted square planar arrangement of four oxygen atoms around copper atoms, with the fifth oxygen atom forming a sort of a pyramid. These copper–oxygen pyramids are joined at their common edges into Cu_2O_8 dimers. The dimers, through the bridging oxygen, form an infinite zigzag Cu_2O_5 copper –oxygen chains. Furthermore, each copper atom is coupled with four other Cu ions along the *b*-axis, forming *ab*-pseudoplanes. The rare earth ions are octahedrally coordinated, and these distorted RO_6 octahedra are linked in a three-dimensional network occupying the space between copper–oxygen planes [3].

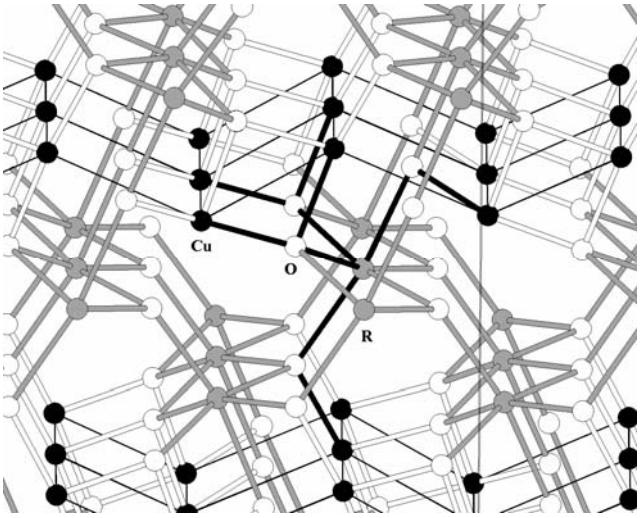

Fig. 1. The crystal structure of $R_2Cu_2O_5$ compounds

All $R_2Cu_2O_5$ compounds are antiferromagnetically ordered at low temperatures and most of them exhibit metamagnetic behaviour below the Neel temperature [4]. The magnetic properties of $Y_2Cu_2O_5$ have been studied extensively [4–10]. Above 120 K, the magnetic susceptibility of this compound is well described by the Curie–Weiss law with a positive Curie temperature, θ = 38.5 K, indicating a considerable contribution of ferromagnetic interaction [4]. At T_N = 11.5 K a sharp maximum in the susceptibility gives a strong indication of an antiferromagnetic ordering. In the antiferromagnetic state two jumps in the $M(H)$ magnetization curve (with the external field H applied along *b*-axis) are observed, corresponding to the two metamagnetic transitions [10]. The magnetic studies of $Tb_2Cu_2O_5$ have been presented in Refs. [11–17]. The magnetic susceptibility of this compound containing two magnetic ions follows the Curie–Weiss law with the antiferromagnetic transition temperature T_N = –10 K. Transition to the antiferromagnetic phase was reported to take place in the 17–21.5 K temperature range. An additional anomaly of magnetic susceptibility was observed in the 5–8 K range. The magnetic structure in an ordered state of $R_2Cu_2O_5$ compound could be viewed as consisting of ferromagnetic CuO layers

parallel to the *ab*-plane coupled antiferromagnetically. The copper magnetic moments are aligned along the *b*-axis (at least for R = Y, Lu, Er, Tb). Despite a large amount of experimental material gathered from magnetic susceptibility and neutron diffraction measurements, the understanding of the nature of magnetic interactions in the $R_2Cu_2O_5$ family is still incomplete.

Conventional X-band electron spin resonance (ESR) has been used to study the magnetic properties of $Y_2Cu_2O_5$ in the paramagnetic state, the sample being in the form of powder [15–22] or single crystals [23, 24]. For the investigation of the antiferromagnetic state, antiferromagnetic resonance (AFMR) was employed [23–26]. At room temperature, a single Lorentzian-shape ESR line, centred at g = 2.13, with a linewidth of ΔB = 90 mT, was recorded. As the temperature was decreased to 50 K, the g-value and the linewidth remained virtually unchanged. Below 40 K, the line started to broaden and the g-value shifted to 2.0 [19]. For certain samples, a number of weaker lines, supposedly arising from clusters of four copper ions coupled by a superexchange interaction through interviewing oxygen ions (copper tetramers), have been detected [21, 22]. Such clusters could form in those portions of the sample in which the oxygen content is reduced. AFMR modes have been analysed in a model assuming the existence of S = l dimers formed by two Cu^{2+} spins. In the Cu^{2+} chains along the *a*-axis, due to 90° and 180° Cu–O–Cu exchange paths, there are alternative strong ferromagnetic (J_0 = 340 K) and weak antiferromagnetic (J_1 = –0.33 K) interactions. Such a model of spin system is capable of showing metamagnetic transitions, although discrepancies between the experimental and calculated results exist [23, 25].

Compositional series of solid solutions of $(R_xR'_{1-x})_2Cu_2O_5$ -type, where R and R' are different rare earth ions, have been the subject study of only a few papers [27-29]. The structure and magnetic properties of $(In_xY_{1-x})_2Cu_2O_5$ compounds were reported in the temperature range between 77 K and room temperature [27]. In another work it was found that the maximum solubility of Gd in $Y_2Cu_2O_5$ is $x \approx 0.3$ and that the low -temperature magnetic phase diagram of $(Gd_xY_{1-x})_2Cu_2O_5$ was established [28]. Within samples of $(Ca_xY_{1-x})_2Cu_2O_5$, where x = 0.05, 0.1 and 0.2, a phase with incommensurate modulated structure has been found [29]. This phase becomes the main phase within the $(Ca_{0.2}Y_{0.8})_2Cu_2O_5$ sample. In the present paper, an attempt has been taken to synthesize $(Tb_xY_{1-x})_2Cu_2O_5$ for the whole range of the terbium index x. Combining a magnetic Tb ion and a non-magnetic Y ions could be especially interesting, because they would allow to investigate the magnetic interaction between the d (Cu) and f (Tb) ions present in the solid solutions. We present X-ray, thermogravimetric, and ESR measurements of the obtained samples and discuss their results.

2. Experimental

Ceramic samples of $(Tb_xY_{1-x})_2Cu_2O_5$ have been prepared by heating in air appropriate stoichiometric amounts of Y_2O_3 (99.99%), Tb_2O_3 (99.99%), and CuO (99.99%) at 1000 °C. The samples with the following values of the terbium index x have been

prepared: x = 1.0, 0.750, 0.50, 0.38, 0.25, 0.125 and 0. Four intermediate grindings and pressings were carried out to homogenize the reaction products. The total firing time was about 100 hours in order to get a complete reaction of the starting powders. The heating was carried out in a Carbolite CTF 12/100/900 tube furnace. An Eurotherm 902P temperature controlled the temperature programs.

X-ray studies were carried out on a Dron-3 diffractometer using $Co_{K\alpha}$/Fe radiation at room temperature. The X-ray patterns were taken by means of step-scanning the sample using the θ–2θ method with a step of 0.02°.

The thermal analysis (simultaneous TGA-DSC measurements) was conducted on a Setaram apparatus model TG 92-16. All measurements were recorded at 4 °C/min under dry synthetic air (N_2:O_2 = 80:20 % vol.) or argon flow in 20–1200 °C temperature range. The ceramic samples (m = 50.7±0.1 mg) were held in a platinum cylinder and placed in 17 cm^3/min gas flow stream. Kinetic parameters of sample decomposition were calculated using a computer program Setsoft Kinetics on DTG by Setaram.

The ESR room temperature experiments were performed on a Bruker E 500 spectrometer operating at X-band microwave frequency equipped with TE_{102} cavity with 100 kHz field modulation. Each sample was in form of loose powder and during the measurements they were placed in quartz tubes.

3. Results and discussion

Solid solutions $(Tb_xY_{1-x})_2Cu_2O_5$ could be synthesized for the whole range of Tb concentration, $0 < x < 1$, showing in all cases a single phase. The X-ray patterns were indexed in the orthorhombic symmetry. Figure 2 presents, as an example, the obtained

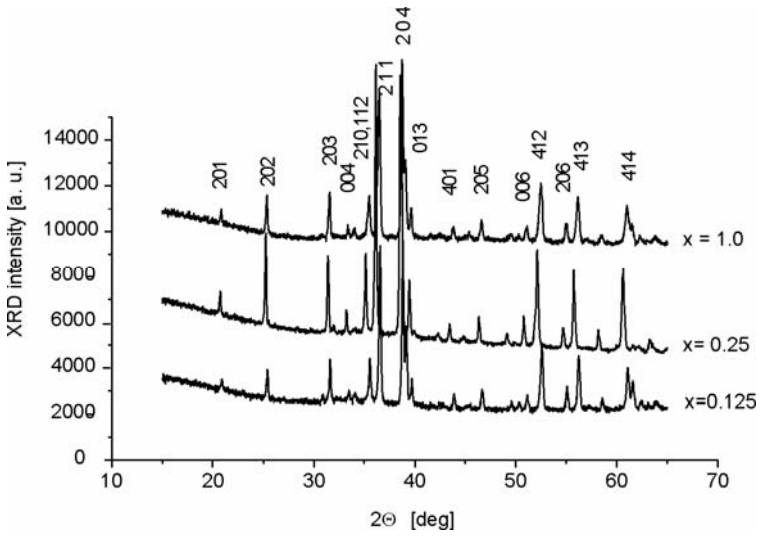

Fig. 2. XRD patterns for the three investigated samples of $(Tb_xY_{1-x})_2Cu_2O_5$. Peaks labelled by the indices *hkl* were used for calculating the lattice parameters

XRD spectra for three selected samples of $(Tb_xY_{1-x})_2Cu_2O_5$. Lattice spacing d_{hkl} was calculated by the Bragg law using all of the 16 peaks labelled in Figure 2. The lattice parameters of the unit cell, *a*, *b* and *c*, were determined by simultaneously fitting the lattice spacing to the following expression for an orthorhombic crystal,

$$\frac{1}{d_{hkl}} = \frac{h^2}{a^2} + \frac{k^2}{b^2} + \frac{l^2}{c^2}$$

with a non-linear least-square fitting procedure.

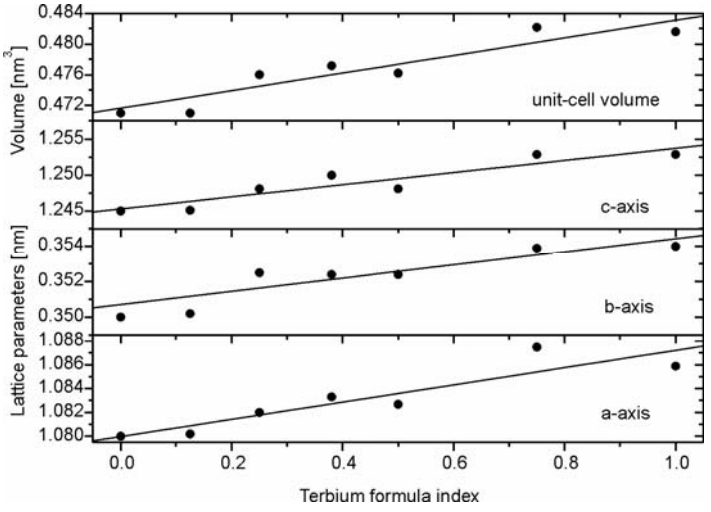

Fig. 3. The variation of the unit cell volume (top panel) and lattice parameters (lower panels) with the terbium index *x*

Figure 3 presents the change of the unit cell volume (top panel) and the unit cell parameters (lower three panels) with the terbium index. The linear increase of these parameters with increasing terbium concentration is in agreement with the larger Tb^{3+} ionic radius (0.923 Å in six-fold coordination) compared to Y^{3+} (0.90 Å). The values of the cell parameters obtained for the limiting ranges of $x = 0$ and $x = 1$ terbium indexes agree with the previous structural data on the $Tb_2Cu_2O_5$ and $Y_2Cu_2O_5$ compounds [3]. The linear change of the lattice parameters and the unit cell volume with the *x* index is in agreement with Vegard's law.

Figure 4 presents the differential thermogravimetry (DTG) curves taken during the heating run for five samples in the 1000–1200 °C range. The observed decomposition of the samples is connected with the endothermic processes and could be divided into three stages. The first two stages, which are sample-dependent, are connected with a small mass loss occurring in the 1030–1050 °C temperature range. The third, main stage of the decomposition is intrinsic. It is related to a larger mass loss that takes place at higher temperatures, above 1100 °C.

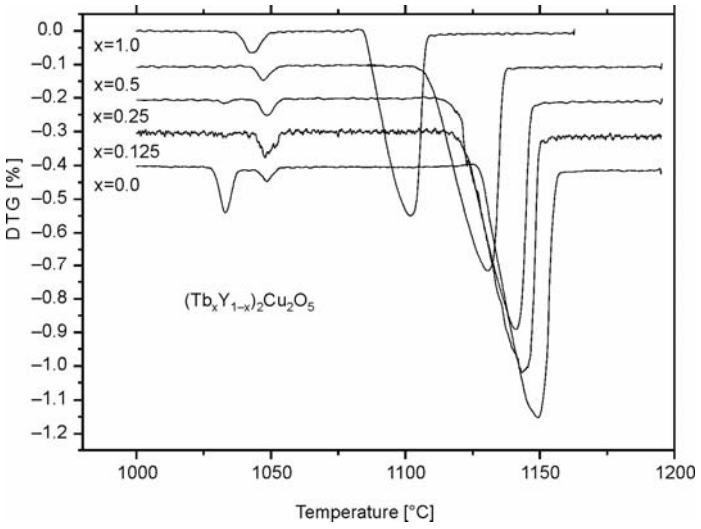

Fig. 4. The DTG traces of $(Tb_xY_{1-x})_2Cu_2O_5$ for five various terbium concentrations. The recordings for $x \neq 1.0$ have been vertically shifted for better visibility

To analyse the obtained DTG curves the Freeman–Carroll method was used, which enables calculation of the reaction order and the activation energy of a decomposing material. The method is based on the following equation for the mass losses:

$$\frac{dm}{dt} = k_0 c^n \exp\left(\frac{E_a}{RT}\right)$$

where n is the reaction order, E_a is the activation energy, and the other symbols have their usual meanings. The calculated values of the main parameters of this equation for the observed three decomposition stages are presented in Table 1. The temperature of the top of the respective DTG peak is designated as T_p. It was found that for the main decomposition stage this temperature varies linearly with the terbium index x (Fig. 5). The obtained values of activation energy for the first two decomposition stages are unrealistically high. As these stages are sample-dependent and a complete chemical and physical characterization of specific samples is lacking, these values must be treated as apparent, not corresponding to real, physically identifiable processes.

Table 1. DTG data for the decomposition processes of the investigated samples

Parameter	I stage	II stage	III stage
Stage character	sample-dependent	sample-dependent	intrinsic
Relative mass loss [%]	0.0–0.18	0.0–0.25	1.90–3.20
T_P [K]	1030–l035	1043–1049	1100–1150
E_a [kJ/mol]	6300–7800	6000–8100	1520–2180
n	1.60–1.90	1.40–1.90	0.40–0.70

The Y–Cu–O ternary can be effectively represented as Y_2O_3 –Cu–O–Cu ternary subsystem below 1 bar oxygen pressure. In this subsystem there are six phases: Y_2O_3, CuO, and $Y_2Cu_2O_5$, which are stable in the air, and Cu metal, Cu_2O and $YCuO_2$, which is only stable at lower oxygen pressure [30]. Oxygen coulometric investigations showed that the $YCuO_2$ is the problem phase, which is easily retained, or even formed under metastable conditions. This metastable $YCuO_2$ disturbs the low-temperature equilibrium of the $Y_2Cu_2O_5$ phase, thus leading to large uncertainty observed for the decomposition temperature of $Y_2Cu_2O_5$ [30]. Lysenko has presented the phase diagram of CuO–$YO_{1.5}$ system at 21 kPa oxygen pressure [31]. For CuO-rich compounds a phase line separates CuO + $Y_2Cu_2O_5$ and Cu_2O + $Y_2Cu_2O_5$ phases at 1027°C. Around 1130°C the decomposition of $Y_2Cu_2O_5$ into $YCuO_2$ occurs. Based on this phase diagram, one of the sample-dependent stages of decomposition recorded for $(Tb_xY_{1-x})_2Cu_2O_5$ could be explained as a result of transformation of excess CuO into Cu_2O, according to the reaction $4CuO \rightarrow 2Cu_2O + O_2$. In samples, where no excess of CuO is present that decomposition stage is missing.

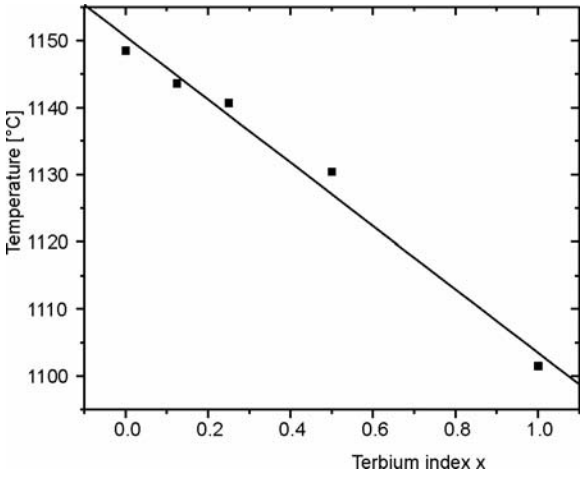

Fig. 5. The dependence of the temperature T_p of the main decomposition DTG peak (third stage) on the terbium index x

On the other hand, the main decomposition stage intrinsic to all samples is probably related to the transformation of $Y_2Cu_2O_5$ into $YCuO_2$, according to the reaction $2Y_2Cu_2O_5 \rightarrow 4YCuO_2 + O_2$. During this stage the oxygen atoms from the bulk of the sample are released causing an irreversible change in the crystal structure. This is confirmed by a quite different X-ray diffractogram of the sample heated above 1200 °C in comparison with the starting diffractogram. Also the ESR spectrum of the overheated sample vanishes after that treatment.

Lowering of the decomposition temperature with the increasing concentration of terbium (Fig. 5) could be most simply seen as a result of lower stability caused by an increased distortion around copper ions. There is a large distortion of coordination

polyhedra around Cu^{2+} in $R_2Cu_2O_5$ compared to that in tenorite (CuO). This distortion increases as the ionic radius of the R^{3+} cation increases. This means that the enthalpy of formation of $Y_2Cu_2O_5$ from the component oxides must increase as the ion radius of R^{3+} increases [32]. This agrees with the results obtained from the structural parameters [3]. Thus substitution of larger ion (Tb^{3+}) for a smaller ion (Y^{3+}) makes the structure less stable and lowers the decomposition temperature.

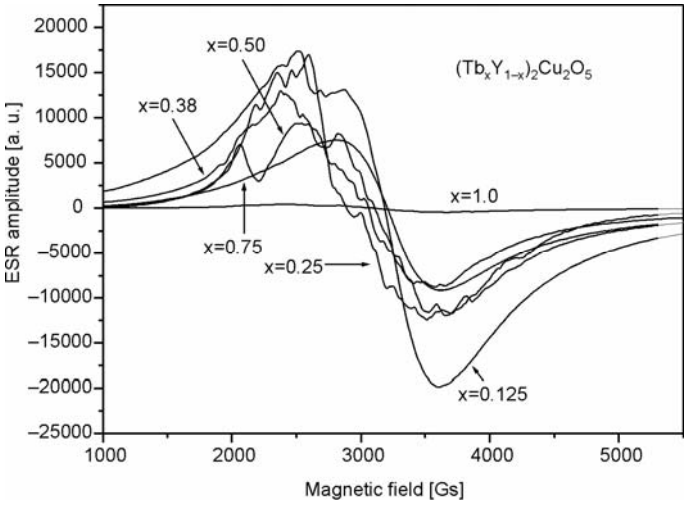

Fig. 6. The ESR spectra for $(Tb_xY_{1-x})_2Cu_2O_5$ solid solutions for various terbium indices x

The ESR spectra of $(Tb_xY_{1-x})_2Cu_2O_5$ solid solutions for various terbium concentrations are presented in Figure 6. Although the spectra are fairly complicated, the overall tendency of decreasing the ESR intensity with increasing terbium concentration is easily to notice. For $x = 1$ the sample is ESR silent. Similar tendency was observed previously for the $(Er_xY_{1-x})_2Cu_2O_5$ and $(Dy_xY_{1-x})_2Cu_2O_5$ compounds [33, 34]. It was found that the relative ESR signal intensity $I(x)$ varies with the magnetic rare earth ion concentration index x according to a simple power law function, $I(x) \sim (1 - x^{1/n})$, where n is the number of the superexchange paths between R^{3+} and Cu^{2+} ions [34]. In the case of the $(Tb_xY_{1-x})_2Cu_2O_5$ compound this dependence does not apply because a large part of the ESR signal arises from the copper defect clusters, among them copper tetramers [22]. Copper tetramers, consisting of copper ions coupled by intervening oxygen ions by an exchange interaction, were identified in $Y_2Cu_2O_5$ powder through sets of four ESR resonance lines. They were interpreted as the fine structure of $S = 2$ system [22]. It was noticed that the emergence of these signals depends upon the oxygen content of the sample, particularly when it is reduced.

The investigated samples of $(Tb_xY_{1-x})_2Cu_2O_5$, although in a ceramic form, showed a significant angular dependence in an external magnetic field. Figure 7 presents the angular anisotropy for the $TbYCu_2O_5$ compound. Successive rotations of the sample

by 30° along the axis perpendicular to the steady magnetic field produces significant changes in the ESR spectrum. Such behaviour is known for other powder or ceramic systems and is explained by the texturing of disk-like particles during the technological operations of pressing and sintering [35]. Since the observed spectra are not fully resolved and there is a superposition of different components, the analysis of the ESR signals could not be very detailed. Considering the overall spread of component lines in the magnetic field, it could be estimated that the value of the zero-field splitting parameter D for tetramers is smaller than 0.05 cm^{-1}. A complex spectrum of the $TbYCu_2O_5$ sample also indicates the presence of trimer copper clusters ($S = 3/2$), evidenced by the appearance of sets of three lines. For such a cluster, the value of D must be smaller than 0.006 cm^{-1}.

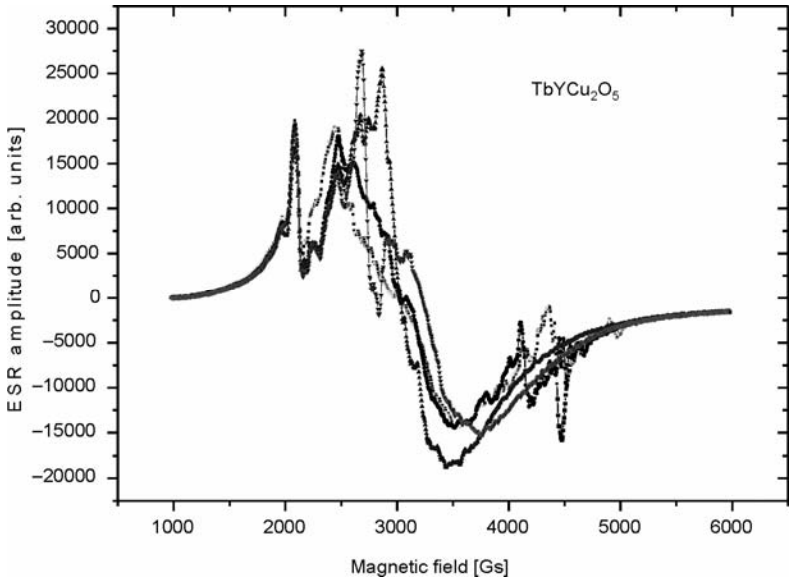

Fig. 7. The angular anisotropy of the ESR spectrum for the $TbYCu_2O_5$ compound. The sample has been successively rotated by 30° along the axis perpendicular to the steady magnetic field between each recording

In conclusion, the synthesis and characterization of $(Tb_xY_{1-x})_2Cu_2O_5$ copper oxides in the whole compositional range of terbium concentration, $1 \geq x \geq 0$, has been performed. The compounds were characterized by XRD, thermogravimetric, and ESR measurements, verifying the existence of a solid solution series, while room temperature ESR data suggest the presence of magnetic defects in the form of copper clusters.

References

[1] BERGERHOFF G., KASPER H., Acta Crystallogr., B 24 (1968), 388.
[2] FREUD H.R., MULLER-BUSCHBAUM H., Z. Naturforsch., B 32 (1977), 609.

[3] GARCIA-MUNOZ J.L., RODRIQUEZ-CARVAJAL J., J. Solid State Chem., 86 (1990), 310.
[4] TROC R., KLAMUT J., BUKOWSKI Z., HORYN R, STEPIEN-DAMM J., Physica, B 154 (1989), 189.
[5] KAZEI Z.A., KOLMAKOVA N.P., LEVITAN R.Z., MILL B.V., MOSHCHALKOV V.V., ORLOV V.N., SNEGIREV V.V., ZOUBKOVA JA., J. Magn. Magn. Mater., 86 (1990), 124.
[6] GARCIA-MUNOZ J.L., RODRIGUEZ-CARVAJAL J., OBRADORS X., Phys. Lett., A 149 (1990), 319.
[7] HORYN R., KLAMUT J., WOLCYRZ M., WOJAKOWSKI A., ZALESKI A.J., Physica, B 205 (1995), 51.
[8] BARAN M., LEVITIN R.Z., MILL B.V., SZYMCZAK R., Zh. Eksp. Teor. Fiz., 109 (1996), 961.
[9] SZYMCZAK R., SZYMCZAK H., BARAN M., LEVITIN R.Z., MILL B.V., J. Magn. Magn. Mater., 157–158 (1996), 667.
[10] MATSUOKA Y., NISHIMURA Y., MITSUDO S, NOJIRI H., KOMATSU H., MOTOKAWA M., KAKURAI K., NAKAJIMA K., KARASAWA Y., NIIMURA N., J. Magn. Magn. Mater., 177–181 (1998), 729.
[11] MOSHCHALKOV V.V., SAMARIN N.A., GRISHCHENKO I.O., J. Magn. Magn. Mater., 90–91 (1990), 533.
[12] GOLOSOVSKII I.V., MILL B.W., PLAKHTII W.P., KHARCHENKOV W.P., Fiz. Tver. Tela, 33 (1991), 3412.
[13] CHEPURKO G.G., PAUKOV I.U., POPOVA M.N., ZOUBKOVA JA., Solid State Commun., 79 (1991), 569.
[14] ZOUBKOVA JA., KRINETSKII I.B., LEVITIN R.Z., Fiz. Tver. Tela, 34 (1992), 1361.
[15] BOWDEN G.J., ELLISTON P.R., WEN K.T., DOU S.X., ESTERLINK K.E., BOURDILLON A., SORRELL C.C., CORNELL B.A., SEPAROVIC F., J. Phys. C: Solid State Phys., 20 (1987), L545.
[16] RAMAKRISHNA B.L., ONG E.W., Solid State Commun., 68 (1988), 775.
[17] ARIDE J., FLANDROIS S., TAIBI M., BOUKHARI A., DRILLON M., SOUBEYROUX L.J., Solid State Commun., 72 (1989), 459.
[18] GENOSSAR J., SHALTIEL D., ZEVIN V., GRAYEVKY A., FISHER B., J. Phys.: Condens. Matter, 1 (1989), 9471.
[19] GANGULY P., SREEDHAR K., RAJU A., DEMAZEAU G., HAGENMULLER P., J. Phys.: Condens. Matter, 1 (1989), 213.
[20] HOFFMANN S.K., CZYZAK B., STANKOWSKI J., Acta Phys. Polon., A 77 (1990), 621.
[21] SINGH R.J., IKRAM M., PUNNOOSE A., MAURYA B.P., KHAN S., Phys. Lett., A 208 (1995), 369.
[22] IKRAM M., SINGH R.J., Indian J. Pure Appl. Phys., 37 (1999), 622.
[23] KIMURA S., OHTA H., MITSUDO S., MOTOKAWA M., JANG W-J., HASEGAWA M., TAKAEI H., J. Phys.: Condens. Matter, 8 (1996), 5461.
[24] KIMURA S., OHTA H., MOTOKAWA M., MITSUDO S., JANG W.J., HASEGAWA M., TAKEI H., Int. J. Infrared Millimeter Spectr., 17 (1996), 833.
[25] KIMURA S., KANEKO K., OHTA H., MOTOKAWA M., Physica, B 201 (1994), 115.
[26] KIMURA S., OHTA H., MOTOKAWA M., J. Phys. Soc. Japan, 65 (1996), 297.
[27] SU Q., CAO X., WANG H., J. Solid State Chem., 111 (1994), 310.
[28] HORYN R., KLAMUT J., WOLCYRZ M., WOJAKOWSKI A., ZALEWSKI A.J., J. Magn. Magn. Mater., 140–144 (1995), 1575.
[29] FENG C.N., LOVETT D.R., Phys. Stat. Sol., (a) 167 (1998), 3.
[30] KONETZKI R.A., SCHMIDT-FETZER R., J. Solid State Chem., 114 (1995), 420.
[31] LYSENKO W.A., Inorg. Mat., 35 (1999), 1076.
[32] KALE G.M., J. Solid State Chem., 125 (1996), 13.
[33] TYPEK J., BUCHOWSKI D., GUSKOS N., SZYMCZYK A., WABIA M., Radiation Eff. Defects Sol., 158 (2003), 105
[34] TYPEK J, KOSTRZEWA J, SZYMCZYK A., GUSKOS N., Mol. Phys. Rep., 39 (2004), 233
[35] KAKAZEY M., VLASOVA M., GONZALEZ-RODRIGUEZ G., SALAZAR-HERNANDEZ B., Mat. Sci. Eng., B 90 (2002), 114

Received 23 September 2004
Revised 25 January 2005

Materials Science-Poland, Vol. 23, No. 4, 2005

Carburisation of nanocrystalline iron with ethylene

U. NARKIEWICZ[1*], I. KUCHAREWICZ[1], W. ARABCZYK[1], S. LENART[2]

[1]Szczecin University of Technology, Institute of Chemical and Environment Engineering, ul. Pułaskiego 10, 70-322 Szczecin, Poland

[2]Szczecin University of Technology, Institute of Materials Engineering, al. Piastów 19, 70-310 Szczecin, Poland

The carburisation of nanocrystalline iron with ethylene has been studied. The carburisation processes were carried out under atmospheric pressure, under the flow of pure ethylene or ethylene–hydrogen mixture at a constant temperature in the range of 310–550 °C. The process was controlled using a spring thermobalance and cathetometer, with the accuracy of 0,1 mg. The phase composition of the samples after carburisation was determined by means of X-ray diffraction (XRD). As a result of the carburisation of nanocrystalline iron with ethylene, the formation of iron carbide Fe_3C occurs, followed by the formation of carbon deposits. Under a C_2H_4/H_2 gas mixture, these two reaction steps can be separated, while under pure ethylene the reactions are much faster and the simultaneous formation of iron carbide and carbon deposits is observed. Depending on temperature and on the carburisation degree, various forms of carbon deposits can be observed using TEM: spherical, helicoidal, and nanotubes. The diameter of these carbon forms is below 100 nm.

Key words: *nanocrystalline iron; carburisation; ethylene; iron carbide; carbonaceous deposit*

1. Introduction

Carbonaceous deposits formed during industrial processes using hydrocarbons causes the deactivation of catalysts [1–3]. As a consequence, the regeneration or exchange of the deactivated catalyst is necessary. On the other hand, carbon deposits formed on metals as fibres or nanotubes have a lot interesting applications [4–11]. The best catalysts for the preparation of such nanocarbon materials are based on iron, nickel and cobalt [12–31].

This paper deals with the preparation of nanocarbon materials by the decomposition of ethylene on nanocrystalline iron.

[*]Corresponding author, e-mail: un@ps.pl

2. Experimental

The nanocrystalline iron used in carburisation experiments was doped with small amounts of two (Al_2O_3 and CaO) or three (Al_2O_3, CaO and K_2O) structural promoter oxides. The samples were obtained by the fusion of magnetite with promoter oxides. The alloy obtained was crushed after cooling and sieved to separate the fraction of 1.2–1.5 mm. To obtain metallic iron, polythermal reduction with hydrogen was performed. The pyrophoric samples obtained after reduction were passivated using nitrogen with an addition of 0,5% of oxygen. The chemical composition after passivation was determined using inductively coupled plasma atomic emission spectroscopy (AES-ICP). Besides iron, the samples contained 2.9 wt. % of Al_2O_3, 3.0 wt. % of CaO, 0.7 wt. % of K_2O, 0.3 wt. % of SiO_2, and 1 wt. % of other metal oxides (Mg, Ni, Cr, Ti, V).

The average crystallite size of iron in the samples, determined using X-ray diffraction (XRD) ($CoK_{\alpha 1}$), and calculated using Scherrer's equation, amounted to 17 nm.

The carburisation process was carried out in a spring thermobalance. A single layer of grains of the sample was placed in a platinum basket and hung in the thermobalance. Changes in the sample mass were recorded with a cathetometer. The accuracy of the measurements was 0.1 mg. Before carburisation, the samples were reduced at a temperature rising from 20 to 500 °C under hydrogen. After reduction (when a constant mass of the sample was reached), the carburisation process was started using ethylene (40 dm^3/h) or an ethylene/hydrogen mixture (1:19). The carburisation processes were carried out isothermally, at a temperature in the range of 310–550 °C.

3. Results and discussion

Examples of the thermogravimetric lines (TG) for the carburisation of nanocrystalline iron with ethylene are shown in Figure 1a. Line (1) corresponds to the carburisation of the sample with a potassium addition, carried out under a mixture of ethylene and hydrogen (1:19). The two other lines correspond to carburisation under pure ethylene – line (2) corresponds to the sample without potassium and line (3) to the one with a potassium added. The carburisation processes were carried out up to a sample mass increase of 0.072 g C/g Fe, which corresponds to the stoichiometric content of carbon in the iron carbide (Fe_3C). In Figure 1b, the derivatives of the TG lines in Figure 1a are shown. Comparing the rates of carburisation under pure ethylene for the two samples – with and without addition of potassium – it can be concluded that the presence of potassium increases the reaction rate. The dilution of ethylene with hydrogen leads to a decrease of the reaction rate (line (1) in Fig. 1b). The reaction rate under a mixture of ethylene with hydrogen for the sample with potassium, however, is higher than the reaction rate on the sample without potassium under pure ethylene.

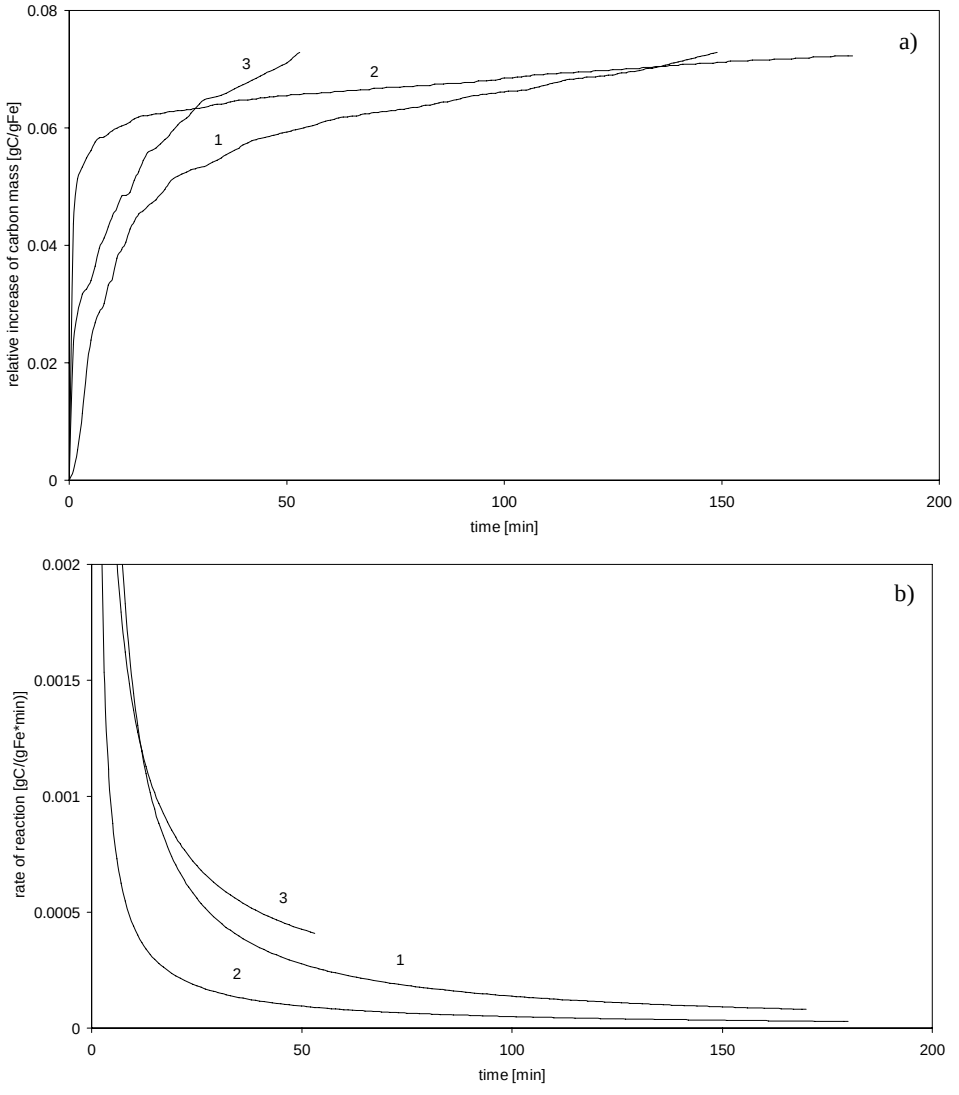

Fig. 1. TG (a) and corresponding DTG (b) curves of the carburisation process of nanocrystalline iron at 370 ºC: 1 – a sample of iron with an addition of potassium, carburised under a C_2H_4/H_2 mixture, 2 – a sample of iron without an addition of potassium, carburised under C_2H_4, 3 – a sample of iron with an addition of potassium, carburised under C_2H_4

The phase composition of the carburised samples was determined using XRD. The results are shown in Figure 2. The number of patterns corresponds to the number of samples in Figure 1. In pattern 4, corresponding to the sample before carburisation, only the peaks corresponding to α-Fe are present. The other peaks visible in patterns 1–3 correspond to iron carbide Fe_3C (cementite). Other iron carbides were not detected.

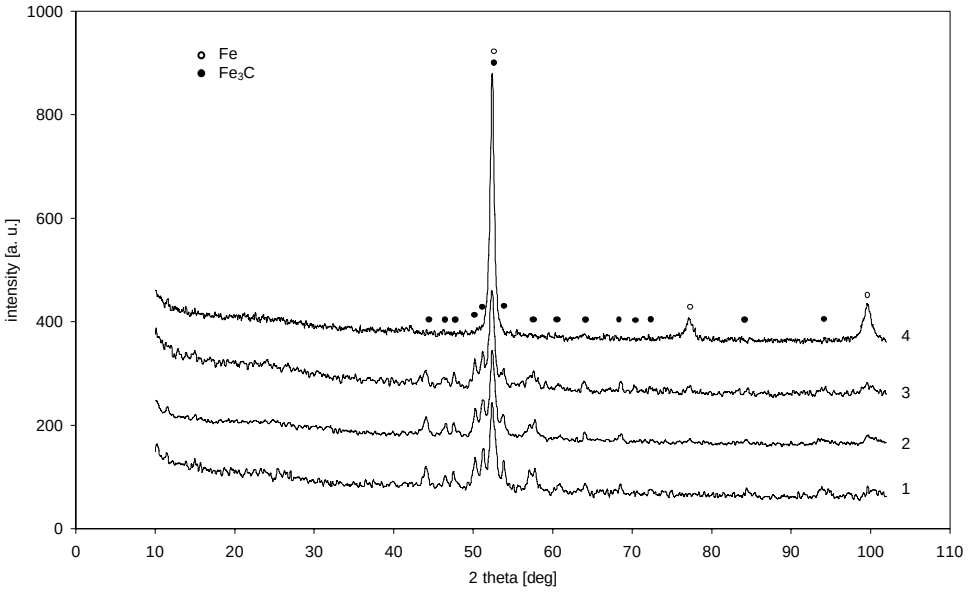

Fig. 2. Diffraction patterns: 1 – triply promoted iron sample after carburisation under a C_2H_4/H_2 mixture, 2 – doubly promoted iron sample after carburisation under C_2H_4, 3 – triply promoted iron sample after carburisation under C_2H_4, 4 – iron sample before carburisation

All samples were carburised to a mass increase corresponding to the amount of carbon sufficient to transform iron into Fe_3C. However, the peaks of unconverted iron can still be observed in the XRD patterns of samples 2 and 3. If free iron is still present in these samples, in spite of the fact that this amount of carbon is sufficient to transform all of the iron into Fe_3C, then carbon deposits have to be formed. Comparing the patterns of these samples, it can be stated that the intensity of the α-iron peak is higher for the sample 3 (with potassium), therefore the formation of carbon deposits occurs earlier on this sample.

In order to determine the range of carbon concentration in which only iron carbide without carbon deposits is formed, the following experiments were carried out. A series of samples with different carbon contents, below the stoichiometric carbon concentration in cementite, was prepared. The phase composition of these samples was determined using XRD. The conversion degree of iron to Fe_3C for each sample was determined on the basis of the surface area of the Fe (200) and Fe_3C (121/210) peaks.

In Figure 3a, the dependences of the conversion degree of iron to Fe_3C on the carbon content are shown for doubly and triply promoted iron samples carburised under pure ethylene at 340 °C. The solid line in this plot corresponds to stoichiometric cementite. For the doubly promoted sample, there are no experimental points below about 0.045 g C/g Fe, since such a substantial mass increase on this sample was measured in a very short period of time at the beginning of the process (during the first 2 minutes). This was the reason for which it was impossible to measure the mass increase for a less carburised sample. For the triply promoted iron sample, it was pos-

sible to obtain a sample with lower carbon content, namely 0.03 g C/g Fe. All of the experimental points for both doubly and triply promoted samples are located below the theoretical straight line corresponding to the formation of cementite. Therefore it can be concluded that for carburisation carried out under pure ethylene at 340 °C both cementite and carbon deposits are formed even at the very beginning of the process.

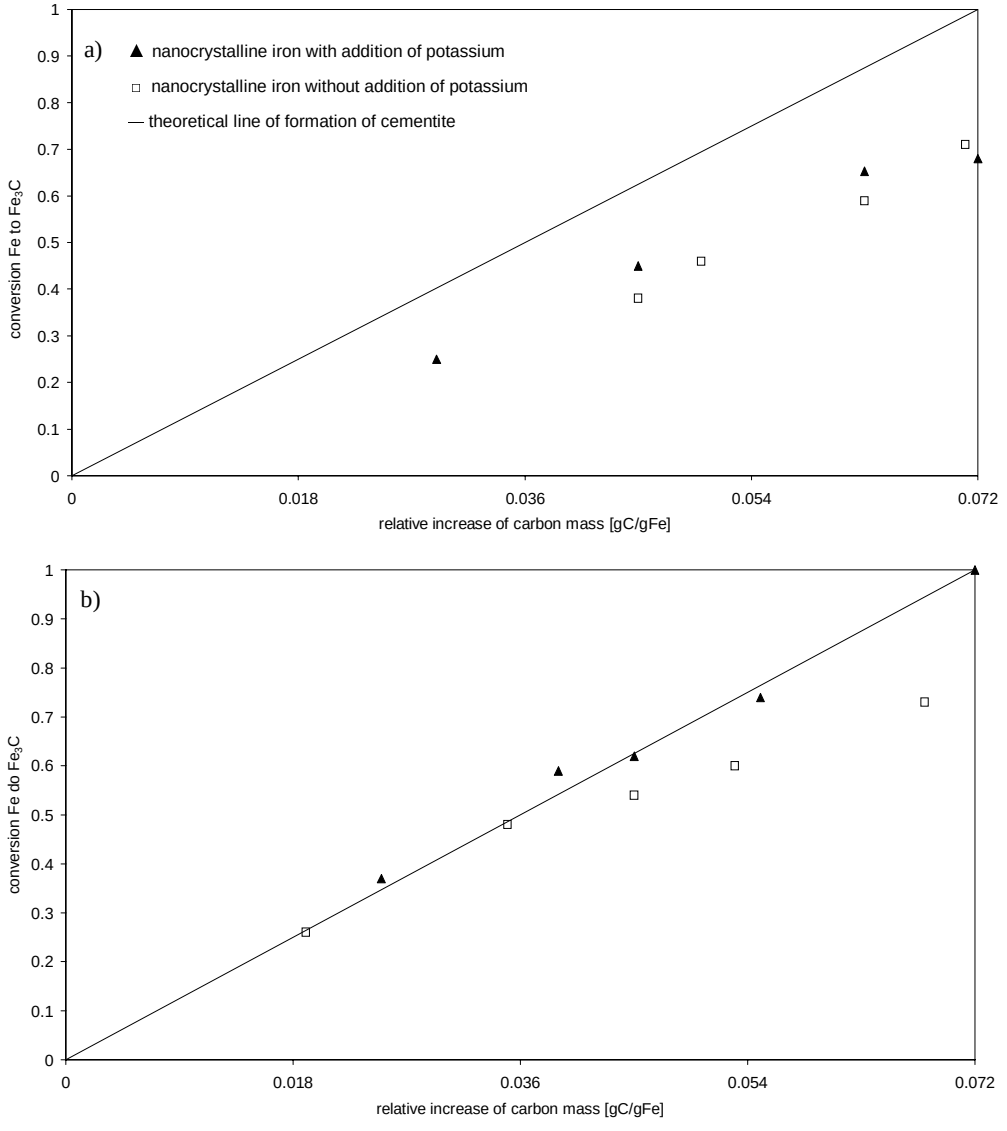

Fig. 3. The dependence of the conversion degree of iron to Fe_3C on the relative increase of carbon mass for: a) doubly and triply promoted iron samples, carburised under pure ethylene at a temperature of 340 °C; b) doubly (at 340°C) and triply (at 370°C) promoted iron samples, carburised under a mixture of ethylene/hydrogen (1:19)

In Figure 3b, a similar dependence is shown for carburisation under a mixture of ethylene with hydrogen (1:19) for the doubly promoted iron sample at 340 °C and for the triply promoted sample at 370 °C. The experimental points for the triply promoted sample are located on the line corresponding to the cementite formation, thus under the conditions of this experiment only cementite is formed, without carbon deposits. The experimental points for the doubly promoted sample are also located on the cementite line, but only below a mass increase of about 0.04 g C/g Fe. Above this value, the experimental points are located below the theoretical cementite line, therefore carbon deposits are then formed simultaneously with cementite.

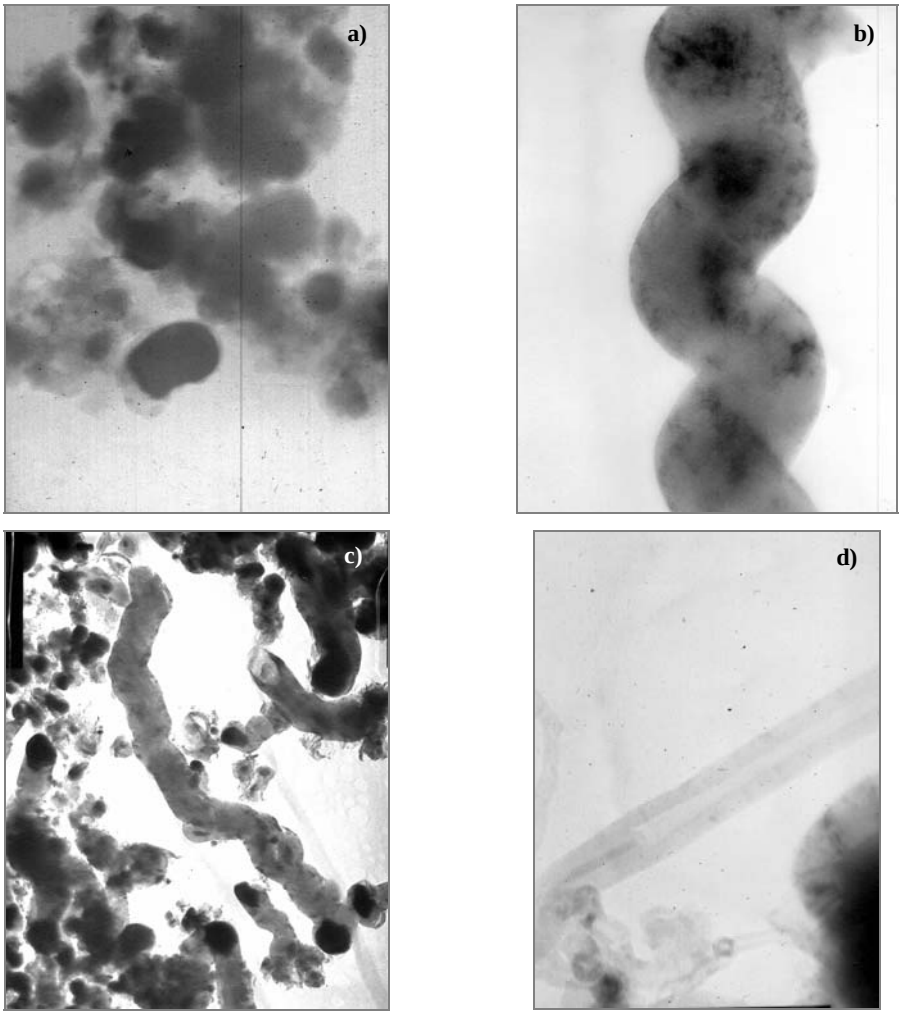

Fig. 4. TEM images of the sample: a) without addition of potassium, carburised under C_2H_4 at of 450 °C; b) without the addition of potassium, carburised under C_2H_4 at 500 °C, c) with the addition of potassium, carburised under C_2H_4 at 550 °C; d) without addition of potassium, carburised under C_2H_4 at the temperature of 550 °C

In order to identify the forms of carbon deposits, a series of samples carburised under pure ethylene for 180 min was prepared. The samples obtained were characterised using TEM. In Figure 4a, TEM image is presented of a doubly promoted iron sample carburised at 450 °C, up to a mass increase of about 0.9 g C/g Fe. Spherical carbon forms 10–20 nm in diameter can be observed.

Fibrous forms of carbon deposits were observed after carburisation to a higher degree (1.7 g C/g Fe) and at higher temperature (500 °C). Under these experimental conditions, carbon fibres about 100 nm in diameter were obtained (Fig. 4b). Figure 4c shows a TEM image of the iron sample containing potassium carburised at 550 °C up to a mass increase of 1.32 g C/g Fe. At the end of the carbon fibres, iron carbide crystallites about 100 nm in diameter can be observed. The diameter of the carbon fibres in this picture is in the range 50–150 nm. Similar carbon structures were observed on the doubly promoted iron sample carburised at the same temperature up to 1.24 g C/g Fe. Hollow carbon fibres were also observed in this case (Fig. 4d). The external diameter of these fibres was about 40 nm and the internal one about 10 nm.

There were no differences in the forms of carbon deposits obtained on the doubly and triply promoted iron samples.

4. Conclusions

The products of the carburisation of nanocrystalline iron with ethylene are iron carbide and carbon deposits. Iron carbide is formed only as cementite, other iron carbides were not detected.

The presence of potassium in the sample enhanced the reaction rate.

The form of carbon deposits depends on the process conditions. In the temperature range of 500–550 °C, carbon fibres are formed.

References

[1] FORZATTI P., LIETTI L., Catal. Today, 52 (1999), 165.
[2] GÓRALSKI J., GRAMS J., LUDOMIRSKA I., PARYJCZAK T., RZEŹNICKA I., Przem. Chem., 5 (1999), 172.
[3] GÓRALSKI J., GRAMS J., LUDOMIRSKA I., PARYJCZAK T., RZEŹNICKA I., Wiad. Chem., 54 (2000), 591.
[4] DE JONG K.P., GEUS J.W., Catal. Rev. Sci. Eng., 42 (2000), 481.
[5] LIPKA S.M., Annu. Battery Conf. Appl. Adv., 13 (1998), 373.
[6] PARK C., ENGEL E.S., CROWE A., GILBERT T.R., RODRIGUEZ N.M., Langmuir, 16 (2000), 8050.
[7] BROWNING D.J., GERRARD M.L., LAKEMAN J.B., MELLOR I.M, MORTIMER R.J., TURPIN M.C., Proc. Power Sources, Conf, 39 (2000), 192.
[8] SEUK YOUN H., RYU H., CHO T., CHOI W., Intern. J. Hydr. Energy, 27 (2002), 937.
[9] HWANG J., LEE S., SIM K., KIM J., Synth. Met., 126 (2002), 81.
[10] PHAM-HUU C., KELLER N., RODDATIS V.V., MESTL G., SCHLOEGL R., LEDOUX M.J., Phys. Chem. Chem. Phys., 4 (2002), 514.
[11] QIAN W., LIU T., WEI F., WANG Z., YU H., Carbon, 41 (2003), 846.
[12] EMMENEGGER C., BONARD J.M., MAURON P., SUDAN P., LEPORA A., GROBETY B., ZÜTTEL A., SCHLAPBACH L., Carbon, 41 (2003), 539.

[13] FAZLE KIBRIA A.K.M., MO Y.H., NAHM K.S., KIM M.J., Carbon, 40 (2002), 1241.
[14] VENEGONI D., SERP P., FEURER R., KIHN Y., VAHLAS C., KALCK P., Carbon, 40 (2002), 1799.
[15] PARK C., BAKER R.T.K., J. Catal., 179 (1998), 361.
[16] ANDERSON P.E., RODRIGUEZ N.M., Chem. Mater., 12 (2000), 823.
[17] MARANGONI R., SERP P., FEURER R., KIHN Y., KALCK P., VAHLAS C., Carbon, 39 (2001), 443.
[18] OTSUKA K., OGIHARA H., TAKENAKA S., Carbon, 41 (2003), 223.
[19] LOPEZ P.N., RAMOS I.R., RUIZ A.G., Carbon, 41 (2003), 2509.
[20] BAKER R.T.K., BARBER M.A., HARRIS P.S., FEATES F.S., WAITE R.J., J. Catal., 26 (1972), 51.
[21] RODRIGUEZ N.M., KIM M.S., BAKER R.T.K., J. Catal., 144 (1993), 93.
[22] RODRIGUEZ N.M., KIM M.S., FORTIN F., MOCHIDA I., BAKER R.T.K., Appl. Catal. A: General, 148 (1997), 265.
[23] VANDER WAL R.L., Carbon, 40 (2002), 2101.
[24] CI L., XIE S., TANG D., YAN X., LI Y., LIU Z., ZOU X., ZHOU W., WANG G., Chem. Phys. Lett., 349 (2001) 191.
[25] LI Z., CHEN J., ZHANG X., LI Y., FUNG K.K., Carbon, 40 (2002), 409.
[26] ERMAKOVA M.A., ERMAKOV D.Y., KUVSHINOV G.G., Appl. Catal. A: General, 201 (2000), 61.
[27] ERMAKOVA M.A., ERMAKOV D.Y., CHUVILIN A.L., KUVSHINOV G.G., J. Catal., 201 (2001), 183.
[28] QIAN W., LIU T., WANG Z., YU H., LI Z., WEI F., LOU G., Carbon, 41 (2003), 2487.
[29] KRISHNANKUTTY N., RODRIGUEZ N.M., BAKER R.T.K., J. Catal., 158 (1996), 217.
[30] HERNADI K., FONESCA A., NAGY J.B., BERNAERTS D., LUCAS A.A., Carbon, 34 (1996), 1249.
[31] BAKER R.T.K., CHLUDZINSKI J.J., J. Catal., 64 (1980), 464.

Received 23 September 2004
Revised 22 March 2005

Materials Science-Poland, Vol. 23, No. 4, 2005

Finite-size analysis via the critical energy -subspace method in the Ising models

A. C. MALAKIS*, I. A. HADJIAGAPIOU, S. S. MARTINOS, N. G. FYTAS

Faculty of Physics, University of Athens, Panepistimioupoli Zografou, GR 15784, Athens, Greece

We briefly review some applications of the critical minimum energy-subspace method (CrMES) using the Wang–Landau sampling for the estimation of the density of states (DOS). These applications concern the two- and three-dimensional Ising models and their important conserved order parameter versions (COP), known also as the Ising models with fixed magnetization (IMFM). The recently developed CrMES scheme greatly facilitates methods for sampling the DOS of classical statistical models in large systems. In effect, the CrMES technique enables the estimation of critical behaviour using only a small part of the energy space. Specific heat curves are obtained, their peaks are located and their scaling behaviour is studied and compared with the results known from literature whenever such results exist.

Key words: *Ising model; Wang–Landau sampling; finite-size scaling*

1. Introduction to the CrMES method

The CrMES method has been developed recently [1]. It is a very efficient technique for studying specific-heat anomalies of a finite lattice model and for extracting, via finite-size analysis, its asymptotic critical behaviour. In order to present the method, let us assume that the statistical model of interest will be approached using an approximation scheme for the density of states (DOS), $G(E)$. There exist a number of such methods, developed recently, such as the Wang–Landau method [2, 3] which uses a random walk in the energy space. Any such scheme will produce errors in the calculation of the specific heat. Additional errors introduced by our CrMES technique are not even observable when compared to those corresponding to the approximate scheme for the DOS, provided that one uses a sufficiently small parameter r (see Eq. (3) below).

According to the CrMES method, the specific-heat peak of the finite system may be estimated by using only a small part of the energy space. This is a very simple idea,

*Corresponding author, e-mail: amalakis@cc.uoa.gr

closely related to the notion of the thermodynamic equivalence of ensembles and to the central limit theorem. Let us follow the basic argument presented in [1]. If $\widetilde{E}$ denotes the energy that produces the maximum term in the partition function at the temperature of interest, we may define a set of approximations to the specific heat value by restricting the statistical sums to energy ranges around the value $\tilde{E}$. Accordingly, the specific heat per particle, for an N particle system of linear dimension L, at the temperature of interest (for instance, the specific heat peak at the "pseudo-critical" temperature T_L^*), is approximated by ($k_B = 1$):

$$C_L(\tilde{E}_-, \tilde{E}_+) \equiv C_L(\Delta) = N^{-1}T^{-2}\left\{\tilde{Z}^{-1}\sum_{\tilde{E}_-}^{\tilde{E}_+} E^2 \exp[\tilde{\Phi}(E)] - \left(\tilde{Z}^{-1}\sum_{\tilde{E}_-}^{\tilde{E}_+} E \exp[\tilde{\Phi}(E)]\right)^2\right\} \quad (1a)$$

$$\tilde{\Phi}(E) = [S(E) - \beta E] - \left[S(\tilde{E}) - \beta\tilde{E}\right], \qquad \tilde{Z} = \sum_{\tilde{E}_-}^{\tilde{E}_+} \exp[\tilde{\Phi}(E)] \quad (1b)$$

where the microcanonical entropy is given by:

$$S(E) = \ln G(E) \quad (1c)$$

In the above, the restricted energy sub-ranges of the total energy range ($E_{\min}$, $E_{i\max}$) are defined with respect to the energy $\tilde{E}$, which corresponds to the maximum term in the partition function at the temperature of interest:

$$(\tilde{E}_-, \tilde{E}_+), \qquad \tilde{E}_\pm = \tilde{E} \pm \Delta^\pm, \qquad \Delta^\pm \geq 0 \quad (2)$$

Depending on the extensions of the sub-ranges in Eq. (2), the above scheme may provide good approximations to the specific heat at a particular temperature. Since by definition $\tilde{\Phi}(E)$ is negative, we should expect that for large lattices "extreme" values of energy (far from $\tilde{E}$) will have an insignificant contribution to the statistical sums, because these terms decrease exponentially fast with the distance from $\tilde{E}$. It follows that, if we request a specified accuracy, then we may greatly restrict the necessary energy range in which the DOS should be sampled. According to our technique, restricting the energy space from ($E_{\min}$, $E_{\max}$) to $(\tilde{E}_-, \tilde{E}_+)$ will therefore substantially facilitate any approximate scheme for the calculation of the density of states. The proposed restriction (CrMES) will be defined below with respect to the specific heat, in such a way that the relative errors of the specific heat maxima will be bounded by a predefined small number r.

The CrMES part of the energy spectrum is well defined if we know the exact DOS for a finite system. Given any small number r and the exact DOS, one can easily calculate the minimum energy subspace (MES), compatible with the above requirements. An algorithmic approach has been described in [1]. The resulting sub-space (its end-

points and its extension) depends, of course, on the temperature, on the value of the small parameter *r*, and on lattice size. We write for its extension:

$$\Delta\tilde{E} \equiv \Delta\tilde{E}(T,r,L) \equiv \min(\tilde{E}_{+} - \tilde{E}_{-}) : \left| \frac{C_L(\Delta^{\pm})}{C_L} - 1 \right| \leq r \tag{3}$$

The extension of this dominant energy subspace, determining the behaviour of the system, is much smaller than the total energy range, $\Delta\tilde{E}(T,r,L) \ll (E_{\max} - E_{\min})$, and we should expect that its value will be of the same order, with the standard deviation of the energy distribution. Therefore, we propose that, given a small parameter *r*, the extensions of the CrMES part of the spectrum satisfy:

$$\Delta\tilde{E} \propto \sigma_E = \sqrt{NT^2C} \tag{4}$$

From the central limit theorem we know that the energy distribution should approach a Gaussian far from the critical point and that the energy subspace determining all thermodynamic properties is at most of the order of $\sqrt{N}$. Close to a critical point, the extensions $\Delta\tilde{E}^* \equiv \Delta\tilde{E}(T_L^*,r,L)$ of the CrMES at the "pseudo-critical" temperature, (as well as the extensions $\Delta\tilde{E}_c \equiv \Delta\tilde{E}(T_c,r,L)$ at the exact critical temperature), should scale as:

$$\frac{\Delta\tilde{E}^*}{L^{d/2}} \approx L^{\alpha/2\nu} \tag{5}$$

where α and ν are the specific heat and correlation length critical exponents, respectively. Note that for the square Ising lattice a logarithmic scaling law should be expected. The proposed scaling equation (Eq. (5)) follows from the well-known finite-size scaling behaviour of the specific heat $(C_L \approx L^{\alpha/\nu})$ and hypothesis (Eq. (4)).

In order to obtain the minimum energy subspace satisfying Equation (3) from the density of states *G*(*E*) we may define successive "minimal" approximations (j = 1, 2, 3, …) to the specific heat $C_L(j)$, as in [1]. With the help of these approximations we obtain the following relative errors:

$$r_j = \left| \frac{C_L(j)}{C_L} - 1 \right| \tag{6}$$

Then we fix our requirements by specifying a particular level of accuracy for all finite lattices. In effect, we define the (critical) MES as the subspace "centered" at $\tilde{E}(\tilde{E}^*)$, corresponding to the minimum subspace for which the relative error of the specific heat satisfies the relation $r_j \leq r$. Demanding the same level of accuracy for all lattice sizes, we produce a size dependence on all parameters of the above energy

ranges. That is, we should expect that the "centre" $\tilde{E}(T,r,L)$ and the end-points $\tilde{E}_{-}(T,r,L), \tilde{E}_{+}(T,r,L)$ of the (critical) MES are all functions of L. In particular, the extensions $\Delta\tilde{E}^{*} = \Delta\tilde{E}(T_L^{*},r,L)$ of the CrMES should obey the scaling law (Eq. (5)). It is therefore possible to find approximations to these functions using the total energy range for small lattices and then to extrapolate in order to estimate the CrMES for larger lattices.

2. Ising models and their COP versions

Let us review here some recent applications of the CrMES method to some well -known models of statistical mechanics, such as the Ising model. The normal Ising model is described by the Hamiltonian:

$$H = -J\sum_{<i,j>} S_i S_j, \quad S_i = \pm 1, \quad i = 1,2...,N \tag{7}$$

and is primarily a model for ferromagnets. Furthermore, according to universality, it describes the properties of several systems of physical significance, including magnetic nuclear systems, and the liquid–vapour critical point [4, 5]. An important variation of the Ising model is the Ising model with fixed magnetization (IMFM), also known as the conserved-order-parameter (COP) Ising model. This variation has the same Hamiltonian, but now the sum of the partition function is restricted by the condition $\sum_i S_i = M_0$, where M_0 is the value of the fixed magnetization. The COP version is used to describe different systems and phenomena, including lattice gases and binary mixtures. Related phenomena are the formation of equilibrium crystal shapes, the roughening transition, and the non-equilibrium processes of diffusing surface clusters, phase separation and demixing [6, 7].

Consider first the three-dimensional case. For the Ising model on a cubic $L\times L\times L$ lattice, we may express the specific heat in the critical region using a renormalization group expansion of the form:

$$C_L \simeq q_0 L^{2y_t-d} + p_0 + rL^{2y_t-d+y_i} \tag{8}$$

where y_i is irrelevant exponent which, according to Deng and Blote [8], is approximately $y_i = -0.821$. The above expansion is, of course, valid in the critical region, which is assumed to include both the "pseudo-critical" and exact critical temperatures for large lattices.

Using the CrMES method combined with Wang–Landau sampling, we have accurately estimated, in the corresponding energy-subspaces, the DOS for cubic lattices with linear sizes L = 4, ..., 32 [1]. The analysis of our specific heat data gives a thermal critical exponent of y_t = 1.5878(31). This is comparable to the best estimate

known in literature [8]. Furthermore, we can use an alternative route for determining the thermal exponent, since the extensions of the CrMES at "pseudo-critical" temperatures are assumed to satisfy a similar scaling law, that is:

$$\left(\frac{\Delta \tilde{E}_r^*}{L^{d/2}} \right)^2 \simeq q(r) L^{2y_t - d} + p(r) L^{2y_t - d + y_i} \tag{9}$$

Using this new scheme, the critical exponent is found to be $y_t = 1.5860(30)$, which is also in excellent agreement with literature [8], verifying our proposal and proving its effectiveness. We point out that this is the first accurate estimation of the thermal critical exponent from specific heat data. In the past, other routes used for estimating this important critical exponent have been used [8], mainly because of the inaccuracy of previous specific heat data, but also due to the corrections due to scaling in the specific heat behaviour. The CrMES technique has improved the situation by allowing us to produce quite accurate finite-size data.

For the COP version of the three-dimensional Ising model, we have developed a non-local spin-exchange Wang–Landau algorithm. The combination of this algorithm with our CrMES scheme appears to be the most efficient route for studying the specific heat anomalies of this important variation of the Ising model. Our study of the three-dimensional COP version of the cubic Ising model has not yet been completed. We observe a striking similarity in the critical behaviour, however, suggesting that the COP version may share the same thermal exponent with the simple model, something that we have already numerically tested for the two-dimensional case, presented below.

Figures 1a, b show the specific heat peaks for several lattice sizes of the 3D Ising model and its COP version. The specific heat curves shown in these figures have been obtained from the CrMES part of the energy spectrum, and it should be pointed out that although these curves are accurate in the region of the peaks they are not reliable far away from them. However, for the COP version (Fig. 1b) and for $L = 8$, 10, and 12 the full low energy part of the energy spectrum is used in order to show an interesting secondary peak to the left of the main peak.

Consider now the two-dimensional case. For the normal square Ising model, a spin-flip Wang–Landau algorithm is used, whereas a non-local spin-exchange Wang–Landau algorithm is used for its COP version. Specific heat values are obtained in the appropriate critical region, implementing the CrMES method. The application is carried out for both the exact critical temperature T_c and the "pseudo -critical" temperature T_L^*, by restricting the Wang–Landau random walk in an appropriate energy range, wide enough to cover both minimum energy subspaces for the two temperatures and to accurately estimate the extensions of the corresponding MES.

Let us now discuss the finite-size behaviour of the specific heat for the normal Ising model (with freely fluctuating magnetization) on a square $L \times L$ lattice. It is known from the work of Ferdinand and Fisher [9] that close to the critical temperature $T_c = 2(J/k_B)/\ln(1+\sqrt{2})$, the finite-size behaviour is described by the following expansion:

$$C_L(T) = A_0 \ln L + B(T) + B_1(T)\frac{\ln L}{L} + B_2(T)\frac{1}{L} + ... \tag{10}$$

where the critical amplitude A_0 and the first B coefficients are given in [9] for both the exact critical and "pseudo-critical" temperature of the normal Ising model. In particular, the coefficient B_1 is zero for the exact critical temperature but non-zero for the "pseudo-critical" temperature. The amplitude A_0 (main singularity) does not vary in the range of the validity of the expansion and is therefore the same for the specific heat sequence at the exact critical and for the sequence of specific heat peaks at the "pseudo-critical" temperatures.

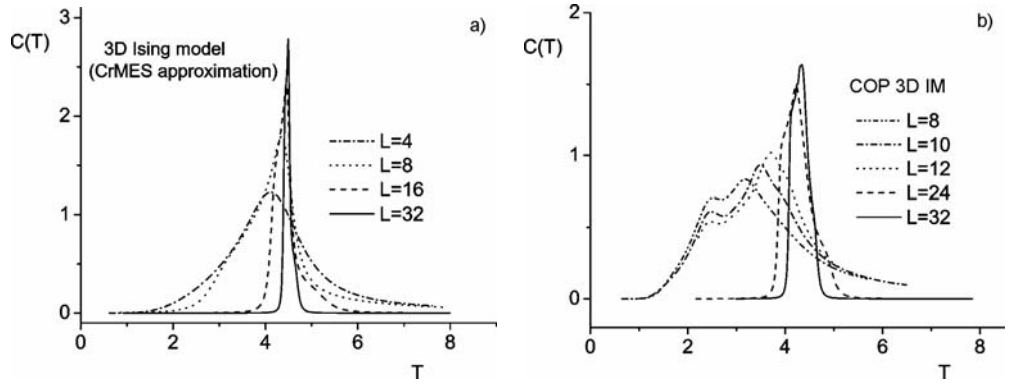

Fig. 1. Specific heat for: a) small lattices in the 3D Ising model. For large sizes, only the neighbourhoods of the peaks are reliable, since the curves have been derived from the corresponding CrMES; b) the COP versions of small lattices in the 3D Ising model. For L = 8, 10, and 12, the CrMES has been intentionally extended to the low-energy part of the spectrum down to the ground state in order to illustrate the existence of a secondary peak

Using our CrMES method and the algorithms mentioned above, we have verified the scaling law (Eq. (10)) for the square Ising model by accurately estimating the amplitude A_0 and the first B-coefficients from our specific heat data [1]. Furthermore, we have confirmed that the finite-size extensions of the CrMES satisfy an analogous scaling law, namely:

$$\left(\frac{\Delta\tilde{E}(r)}{L^{d/2}}\right)^2 \simeq A(r)\ln L + B_1(r)\frac{\ln L}{L} \tag{11}$$

Figure 2 presents the behaviour of the CrMES extensions in function of lattice size. As proposed based on physical grounds, this figure shows a clear logarithmic dependence, pointing out that our technique is a new route for estimating the critical behaviour. Our scaling proposal (Eq. (5)) also gives an interesting interpretation of the ratio α/ν, as discussed in the concluding remarks.

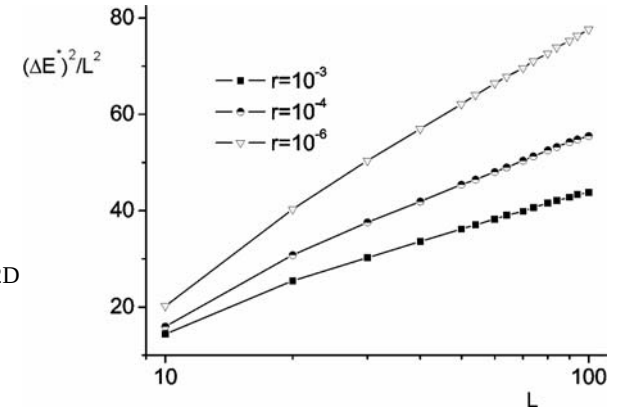

Fig. 2. Demonstration of the proposed logarithmic scaling law (Eq. (11)) for the 2D Ising model. Three levels of accuracy (r) have been used in order to define the corresponding CrMES parts of the energy spectrum

Finally, we present some new results for the COP version of the square Ising model, which we have extensively studied for several values of the fixed magnetization. For the IMFM, a critical temperature for any constant value of magnetization M_0 has been proposed by Kastner [7]:

$$M_0 = \left[1 - \left(\sinh\frac{2J}{k_B T_0}\right)^{-4}\right]^{1/8}, \qquad T_0 = T_c(M_0) \tag{12}$$

Note that for $M_0 = 0$, the above formula (Eq. (12)) produces a critical temperature that has the same value as the normal Ising model ($T_c = T_c(M_0 = 0)$). We have verified that for the main component $M_0 = 0$ the Ferdinand–Fisher expansion is well obeyed, and we have estimated the first B-coefficients and the main amplitude A. We found that the amplitude A of the main logarithmic term is also the same for the IMFM at both the "pseudo-critical" and exact critical temperatures and obeys the value of the normal Ising model case, namely:

$$A(M_0 = 0) = A_0 = \frac{8}{\pi}K_c{}^2 = \frac{2}{\pi}\left[\ln(1+\sqrt{2})\right]^2 = 0.494538 \tag{13}$$

Furthermore, the coefficient B_1 of the expansion appears to be very close to zero at the exact critical temperature, and in fact our optimum fitting attempts are based on this conjecture. In conclusion, for the $M_0 = 0$ IMFM shares an exceptionally similar scaling behaviour with the normal Ising model.

We have also studied the scaling behaviour of the specific heat for several other values of fixed magnetization. For lattice sizes L in the range of 10–150, the logarithmic behaviour of the specific heat seems to prevail and the amplitude A of the optimum fitting tends to zero as $M_0 \to 1$. Note that, according to our data, if this behaviour is correct, then the amplitude A is much smaller at the critical temperature proposed in Equation (12) than the value obtained for the sequence of "pseudo-critical" temperatures. It will be interesting to see whether this behaviour will also be observed for much larger lattice sizes.

3. Conclusions

The CrMES technique is an efficient approximation scheme which greatly facilitates the sampling of the density of states in large systems. The relevant energy range used is in general a very small portion of the whole energy space. Therefore, the method is very efficient compared to the original Wang–Landau random walk, which covers the entire energy space. In effect, our proposal combines the idea of entopic sampling with that of importance sampling in a systematic way, without producing additional errors. The applications presented here have shown that the general approach is very reliable, and that not only the critical temperatures, but also the critical exponents can be estimated with high accuracy. This new method might be applicable to complex systems. The route proposed for calculating the ratio of the critical exponents α/ν from the scaling law (Eq. (5)) also provides an interesting interpretation for this ratio. Thus, α/ν may be comprehended as an index that determines the expansion of the dominant energy-subspace as we increase the lattice size. This provides new insight into the critical behaviour of a statistical system, and we think that similar interpretations may be found for other critical exponents.

References

[1] MALAKIS A., PERATZAKIS A., FYTAS N. G., Phys. Rev. E, 70 (2004), 066128.
[2] WANG F., LANDAU D. P., Phys. Rev. Lett., 86, 2050, (2001).
[3] WANG F., LANDAU D. P., Phys. Rev. E, 64(2001), 056101.
[4] DOMB C., Adv. Phys., 9 (1960), 149.
[5] FISHER M. E., Rep. Prog. Phys., 30 (1967), 615.
[6] PLEIMLING M., SELKE W., J. Phys. A: Math. Gen., 33 (2000), L199–L202.
[7] KASTNER M., J. Stat. Phys., 109 (2002), 133.
[8] DENG Y., BLOTE H. W. J., Phys. Rev. E, 68 (2003), 036125.
[9] FERDINAND A. E., FISHER M. E., Phys. Rev., 185 (1969), 832.

Received 23 September 2004
Revised 5 May 2005

Materials Science-Poland, Vol. 23, No. 4, 2005

The linewidths and pintegrated intensities of the d–d transitions in photoacoustic spectra of polyamine copper(II) complexes

N. GUSKOS[1, 2*], J. TYPEK[2], G. J. PAPADOPOULOS[1], M. MARYNIAK[2], K. AIDINIS[3]

[1]Solid State Section, Department of Physics, University of Athens, Panepistimiopolis, 15 784 Zografos, Athens, Greece

[2]Institute of Physics, Szczecin University of Technology, al. Piastów 17, 70-310 Szczecin, Poland

[3]Applied Physics Section, Department of Physics, University of Athens, Panepistimiopolis, 15 784 Zografos, Athens, Greece

Photoacoustic spectra of the d–d transitions for three different series of copper(II) complexes of spermidines Spn (Spn323, Spn333, Spn343), Spm (Spm323, Spm333, Spm343) and Spc (Spc323, Spc333) have been investigated. Replacements of distant atoms, the presence or absence of water molecule in the structure, the kind of ligands surrounding the metal(II) ions have a strong influence on the crystal field splitting and the intensities of the non-radiative transitions. Non-radiative processes are involved in important mechanisms of the dynamic interactions between the electrons and the lattice. Studies of the intensities of the non-radiative transitions provide a very important data for the thermodynamic states of these systems. Photoacoustic absorption band of the d–d transitions could be decomposed into three lines (due to the crystal field splitting) with different intensities, positions and linewidths. The integrated intensities may yield information about the number of non-radiative processes, while the linewidths about the mechanisms of the relaxation processes.

Key words: *photoacoustic spectroscopy; copper complexes*

1. Introduction

Crystal field splittings of the d–d transitions for three different series of copper(II) complex of spermidines: Spn (Spn323, Spn333, Spn343), Spm (Spm323, Spm333, Spm343) and Spc (Spc323, Spc333) have been investigated by using photoacoustic (PA) and electron paramagnetic resonance (EPR) methods [1–3]. The following fac-

* Corresponding author, e-mail: ngouskos@cc.uoa.gr

tors: (i) replacement of distant atoms, (ii) the presence of additional water molecules, and (iii) different kinds of ligands, strongly influence the crystal field splittings and the lineshape of the PA spectra of the d–d transitions. The complexes of spermidines are very important in the bio-active systems due to their role in the processes of information transfer between the DNA and proteins [4–6]. It has been proposed that the transition metal complexes of spermidine act as a channel selector in bio-active systems, e.g. by switching between the ground and excited d-orbital states after irradiation by proper electromagnetic wave [7].

Non-radiative processes might be very important for this kind of mechanism. Thus the study of the intensities of the non-radiative processes could provide important data for determination of the thermodynamic state of systems including the DNA and proteins involved in the bio-active activities with. The d–d absorption band observed in photoacoustic spectroscopy (PAS) could be decomposed into three lines (due to the crystal field splitting) with different intensities, positions and linewidths. The integrated line intensities yield information about the amount of non-radiative processes while the linewidths about the relaxation processes. The PA spectra of hematite, spermidine and organometallic rare earth complexes exhibit an intense absorption (near 586 nm – yellow colour) in the same region of electromagnetic spectrum. It has been suggested that this radiation plays an important role in the living systems [8]. It is especially important because the most intense Sun radiation occurs in this very region. The study of the d–d and n–π^* transitions in spermidines may be very useful for a proper understanding of the static and dynamical processes occurring in the living matter [9–11].

In this report, we present and discuss the variations of the intensities and the linewidths in PA spectra of the d–d transitions for three different series of spermidine copper(II) complexes.

2. Experimental

Three series of copper(II) complexes of spermidines (designated as Spm, Spn and Spc) have been prepared according to the procedure described elsewhere [1–3].

The PA spectra of polycrystalline powder samples have been obtained by using a modified PAS method initially proposed by Papadopoulos and Mair [12]. A 1 kW Xenon arc lamp and a 1/4 m ORIEL monochromator were used as light sources, with bandpass widths of 5 nm (at 500 nm). The light, with intensity modulated by a chopper at frequency of 10 Hz was directed into a photoacoustic cell equipped with TREVI EM27 microphone. A dual SR830 lock-in amplifier measured the amplitude and phase of the PA signal detected on the microphone. Data acquisition ensured that each final value was an average of 20 runs at the same wavelength of the incident light. A carbon black was used as a standard to re-calibrate the final spectrum. The PA spectra of all the complexes were recorded at room temperature in the range of 300–700 nm.

3. Results and discussion

The absorption of three series of investigated copper(II) complexes of spermidine (Spm, Spn and Spc) have been investigated by using PAS in the visible region. It has been suggested that the observed broad band arises from the d–d transitions between the energy levels split by the crystal field [1–3]. For illustration, the PA spectrum of Spc323 organic complex simulated by three lines, is given in Fig. 1. The PA spectra can be described very well by the superposition of three lines resulting from the crystal field splitting. In Figures 2 and 3, such composite three-line spectra are presented for the Spn 323 and Spm 323 examples, respectively. A very good agreement has been obtained between this assumption and the results of analysis of the EPR spectra of copper(II) ions in orthorhombic crystal field for all eight investigated copper(II) complexes. The obtained wavelengths λ_i (i = 1, 2, 3) for the three electronic transitions (between the ground state d(x^2–y^2) and excited states (d(xy), d(zx), d(yz)) are listed in Table 1. It is very important to know the dependence of the linewidths (related the relaxation processes) and the line intensities (related to the strength of the non -radiative transitions) in these systems since exactly these processes may play important role in the living matter. The crystal field splittings, the linewidths, and the intensities strongly depend on the kind of complex and the replacement of distant groups in the molecules under investigations.

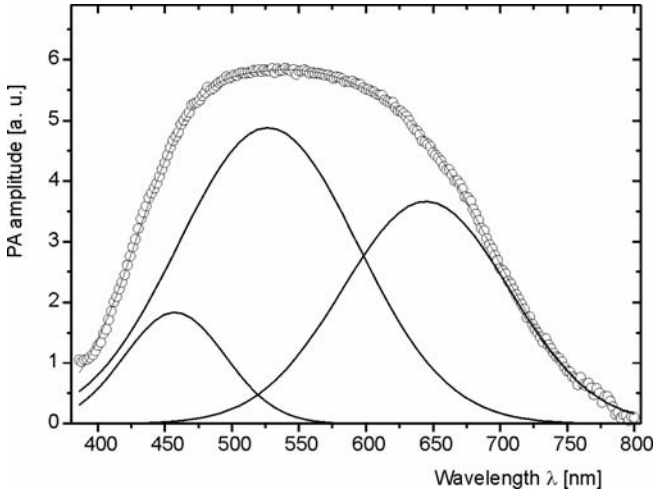

Fig. 1. PA spectrum of the copper(II) complex of spermidine Spc323 and its decomposition into three component lines

The PA spectra were recorded by using detection of the heat generated through the non-radiative relaxation, released by the sample absorbing the modulated incident light. The PA intensity (I) is given by the relation [13]:

$$I = \kappa \alpha_{\text{abs}} \gamma \tag{1}$$

where α_{abs} is the absorbance of the sample, γ is the probability for the non-radiative transitions between the excited and ground states, and κ is a coefficient determined by the thermal properties of the sample and the spectrometer. It is assumed that the coefficients κ and α_{abs} are the same for all samples. The main intensity contribution arises from the coefficient γ related to the non-radiative transitions. Replacement of distant water molecules or Cl atoms influences strongly not only the crystal field splitting of the d–d electronic levels but also the linewidths and intensities of the non-radiative transitions (Table 1).

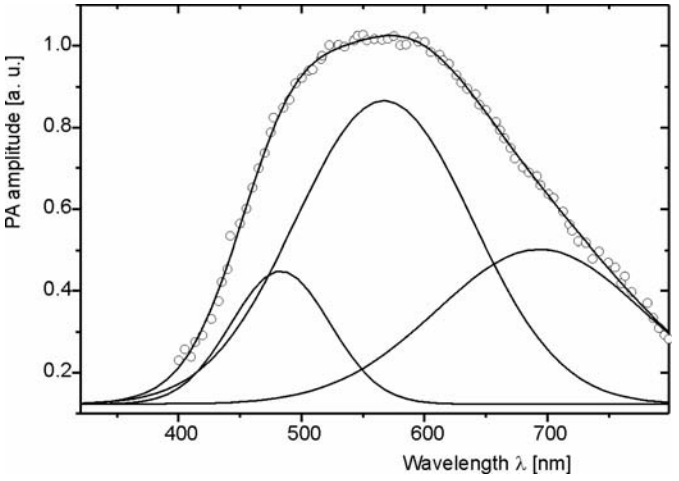

Fig. 2. PA spectrum of the copper(II) complex of spermidine Spn323 and its decomposition into three component lines

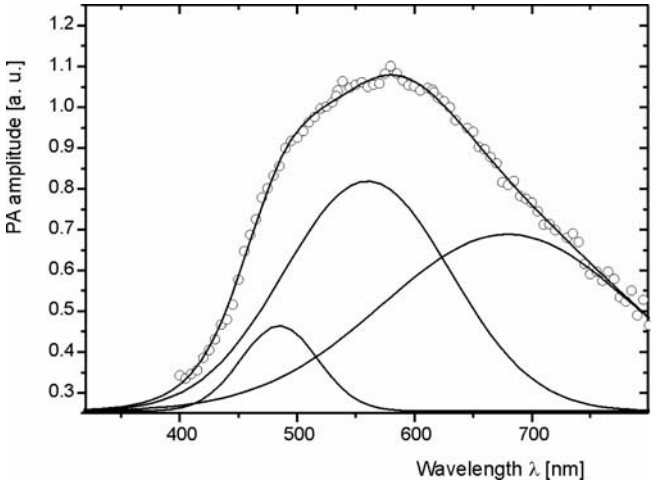

Fig. 3. PA spectrum of the copper(II) complex of spermidine Spm323 and its decomposition into three component lines

Table 1. The values of the photoacoustic spectral parameters (λ_i – position, $\Delta\lambda_i$ – linewidth, I_i – intensity) for the d–d electron transitions in polyamine copper(II) complexes [1–3]

Complex	Transition 1			Transition 2			Transition 3		
	λ	$\Delta\lambda$	I	λ	$\Delta\lambda$	I	λ	$\Delta\lambda$	I
Spn323	483(2)	80(3)	3(1)	568(9)	143(9)	14(9)	694(9)	167(50)	8(5)
Spn333	517(9)	99(3)	6(2)	612(9)	155(9)	11(5)	730(9)	203(50)	12(4)
Spn343	483(2)	58(6)	1(1)	565(9)	144(9)	11(5)	681(9)	113(10)	3(5)
Spm323	485(2)	66(5)	2(1)	560(9)	141(9)	10(3)	679(9)	212(30)	12(6)
Spm333	577(9)	126(3)	13(3)	703(6)	120(9)	14(5)	798(5)	72(6)	5(2)
Spm343	498(2)	73(3)	3(1)	577(9)	144(9)	9(4)	687(9)	221(30)	13(6)
Spc323	457(1)	79(3)	2(1)	526(6)	130(9)	8(5)	642(4)	120(15)	6(3)
Spc333	476(2)	53(3)	1(1)	540(2)	92(9)	4(2)	662(6)	160(30)	10(5)
Average	497	79	4	585	134	10	695	158	9

The line positions λ_i vary by over 100 nm for the eight investigated spermidine copper(II) complexes. The average values of the wavelengths ($\lambda_{av} = \Sigma_i\lambda_i/8$) for the corresponding d–d transitions split by the crystal field are the following: λ_{1av} = 497 nm, λ_{2av} = 585 nm, and λ_{3av} = 695 nm. The second transition has the same energy as that recorded by the PAS in hematite [14] and organometallic neodymium(III) complex (the f–f transitions) [7]. It was suggested that exactly this region of radiation could be very important for the living matter [8].

The linewidths $\Delta\lambda_i$ (the difference of wavelengths between the centre of the line and at the point of half height) depend strongly on the kind of spermidine complexes and the following average linewidths ($\Delta\lambda_{av} = \Sigma_i\Delta\lambda_i/8$) were obtained: $\Delta\lambda_{1av}$ = 79 nm, $\Delta\lambda_{2av}$ = 134 nm, $\Delta\lambda_{3av}$ = 158 nm for the three d–d transitions split by the crystal field. The relation $\Delta\lambda_{1av} < \Delta\lambda_{2av} < \Delta\lambda_{3av}$ indicates that in near infrared the relaxation processes are more intense.

Concerning the integrated intensities I_i defined as the area under the line, more significant differences are observed. The following average ($I_{av} = \Sigma_i I_i/8$) values of the corresponding d–d transitions: I_{1av} = 4, I_{2av} = 10, I_{3av} = 9, were calculated. The relation $I_{1av} < I_{2av} \approx I_{3av}$ differs from that for the linewidths, namely the last two intensities are of comparable strength and much stronger than the rather weak first line. Hence the non-radiative processes are more intense for the region of radiation with longer wavelengths.

Complex functional materials are formed by biogenic systems where the spermidine complexes in protein play a very important role in the information transfer to DNA. Dynamical processes like relaxation or non-radiative processes are of importance for the phenomena occurring in the living matter. We believe that a vital role in the forming processes of the living matter is played by species created by the “glass” phenomenon upon irradiation in the yellow spectral range. Such systems (e.g., membranes) allow an easy transfer of radiation while being insulating to the heat transfer.

4. Conclusions

The PA spectroscopy enabled studies of splittings of the d–d energy levels by the crystal field. All spectral parameters of the PA lines (positions, linewidths and intensities) strongly depend on the kind of spermidine. The average values of the linewidths and intensities show the same tendency to increase with increasing wavelengths ($\Delta\lambda_{1av}<\Delta\lambda_{2av}<\Delta\lambda_{3av}$ and $I_{1av}<I_{2av}\approx I_{3av}$) for the d–d levels split by the crystal field. The relaxation and non-radiative processes are more effective upon irradiation with light of higher wavelengths. As it might be expected, these phenomena are more intensive in the infrared regions but the photoacoustic reaction in the yellow region could be responsible for many important processes studied in biophysics.

References

[1] GUSKOS N., PAPADOPOULOS G.P., LIKODIMOS V., MAIR G.L.R, MAJSZCZYK J., TYPEK J., WABIA M., GRECH E., DZIEMBOWSKA T., PERKOWSKA A., J. Phys. D, 33 (2000), 1.

[2] GUSKOS N., PAPADOPOULOS G.P., LIKODIMOS V., MAJSZCZYK J., TYPEK J., WABIA M., GRECH E., DZIEMBOWSKA T., PERKOWSKA A., AIDINIS K, J. Appl. Phys., 90 (2001), 1436.

[3] GUSKOS N., TYPEK J., ANAGNOSTAKIS E.A., PASCHALIDIS D.G., submitted for publication to Rev. Adv. Mat. Sci. (Russia).

[4] TABOR C.W., TABOR H., Annu. Rev. Biochem., 53 (1984), 749.

[5] VERMA A., BOUTWELL R.K., [in:] *Inhibition of Oilyamine Metabolism, Biological Significance and Basis for New Therapies*, P. P. McCann, A. E. Pegg, and A. Sjoredsma (Eds.), Academic, Orlando, 1987, p. 113.

[6] LOMZIK L., [in:] *Handbook of Metal-Ligand Interactions in Biological Fluids*, Vol. I, G. Berton (Ed.), Dekker, New York, 1995, p. 686.

[7] GUSKOS N., PAPADOPOULOS G.P., MAJSZCZYK J., TYPEK J., WABIA M., LIKODIMOS V., PASCHALIDIS D.G., TOSSIDIS I.A., AIDINIS K., Acta Phys. Pol. A, 103 (2003), 301.

[8] GUSKOS N., MAJSZCZYK J., TYPEK J., WABIA M., ANAGNOSTAKIS E.A., Mol. Phys. Rep., 39 (2004), 66.

[9] GUSKOS N., GLENIS S., LIKODIMOS V., TYPEK J., FUKS H., WABIA M., SZYMCZAK R., LIN C.L., PERKOWSKA A., J. Appl. Phys., 93 (2003), 9834.

[10] GUSKOS N., MAJSZCZYK J., TYPEK J., GRECH E., KOLODZIEJ B., submitted for publication to Mat. Res. Bull.

[11] GUSKOS N., LIKODIMOS V., TYPEK J., FUKS H., GLENIS S., WABIA M., LIN C.L., GRECH E., DZIEMBOWSKA T., PERKOWSKA A., NATO Science series: Math. Phys. Chem., 76 (2002), 519.

[12] PAPADOPOULOS G.P., MAIR G.L.M., J. Phys. D: Appl. Phys., 25 (1992), 722.

[13] ADAMS M.J., HIGHFIELD J.G., KIRKBRIGHT G.F., Anal. Chem., 52 (1980), 1260.

[14] GUSKOS N., PAPADOPOULOS G.J., LIKODIMOS V., PATAPIS S., YARMIS D., PRZEPIERA A., PRZEPIERA K., MAJSZCZYK J., TYPEK J., WABIA M., AIDINIS K., DRAZEK Z., Mat. Res. Bull., 37 (2002), 1051.

Received 17 October 2004
Revised 11 February 2005

Materials Science-Poland, Vol. 23, No. 4, 2005

The kinetics of nucleation in inhomogeneous media based on the classical Avrami model

R.Z. ROGOWSKI*

Institute of Physics, Technical University of Szczecin, al. Piastów 48, 70-311 Szczecin, Poland

In this paper, the kinetics of nucleation is studied in inhomogeneous media such as a mixture of the nematic liquid crystals *p*-methoxybenzylidene-*p*-butylaniline (MBBA) and *p*-ethoxybenzylidene-*p*-*n*-butylaniline (EBBA). Experimental data are analysed in terms of the classical Avrami model for nucleation. The observed non-uniform nucleation is explained within the framework of the Landau model for phase transitions. A modification to the Avrami model is proposed in order to describe the kinetics of nucleation in highly inhomogeneous media.

Key words: *Avrami model; nucleation kinetics; inhomogeneous medium; phase transformations; nematic liquid crystal; ferroelectric switching*

1. Introduction

Most of the theoretical treatments of processes occurring by nucleation and growth are based on works by Kolmogorov and Avrami [1–3]. The Avrami model was originally proposed for the process of crystal growth and describes the kinetics of nucleation on the basis of statistical considerations. This model has also been extensively applied for describing many solid-state transformations, such as crystallization from amorphous or glassy states, solidification in metallic and polymeric systems, solid-state phase transformations, adsorption and surface kinetics in electrochemical environments, and domain switching in ferroelectrics and ferromagnets. All of these phenomena take place by nucleation and growth mechanisms.

The analysis of the kinetics of these processes, based on this model, can yield physically unclear values for some fitting parameters [4, 5]. Thus, the predictions concerning the kind of nucleation kinetics based on these parameters are often inconsistent with direct microscopic observations. For example, Matyjasek showed that during the switching process in the tryglicine sulphate (TGS) ferroelectric crystal, the domain nuclei appeared almost simultaneously and in a nonuniform manner, present-

*E-mail: rrogowski@ps.pl

ing so called “one-step” nucleation, contrary to the predictions based on the value of the fitting parameter suggesting a “continuous process” [6]. Such a discrepancy is clearly seen in inhomogeneous systems (i.e., ferroelectric crystals with an internal bias field [7] or nematic liquid crystal (NLC) mixtures).

In this study, we restricted ourselves to the investigation of the nucleation kinetics of thermally driven isotropic–nematic phase transition in a NLC mixture of *p*-methoxybenzylidene-*p*-butylaniline (MBBA) and *p*-ethoxybenzylidene-*p*-*n*-butyl-aniline (EBBA). In the first part, experimental data are analysed and discussed in terms of the classical Avrami model. It is shown that non-uniform nucleation can appear as a superposition of uniform ones, separated in space and time. Then, an explanation of such a superposition is given on the basis of the Landau approach to first order phase transformations. Additionally, an attempt is made to show that the Avrami model can also be applied to describe transformation kinetics in inhomogeneous media (with complex nucleation mechanisms) on the basis of more general assumptions.

2. The kinetics of nucleation within the framework of the Avrami model

The Avrami model is formulated for infinite media, i.e. the linear size of a system is much larger than the distance between the nuclei in a new phase forming during the phase transformation. The nuclei are randomly distributed over the volume of the system. Additionally, two physically different mechanisms of nucleation can be distinguished. The first, one-step nucleation, takes place when all nuclei arise only at the very beginning of the process and there is no further nucleation. The other, continuous nucleation, occurs when the nuclei continue to grow during the entire phase transformation. The growing nuclei begin to create macroscopic areas (usually called domains), which expand with a constant velocity. The rate of nucleation $R(t)$, defined as the number of nuclei per unit area and unit time, is different from zero only at the very beginning of the one-step nucleation process and is constant for continuous nucleation.

These assumptions allow a formula to be obtained for the temporal dependence of the untransformed volume fraction $q(t)$ of a system, with condition that the initial radii of all nuclei can be neglected:

$$q(t) = \exp\left(-\int_0^t R(\tau) C_d v^d \left(t-\tau\right)^d d\tau\right) \tag{1}$$

where the factor C_d is equal to 2, π or $4\pi/3$ for one, two, and three-dimensional growth of nuclei, respectively, v is the velocity of the expanding domains and d is the geometrical dimensionality of the domain growth. Thus, the transformed volume fraction $Q(t)$ of the system can be expressed as follows

$$Q(t) = 1 - \exp\left(-\int_0^t R(\tau) C_d v^d \left(t - \tau \right)^d d\tau \right) \tag{2}$$

$Q(t)$ and $q(t)$ can also be interpreted as the probabilities that an arbitrarily chosen point in the medium is respectively covered or uncovered by the growing domains.

By integrating Equation (1), with $R(\tau) = R\delta(\tau)$ for the one-step process and $R(\tau) = R$ = const for the continuous process, one can find

$$q(t) = \exp\left(-RC_d v^d t^d \right)$$

for one-step nucleation, and

$$q(t) = \exp\left(-RC_d v^d t^{d+1} \right)$$

for continuous nucleation.

Introducing a characteristic time t_0 and an effective dimensionality n (also called the Avrami exponent), Equation (2) can be rewritten for the both mechanisms of nucleation in the following form

$$Q(t) = 1 - \exp\left[-\left(\frac{t}{t_0} \right)^n \right] \tag{3}$$

The characteristic time t_0 and the effective dimensionality n are respectively equal to $1/v(1/(RC_d)^{1/d}$ and d for one-step nucleation and $((d + 1)/(RC_d v^d)^{1/(d+1)}$ and $d + 1$ for continuous nucleation. It is clearly seen that, according to the model assumptions, the Avrami exponent n should be an integer and not larger than four ($n = 4$ for three -dimensional growth, $d = 3$) and continuous nucleation ($n = d + 1$). Other values of n imply a more complicated process of nucleation, with different contributions of the one-step and continuous mechanisms.

In the case of complex nucleation ($n \notin \{1, 2, 3, 4\}$), an estimated expression for $R(t)$ can be obtained by comparing Equations (2) and (3). Thus, by using the Laplace transformation we have

$$R(t) = a(n, v, d, t_0) t^{n-d-1} \tag{4}$$

where

$$a = \left| \frac{\Gamma(n+1)}{\Gamma(n-d)\Gamma(d+1) C_d v^d t_0^n} \right|$$

The values of the Avrami exponent n, characteristic time t_0 and velocity of domain wall motion v are measured in the experiment.

Expression (4) allows information about the mechanism of nucleation and the number of nucleation events per unit area and time to be obtained.

3. Experimental

MBBA and EBBA nematic liquid crystals were mixed in the proportions 2:1. In the examined NLC mixture, the temperature of transition from the isotropic to the nematic phase was about 323 K. The transition temperatures are different for MBBA and EBBA – 319 K and 353 K, respectively. The mixture, with a thickness of 0.01 mm and a surface area of approximately 1.98 mm^2, was placed in a heater and observed under a polarizing microscope during a cooling process from 355 K through the transition point with the rate of 0.008 K/s. During the transformation from the isotropic to nematic state, the process was recorded with a video camera and the images were processed by a microcomputer. Two particularly interesting regions of the sample with a significant difference in nucleation kinetics were revealed. Experimental data were analysed in terms of the Avrami theory.

4. Experimental results and discussion

Direct observation of the isotropic–nematic phase transition in the NLC mixture revealed the existence of regions with uniform and non-uniform nucleation. Figure 1 presents a temporal evolution of the domain nuclei pattern of the nematic phase in the area with a nearly uniform initial distribution of nuclei (Fig. 1a).

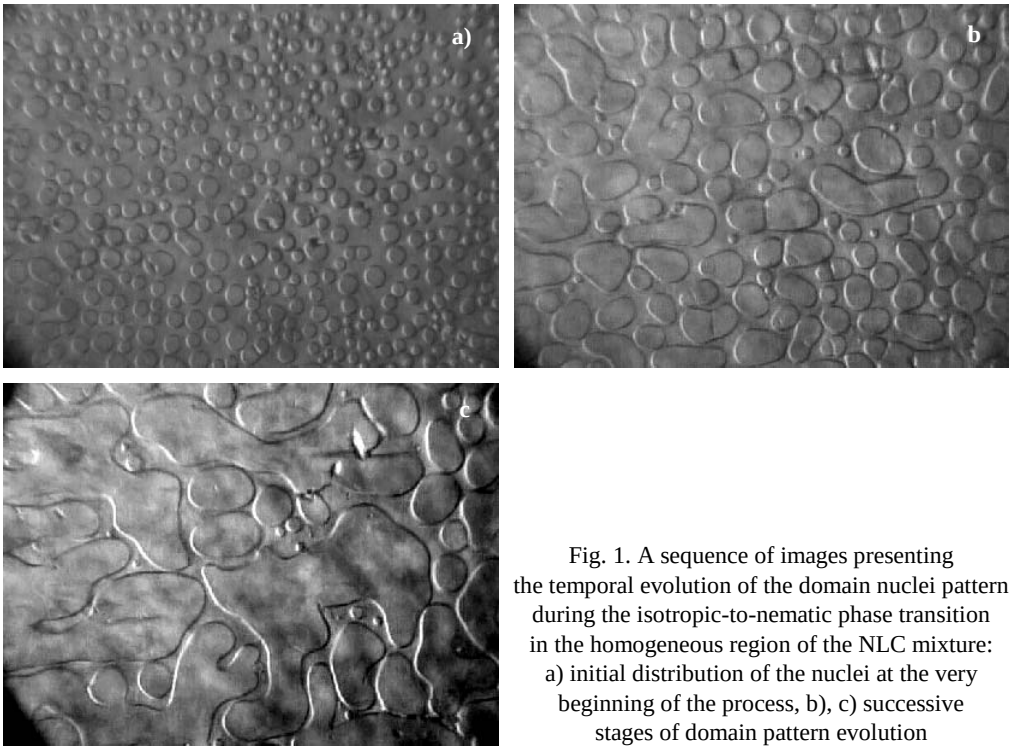

Fig. 1. A sequence of images presenting the temporal evolution of the domain nuclei pattern during the isotropic-to-nematic phase transition in the homogeneous region of the NLC mixture: a) initial distribution of the nuclei at the very beginning of the process, b), c) successive stages of domain pattern evolution

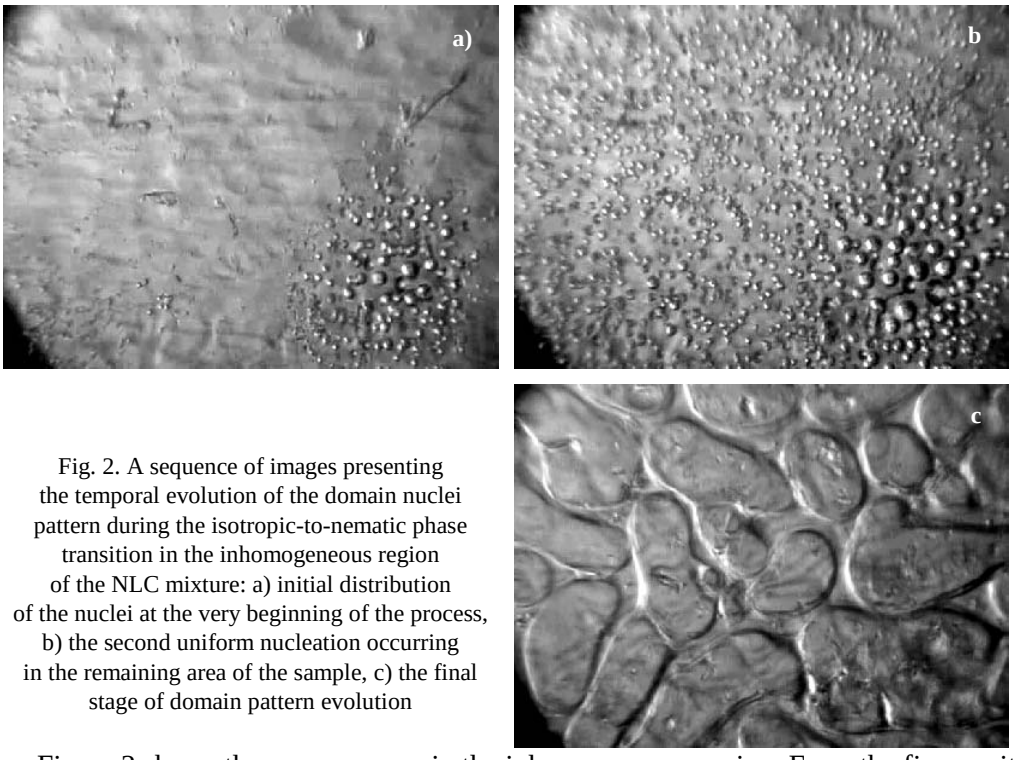

Fig. 2. A sequence of images presenting the temporal evolution of the domain nuclei pattern during the isotropic-to-nematic phase transition in the inhomogeneous region of the NLC mixture: a) initial distribution of the nuclei at the very beginning of the process, b) the second uniform nucleation occurring in the remaining area of the sample, c) the final stage of domain pattern evolution

Figure 2 shows the same process in the inhomogeneous region. From the figures, it is clearly seen that the nucleation processes are initiated with the creation of circular nuclei expanding two-dimensionally, but afterwards anisotropy appears in the expansion of some domains, and finally they begin to coalesce (Figs. 1c and 2c). It was found that the velocity of domain wall motion is constant and equal to about 0.001 $mm \cdot s^{-1}$ for the both investigated areas. The whole phase transformations took approximately the same amount of time (~115 s), regardless the kind of nucleation kinetics. Furthermore, the process of nucleation in the inhomogeneous region seems to be composed of two one-step nucleation processes, separated in time and space (compare Figs. 2a and 2b). At the beginning, the nuclei cover almost 28% of the whole surface area, then a second one-step nucleation occurs in the remaining surface area.

Figure 3 presents the temporal dependences of the fractions of the transformed phase, obtained by fitting the experimental data to Equation (3) by the least squares method. The values of the fitting parameter n are presented in the plot. The solid curve shows the results obtained for the homogeneous region, while the dotted one for the inhomogeneous region. For comparison, the dashed line shows the kinetics of nucleation only in the homogeneous part of the inhomogeneous region as seen in Figure 2a. The value of $n = 3.05$, obtained for the inhomogeneous part of the NLC sample, suggests a continuous nucleation process ($d = 2$, $n = d + 1$, see Eq. (3)) contrary to the results of the microscopic observations mentioned above. By using Equation (4), the temporal dependences of nucleation rates can be calculated. These de-

pendences, seen in Figure 4, confirm the almost one-step nucleation kinetics in the mentioned homogeneous regions.

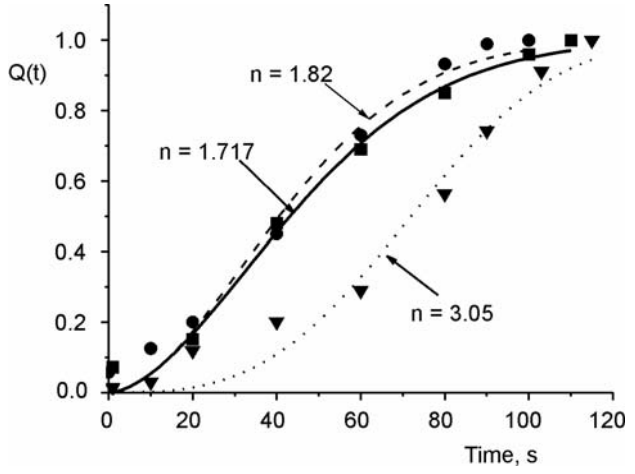

Fig. 3. Temporal dependences of the fraction of the transformed phase $Q(t)$ for three various regions of the NLC mixture: solid curve – homogeneous region (Fig. 1), dotted curve – inhomogeneous region (Fig. 2), dashed curve – small homogeneous area within the inhomogeneous region (Fig. 2a)

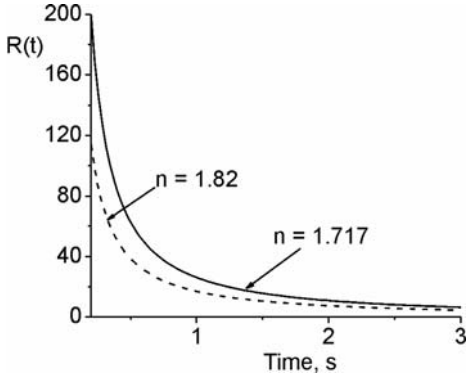

Fig. 4. Temporal dependences of the nucleation rate $R(t)$ for the homogeneous region (solid line) and small homogeneous region within the inhomogeneous one (dashed line), calculated by means of Eq. (4)

Figure 5 presents a plot of the number of all single domains as a function of time for the two investigated regions. The influence of the second one-step nucleation on the kinetics of the phase transformation in the inhomogeneous region is seen as a displacement of the maximum on the time axis. As it can be seen from the microscopic observations, the beginning of domain coalescence appears at the maximum of each curve. There is also no significant difference between these curves.

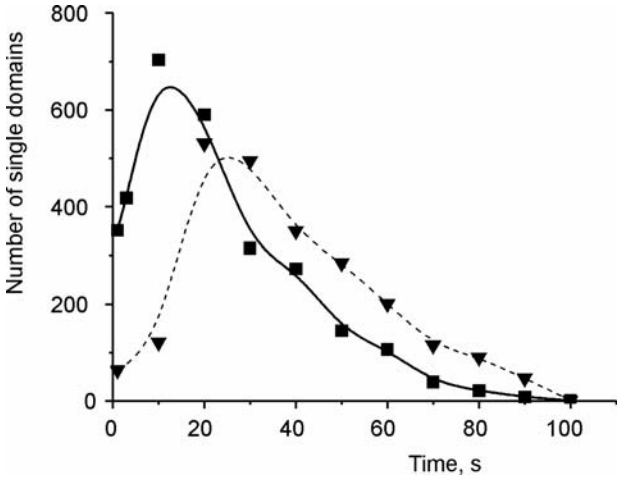

Fig. 5. Temporal dependences of the number of single domain nuclei for the homogeneous and inhomogeneous regions of the NLC mixture: solid curve – uniform nucleation, dashed curve – two one-step nucleation processes separated in time and space

From the above discussion it is clear that predictions based on the value of the Avrami exponent can yield incorrect results concerning the mechanism of nucleation.

5. Interpretation of the experimental data within the framework of the Landau model

The revealed complex character of nucleation kinetics in the inhomogeneous region of the NLC mixture can follow from a non-uniform distribution of the mixture components. This non-uniformity may strongly influence the distribution and values of the local temperatures of phase transformation and hence affect the time and type of nucleation kinetics in various regions of the medium. They may also produce the temporal and spatial separation of successive nucleation processes in various parts of the sample.

The influence of the concentration on the value of the local transition temperature can be explained in the framework of the classical Landau theory of phase transformation. Expanding the density of free energy F in powers of an order parameter p up to the third order, and assuming the coefficient of the second power of the order parameter to be temperature- and concentration–dependent, we can write

$$F = F_0 + \frac{1}{2}\left[a\left(c_c - c\right) + a'\left(T - T_c\right)\right] p^2 + \frac{1}{3}Bp^3 + \frac{1}{4}Cp^4 + \ldots \tag{5}$$

where c and c_c denote a common and a critical concentration, respectively, and $B < 0$ as appropriate for the first order phase transformation [8, 9]. From the above expansion it is clearly seen that an ordered (nematic) phase is stable for $T < T_c$ and $c > c_c$.

Otherwise, an isotropic phase exists. The natural equilibrium condition $F = 0$ leads to an inequality describing the existence of the stable phase

$$a(c_c - c) + a'(T - T_c) < \frac{2B^2}{9C} \tag{6}$$

Finally, for the transition temperature T_t we obtain

$$T_t = T_c + \frac{2B^2}{9C} - \frac{a'}{a}(c_c - c) \tag{7}$$

This formula is a phenomenological confirmation of our interpretation of the experimental data. A more detailed study of this problem in the case of first and second order phase transformations is presented in [10].

6. A generalization of the Avrami model assumptions

The description of the nucleation kinetics of first order phase transformations in inhomogeneous media on the basis of Avrami theory also seems to be possible, but in the framework of more general assumptions. In relaxor physics, an approach based on the Gaussian distribution of the local Curie temperatures around an average T_c is used to describe the diffuse phase transitions (DFT)

$$f(T, T_c, \sigma) = \frac{1}{\sqrt{2\pi}\sigma} \exp\left[-\frac{\left(T_c - T\right)^2}{4\sigma^2} \right] \tag{8}$$

where σ stands for the width of the Gaussian distribution [11].

Nucleation in a medium with a great number of temporally and spatially separated regions with homogeneous nucleation kinetics (one-step or continuous) is a similar problem. In such a case, the application of the Gaussian distribution of characteristic nucleation times t_{0i} around the value t_0 obtained by fitting experimental data to Eq. (3) may give correct results. This generalized assumption can be expressed as follows

$$Q(t) = \frac{\text{const}}{\sqrt{2\pi}\sigma} \int \left[1 - \exp\left(-\left(\frac{t}{t_{0i}} \right)^n \right) \right] \left[-\frac{\left(t_0 - t_{0i}\right)^2}{4\sigma^2} \right] dt_{0i} \tag{9}$$

where now $n \in \{1, 2, 3, 4\}$ and t_0 and σ are the fitting parameters.

7. Conclusions

It was found that the transition from the isotropic to nematic phase in an MBBA and EBBA NLC mixture occurs by almost one-step nucleation processes and a further growth of domain nuclei. The nucleation rates are then rapidly decreasing functions of time. It was revealed that, due to the nonuniform distribution of mixture components, the one-step processes of nucleation can be temporally and spatially separated. This separation has been explained within the framework of the classical Landau model for first order phase transformations by assuming the concentration dependence of the first coefficient in the free energy expansion. Nonuniform nucleation, observed in the inhomogeneous region, is a result of such a separation. It was shown that interpretations concerning the kinetics of nucleation performed on the basis of the Avrami exponent n may lead to incorrect results.

The application of the Avrami model for describing the kinetics of nucleation in highly inhomogeneous media (with a great number of separated areas with homogeneous nucleation kinetics), however, seems to be possible on the basis of a more general approach. Such an approach has been proposed on the basis of a model for DFT developed in relaxor physics.

Acknowledgements

The author would like to thank Dr. K. Matyjasek of the Institute of Physics, Technical University of Szczecin for valuable remarks and discussion.

References

[1] KOLMOGOROV A.N., Izv. Akad. Nauk, 3 (1937), 355.
[2] AVRAMI M.J., J. Chem. Phys., 7 (1939), 1103.
[3] AVRAMI M.J., J. Chem. Phys., 8 (1939), 212.
[4] ISHIBASHI Y., Integ. Ferroelectrics, 2 (1992), 41.
[5] ISHIBASHI Y., ORIHARA H., YAMADA Y., J. Phys. Soc. Japan, 57 (1988), 12.
[6] MATYJASEK K., J. Phys. D: Appl. Phys., 34 (2001), 2211.
[7] ROGOWSKI Z. R., MATYJASEK K., JAKUBAS R., J. Phys. D: Appl. Phys., 38 (2005), 4145.
[8] LANDAU L.D., Zh. Theor. Exp. Phys. (UssR), 7 (1937), 627.
[9] NESRULLAJEV A., YURTSEVEN H., KAZANCI N., *Liquid Crystals: Structures, Properties, Applications*, Ege University, Izmir, 2000.
[10] MOLDOVAN R., PUICA M., Phys. Lett. A, 286 (2001), 205.
[11] SKULSKI R., *The Diffusion of Phase Transitions in the Selected Groups of Ferroelectrics and Relaxors*, Silesian University Press, Katowice, Poland, 1999.

Received 23 September 2004
Revised 23 November 2004

Materials Science-Poland, Vol. 23, No. 4, 2005

FMR study of γ-Fe_2O_3 magnetic nanoparticles in a multiblock poly(ether-ester) copolymer matrix

N. GUSKOS[1, 2*], J. TYPEK[2], M. MARYNIAK[2], Z. ROSLANIEC[3], D. PETRIDIS[4], M. KWIATKOWSKA[3]

[1]Solid State Section, Department of Physics, University of Athens, Panepistimiopolis, 15 784 Zografos, Athens, Greece

[2]Institute of Physics, Szczecin University of Technology, al. Piastów 17, 70-310 Szczecin, Poland

[3]Institute of Engineering Material Sciences, Technical University of Szczecin, al. Piastów 17, 70-310 Szczecin, Poland

[4]NCSR „Demokritos“, Athens, Greece

Four samples containing γ-Fe_2O_3 magnetic nanoparticles dispersed at a concentration of 0.1 % (samples I and I′) and 0.3 % (samples II and II′) in a polymer matrix have been prepared. The polymer filler was in two forms: as solid-state grains (samples I and II) and as a liquid solution in trichloromethane (samples I′ and II′). The typical size of the magnetic nanoparticles was 10 nm. The samples were characterized by XRD and TEM spectroscopy. Ferromagnetic resonance (FMR) measurements were carried out at room (RT) and liquid nitrogen (LNT) temperatures for all four samples. An intense resonance absorption line from γ-Fe_2O_3 was recorded, with a slightly asymmetric line shape. The FMR spectra at RT and LNT are almost the same, as could be expected for the composite matrix. For samples II and II′, the resonance lines are centred at H_r = 3039(10) Gs and H_r = 3197 (10) Gs, respectively, with linewidths of ΔH = 1289(5) Gs and ΔH = 1364(5) Gs, respectively. For samples I and I′, the following values of resonance line parameters were obtained: H_r = 3172(10) Gs for sample I′, and H_r = 2958(10) Gs for sample I, with linewidths of ΔH = 1279(5) Gs and ΔH = 1200(5) Gs, respectively. In both cases the resonance field for samples obtained from a solid state filler is shifted to lower magnetic fields as compared to samples made from a suspension filler, which suggests stronger ferromagnetic interactions in these materials.

Key words: *magnetic nanoparticle; ferromagnetic resonance*

1. Introduction

Iron oxides, especially maghemite (γ-Fe_2O_3), in the form of nanoparticles, are very interesting materials not only due to their potential applications (high density mag-

* Corresponding author, e-mail: ngouskos@cc.uoa.gr

netic recording [1]), but also due to the possibility of rich fundamental research in magnetism, e.g. superparamagnetism or the quantum tunnelling of magnetization [2–4]. Nanocomposite materials with magnetic fillers are gaining a widening range of applications [5]. For example, magnetic nanoparticles embedded in polymer matrices have excellent potential for electromagnetic devices like those used for electromagnetic interference suppression [6]. FMR measurements give information about local magnetic properties and, in principle, about the nature of spin–spin interactions, the distribution of internal fields, or about spin–spin correlation [7–9].

The aim of this paper is to report the preparation of samples of γ-Fe_2O_3 magnetic nanoparticles dispersed at a concentration of 0.1 % and 0.3 % in a polymer matrix of (PTMO–block–PET), and to present the results of their characterization by the SEM and FMR methods.

2. Experimental

Two forms of γ-Fe_2O_3 nanoparticles were used to prepare the polymer composite: one as a solid powder (samples designated as I and II) and the other as a suspension of nanoparticles dispersed in trichloromethane so as to prevent phase separation (samples designated as I′ and II′).

The basic components used in the synthesis were: ethanediol (ethylene glycol), purchased from BASF (Germany); dimethyl terephthalate (M_n = 194 g/mol), supplied by Elana S.A. Toruń (Poland); α,ω-dihydroxy-polyoxytetramethylene (M_n = 970 g/mol), produced by Du Pont (USA).

The nanocomposites were obtained by *in situ* polycondensation in a molten state, where nanoparticles were introduced into the polymer during its synthesis. The whole process was carried out in an acid resistant steel reactor equipped with a controlled heating system and a horseshoe stirrer with perpetual torque measurement. As the polymer matrix, a multiblock poly(ether-ester) copolymer (PEE) was used. In the first step of preparation, an appropriate amount of γ-Fe_2O_3 nanoparticles were dispersed in ethanodiol (ED) by means of shear force (ultra-high speed stirrer) and ultrasonication (Sonoplus-Homogenisator), in order to ensure a homogeneous distribution of the nanofiller in the matrix. All substrates were introduced into the reactor, in which a two-stage process of PEE synthesis was accompanied by continuous mixing. In the first stage, the transesterification of dimethyl terephthalate (DMT) with ED under atmospheric pressure and at a temperature between 150 and 190 °C was carried out. The progress of the reaction was measured by the amount of distilled methanol in relation to the theoretical amount. In the second stage, the transesterification of di(2-hydroxytetramethylene) terephthalate with α,ω-dihydroxy-polyoxytetramethylene (PTMEG) and polycondensation were performed. Polycondensation proceeded at 200–260 °C under the pressure of 0.1 hPa and was carried out until the desirable torque value of the stirrer was achieved. The polymer composite filled with γ-Fe_2O_3 nanoparticles was extruded from the reactor by compressed nitrogen in the form of a filament.

Four samples were synthesized in the same way. The samples I and I′ contained 0.1 wt. % of the nanofiller, and samples II and II′ contained 0.3 wt. % of the nanofiller. The nanofiller used in samples I and II was in the form of a solid powder, and in the samples I′ and II′ it was in the form of a suspension of γ-Fe_2O_3 nanoparticles in trichloromethane.

The nanomaterials were prepared using nanocrystalline iron oxide (γ-Fe_2O_3) as the starting material, which was synthesized by the fusion of magnetite with small amounts of Al_2O_3 and CaO (3 wt. %).

After reduction, nanocrystalline iron was obtained, while the promoter oxides remained in the oxidised states. The role of the additives (CaO, Al_2O_3) was to stabilise a well-developed nanocrystalline iron oxide structure. To avoid oxidation, the sample was subsequently passivated with nitrogen containing traces of water vapour. X-ray diffraction (XRD) measurements were then performed on a Philips X Pert powder diffractometer using $CoK_{\alpha 1}$ radiation. The mean size of iron crystallites was estimated from the width of the main reflections of the diffractogram using the Scherrer equation, which yielded an average value of 10 nm. The specific surface area and the pore distribution of the carburised sample were measured using low-temperature nitrogen adsorption (Micromeritics, ASAP), yielding 180 m^2/g and 5.5 nm for the specific surface area and the average pore diameter, respectively. The analysis of the SEM images showed an almost homogenous distribution of fine graphite fibres with similar shape and size and with diameters below 1 μm.

Ferromagnetic resonance measurements were carried out using a conventional X-band (v = 9.43 GHz) Bruker E 500 spectrometer, with 100 kHz magnetic field modulation. The measurements were performed at room temperature. A square-shaped 3.5×3.5 mm^2 sample, cut out from a polymer sheet, was attached to a sample holder made of a quartz rod 4 mm in diameter. The sample holder was accommodated in the centre of the TE_{102} cavity, i.e., at the local maximum of the microwave magnetic component H_1, and in the nodal plane of the electric component E_1. Prior to measurements, the samples were magnetized with a steady magnetic field of 16 kG in order to saturate any domain structure.

3. Experimental results and discussion

The crystalline sizes of the magnetic phases grown by the reduction of γ-Fe_2O_3 powder were estimated from the broadening of prominent diffraction lines using the Scherrer equation: $d = 0.89\ \lambda/\beta\cos\theta$, where λ, β, θ and d are the wavelength of radiation, line broadening, angle of diffraction, and particle size, respectively. The average size of magnetic particle of γ-Fe_2O_3, estimated from X-ray line broadening, was about 10 nm.

The morphologies of the prepared samples and magnetic powders were studies by Scanning Electron Microscopy (SEM). Figure 1 presents SEM pictures of solid-state γ-Fe_2O_3 magnetic nanoparticles with concentrations of 0.1 % and 0.3% and of solution (0.1%) in a polymer matrix, respectively. The magnetic nanoparticles are organized in

agglomerates of particles having a maximum length of about 10 μm for sample I (Fig. 1a) and 20 μm for sample II (Fig. 1b). For magnetic nanoparticles kept in suspension and embedded in the polymer, their homogenous dispersion in the matrix was observed by the SEM technique (Fig. 1c).

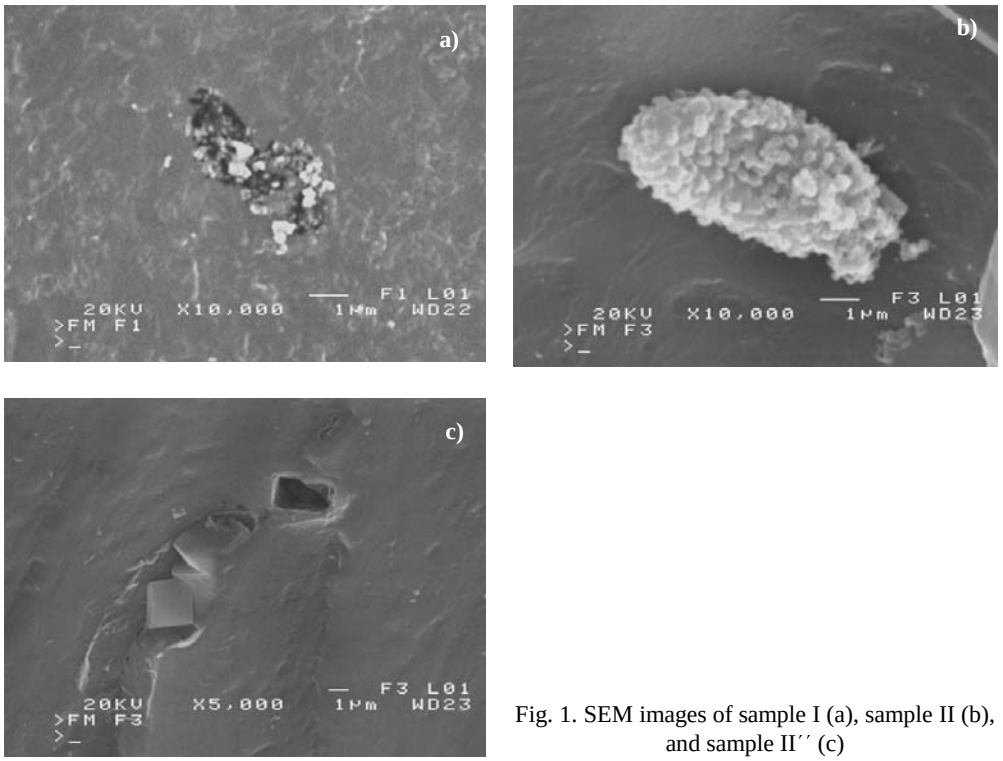

Fig. 1. SEM images of sample I (a), sample II (b), and sample II′′ (c)

Figure 2 presents the FMR spectra of all four samples. A slightly asymmetrical and intense line is observed for the samples. For all investigated samples, the recorded FMR spectra were similar, the resonance fields roughly the same and magnetic nanoparticles in aggregates or agglomerates were dispersed homogeneously in polymer matrices. Additionally, magnetic nanoparticles in nanocomposites were frozen to liquid nitrogen temperature. In this case, the FMR spectra of non-frozen and frozen samples did not yield any essential differences – the intensities, linewidths, and resonance fields were exactly the same.

For a proper description of the FRM spectra of γ-Fe_2O_3, the parameters H_L, H_R, and $H_{res} = (H_L + H_R)/2$ have been introduced, being the left, the right peak positions of the line, and the effective resonance field position, respectively [10]. Table 1 shows the values of the peak-to-peak linewidth $\Delta H = H_R - H_L$, the positions of the resonance field H_{res}, and the relative integrated intensities $I_{int} = A\Delta H^2$ (A is the peak-to-peak amplitude) for all samples. A comparison of the resonance fields obtained for samples I and II (solid state filler) with analogous fields for samples I′ and II′ shows that they

are strongly shifted (over 200 Gs) and their linewidths display an opposite temperature dependences. The intensities are greater for samples obtained from γ-Fe_2O_3 filler in the form of suspension. Increasing filler concentration shifts the resonance line to higher magnetic fields, while its linewidth and intensity increase (Table 1).

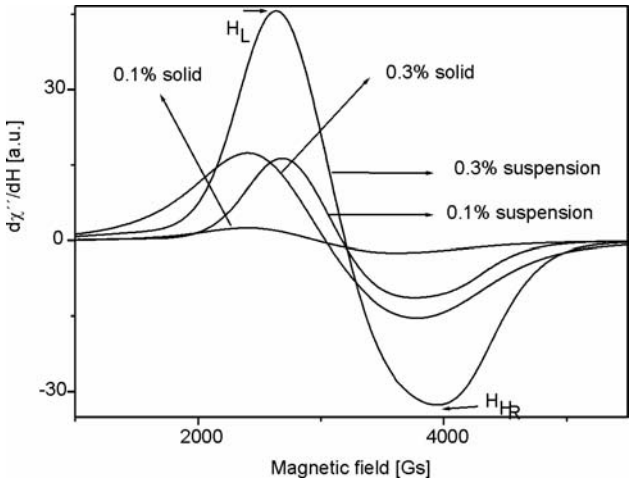

Fig. 2. FMR spectra of the investigated samples at room temperature

For γ-Fe_2O_3 nanoparticles, with sizes ~2.5 nm, embedded in polyethylene, an FMR line with the linewidth of ΔH = 400 Gs, centred at g ~ 2.07, has been recorded [10]. A simulation of the FMR spectra for iron oxide has shown that the intensity and linewidth increase strongly with increasing nanoparticle size. For 10 nm nanoparticles the FMR spectrum is almost the same as that obtained in this work [4].

Table 1. The linewidths ΔH, resonance field H_{res}, integrated intensities I_{int}, and g-factors of γ-Fe_2O_3 nanoparticles in the polymer matrix

Sample	Resonance field H_{res} [Gs]	Linewidth ΔH [Gs]	Intensity I_{int} [a.u.]	g_{eff}
I	2992(10)	1213(5)	1.0	2.259
I′	3222(10)	1079(5)	3.0	2.098
II	3073(10)	1376(5)	6.3	2.199
II′	3272(10)	1274(5)	13.6	2.066

With decreasing temperature, the resonance field of magnetic nanoparticles is shifted to lower magnetic fields, the linewidth increases, and the integrated intensity decreases [2, 4, 7]. Samples synthesized from solid-state magnetic nanoparticles have a blocking temperature shifted toward higher values, which is opposite to that seen for samples obtained from filler in a suspension form.

If the ferromagnetic nanoparticles are not well separated, the spin of a nanoparticle is subject to the following total magnetic field [11]:

$$H_{\mathrm{tot}} = H_{\mathrm{dem}} + H_{\mathrm{app}} + H_{\mathrm{dip}} + H'_{\mathrm{dip}}$$

where the first term represents the demagnetisation field, the second term the applied external magnetic field, the third term the dipole field originating from the neighbouring nanoparticles, and the last term the dipole-dipole interaction between aggregates. The collective spins of agglomerates could recognize an additional magnetic field, which broadens the FMR line and shifts it in the direction of lower magnetic fields.

4. Conclusions

Intense FMR spectra were recorded for all four samples of γ-Fe_2O_3 in polymer matrix. FMR studies confirmed that the agglomerates are distributed homogeneously in the polymer matrix. Cooling samples to liquid nitrogen temperature did not influence the FMR spectra. The resonance field, linewidth, and intensity strongly depend on filler concentration and on the form of the magnetic nanoparticles (solid or suspension) used to fill the polymer matrix. Solid magnetic nanoparticles more easily build conglomerates of great sizes in the polymer matrix than those being in a suspension form. The internal magnetic field is significantly greater in the former type of samples. This field decreases with increasing filler concentration; that trend is the same for samples formed by magnetic nanoparticles in a suspension form.

References

[1] SPELIOTIS D.E., J. Magn. Magn. Mater., 193 (1999), 29.
[2] KOKSHAROV YU.A., PANKRATOV D.A., GUBIN S.P., KOSOBUDSKY I.D., BELTRAN M., KHODORKOVSKY Y., TISHIN A.M., J. Appl. Phys., 89 (2001), 2293.
[3] CHEN X., KLEEMANN W., PETRACIC O., SICHELSCHMIDT O., CARDOSO S., FREITAS P.P., Phys. Rev., B68 (2003), 054433.
[4] HSIEH C.T., LUE J.T., Eur. Phys. J., B35 (2003), 337.
[5] XIAOTUN Y., LINGGE X., CHOON N.S., HARDY C.S.O., Nanotechnology, 14 (2003), 624.
[6] WILSON J.L., PODDAR P., FREY N.A., MOHOMED K., HARMON J.P., KOTHA S., WACHSMUTH J., J. Appl. Phys., 95 (2003), 1439.
[7] HUBER D.L., Phys. Rev., B6 (1972), 3180.
[8] CAMPBELL I.A., HURDEQUINT H., HIPPERT F., Phys. Rev., B33 (1986), 3540.
[9] RETTORI C., RAO D., OSSEROFF S.B., AMORETTI G., FISK Z., CHEONG S.W., VIER D., SCHULTZ S., TOVAR M., ZYSLER R.D., SCHIBER J.E., Phys. Rev., B47 (1993), 8156.
[10] KOKSHAROV YU.A., GUBIN S.P., KOSOBUDSKY I.D., YURKOV G.YU., PANKRATOV D.A., PONOMARENKO L.A., MIKHEEV M.G., BELTRAN M., KHODORKOVSKY Y., TISHIN A.M., Phys. Rev., B63 (2000), 012407.
[11] NARKIEWICZ U., GUSKOS N., ARABCZYK W., TYPEK J., BODZIONY T., KONICKI W., GASIOREK G., KUCHAREWICZ I., ANAGNOSTAKIS E.A., Carbon, 42 (2004), 1127.

Received 1 December 2004
Revised 13 May 2005

Materials Science-Poland, Vol. 23, No. 4, 2005

Anomalous relaxation in dielectrics. Equations with fractional derivatives

V.V. NOVIKOV[1], K.W. WOJCIECHOWSKI[2*], O.A. KOMKOVA[1], T. THIEL[3]

[1]Odessa National Polytechnical University, 1 Shevchenko Prospekt, 65044 Odessa, Ukraine

[2]Institute of Molecular Physics, Polish Academy of Sciences,
M. Smoluchowskiego 17, 60-179 Poznań, Poland

[3]Poznań University of Technology, Piotrowo 5, 60-695 Poznań, Poland

It has been shown that anomalous relaxation in dielectrics can be described in terms of equations with fractional derivatives. The solutions of the resulting equation with fractional derivatives are expressed by the Mittag –Leffler function and the Fox function. The conditions of a change from the Debye relaxation to "slow" (anomalous) relaxation with a power time dependence have been examined in the limits $t \to 0$ and $t \to \infty$.

Key words: *relaxation; fractional derivative; dielectric*

1. Introduction

Anomalies of dynamic dielectric properties appear to be a characteristic feature of disordered ferroelectrics and polymers, as well as composites and other materials. In particular, strong dispersion of dynamic magnetic or dielectric susceptibility was observed in many spin or dipole glasses (see e.g., [1]). This dispersion is usually explained by the fact that the disordered systems have a wide spectrum of relaxation times, which may be extracted from the observed frequency dependence of susceptibility [2]. Examples include the dielectric response of ferroelectric relaxors of the following types: $PbMg_{1/3}Nb_{2/3}O_3$ $PbSc_{1/2}Nb_{1/2}O_3$, $Pb_{1-x}La_xZr_{0.35}Ti_{0.65}O_3$ (x = (0.7–0.9)) [3–6].

It has been shown [1–7] that it is necessary to have different complicated empirical formulae, such as the Cole–Cole, Cole–Davidson, Havriliak–Negami, and others in order to describe responses different from Debye.

*Corresponding author, e-mail: kww@man.poznan.pl

The empirical principles of Cole–Cole, Cole–Davidson, and Havriliak–Negami have been used for many years to describe relaxation processes in ordinary glasses, polymers, composites, disordered ferroelectrics, and other systems. Various data, obtained by means of methods including dielectric spectroscopy, nuclear magnetic resonance, quasi-elastic scattering of neutrons were successfully fitted with the Cole –Cole, Cole–Davidson, and Havriliak–Negami formulae. It is evident, however, that the application of distribution functions extracted from experimental dielectric responses, does not allow one to elucidate the physical nature of the anomalies in the responses of the disordered systems.

Relaxation characterizes the reaction of a thermodynamic system to outer changes. Based on the observation that the rate at which a system approaches equilibrium is proportional to the value of the deviation from equilibrium, the governing differential equation can be obtained, and its solution leads to an exponential (Debye) relaxation [7]:

$$f(t) \sim \mathrm{e}^{-t/\tau} \tag{1}$$

Many experimental investigations of relaxation processes in random media do not coincide, however, with the above exponential (Debye) law. There, Kohlrausch explored the phenomenon of charge decrease in the "Leiden jar" 150 years ago [8]. He experimentally determined that the decrease of charge with time, $q(t)$, occurred according to the law:

$$q(t) = q(0)\exp\left[-\left(\frac{t}{\tau}\right)^{\beta}\right] \tag{2}$$

In accordance with Kohlrausch's experimental data, β = 0.43 (β – the Kohlrausch constant).

More recently, different dependences for the relaxation function have been obtained, such as Cole–Cole, Cole–Davidson, and Havriliak–Negami, all determined empirically. No results of the calculations of the distribution function of the relaxation times have been published in the case of a particular model, i.e. no models allowing one to describe dielectric responses more complicated than the simple Debye principle have been formulated. Below, we will construct a mathematical model that leads to an anomalous (non-Debyan) relaxation of the type described by Equation (2).

2. Anomalous relaxation

At present, there is no quantitative microscopic theory capable of explaining the experimental dependences of the Cole–Cole, Cole–Davidson, and Havriliak–Negami types [1–33]. Sometimes it is even stated that such a theory cannot be developed [22]. This is due to the fact that spatial heterogeneity connected, for instance, with the random positions of admixture molecules in a matrix or with the positions of atoms in an

amorphous semiconductors leads to a rather wide range of microscopic change rates. Such a spatial disorder will lead to a temporal and sometimes energetic disorder.

In a number of works, different models were shown to describe anomalous relaxation. These were based on fractal concepts about processes producing anomalous relaxation [9–35].

The mathematical language of a fractional derivative [36–39], based on the representation of the Riemann–Liouville operator of fractional differentiation, is used to describe and explore relaxation processes produced by fractal structures

$$D^{\alpha}\left[f(t)\right]=\frac{1}{\Gamma(1-\alpha)}\frac{d}{dt}\int_{c}^{t}(t-\tau)^{-\alpha}f(\tau)d\tau \tag{3}$$

Investigations in this field gave fruitful results [9–35]. Representing a fractional derivative by Equation (3), however, makes it difficult to interpret the operations of differentiation and their connection with the fractal set: for example, a fractional derivative of a constant is not equal to zero. The use of fractional derivatives has a phenomenological and formal character. Equations with fractional derivatives have made different attractive analogies. Foundations for the connection of a fractional derivative with a fractal set, which produces the anomalous behaviour of dielectric relaxation, has been given in [25–28, 34, 35].

To make calculations more convenient, one connects the fractional differentiation operator $D_{0+}^{\alpha}f(t)$ with the fractional integration operator $I^{\alpha}f(x)$ defined as [36–39]

$$I^{\alpha}f(x)=\Phi_{\alpha}(x) \tag{4}$$

where the function $\Phi_{\alpha}(x)$ is

$$\Phi_{\alpha}(t)=C\int_{0}^{t}\frac{\left[f(\tau)-f(0)\right]}{(t-\tau)^{\alpha}}d\tau \tag{5}$$

and

$$C=\frac{1}{\Gamma(1-\alpha)}$$

It can be shown that

$$D_{0+}^{\alpha}f(t)=\frac{d}{dt}\Phi_{\alpha}(t) \tag{6}$$

i.e., the function $\Phi_{\alpha}(x)$ can be thought of as a primitive function for $f(t)$. The Laplace transformation gives [36–39]

$$L\left[D_{0}^{\alpha}f(t)\right]=p^{\alpha}L\left[f(t)\right]-p^{\alpha-1}f(0) \tag{7}$$

Now we consider a medium whose non-equilibrium state is of a fractal nature. We will assume that the non-equilibrium state is defined by a set of time events, in which subsequent events occur some time after the previous event has finished. In this case, some segments are excluded from the continuous states of the system during evolution according to a certain law. Such a process can be characterized as a process formed by a fractal state with a certain fractal dimension d_f.

The relaxation equation will have the following operator form [35]:

$$\left(\tau^{-\alpha} + D_{0+}^{\alpha}\right) P(t) = \frac{\chi_0 E}{\tau^{\alpha}} \tag{8}$$

where D^{α} is the fractional differentiation operator

$$D^{\alpha}{}_{0+}\left[f(t)\right] = C\frac{d}{dx}\int_{0+}^{x}\frac{f(t)}{(x-t)^{\alpha}}dt \tag{9}$$

The initial condition of Equation (8) is $P(0) = 0$. In accordance with (8), the Laplace transform of the function $P(t)$ can be obtained as:

$$\bar{P}(p) = \frac{\chi_0 E}{p}\frac{1}{1+(\tau p)^{\alpha}} \tag{10}$$

According to Equation (10), the Laplace transform $\bar{P}(p) = L(P(t))$ can be expressed as the series

$$\begin{aligned}\bar{P}(p) &= \frac{\chi_0 E}{p}\frac{1}{1+(\tau p)^{\alpha}} = \chi_0 E\left(\frac{1}{p} - \frac{(\tau p)^{\alpha-1}}{1+(\tau p)^{\alpha}}\right)\\ &= \chi_0 E\left(\frac{1}{p} - \frac{(\tau p)^{-1}}{1+(\tau p)^{-\alpha}}\right) = \chi_0 E\left(\frac{1}{p} - \sum_{n=0}^{\infty}(-1)^n(\tau p)^{-\alpha n-1}\right)\end{aligned} \tag{11}$$

Thus, the solution of (8) in the space of originals is:

$$P(t) = \chi_0 E\left(1 - \sum_{n=0}^{\infty}\frac{(-1)^n\left(\frac{t}{\tau}\right)^{\alpha n}}{\Gamma(\alpha n+1)}\right) = \chi_0 E\left(1 - M_{\alpha,1}(z)\right) \tag{12}$$

where $M_{\alpha,1}(z)$ is the Mittag–Leffler function

$$M_{\alpha,\gamma}(z) = \sum_{n=0}^{\infty}\frac{z^n}{\Gamma(\alpha n+\gamma)}, \quad z = -\left(\frac{t}{\tau}\right)^{\alpha} \tag{13}$$

In our case, $\gamma = 1$.

It is convenient to use the Fox functions (i.e., the generalized Mellin–Barnes integrals) when solving equations with fractional derivatives, since the Laplace and Fourier transforms for the Fox functions are expressed through the Fox functions with other parameters. The connection between the Mittag–Leffler functions and the Fox functions is the following [40, 41]:

$$M_{\alpha,\gamma}(-z) = H_{1,2}^{1,1}\left[z \left| \begin{matrix} (0,1) \\ (0,1),(1-\gamma,\alpha) \end{matrix} \right. \right] \tag{14}$$

Therefore, Equation (12) can be written as

$$P(t) = \chi_0 E\left(1 - H_{1,2}^{1,1}\left[\left(\frac{t}{\tau} \right)^{\alpha} \left| \begin{matrix} (0,1) \\ (0,1),(0,\alpha) \end{matrix} \right. \right] \right) \tag{15}$$

If $\alpha = 1$, we obtain from Equation (15):

$$P(t) = \chi_0 E\left(1 - \sum_{n=0}^{\infty} \frac{(-1)^n \left(\frac{t}{\tau} \right)^n}{\Gamma(n+1)} \right) = E\chi_0 \left(1 - \mathrm{e}^{-t/\tau} \right) \tag{16}$$

If $\alpha \neq 1$, according to Equation (15), it follows that

$$P(t) \approx 1 - \left(\frac{t}{\tau} \right)^{-\alpha}, \qquad \left(\frac{t}{\tau} \right) \to \infty \tag{17}$$

and

$$P(t) \approx \left(\frac{t}{\tau} \right)^{\alpha}, \qquad \left(\frac{t}{\tau} \right) \to 0 \tag{18}$$

Thus, the solution of the equation with the fractional derivative (Eq. (8)) describes relaxation in dielectrics having a power time dependence with the asymptotic approximations of Equations (17) and (18).

Now let us generalize the results obtained. Instead of Equation (8), another operator of fractional differentiation will be examined:

$$\left(\tau^{-\alpha} + D^{\alpha} \right)^{\nu} = \sum_{n=0}^{\infty} \left(\tau^{-\alpha} \right)^n \binom{\nu}{n} D^{\alpha(\nu-n)} \tag{19}$$

where $\binom{\nu}{n} = \frac{\nu!}{n!(\nu-n)!}$ is a binomial coefficient and D^{α} is the operator of fractional differentiation,

$$D^{\alpha}{}_{0+}\left[f(t)\right] = C\frac{d}{dx}\int_{0+}^{x}\frac{f(t)}{(x-t)^{\alpha}}dt$$

In this case, the equation describing relaxation processes in dielectrics can be written in the following way

$$\left(\tau^{-\alpha} + D^{\alpha}\right)^{\nu}\left[P(t)\right] = \frac{\chi_0 E_0}{\tau^{\alpha\nu}} \tag{20}$$

where the initial condition is $P(0) = 0$.

In accordance with Equation (5), the Laplace transform of the function $P(t)$ is:

$$\bar{P}(p) = \frac{\chi_0 E}{p}\frac{1}{(1+(\tau p)^{\alpha})^{\nu}} \tag{21}$$

where

$$\bar{P}(p) = \int_0^{\infty} e^{-pt}\frac{1}{2}(t)\,dt$$

By substituting $p \to i\omega$ and taking into account Equation (21), the complex susceptibility can be written in the form

$$\chi(i\omega) = \frac{\chi_0}{\left(1+(i\omega\tau)^{\alpha}\right)^{\gamma}} \tag{22}$$

Dependence (22) coincides with the experimental principle of Havriliak–Negami [7]. Hence it appears that the complex relative permittivity is equal to

$$\varepsilon^{*}(i\omega) = \varepsilon_{\infty} + \frac{\varepsilon_0 - \varepsilon_{\infty}}{[1+(i\omega\tau)^{\alpha}]^{\gamma}} \tag{23}$$

Where

$$\varepsilon'(\omega) = \mathrm{Re}\left[\varepsilon^{*}(i\omega)\right] = \varepsilon_{\infty} + (\varepsilon_0 - \varepsilon_{\infty})\frac{\cos\left[\gamma\arctan\left(\dfrac{\sin\dfrac{\alpha\pi}{2}(\omega\tau)^{\alpha}}{1+\cos\dfrac{\alpha\pi}{2}(\omega\tau)^{\alpha}}\right)\right]}{\left(1+(\omega\tau)^{2\alpha}+2(\omega\tau)^{\alpha}\cos\dfrac{\alpha\pi}{2}\right)^{\gamma/2}} \tag{24}$$

$$\varepsilon''(\omega)=\mathrm{Im}\left[\varepsilon^{*}(i\omega)\right]=(\varepsilon_0-\varepsilon_\infty)\frac{\sin\left[\gamma\arctan\left(\dfrac{\sin\dfrac{\alpha\pi}{2}(\omega\tau)^{\alpha}}{1+\cos\dfrac{\alpha\pi}{2}(\omega\tau)^{\alpha}}\right)\right]}{\left(1+(\omega\tau)^{2\alpha}+2(\omega\tau)^{\alpha}\cos\dfrac{\alpha\pi}{2}\right)^{\gamma/2}} \tag{25}$$

Moving from the image in Equation (21) to the original, we get the solution of Equation (20), which describes a dielectric relaxation that coincides with the experimental principle of Havriliak–Negami:

$$P(t)=-\frac{1}{\Gamma(\gamma)}\sum_{k=0}^{\infty}\frac{(-1)^k\,\Gamma(k+\gamma)}{\Gamma(\alpha k+\alpha\gamma)\Gamma(k+1)}\left(\frac{t}{\tau}\right)^{\alpha(k+\gamma)},\quad 0<\alpha<1,\quad 0<\gamma<1 \tag{26}$$

Thus, the dependence of the dielectric polarization $P(t)$ on time has the form of Equation (26) for Havriliak–Negami relaxation.

When $\gamma = 1$, the dependence (26) turns into the relaxation principle of Cole–Cole, and when $\alpha = 1$, it turns into the principle of Cole–Davidson. Hence, one can conclude that the operator in (19) is a generalized operator of fractional differentiation.

Thus, a mathematical model, i.e. a differential equation with fractional derivatives, was constructed to describe the relaxations of the Cole–Cole, Cole–Davidson, and Havriliak–Negami types in dielectrics.

The obtained solution of the differential equation with fractional derivatives allows one to predict anomalous dynamic dielectric properties in disordered materials, such as ferroelectrics, polymers, and composites used in various fields of human activity, e.g. in electronics.

Acknowledgements

This work was partially supported by the Polish Committee for Scientific Research (KBN) within the grant 4T11F01023 and by the Agreement between the Polish and Ukrainian Governments.

References

[1] KORENBLIT I.YA., SHENDER E.F., Usp. Fiz. Nauk, 157 (1989), 267 (in Russian).
[2] COLLA E.V., KOROLEVA E.YU., OKUNEVA N.M., VAKHRUSHEV S.B., J. Phys.: Cond. Matter, 4, 3671 (1992).
[3] GLINCHUK M.D., STEPHANOVICH V.A., HILCZER B., WOLAK J., CARANONI C., J. Phys.: Cond. Matter, 11 (1999), 6263.
[4] GLINCHUK M.D., STEPHANOVICH V.A., J. Phys.: Cond. Matter, 10 (1998), 11081.
[5] GLINCHUK M.D., STEPHANOVICH V.A., J. Phys.: Cond. Matter, 6 (1994), 6317.
[6] GLINCHUK M.D., FARHI R., STEPHANOVICH V.A., J. Phys.: Cond. Matter, 9 (1997), 10 237.
[7] JONSCHER A.K., *Dielectric Relaxation in Solids*, Chelsea Dielectric, London, 1983.
[8] KOHLRAUSCH R., Ann. Phys. (Leipzig), 12 (1847), 393; Pogg. Ann. Phys. Chem., 91 (1854), 179.

[9] WILLIAMS G., WATTS D.C., Trans. Faraday Soc., 66 (1970), 80.
[10] INOKUTI M., HIRAYAMA F., J. Chem. Phys., 43 (1965), 1978.
[11] SCHER H., LAX M., Phys. Rev. B, 7 (1973), 4491.
[12] SCHER H., MONTROLL E.W., Phys. Rev. B, 12 (1975), 2245.
[13] NGAI K.L., JONSCHER A.K., WHITE C.T., Nature, 277, (1979), 185.
[14] BLUMEN A., KLAFTER J., WHITE B.S., ZUMOFEN G., Phys. Rev. Lett., 53 (1984), 1301.
[15] KLAFTER J., BLUMEN A., ZUMOFEN G., J. Stat. Phys., 36 (1984), 561.
[16] BLUMEN A., KLAFTER J., ZUMOFEN G., *Models for reaction dynamics in classes* [in:] *Optical Spectroscopy of Glasses*, I. Zschokke (Ed.), Kluwer, Dordrecht, 1986, pp. 199–265.
[17] SHLESINGER M.F., MONTROLL E.W., Proc. Natl. Acad. Sci. USA, 81 (1984),1280.
[18] GOETZE W., SJOGREN L., Rep. Prog. Phys., 55 (1992), 241.
[19] HARROWELL P., Phys. Rev. E, 48 (1993), 4359.
[20] PHILLIPS J.C J., Non-Cryst. Solids, 172 (1994), 98 ; Rep. Prog. Phys., 59 (1996), 1133.
[21] METZLER R., GLOCKLE W.G., NONNENMACHER T.F., Physica A, 211 (1994), 3; METZLER R., SCHICK W., KLIAN H-G., NONNENMACHER T.F., J. Chem. Phys., 103 (1995), 7180; METZLER R., NONNENMACHER T.F., J. Phys. A : Math. Gen., 30 (1997), 1089.
[22] FUJIWARA S., YONEZAWA F., J. Non-Cryst. Solids, 198–200 (1996), 507.
[23] GOMI S., YONEZAWA F., J. Non-Cryst. Solids, 198–200 (1996), 521.
[24] DOUGLAS J.F., J. Phys.: Cond. Matter, 11 (1999), A329.
[25] NIGMATULLIN R.R., Phys. Stat. Sol. (b), 124 (1984), 389.
[26] NIGMATULLIN R.R., Phys. Stat. Soli. (b), 133 (1986), 425.
[27] NIGMATULLIN R.R., Teor. Mat. Fiz., 90 (1992), 354.
[28] NIGMATULLIN R.R., RYABOV YA.E., Fiz. Tv. Tela, 39, 101 (1997).
[29] FELDMAN Y., KOZLOVICH N., ALEXANDROV Y., NIGMATULLIN R.R., RYABOV YA., Phys. Rev. E, 54 (1996), 5420.
[30] METZLER R., BARKAI E., KLAFTER J., Phys. Rev. Lett., 82 (1999), 3563.
[31] BARKAI E., METZLER R., KLAFTER J., Phys. Rev. E, 61 (2000), 132.
[32] KOLWANKAR K.H., GANGAL A.V., Phys. Rev. Lett., 80 (1998), 214.
[33] SCHIESSEL H., METZLER R., BLUMEN A., NONNENMACHER T.F., J. Phys. A : Math. Gen., 28 (1995), 6567.
[34] NOVIKOV V.V., WOJCIECHOWSKI K.W., J. Appl. Tech. Physics, 41, (2000), 149
[35] NOVIKOV V.V., PRIVALKO V.P., Phys. Rev. E, 64 (2001), 031504.
[36] OLDHAM K., SPANIER J., *The Fractional Calculus*, Academic Press, New York, 1974.
[37] SAMKO S.G., KILBAS A.A., MARYCHEV O.I., *Fractional Integrals and Derivatives. Theory and Applications*, Gordon and Breach, Amsterdam, 1993.
[38] PODLUBNY I., *Fractional Differential Equations*, Academic Press, New York, 1999.
[39] *Applications of Fractional Calculus in Physics*, R. Hilfer (Ed.), World Scientific, London, 2000.
[40] FOX C., Trans. Am. Math. Soc., 98 (1961), 395.
[41] PRUDNIKOV A.P., BRYCHKOV YU.A., MARICHEV O.I., *Integrals and Series*, Vol. 3, Gordon and Breach, New York, 1990.

Received 16 December 2004
Revised 22 April 2005

Materials Science-Poland, Vol. 23, No. 4, 2005

Persistent photoconductivity in a InP:Fe single layer structure at room temperature

G. E. ZARDAS[1*], P. H. YANNAKOPOULOS[2],
CH. I. SYMEONIDES[1], O. CSABAY[3], P. C. EUTHYMIOU[1]

[1]University of Athens, Physics Department, Solid State Section

[2]T.E.I. Piraeus, Computer Systems Engineering Department

[3]Department of Microelectronics, Slovak Technical University, Bratislava

Measurements of current in the dark and under illumination were carried out at room temperature on samples of semi-insulating (SI) InP:Fe, on which a layer of low resistivity InP:Fe was deposited. A voltage of 25 mV was applied. After the illumination was switched off, a remaining current was observed, for at least one hour, higher than the current before the illumination. This phenomenon is known as persistent photoconductivity (PPC) and, according to the suggested models, is due to the barriers separating electrons and holes and preventing their recombination.

Key words: *semiconductors; photoconductivity; recombination and trapping; photoelectron spectroscopy*

1. Introduction

In many semiconductor structures, a change in electric conductivity under illumination persists some time after switching off the light. This phenomenon is called persistent photoconductivity (PPC) and has been studied extensively during the two last decades. Measurements of the relaxation and decay of photocurrent have been carried out on the surfaces of epilayers of pure InP [1], n-InP/GaInAs [2], and $Ga_xIn_{1-x}P$/InP:Fe [3]. Two prevailing theoretical models for the interpretation of PPC have been adopted up to date [4].

The first model is based on a spatial separation of photocarriers (electrons and holes) due to microscopic potential barriers, which are in turn due to zone bending on surfaces, interfaces, junctions, or around inhomogeneities (induced by implantation). If these potential barriers are high enough compared to the thermal potential kT/q, the

[*]Corresponding author: e-mail: gzardas@cc.uoa.gr

lifetime of the remaining electrons and holes becomes very high. The other theoretical model accepts microscopic (atomic) energy barriers in centres with large relaxation times (DX centres). Another theoretical model, which is an extension of the first one [5], refers to the existence of clusters of faults (defect clusters). These clusters are local inhomogeneities, where the density of faults is much higher than the impurity density in the other parts of the crystal. Deep levels in the cluster are charged by electrons trapped from the surrounding material. In this way, a charge of opposite polarity is created around the cluster and consequently an overall potential barrier, separating the photocarriers and resulting in the appearance of the PPC.

In the present work, SI InP:Fe samples were used, with low resistance InP:Fe epilayers, (carrier concentration of 10^{16} cm^{-3}, and thickness of 0.5 μm). In our samples, the relaxation photoconductivity (PP) was measured as a function of the illumination time (photon dose) and the decay of PP as a function of time after switching off the light at the temperature of 300 K.

2. Experimental

Measurements were carried out on two SI-InP:Fe samples (carrier concentration $n = 2.68\times10^{8}$ cm^{-3} and resistivity $\rho = 1.0\times10^{7}$ Ω·cm), on which there was an InP:Fe layer of low resistivity and concentration 10^{16} cm^{-3} and with the thickness of 0.5 μm. Two orthogonal Au:Ge ohmic contacts were made, their separation amounting to 5 μm. The samples were placed in a cryostat, the window of which was closed with a Mylar sheet 25 μm thick.

The illumination system consisted of a small 250 W halogen lamp with an external elliptical mirror and a small computer controlled Oriel Optics Co monochromator. The illumination beam stroke incided vertically onto the surface where the contacts were made. For sample 1, light with the wavelength of $\lambda = 925.4$ nm was used, which corresponds to its energy gap, while for the sample 2 the wavelength of $\lambda = 850$ nm was used, which corresponds to the energy higher than the energy gap.

The photocurrent was measured with a Keithley electrometer at room temperature ($T = 300$ K).

3. Results and discussion

Before the PPC measurements, the specimens were heated in the dark to a temperature of 400 K in order to ensure that some of the photocarriers, created during the installation of the specimen in the cryostat, recombined. The photocurrent as a function of time for sample 1 is plotted in Fig. 1.

During the second hour of illumination, the photocurrent increased quickly to a maximum, at which the illumination was switched off. After the illumination was

switched off, the current was measured for an additional hour, and its value remained higher than the dark current before illumination.

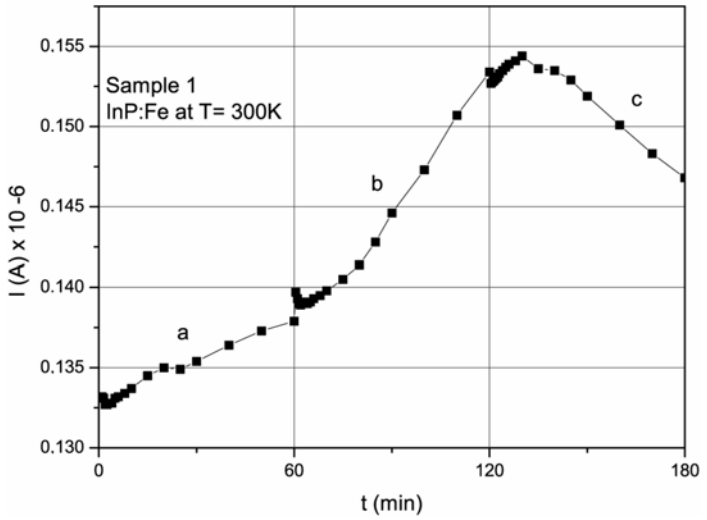

Fig. 1. Sample 1, current versus time: a) first hour, before any illumination, b) second hour, under illumination with λ = 925,4 nm, c) third hour, after illumination was switched off

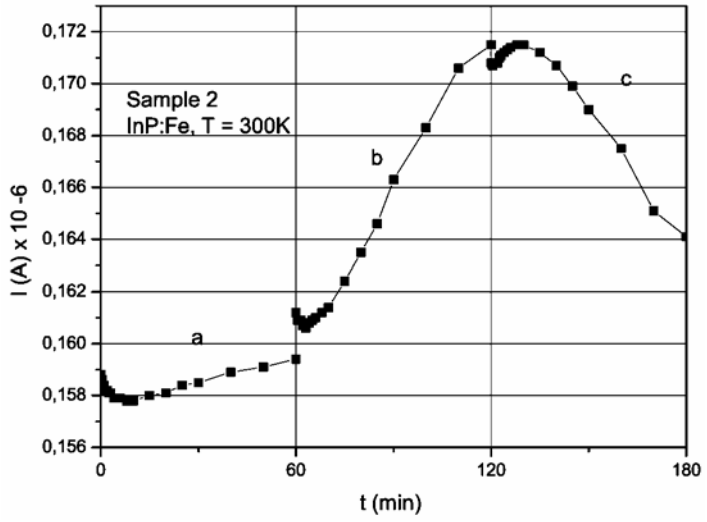

Fig. 2. Sample 2, current versus time: a) first hour, before any illumination, b) second hour, under illumination with λ = 850 nm, and c) third hour, after illumination was switched off

The photocurrent decay presents an obvious PPC, which can be attributed to the fact that electrons, excited by the substrate layer, are separated from their holes due to the presence of an internal electric field of the junction of the semiconductor layer

and high resistance semiconductor (substrate) [1]. A similar behaviour was observed for sample 2 (Fig. 2).

References

[1] GAUTHIER D., GOUTIERS B., PORTAL J.C., DMOWSKI L., RAZEGHI M., Semicond. Sci. Technol., 4 (1989), 220.
[2] ZHAO Y.-G., ZHAO G., BENSAADA A., MASUT R.A., Semicond. Sci. Technol., 7 (1992), 1359.
[3] TSUBAKI K., FUKUI T., SAITO H., J. Appl. Phys., 60 (1986), 3224.
[4] ZARDAS G.E., THEODOROU D.E., EUTHUMIOU P.C., SYMEONIDES CH.I., RIESZ F., SZENTPALI B., Solid State Commun., 105 (1998), 77.
[5] VAVILOV V.S., EUTHYMIOU P.C., ZARDAS G.E., Phys. Usp., 42 (1999), 199.

Received 23 September 2004
Revised 20 May 2005

Materials Science-Poland, Vol. 23, No. 4, 2005

Structure recognition in MD-simulated materials. A case study of BO_3 triangles in borate glasses

G. BERGMAŃSKI[1], M. BIAŁOSKÓRSKI[1, 2], M. RYCHCIK-LEYK[1], J. RYBICKI[1, 2*]

[1]Department of Solid State Physics, Faculty of Technical Physics and Applied Mathematics, Gdańsk University of Technology, Narutowicza 11//12, 80-952 Gdańsk, Poland

[2]TASK Computer Centre, Narutowicza 11/12, 80-952 Gdańsk, Poland

In computer simulations of the structure of matter, one usually obtains the Cartesian coordinates of all the particles involved. A non-trivial problem of structure recognition and characterization arises. In the present contribution, we study in detail the geometrical properties of a fuzzy-vertex CA_3 structural unit (C – cation, A – anion). Two deformation degree estimators are introduced and examined. The Monte Carlo-generated stochastic characteristics of fuzzy CA_3 triangles constitute conventional reference data that can be compared with the corresponding distributions calculated for a computer-simulated material. A quantitative estimation of the deformation degree of CA_3 units in the simulated structure can thus be obtained. We apply the methods developed to quantitatively characterize the geometry of BO_3 structural units in B_2O_3 glass.

Key words: *short-range order; shape parameters; molecular dynamics; borate glass*

1. Introduction

Computer simulations are widely used to calculate the structure of matter at the atomic level. The most common techniques are molecular dynamics (MD, e.g. [1–3]) and Monte Carlo (MC, e.g. [4, 5]) methods. At present, one can simulate fairly large systems, containing up to about 10^9 particles. Up to the date, structures of thousands of various materials have been simulated, including functional materials, very complex in their structure and behaviour. Computer technology development itself, however, does not automatically guarantee sufficiently good reliability of the simulation results. Even for relatively simple materials one encounters enormous difficulties in reproducing their correct structure.

*Corresponding author, e-mail: ryba@pg.gda.pl

The result of a direct MD simulation is a set of the Cartesian coordinates (and velocities) of all the particles versus time. A non-trivial problem of structure recognition arises. As far as the short-range ordering in the simulated material is concerned, it is often sufficient to analyse partial pair distribution functions (pPDF) together with angular distribution functions[*]. The detected structural units are often claimed vaguely to be more or less distorted, usually with little effort to provide a precise, quantitative characterization of the degree of distortion.

In the present contribution, we make a step towards the development of tools allowing a conventional quantitative characterization of the deformation degree of simple structural units appearing in computer-simulated material structures. We study in detail geometrical properties of a CA_3 structural unit (C – cation, A – anion), i.e. of a flat equilateral triangle with three anions in its vertices and a cation in the triangle's centre. In particular, we use the Monte Carlo method to obtain the distributions of AAA, ACA, and CAA angles in a fuzzy-vertex CA_3 unit, i.e. with random positions of anions, assumed to have uniform probability densities within spheres of radius r (the deformation amplitude), centred on the ideal vertex positions. We scan the interval $0 < r \leq r_{max}$, r_{max} being equal to 10% of the AA distance, with the step of 0.001. Moreover, two deformation degree estimators are introduced (cf. [12]), and the distributions of their values as functions of the deformation amplitude r are calculated. The MC-generated distributions constitute conventional reference data (obtained for a non-interaction purely stochastic geometry model) that can be compared with the corresponding distributions calculated for a computer-simulated material. A quantitative estimation of the deformation degree of CA_3 units in the simulated structure can thus be obtained. We apply the developed methods to quantitatively characterize the geometry of BO_3 structural units in B_2O_3 glass, simulated using an MD technique with three various inter-atomic potentials, each of them adequately reproducing the experimental short-range correlations. We show that the degree of deformation of the basic structural units appear to be highly potential-dependent.

Although B_2O_3 glass has been known for many years and has found numerous important practical applications (e.g., in optical fibre technology), its structure is still intensively studied, and several questions and doubts on B_2O_3 structure remain open. Goubeau and Keller [13] suggested that B_2O_3 glass consists of planar hexagonal B_3O_3 boroxyl rings interconnected by bridging oxygen atoms. Although Krogh-Moe [14] showed that several properties of borate glass are consistent with this model, its uniqueness has not been proven, and the existence of boroxyl rings has been seriously questioned. There is strong evidence from nuclear magnetic resonance (NMR) studies that each B atom is at the centre of an equilateral triangle having oxygen atoms in its corners [15]. Mozzi and Warren [16] have found their X-ray-extracted radial distribution functions to be fitted better by a model in which most of these triangles are or-

[*]There are other ways to characterise the local structure, such as the Voronoi polyhedra or Delunay simplexa techniques [6–11].

dered in flat boroxyl rings. Elliott [17] has calculated pPDFs from computer-simulated structures and concluded that the X-ray data can be better understood by a continuous random network (CRN) of BO_3 triangles (no boroxyl rings). In the opinion of Galeener et al. [18], borate glasses reveal fractions of both of the above-mentioned structural features. More recently, Swenson and Borjesson [19], using the reverse Monte Carlo modelling, have argued that a fraction of BO_3 triangles form deformed (not flat) boroxyl rings.

The paper is organized as follows. In Section 2, we investigate the stochastic geometry properties of fuzzy CA_3 structural units. In Section 3, we describe our MD simulations of B_2O_3 glass and apply the developed tools to analyse the structure of BO_3 units. Section 4 contains concluding remarks.

2. Geometric properties of fuzzy CA_3 triangles

The actual displacements of atoms from their ideal positions are correlated within a thermally vibrating unit and influenced in a complicated way by the instantaneous configurations of neighbouring atoms. Thus, the realistic generation of reference data is quite difficult and we have used a very simple, non-interaction model of vortex displacements, viz. a uniform probability distribution within a sphere centred on the ideal (equilibrium) anion position.

An equilateral triangle with the fourth site in its geometrical centre was repeatedly distorted at random: vortices were shifted at random within spheres of radii equal to a fraction r of the ideal AA distance, whereas the C-site position remained fixed. 10^7 distorted polyhedra were generated in order to calculate the distributions of the AAA, ACA, and CAA angles and the distortion parameters, Tr_1 and Tr_2 (defined below). Such Monte Carlo calculations were performed for a series of subsequent values of r, varying with a step of $\Delta r = 0.001$ from zero to $r_{max} = 0.1$ of the AA distance. The AAA, ACA, and CAA angular distributions in fuzzy-vertex CA_3 units for several values of the deformation amplitude r are shown in Figure 1.

Let us consider the central tendencies of the AAA, ACA, and CAA angular distributions. The arithmetic mean $\overline{x}$, for the frequency distribution f_i of finding values of x_i is defined as $\overline{x} = \sum_{i=1}^{k} x_i f_i \Big/ \sum_{i=1}^{k} f_i$, where k is the number of classes of x values. The variance of x is expressed as $\sigma^2 = \overline{x^2} - \overline{x}^2$ and measures the dispersion of the distribution values around the mean value. The shape of the distributions shape can be characterised by the Fischer asymmetry coefficient β and the Pearson coefficient of kurtosis K:

$$\beta = \frac{\sum_{i=1}^{k} \left(x_i - \overline{x}\right)^2 f_i}{\left(\sum_{i=1}^{k} f_i\right)\sigma^3}, \qquad K = \frac{\sum_{i=1}^{k} \left(x_i - \overline{x}\right)^4 f_i}{\left(\sum_{i=1}^{k} f_i\right)\sigma^4} \tag{1}$$

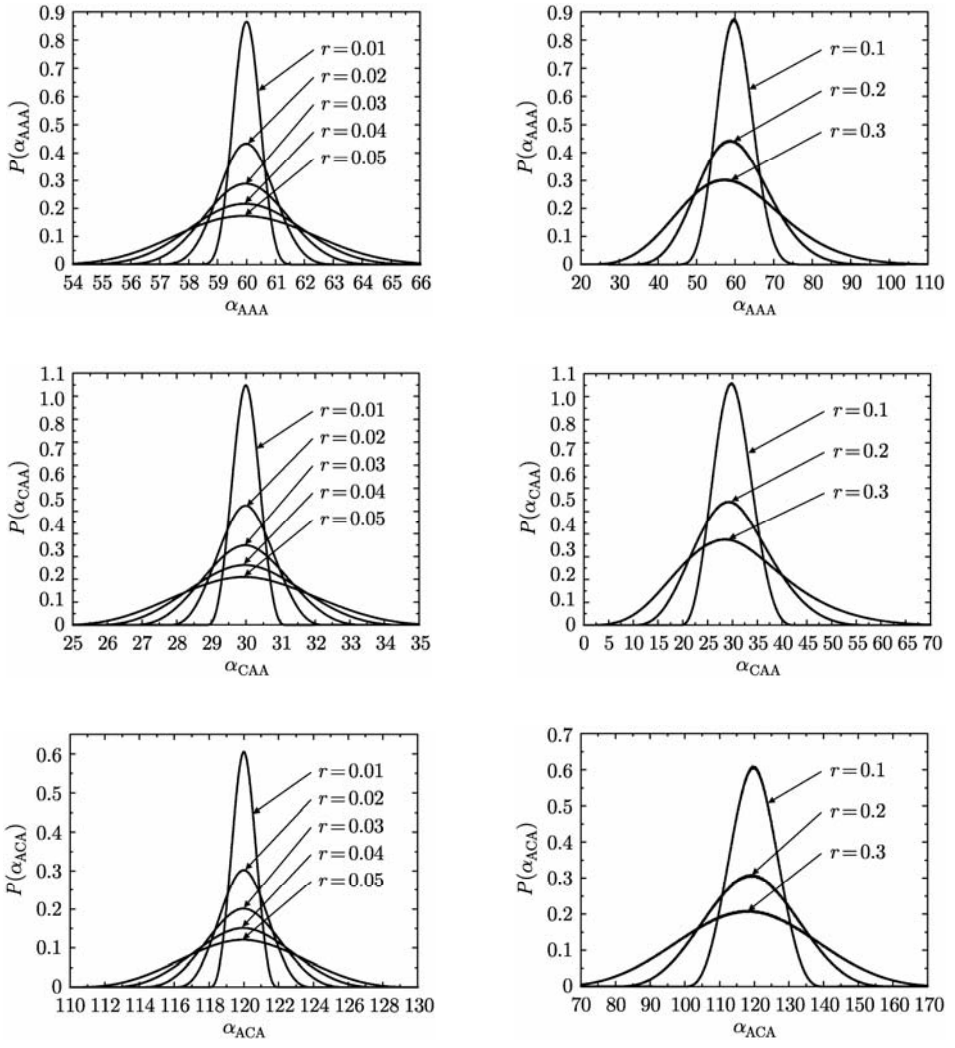

Fig. 1. Probability densities $P(\alpha)$ for the AAA, CAA, and ACA angular distributions

The β parameter is zero for symmetric distributions. The higher the absolute value of β, the higher is the degree of asymmetry. Positive and negative values of β correspond to distributions with a right and left asymmetry, respectively. The K parameter measures the deviation of a given distribution from the normal distribution. For exactly normal distributions, $K = 3$. For $K \in (0,3)$, the analysed distribution is platicurtic, i.e. flatter than the normal distribution, while for $K \in (3,\infty)$ it is leptokurtic, i.e. more peaked than the normal distribution. The r-dependences of the mean values of the AAA, ACA, and CAA angular distributions, their variances, and Fisher and Pearson parameters are shown in Figure 2.

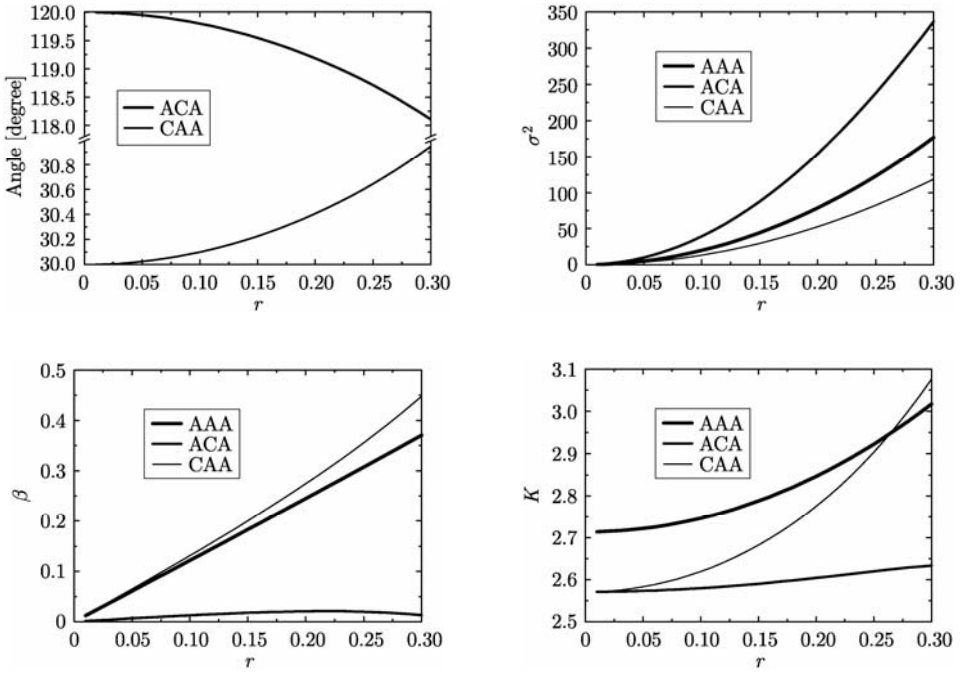

Fig. 2. Central tendencies of the probability densities $P(\alpha)$ for the angular distributions AAA, ACA and CAA for which vertices (A-sites) assume random positions within 3D spheres with uniform probability. Upper left: mean angle, upper right: angle variance, lower left: the Fischer asymmetry coefficient β, lower right: the Pearson coefficient of kurtosis K. The mean value of the AAA angle is r-independent and equal to 60°

In order to measure the overall degree of deformation of CA_3 triangles, we define two estimators (cf. [12]):

$$Tr_1 = \frac{\sum_{i=1}^{3} (\bar{l}_{A-A} - l_{A-A,i})^2}{3\bar{l}_{A-A}^2} \tag{2}$$

and

$$Tr_1 = \frac{\sum_{i=1}^{3} (\bar{l}_{A-A} - l_{A-A,i})^2}{3\bar{l}_{A-A}^2} + \frac{\sum_{i=1}^{3} (\bar{l}_{C-A} - l_{C-A,i})^2}{3\bar{l}_{C-A}^2} \tag{3}$$

where $\bar{l}_{A-A}$ and $\bar{l}_{C-A}$ denote the average AA and CA distances, whereas $\bar{l}_{A-A,i}$ and $\bar{l}_{C-A,i}$ the actual lengths of the i-th AA sides and CA distances, respectively. The above deformation estimators are zero for a regular (ideal) geometry and positive for deformed structures. MC simulation results for the CA_3 unit are shown in Figure 3.

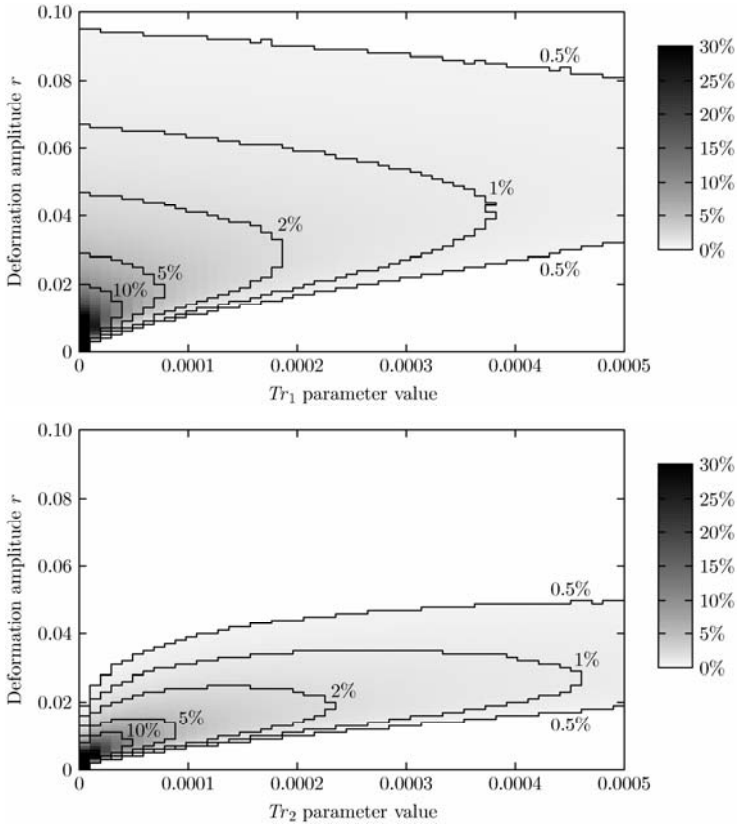

Figure 3. Distributions of Tr_1 and Tr_2 parameter values in the function of the anion shift amplitude

In order to see whether the CA_3 triangles are flat, a simple additional parameter, $\bar{H}$, has been introduced. $\bar{H}$ is defined as the average distance from the central cation to the plane spanned by the three neighbouring anions. The lower $\bar{H}$ is, the flatter the CA_3 unit. The dependences of $T\bar{r}$ and $\sigma^2(Tr)$ are shown in Figure 4. The mean values of the distributions of Tr_1 and Tr_2 depend on r approximately quadratically, i.e. as ar^{α}, where α is close to 2 (up to about 0.01), whereas the coefficient a assumes the values of 0.20 and 0.58 for Tr_1 and Tr_2, respectively. The variances follow a cr^{γ} dependence with γ close to 4 (up to about 0.03), while the coefficient c equals 0.03 and 0.18 for Tr_1 and Tr_2, respectively. The r-dependences of β and K are linear:

$$\beta_{Tr1} = 0.72 + 0.35r, \qquad K_{Tr1} = 3.50 + 0.32r$$

$$\beta_{Tr1} = 0.52 + 0.40r, \qquad K_{Tr2} = 3.21 + 0.66r$$

The mean value of the parameter H related to CA_3 triangles, $\bar{H}$, also depends linearly on r, according to $\bar{H}(r) = 0.21r$, where 0.21 is an empirical MC coefficient.

Having a numerically simulated structure of a particular material at one's disposal (in the present case, B_2O_3 glass structure from a molecular dynamics simulation), it is possible to calculate the values of estimators and angles for all the BO_3 units detected within the simulation box and construct the corresponding histogram of the occurrence frequencies of these values. Data obtained in this way, however, are difficult to interpret quantitatively. In order to enable such an interpretation, the properties of the angular distributions and deformation degree estimators were studied separately (independently of any physical system), providing reference data, which is presented in proceeding paragraphs. A comparison of the distributions of estimators and angles for a given numerically simulated material with the above reference makes it possible to quantitatively characterize the degree of disorder in a material structure obtained from a simulation.

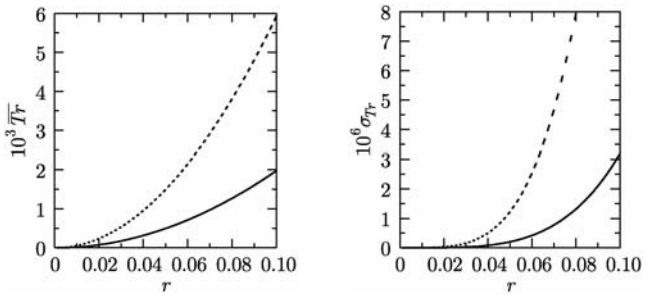

Fig. 4. The r-dependence of the distributions $\overline{Tr}_1$ and $\sigma^2(Tr_1)$ (solid lines) as well as $\overline{Tr}_2$ and $\sigma^2(Tr_2)$ (dashed lines)

A quantitative evaluation of the deformation degree of the simulated CA_3 triangles can be realised in the following steps:

- Calculating the distribution (histogram) of the values of estimators and angles for all the structural units detected in a numerically generated solid (i.e., for the MD simulation, the results of which are to be analysed). For this distribution, one can calculate its average value, standard deviation, asymmetry parameters (e.g. the Fisher parameter), and the Pearson kurtosis parameter.
- Minimum-square fitting of the Monte Carlo-generated distributions of estimators and angles (with the reference data described above) to the corresponding distribution obtained from a structure simulation yields the optimal value of r, $r_{\min} = q$. Mean values, standard deviations, and the Fisher and Pearson parameters obtained for the reference data and those obtained from structural simulations can also be compared.

Conclusions emerging from such comparisons may be that the overall deformation degree of a structural unit AC_3 appearing in our MD structural simulation is effectively the same as that of the unit with fuzzy vertices, i.e. assuming random positions within spheres of radius q (with a uniform probability density). Thus, our procedure provides a conventional quantitative characterization of the deformation degree of basic structural units obtained in structural simulations.

3. BO_3 units in borate glasses – results of the simulation and discussion

Our MD simulations of borate glasses have been performed in the microcanonical ensemble (NVE) using the *mdsim* code [20]. The number of atoms within a cubic simulation box with periodic boundary conditions amounted to 5000. The glasses of 1800 kg/m^3 density were initially prepared in a well equilibrated molten state at 10 000 K, then cooled down to 300 K at an average rate of $2 \cdot 10^{13}$ K/s, passing equilibrium states at 8000 K, 6000 K, 5000 K, 4000 K, 3000 K, 2500 K, 2000 K, 1500 K, 1000 K, and 600 K. Temperature scaling was applied whenever the rolling average of temperature (calculated over the last 100 time steps) went out of the $(T - \Delta T, T + \Delta T)$ interval. At each intermediate temperature, the system was equilibrated during 30 000 fs time steps, using ΔT = 100 K for $T \geq 1000$ K, ΔT = 20 K for T = 600 K, and ΔT = 10 K for 300 K. Equilibrated systems were sampled during 10 000 fs time steps.

Three various force field models were applied: that of Takada et al. [21, 22] (I), Xu et al. [23] (II), and Soules [24] (III). All the above-cited interaction potentials are of the Born–Meyer–Huggins type (with full ionic charges) and have been parameterised to reproduce the short-range structure inferred from experimental investigations.

One can calculate the angular OOO, OBO, and BOO distributions and the distributions of the parameters Tr_1 and Tr_2 (and various characteristics of the obtained distributions, such as central tendencies and standard deviation) for MD-simulated structures. For a complete quantitative analysis, however, one should compare the MD-extracted data for BO_3 triangles with the reference data presented in Section 2.

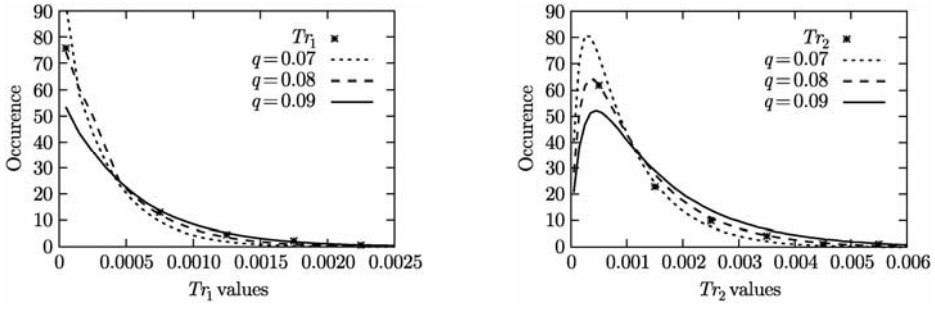

Fig. 5. Example MD-extracted distributions of the Tr_1 and Tr_2 parameters (potential (I) simulation), compared with the best-fit (q = 0.08) model Monte Carlo reference data. The Monte Carlo reference data for r = 0.07 and r = 0.09 are shown for comparison

Cation–anion adjacency graphs have been constructed with a cut-off distance on the B–O bond length equal to R_{cut} = 1.87 A, common to all the simulations. In the final structures obtained with force field (I), 99.9% of the B atoms have a three-fold oxygen co-ordination, whereas the (II) and (III) force fields produced structures with 97.75% and 99.6% of the B cations with three oxygen neighbours, respectively. Shape analysis has been performed on all of the BO_3 triangles found.

The analysis of the distributions of the Tr_1 and Tr_2 parameters consisted of their calculation for all the BO_3 triangles found in the simulated atomic configurations and of a minimum-square fitting to the Monte Carlo-generated reference data. In Figure 5, we have shown an example of MD-extracted distributions of the parameters Tr_1 and Tr_2 (for potential (III)), compared with the best-fit Monte Carlo reference data.

BO_3 units are the most deformed in structures obtained using potential (I) (the best-fit *r*-value, $q = 0.08$, $\bar{H} \approx 0.07$ Å). The most regular BO_3 triangles were obtained with interaction model (II) ($q = 0.03$, $\bar{H} \approx 0.05$ Å). Interaction model (III) yielded rather irregular BO_3 units, with $q = 0.045$ and $\bar{H} \approx 0.07$ Å.

All of the $\bar{H}_{MD}$ values have been compared with theoretically calculated $\bar{H}_{MC} = 0.21q$ values (Monte Carlo reference data). For all the cases, the $\bar{H}_{MD}$ values exceeded significantly the corresponding $\bar{H}_{MC}$ values. This means that the distance of B atoms from the oxygen plane is due to a structural deformation (low BO_3 pyramids) rather than from oxygen thermal vibrations of the flat BO_3 triangle.

Table 1. The *q* values obtained from fitting the Monte Carlo reference data of the angular distribution functions and the Tr_1 and Tr_2 parameters to the MD data obtained with potentials (I), (II), and (III). The fitting error does not exceed 0.005

Potential	OOO angles	OBO angles	BOO angles	Tr_1	Tr_2
(I)	0.07	0.08	0,07	0.08	0.08
(II)	0.02	0.03	0.03	0.03	0.03
(III)	0.05	0.05	0.05	0.04	0.05

The angular distribution functions for OOO, OBO, and BOO triples were also calculated for the MD-simulated structures and compared with the reference MC data. The best-fitting procedure yielded the *q* values listed in Table 1. Almost the same deformation amplitudes can be inferred by comparing the MD data with Monte Carlo reference data of the Tr_1 and Tr_2 parameters or of the AAA, ACA, and CAA angular distributions (A = O, C = B).

4. Concluding remarks

In this brief contribution, we have made a step towards developing useful tools that allow a conventional quantitative characterization of the deformation degree of the simple structural unit CA_3, which often appears in computer-simulated material structures. We have presented Monte Carlo reference data relative to angular AAA, ACA, and CAA distributions and deformation estimator value distributions in fuzzy vertex CA_3 triangles. The usefulness of MC reference data for characterising the degree of deformation of BO_3 structural units in MD-simulated B_2O_3 glass is demonstrated.

In MD simulations realised with three different parameterisations of the Born-Meyer-Huggins potential, almost all B atoms are at the centre of an equilateral triangle having an oxygen atom at each corner. A comparison of the MD-simulated OOO, OBO, and BOO angular distributions and distributions of the deformation estimator values with reference MC data for fuzzy vertex CA_3 triangles yielded the following quantitative characteristics for BO_3 units in borate gasses. The most regular BO_3 triangles were obtained using interaction model (II) ($q \approx 0.03$, $\bar{H} \approx 0.05$ A), less regular for interaction model (III) ($q \approx 0.045$, $\bar{H} \approx 0.07$ A), and the most distorted units were obtained for potential parameters (II) ($q \approx 0.08$, $\overline{H} \approx 0.07$ A). Such a high value of $\bar{H}$ for all potentials was classified as structural deformation, as $\overline{H_{MD}} > \overline{H_{MC}}$. The results described above mean that the overall deformation degrees of a structural unit BO_3 appearing in our MD structural simulation are effectively the same as for the unit with fuzzy vertices, which assumes random positions (with uniform probability density) within spheres of radii equal to 8%, 3%, and 4.5% of the mean OO distance for force fields (I), (II), and (III), respectively. Finally, it should be noted that the overall deformation degree of the BO_3 units inferred from the analysis of angular distributions and from the *Tr* estimator distributions are essentially the same, therefore practically it is sufficient to analyse only the angular correlations or deformation estimator distributions.

Acknowledgements

The MD simulations were performed at the TASK Supercomputer Centre (Gdańsk, Poland). The work was partially sponsored by the Polish Committee for Scientific Research, under grant numbers 7T11F01321 and 4T11F01925.

References

[1] ALLEN M.P., TILDESLEY D. J., *Computer Simulation of Liquids*, Clarendon Press, Oxford, 1987.
[2] HOCKNEY R.W., EASTWOOD J.W., *Computer Simulation Using Particles*, McGraw-Hill, 1987.
[3] RAPAPORT D.C., *The Art of Molecular Dynamics Simulations*, Cambridge University Press, 1995.
[4] *Monte Carlo Methods in Statistical Physics*, K. Binder (Ed.), Springer-Verlag, Berlin, 1979.
[5] BINDER K., HEERMAN D.W., *Simulation in Statistical Physics*, Springer-Verlag, Berlin, 1988.
[6] FINNEY J.L., Proc. R. Soc. London, A3 (1970), 19 479; ibid A3 (1970), 19 495.
[7] BROSTOW W., DUSSAULT J-P., FOX B.L., J. Comput. Phys., 29 (1978), 81.
[8] TANEMURA M., OGAWA T., OGITA N., J. Comput. Phys., 51 (1983), 191.
[9] MEDVEDEV N.N., J. Comput. Phys., 67 (1986), 223.
[10] BROSTOW W., CHYBICKI M., LASKOWSKI R., RYBICKI J., Phys. Rev., B 57 (1998), 13448.
[11] LASKOWSKI R., TASK Quart., 4 2000), 531.
[12] BERGMAŃSKI G., BIAŁOSKÓRSKI M., RYBICKI J., FELIZIANI S., phys. status sol. (b), 242 (2004), 519.
[13] GUBEAU J., KELLER H., Z. Anorg. Chem., 272 (1953), 303.
[14] KROGH-MOE J., J. Non-Cryst. Solids, 1 (1969), 269.
[15] SILVER A H., BRAY P.J., J. Phys. Chem., 29 (1958), 984.
[16] MOZZI R.L., WARREN B.E., J. Appl. Crystallogr., 3 (1970), 251.
[17] ELLIOTT S.R., Phil. Mag., B37 (1978), 435.

[18] GALEENER F.L., LUCOVSKY G., MIKKELSEN J.C. Jr., Phys. Rev. B22 (1980), 3983.
[19] SWENSON J., BORJESSON L., Phys. Rev., B55(1997), 11138.
[20] ALDA W., 2003, http://www.task.gda.pl/nauka/software/.
[21] TAKADA A., CATLOW C.R.A., PRICE G.D., J. Phys. Condens. Matter,7 (1995), 8659.
[22] TAKADA A., CATLOW C.R.A., PRICE G.D., J. Phys. Condens. Matter, 7 (1995), 8693.
[23] XU Q., KAWAMURA K., YOKOKAWA T., J. Non-Cryst. Solids, 104 (1988), 261.
[24] SOULES T.F., J. Chem. Phys., 73 (1980), 4032.

Received 8 December 2004
Revised 3 April 2005

Materials Science-Poland, Vol. 23, No. 4, 2005

FMR study of agglomerated nanoparticles in a Fe_3C/C system

N. GUSKOS[1, 2*], J. TYPEK[2], M. MARYNIAK[2],
U. NARKIEWICZ[3], I. KUCHAREWICZ[3], R. WRÓBEL[3]

[1]Solid State Section, Department of Physics, University of Athens,
Panepistimiopolis, 15 784 Zografos, Athens, Greece

[2]Institute of Physics, Szczecin University of Technology, al. Piastów 17, 70-310 Szczecin, Poland

[3]Institute of Chemical and Environment Engineering,
Technical University of Szczecin, al. Piastów 17, 70-310 Szczecin, Poland

Three samples with various Fe_3C/C ratios have been prepared by the carburisation of iron with ethylene or an ethylene–hydrogen mixture. Carburisation was controlled with thermogravimetry. After carburisation, the samples were characterized using XRD and scanning electron microscopy. XRD measurements have shown the presence of the Fe_3C (cementite) phase only. The mean size of cementite crystallites estimated using Scherrer's equation was in the range of 40–46 nm. Ferromagnetic resonance (FMR) absorption signals were investigated at room temperature. In all samples an asymmetric, very broad, and intense FMR line shifted toward low magnetic field was recorded. The linewidth, intensity, and position of the resonance field depended strongly on carbon concentration. With increasing carbon concentration the linewidth and integrated intensities of the FMR spectra decreased, and the resonance line shifted towards higher magnetic fields. The separation of granules from each other by carbon could drastically influence the FMR absorption spectrum due to decreasing intergranular interaction with increasing carbon concentration.

Key words: *magnetic resonance; nanoparticle; cementite*

2. Introduction

Carbon–iron based nanoparticles are of growing interest due to their improved magnetic properties as well as their potential applications in catalysis, sensor techniques, and the potential reduction of costs required to produce bulk quantities of these products [1–5]. In particular, nanocomposites of iron carbides, such as the ce-

*Corresponding author, e-mail: ngouskos@cc.uoa.gr

mentite phase (Fe_3C), are further suited to diverse technological exploitation due to their enhanced mechanical properties [6] and importance in ferrous metallurgy [7]. Meanwhile, Fe_3C nanoparticles were found to be more resistant to oxidation than α-Fe nanoparticles due to the formation of amorphous carbon layers on their surfaces [1, 2].

Ferromagnetic resonance (FMR) has been long exploited to measure the magnetocrystalline anisotropy of magnetite single crystals as a function of temperature [8], as well as the shift of the FMR spectra of polycrystalline Fe_3O_4 as a function of oxidation below the Verwey transition [9], and to identify fine-grained iron and iron oxide precipitates in natural glasses [10–12] and coal minerals [13]. More recently, FMR has emerged as a powerful and sensitive method to characterize magnetic nanoparticles. It relies mainly on the averaging effect of superparamagnetism on the FMR spectra of an assembly of non-interacting single domain nanoparticles, characterized by an orientation distribution of local anisotropy axes [14–21]. Relatively narrow FMR lines have been commonly observed in the high temperature regime in either dilute suspensions of iron-based oxide nanoparticles in ferrofluids [14] or dispersed in glass [13] or polymer matrices [20]. A narrow resonance line is considered as a fingerprint of superparamagnetic resonance at high temperatures, where thermal fluctuations partially average orientation distributions of local anisotropy fields, which become important at lower temperatures and lead to resonance line shapes similar to the FMR of polycrystalline systems [14–16]. In the case of iron non-oxide systems (e.g. α-Fe or Fe_3C) with strong exchange interactions, a very intense broad resonance line is observed [17, 18]. The FMR spectrum of nanoparticle agglomerates of iron carbide in a carbon matrix strongly depends on the concentration of magnetic nanoparticles.

The aim of this work is to study the FMR spectra of three samples differing in their Fe_3C/C ratio. The separation of iron carbide granules by carbon could influence the FMR absorption spectrum through intergranular and intermolecular interactions that vary with carbon concentration.

2. Experimental

Three samples with various cementite to carbon ratios (sample I – 1:0, sample II – 1:1, and sample III – 1:3) have been prepared by the carburisation of nanocrystalline iron with an ethylene–hydrogen mixture (sample I) or with pure ethylene (samples II and III).

The fusion of magnetite with small amounts of promoter oxides (Al_2O_3 and CaO) has been used for obtaining nanocrystalline iron. The obtained material was crushed, sieved (to obtain the fraction 1.2-1.5 mm), and reduced under hydrogen. After reduction, the obtained pyrophoric sample was cooled to room temperature and passivated under nitrogen with traces of oxygen, in order to avoid dramatic oxidation in contact with air.

The chemical compositions of samples were determined using an inductively coupled plasma atomic emission spectroscope (AES-ICP). Beside iron, the samples con-

tained about 3 wt. % of both Al_2O_3 and CaO. The average size of iron crystallites, determined using X-ray diffraction (Philips X'Pert equipment, $CoK_{\alpha 1}$ radiation) and calculated using Scherrer's equation, amounted to 17 nm. The specific surface area of the samples, determined by the thermal desorption of physisorbed nitrogen (ASAP 2010, Micromeritics), was 22 m^2/g.

The carburisation process was monitored using a thermogravimetric method. The grains of the sample (0.5 g) were placed as a single particle layer in a platinum basket hung in a thermobalance and changes in the mass of the sample were recorded. Before carburisation, the samples were reduced (in order to remove the passivation layer) at temperatures rising from 293 to 773 K under a hydrogen flow. After achieving the reduction process (when a constant mass of the sample was maintained), carburisation was started through the addition of ethylene to hydrogen (sample I) or through a replacement of hydrogen by ethylene (sample II and III). A gas flow of 1.3 $dm^3 \cdot g^{-1} \cdot min^{-1}$ was applied at a constant temperature of 673 K. An increase in the mass of the sample during the process was recorded, and when a determined degree of carburisation was reached the process was stopped by rapidly cooling the sample in a nitrogen atmosphere. After carburisation the samples were characterised by XRD (Philips X'Pert equipment, $CoK_{\alpha 1}$ radiation) and SEM (digital scanning electron microscope Zeiss LEO).

The FMR measurements were carried out at room temperature, using a Bruker 500 D spectrometer working in the X-band (ν = 9.43 GHz) at a 100 kHz magnetic field modulation. The samples, each containing around 10 mg of the material, were placed into 4 mm diameter quartz tubes.

3. Results and discussion

The relative change of the mass of the samples during carburisation, expressed as the ratio of carbon to iron carbide mass, is presented in Figure 1. The first sample was carburised under an ethylene:hydrogen 1:3 mixture until the mass increase equivalent to the formation of iron carbide (Fe_3C – 0.072 g C/g Fe) was reached (TG 1). Then the ethylene/hydrogen mixture was replaced by nitrogen and the heating of the reactor was stopped. The carburisation of the second sample was carried out under pure ethylene and to a higher carburisation degree – in order to obtain a mass increase equal to 0.154 g C/g Fe (TG 2). The same procedure was repeated to obtain the third sample, containing 0.328 g C/g Fe (TG 3).

The XRD spectra of the samples after carburisation are shown in Figure 2. Under the conditions of the experiments, no α-Fe peaks were detected for any of the samples. The non-marked peaks in the spectra correspond to the Fe_3C phase. The mean crystallite size of the obtained iron carbide, calculated using the Scherrer equation, was found to be in the range of 40–46 nm.

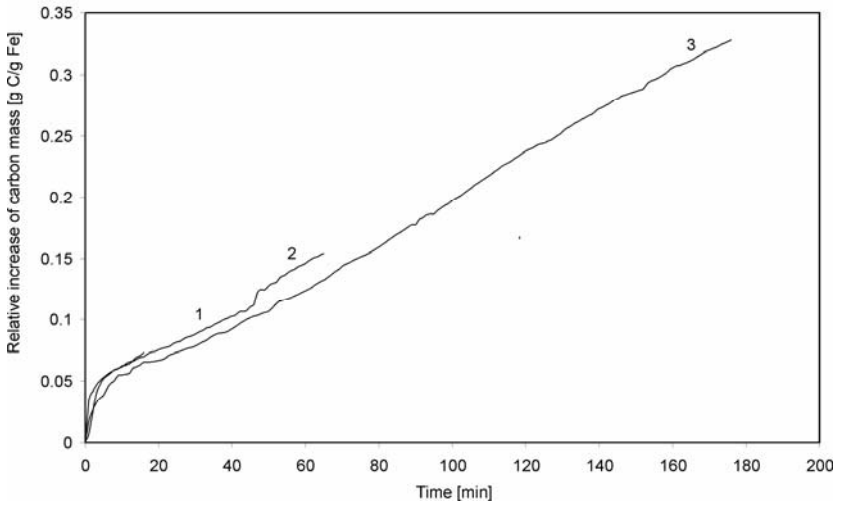

Fig. 1. TG curves of the carburisation process of nanocrystalline iron at 400 °C:
1 – carburisation under an ethylene–hydrogen mixture (1:3) up to 0,072 g C/g Fe,
2 – carburisation under pure ethylene up to 0,154 g C/g Fe,
3 – carburisation under pure ethylene up to 0,328 g C/g Fe

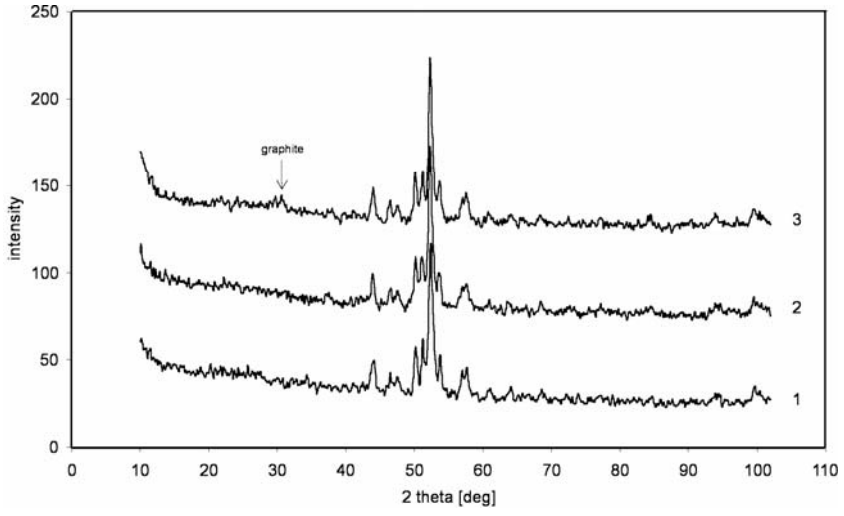

Fig. 2. XRD spectra of samples I–III after carburisation

The intensity of Fe_3C peaks in all the investigated samples is approximately the same. The amount of carbon in the samples is different, however, and samples II and III contain free carbon. It is difficult to distinguish the peak of graphite at $2\theta = 30°$ in the diffraction pattern No. 2. This peak can be observed only in the case of the most carburised sample (diffraction pattern No. 3). Even in this case the peak of graphite is weak and wide, indicating the formation of very fine crystallites of graphite.

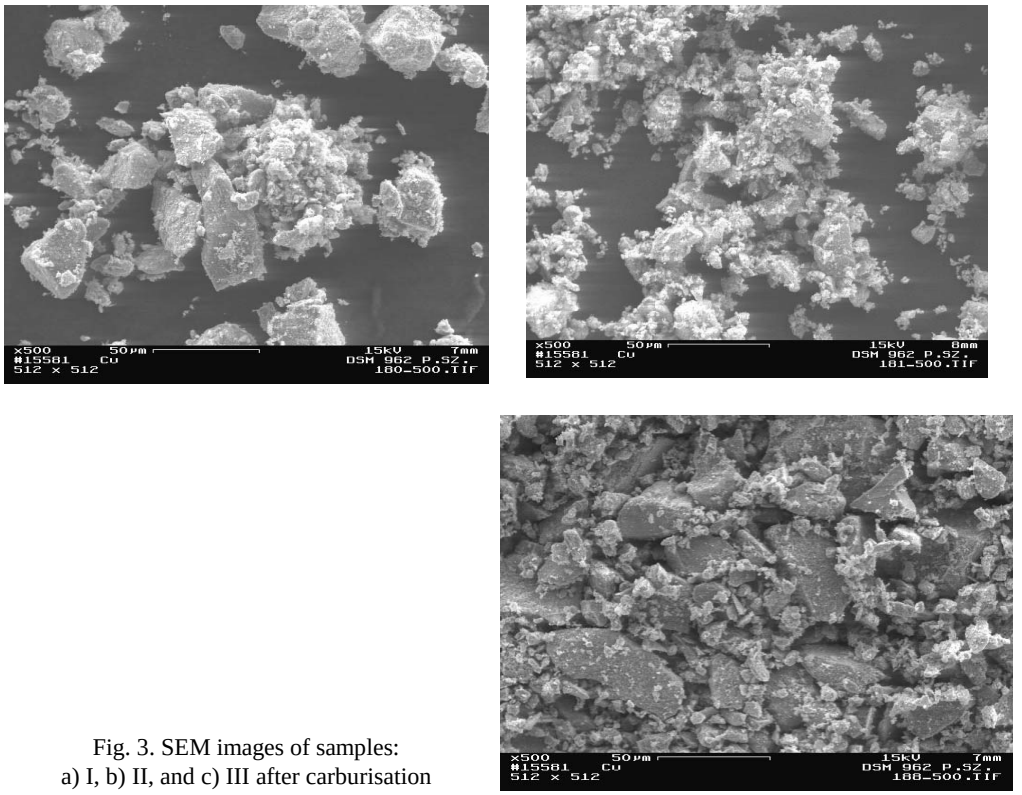

Fig. 3. SEM images of samples:
a) I, b) II, and c) III after carburisation

SEM images of the samples are presented in Figure 3. The resolution does not allow final conclusions to be drawn about the form of carbon deposits on the sample surface. There are insignificant differences between the SEM images of the samples, which is not astonishing taking into account that the SEM technique concerns only the morphology of the surfaces of grains and that carbon deposits form mainly inside the porous grain. The initial material is very porous (about 50%) and each grain of the sample is composed of fine iron crystallites 17 nm in diameter. After the reaction, carbon deposits form on the surface of each iron crystallite (transformed into iron carbide crystallite as a result of the reaction).

The strongly magnetic materials Fe_3C and Fe_3C/C were forced into the rigid state by a special procedure involving a non-magnetic material in a quartz tube. Before FMR measurements were performed, the samples had been magnetized several times in a steady magnetic field up to 1.6 T. This process allowed the same FMR spectra to be recorded, independent of whether the magnetic field is swept with increasing or decreasing values. This is especially important for the low-magnetic-field part of the FMR spectrum, where the line position displays a large shift (shifts to higher magnetic fields in the case of a sweep with increasing values). Figure 4 presents the FMR spectra for the investigated samples for an increasing and decreasing sweep of the applied magnetic field. Very intense and strongly asymmetric absorption lines, shifted

in the direction of low magnetic fields, were obtained. It was observed that for samples with an increased carbon concentration the intensity of the FMR spectrum decreased, while the position of the resonance line shifted to higher magnetic fields.

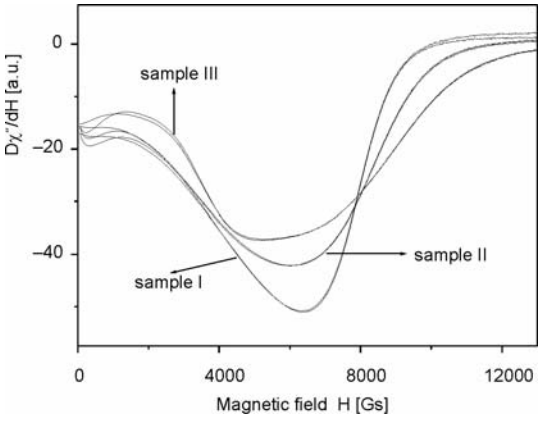

Fig. 4. The FMR spectra of iron carbide with different carbon concentrations at room temperature. Each spectrum is swept toward increasing and decreasing values of the applied magnetic field

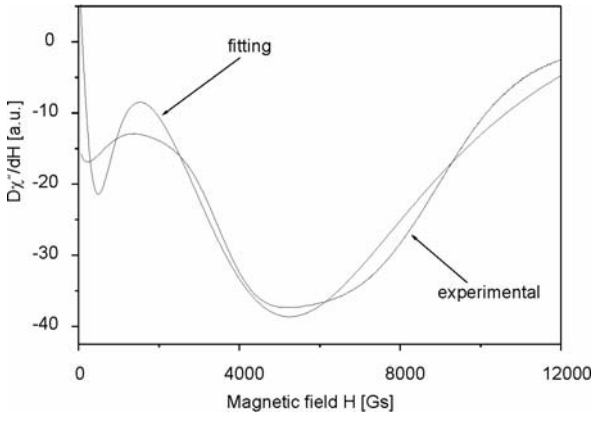

Fig. 5 The fitted and experimental FMR spectra of sample I

As a first approach, a rough fitting of the extended FMR signal was performed using the Lorentzian-type curves, taking into account the absorption at both H_r and $-H_r$ magnetic fields, induced by the two oppositely rotating components of the linearly polarised rf field. The FMR spectra for all samples were satisfactory fitted with two Lorentzian curves, having resonance magnetic fields near zero and at higher values (Fig. 5). Table 1 shows the obtained values of the resonance field H_r, the peak-to-peak linewidth ΔH, and integrated intensity I_{int} ($I_{\text{int}} = A\Delta H^2$, where A is the signal amplitude). With an increase of the carbon concentration, the resonance field of the main line strongly shifts to higher magnetic fields, while the linewidth and intensity de-

crease. The shift of the resonance field is connected to the strong ferromagnetic interaction between agglomerates. As the carbon concentration increases, the separation between agglomerates increases and the magnetic interaction decreases. The internal field produced by neighbouring magnetic dipoles is averaged due to the spherical symmetry of the environment. The broadening of the FMR line is caused by dipole –dipole interaction, which has the largest influence on the spectra.

Table 1. The values of FMR spectra parameters
for the three studied samples of iron carbide with different carbon concentrations

Sample	Resonance field H_r [Gs]	Linewidth ΔH_1 [Gs]	Linewidth ΔH_2 [Gs]	Relative intensity I_1 [a. u.]
I	2660(10)	11900(10)	3270(10)	10.9
II	2832(10)	10740(10)	2140(10)	5.9
III	2990(10)	9050(10)	3270(10)	3.9

In conclusion, three samples of iron carbides, with various carbon concentrations, have been prepared. The carbon concentration had a strong influence on the observed FMR spectra of all samples. The ferromagnetic interaction between agglomerates strongly decreases with increasing carbon concentration.

Acknowledgements

This work was partially supported by the grant PBZ-KBN-095/TO8/2003.

References

[1] BI X-X., GANGULY B., HUFFMAN G.P., HUGGINS F.E., ENDO M., EKLUND P.C., J. Mater. Res., 8 (1993), 1666.
[2] ZHAO X.Q., LIANG Y., Z.HU Q., LIU B.X., J. Appl. Phys., 80 (1996), 5857.
[3] GRIMES C.A., HORN J.L., BUSH G.G., ALLEN J.L., EKLUND P.C., IEEE Trans. Magn., 33 (1997), 3736.
[4] GRIMES C.A., QIAN D., DICKEY E.C., ALLEN J.L., EKLUND P.C., J. Appl. Phys., 87 (2000), 5642.
[5] DENES F.S., MANOLACHE S., MA Y.C., SHAMAMIAN V., RAVEL B., PROKES S., J. Appl. Phys., 94 (2003), 3498.
[6] GOODWIN T.J., YOO S.H., MATTEAZZI P., GROZA J.R., Nanostruct. Mater., 8 (1997), 559.
[7] YUMOTO H., NAGAMINE Y., NAGAHAMA J., SHIMOTOMAI M., Vacuum, 65 (2002), 527.
[8] PSARRAS G.C., MANOLAKAKI E., TSANGARIS G.M., Composites A, 34 (2003), 1187.
[9] BICKFORD L.R., Phys. Rev., 78 (1950), 449.
[10] SHARMA V.N., J. Appl. Phys., 36 (1965), 1450.
[11] GRISCOM D.L., FRIEBELE E. J., SHINN D. B., J. Appl. Phys., 50 (1979), 2402.
[12] GRISCOM D.L., IEEE Trans. Magn. MAG, 17 (1981), 2718.
[13] GRISCOM D.L., J. Non-Crystalline Solids, 67 (1984), 81.
[14] MALHOTRA V.M., GRAHAM W.R.M., J. Appl. Phys., 57 (1985), 1270.
[15] SHARMA V.K., WALDNER F., J. Appl. Phys., 48 (1977), 4298.
[16] DE BIASI R.S., DEVEZAS T.C., J. Appl. Phys., 49 (1978), 2466.

[17] NARKIEWICZ U., GUSKOS N., ARABCZYK W., TYPEK J., T BODZIONY., KONICKI W., GASIOREK G., KUCHAREWICZ I., ANAGNOSTAKIS E.A., Carbon, 42 (2004), 1127.
[18] GUSKOS N., ANAGNOSTAKIS E.A., TYPEK J., BODZIONY T., NARKIEWICZ U., Mol. Phys. Rep., 39 (2004), 58.
[19] GUSKOS N., TYPEK J., NARKIEWICZ U., MARYNIAK M., AIDINIS K., Rev. Adv. Mater. Sci., 8 (2004), 10.
[20] BODZIONY T., GUSKOS N., TYPEK J., ROSLANIEC Z., NARKIEWICZ U., MARYNIAK M., Rev. Adv. Mater. Sci., 8 (2004), 86.
[21] GUSKOS N., ANAGNOSTAKIS E.A., LIKODIMOS V., TYPEK J., BODZIONY T., NARKIEWICZ U., J. Appl.Phys., 97 (2005), 024304.

Received 2 December 2004
Revised 25 March 2005

Materials Science-Poland, Vol. 23, No. 4, 2005

Nonlinear current oscillations in the fractal Josephson junction

S. P. KRUCHININ[1*], V. F. KLEPIKOV[2], V. E. NOVIKOV[2], D. S. KRUCHININ[3]

[1]Bogolyubov Institute for Theoretical Physics, 14-b, Metrologichna Str., Kyiv, 03143, Ukraine

[2]Scientific and Technological Centre of Electrophysics, NASU
28 Chernyshevs'kyi Str., Kharkiv, 310002, Ukraine

[3]National Taras Shevchenko University, 64 Volodymurska Str., Kyiv, 01033, Ukraine

In the present paper, a generator of chaotic oscillations based on the Josephson tunnel junction of the S–NF–S type, where S designates a superconducting material and NF is a thin fractal resistive layer, is offered. The nonlinearity and memory properties of the fractal junction allow us to use such junction as an effective generator of chaotic signals with a controllable statistical structure. Such a generator of chaotic signals can serve as a technological basis for chaotic communications.

Key words: *Josephson junction; fractal; nonlinearity; chaotic communications*

1. Introduction

The physics of electronic transport through nanodevices has generated an active interest in recent years [1, 2]. The number of applications of composite materials with complex fractal structures has recently increased in many areas of physics and technology. Fractal materials are characterized by macroscopic properties (heat conductivity, electric conductivity, diffusion, etc.) depending on fractal characteristics such as the fractal dimension of a material and its porosity [3]. It is very important, in particular, that fractal materials possess nonlinear electric conductivity. One of their basic properties is irreversibility, and we see [4] that irreversibility characterizes stochastic processes. These distinctive features of fractal materials allow us to hope that they can be effectively used in many radio-physical devices.

In the present paper, presented is a generator of chaotic oscillations based on the Josephson tunnel junction with a fractal non-conductive layer. Current fluctuations in

*Corresponding author, e-mail: skruchin@i.com.ua

a contour with the Josephson tunnel junction of the S–NF–S type (see Fig. 1), where S designates a superconducting material and NF – a thin fractal resistive layer. The nonlinearity and memory properties of fractal junctions allow us to use such a contact as an effective, easy to modify generator of chaotic signals with a controllable statistical structure. Such a generator can serve as the technological basis for the chaotic communication [5].

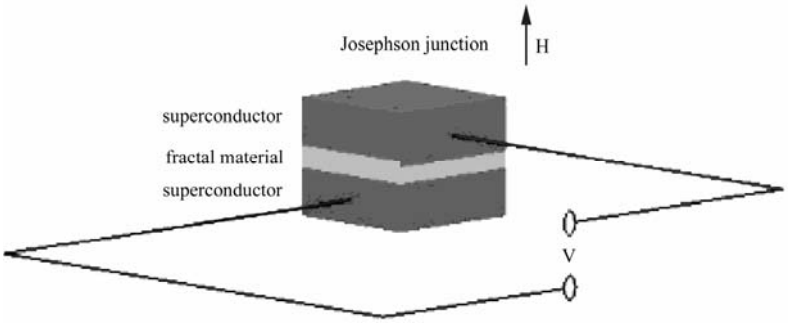

Fig.1. Scheme of the junction

2. Results

Let an insulating layer in a tunnel junction consist of a mixture of two components, such as a conducting and a dielectric one. If σ_m is the conductivity of the metal component, and σ_D the conductivity of the dielectric component, then the effective conductivity σ_e of the two-component infinite medium in a threshold behaviour depends only on $\xi = \sigma_D/\sigma_m$ and is described by the power law

$$\sigma_e = \sigma_m \xi^u \tag{1}$$

where u is a critical index. In the two-dimensional case, u is equal to 1/2 [4]. The conductivity at small values of σ decreases, and it is shown [3] that nonlinear effects in the conductivity σ at the phenomenological level are described by the effective linear conductivity σ_e and nonlinear conductivity α_e

$$\sigma = \sigma_e + \alpha_e E^2 \tag{2}$$

where E is the average electric field, and the nonlinear conductivity α_e is described by a power dependence on ξ:

$$\alpha_e \approx \alpha_D \xi^{-w} \tag{3}$$

where for a thin layer w = 1.5. We should emphasize that the nonlinear conductivity of an isolated fractal layer increases when $\xi \to 0$, and the effective field of nonlinear-

ity decreases, i.e. the fractal layer becomes quasi-nonlinear in a threshold behaviour. This property of the nonlinear conductivity of fractal materials creates additional nonlinearity when they are in contact with two superconductors and allows the properties of this junction to be controlled.

As is known, the system consisting of two weakly connected superconductors with the applied potential difference $U(t)$ is phenomenologically described by the difference in the phases of the wave functions in the superconductors with regard to

$$\frac{\partial \varphi}{\partial t} = \frac{2e}{\hbar} U(t) \tag{4}$$

and by existence of an oscillating superconducting part of the current I_s within the full current of the system I (due to the connection between the superconductors):

$$I_s = I_c \sin\left(\varphi(t)\right) \tag{5}$$

Taking into account that the junction possesses a capacity C, we add the equation for currents in the circuit to the obtained relations. It follows that the sum of the superconducting current, the conductivity current $\frac{\hbar}{2e}\frac{\partial \varphi}{\partial t}\frac{1}{R}$ and the displacement current $\frac{\hbar C}{2e}\frac{\partial^2 \varphi}{\partial t^2}$ is the full current in the circuit [4]:

$$\frac{\hbar C}{2e}\frac{\partial^2 \varphi}{\partial t^2} + \frac{\hbar}{2e}\frac{1}{R}\frac{\partial \varphi}{\partial t} + I_c \sin\left(\varphi(t)\right) = I(t) \tag{6}$$

Taking into account equations (4) and (6) and the conductivity nonlinearity of a fractal isolating layer (3), we obtain a system of first-order equations for the potential difference $U(t)$ on the tunnel junction. This system consists of Equation (4), which connects the phase and potential difference, and an equation for the phase:

$$\frac{\hbar C}{2e}\frac{\partial^2 \varphi}{\partial t^2} + \frac{\hbar}{2e}\frac{1}{R_0}(\xi^{1/2} + \alpha_D \xi^{-3/2} \alpha_e U(t)^2)\frac{\partial \varphi}{\partial t} + I_c \sin\left(\varphi(t)\right) = I(t) \tag{7}$$

We can see that these equations represent equations for a nonlinear oscillator of the Van der Pole type, with nonlinear decay and an external force. The external force acting on the oscillator is defined by a current I flowing through the junction, which can be constant or variable. If the current is a harmonic function of frequency close to the resonant frequency of the Josephson junction, then the system (7) can have both regular solutions and chaotic solutions of a complex structure.

The phase trajectory of the solutions of the system, when a normal metal is used instead of a fractal insulating layer in the tunnel junction, is shown in Fig. 2. As is seen, the fluctuations are similar to those for the ordinary Van der Pole oscillators.

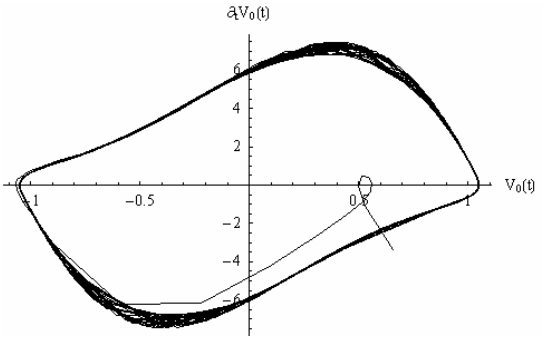

Fig. 2. Phase trajectory of voltage oscillations
for the ordinary Josephson junction

The modes of current oscillations and voltage modes in the Josephson junction depend essentially on the conductivity ratio of a unit of the composite material ξ. This fact is clearly seen from the phase portraits matching the voltage oscillations in the Josephson junction for close but different values of the parameter ξ (Fig. 3).

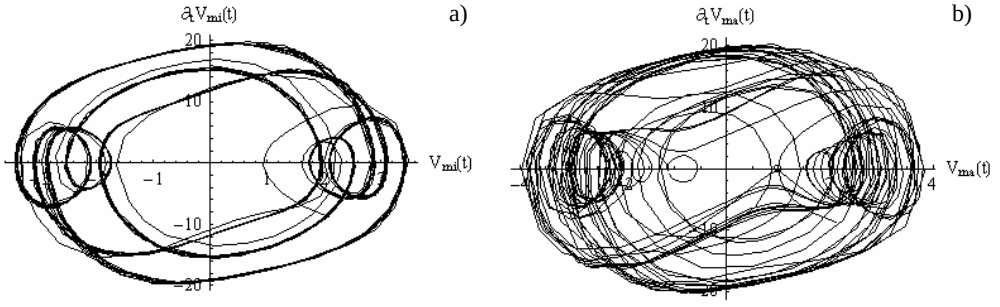

Fig. 3. Phase trajectories of voltage oscillations for the fractal
Josephson junction for $\xi = 0.1$ (a) and $\xi = 0.09$ (b)

As the characteristics of oscillations are very sensitive to modifications of the parameter ξ, it is possible to use slow signal modulation (compared to its own junction frequency) to record information on the statistical characteristics of realization in time. Such a modulation can be carried out, for example, by using a slowly changing magnetic field. We now consider the elementary time dependence $\xi(t)$. Let all the intervals of time evolution be split into three equal parts, so that from the onset up to $t = 18$ the value $\xi = 0.1$, then $\xi = 0.09$, and in time interval $36 < t < 50$ again. The realization and phase portrait for the solution of the system equations for such a non-stationary parameter are shown in Figure 4.

It is possible to show that the analysis of the statistical characteristics of the obtained realization by ATD (adaptive testing of device) [5] gives the possibility of restoring the slow evolution of the parameter ξ, and hence the possibility of restoring the information signal that affected the modulation.

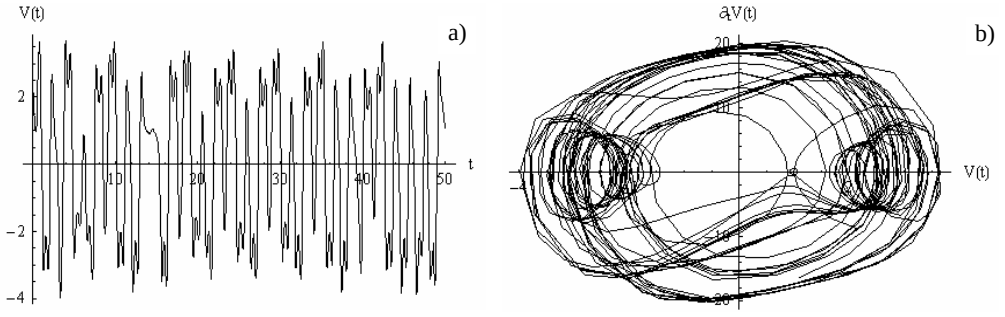

Fig. 4. The realization and phase trajectory of voltage oscillations for the fractal Josephson junction with a non-stationary parameter ξ. From the beginning of the evolution up to $t = 18$ the value $\xi = 0.1$, then $\xi = 0.09$, after which in the time interval $36 < t < 50$ again $\xi = 0.1$

3. Conclusions

In summary, the Josephson junction with a fractal layer is characterized by nonlinear properties, which permits the oscillation mode to be operated effectively by slowly changing the conductivity ratio of the unit of composite materials.

The Josephson junction with a fractal layer displays even more interesting properties, due to the fact that the fractal medium possesses memory. A more adequate model of the tunnel junction that takes the fractal medium into account can be built from the generalized oscillation equation using fractional operators. A detailed analysis of the model for chaotic communications on the basis of the fractal Josephson junction will be presented in our further investigations.

Acknowledgements

This research was partially supported by the project No. 16579 of the Royal Society.

References

[1] JIAN-XIN ZHU, BALATSKY A., Phys. Rev. B, 67 (2003), 174505.
[2] SUGAHARA M., KRUCHININ S., Mod. Phys. Letters B, 15 (2001), 473.
[3] KITAMURA T., YOKOYAMA M., J. Appl. Phys., 69 (1991), 821.
[4] OLEMSKOI A.I., KLEPIKOV V.F., Phys. Rep., 338 (2001), 571.
[5] ASLAMAZOV L.G., LARKIN A.I., Lett. JETP., 9 (1969),150.

Received 19 December 2004
Revised 30 May 2005

Materials Science-Poland, Vol. 23, No. 4, 2005

Development trends in pressure-sensitive adhesive systems

Z. CZECH[1*], R. MILKER[2]

[1]Szczecin University of Technology, Polymer Institute, al. Piastów 17, 70-310 Szczecin, Poland

[2]Klebstoff GmbH, Industriepark 23, D 56593 Horhausen, Germany

Pressure-sensitive adhesives (PSA) present an interesting class of products that offers a potential to produce a novel generation of self-adhesives with a great number at excellent properties. The term *pressure-sensitive* describes adhesives that are aggressively and permanently tacky in the dry form at room temperature and firmly adhere to a variety of dissimilar surfaces upon mere contact, without the need of more than finger or hand pressure. Acrylic self-adhesive polymers are nowadays synthesized from a wide selection of acrylic ester monomers, often with low levels of monomers having pendant functional groups. The three basic types of acrylic common today are solvent-borne, water-borne, and solvent-free acrylic PSAs. They can be used in the production of single- and double-sided self-adhesive tapes, foil labels, carrier-free tapes, self-adhesive bioelectrodes, and decorative PVC signs and marking films. A pressure-sensitive adhesive requires a balance of cohesive strength and viscoelastic properties. These characteristics are based on three parameters: tack, adhesion, and cohesion.

Key words: *pressure-sensitive adhesive; acrylic polymer*

1. Introduction

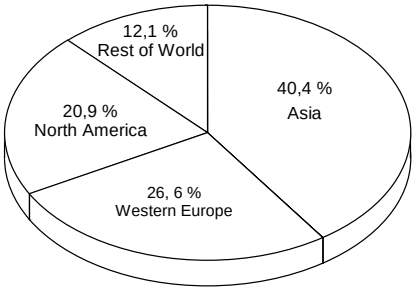

Fig. 1. Market share in production of pressure-sensitive adhesive tapes

The market and technology of high-performance PSAs are expanding rapidly. A growing market is the result of expansion in both current and new application areas.

* Corresponding author: e-mail: Zbigniew.Czech@ps.pl

Self-adhesive polymers possess inherent properties due to their structure that make them unique. The world market for pressure-sensitive adhesive tapes will expand at 5.5% p.a., reaching 25.4 billion m^2 worth $ 20.8bn in 2006 (Fig. 1) [1].

2. Pressure-sensitive adhesives

For commercially used PSA systems with excellent performance levels, synthetic polymers based on acrylics, silicones, polyurethanes, and polyesters are preferred (Fig. 2). These technologies exist in the market of PSA today [2].

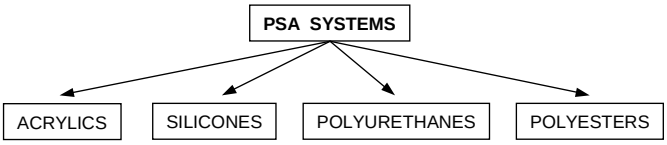

Fig. 2. PSA types used for the production o self-adhesive articles

2.1. Acrylics

Acrylates and other suitable monomers are copolymerised to yield an acrylic copolymer of a specific composition. Crosslinking agents are usually added for improved cohesion. Acrylics can be synthesized in organic solvents. In this case, no further formulation is generally needed, although it is done from time to time in order to fine-tune their properties. Acrylics can also be synthesized in water but surfactants need to be added to make the polymer dispersible. The third group of acrylics is solvent-free acrylic PSA (Fig. 3) [2].

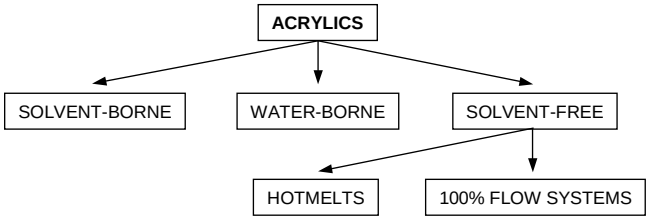

Fig. 3. Acrylic types of PSAs

2.1.1. Solvent-borne acrylic PSAs

The market and technology of high performance solvent-borne acrylic pressure -sensitive adhesives are still expanding. A growing market is the result of expansion in both current and new application areas [3].

The composition of acrylate polymers that are inherently pressure-sensitive is a combination of soft (low T_g), hard (high T_g), and functional monomers in the polymer chain (Fig. 4) [4].

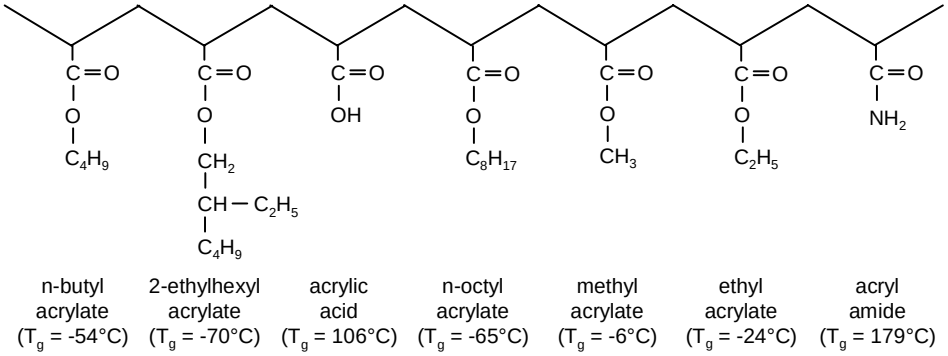

Fig. 4. Scheme of the chain composition of acrylic pressure-sensitive adhesives

Tack and peel adhesion are imparted by soft or low glass transition temperature monomers such as *n*-butyl, 2-ethylhyxyl, and *n*-octyl acrylate. Harder monomers, such as methyl and ethyl acrylate, are included to provide internal strength. Functional monomers, such as acrylic acid and acrylic amide, are incorporated for specific adhesion to desired substrates and in order to provide reactive sites for crosslinking reactions.

Solvents containing acrylic PSAs can also become an efficient technology in the future for water-soluble PSAs, UV-crosslinkable PSAs, and structural acrylic adhesives (Fig. 5).

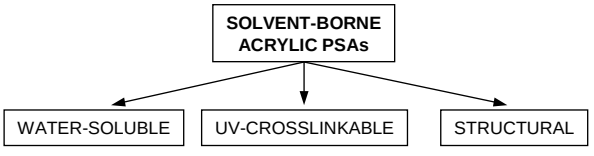

Fig. 5. The kinds of solvent-borne acrylic PSAs

Water-soluble acrylic PSAs. Water-soluble polyacrylate pressure-sensitive adhesives are used primarily in the production of industrial single-sided, double-sided, and transfer adhesive tapes, which are being increasingly used in the paper industry to splice paper webs during manual and flying reel changing. A special area of use resides in the manufacture of water-soluble labels. The latest application is in the field of medical products, where neutral electrodes and adhesive tapes for securing operating theatre sheets are of special importance [5].

An unusual and interesting challenge is that of giving PSA a certain water solubility, which depends greatly on the hydrophilic properties of the groups incorporated into the polymer chain. The glass transition temperature T_g of the water-soluble raw monomers (Fig. 6) is the main criterion for the adhesive properties and water solubility of the synthesized copolymers. The preferred tackifying but water-insoluble alkyl acrylates (Fig. 6) reduce T_g and improve the tack and adhesion properties.

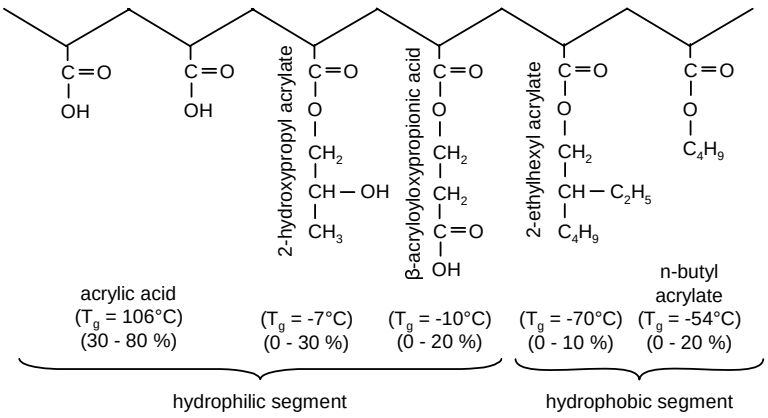

Fig. 6. Polymer chain scheme of water-soluble acrylic PSAs

UV-crosslinkable acrylic PSAs. In the case of saturated acrylic pressure-sensitive adhesives, the photogeneration of initiator radicals by α-cleavage photoinitiators or

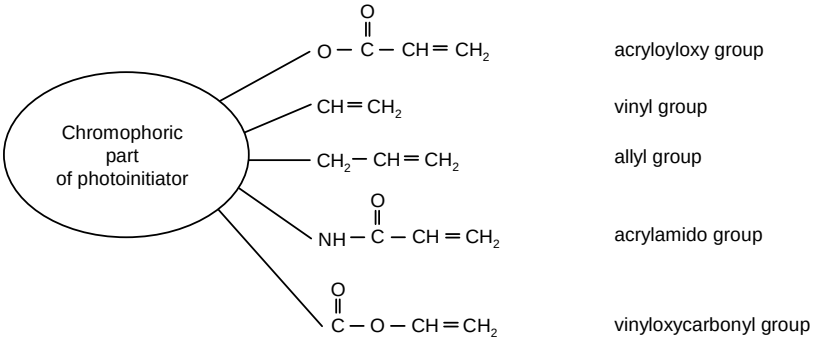

Figure 7. General examples of the chemical structure of unsaturated photoinitiators

H-abstraction photoinitiators is followed by a reaction with the acrylic chain that produces a new radical reacting with a neighbouring acrylic chain.

A very interesting alternative to conventional photoinitiators are unsaturated photoinitiators. The most typical directions, however, are in the development of func-

tionalised type I and type II initiators, e.g. acrylated, vinylated, allylated, acrylamidated, or vinyloxylated (Fig. 7) [6].

A typical behaviour of tested novel unsaturated photoinitiators showed that the best PSA properties were achieved for the type II photoinitiator 4-acryloyloxy benzophenone (ABP):

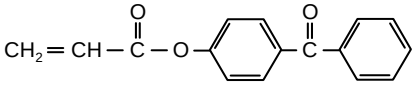

ABP was the most efficient H-abstractor for the common solvent-based acrylic self -adhesives [7].

Structural acrylic PSAs. This new adhesive, known as structural bonding tape, is an acrylic pressure-sensitive tape impregnated with an epoxy that cures under heat. This product can be cured in an oven at about 145 °C for 20 min or hot bar cured.

The composition of PSA polymers (before the curing process begins they are inherently pressure-sensitive) is a combination of soft acrylate monomers with low T_g and hard epoxy monomers with high T_g in the polymer chain (Fig. 8) [8].

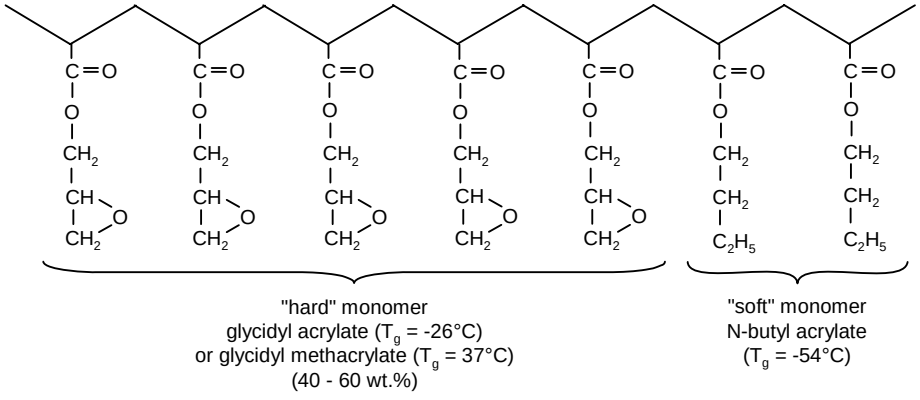

Fig. 8. The polymer chain architecture of a structural acrylic adhesive

The acrylic ester/epoxy resin pressure-sensitive thermosetting adhesive is an initially tacky and conformable thermosetting adhesive, which is obtained from a blend comprising epoxy resin or a mixture of about 20–60 wt. % epoxy resin and 0,5–10 wt. % heat-activatable hardener for the epoxy resins.

2.1.2. Solvent-free acrylic PSAs

Deficiencies of hot melt pressure-sensitive adhesives made of traditional solvent-free acrylic PSA are due to the use of relatively low molecular weight polymers, which results in limited heat and plasticiser resistance. Other groups of solvent-free acrylic PSAs are 100% systems, characterized at room temperature coated flow polymers. Solvent-free acrylic pressure-sensitive adhesives are crosslinked using UV radiation [9].

UV-crosslinkable acrylic HMPSAs. Crosslinkable acrylic hot melt PSAs (HMPSAs) that are designed to be crosslinked by a UV-lamp or UV-laser light are now available. These products offer high processing speeds, relatively low application viscosity at higher temperatures, high resistance to plasticisers and solvents, aggressive tack, and very high heat resistance after crosslinking.

UV-acrylic hot melts consist of acrylic copolymers with chemically built-in photoreactive groups. They are free of solvents and are processed in the form of hot melts. After the acrylic film for self-adhesive material production has been coated with the UV-acrylic hot melt, the adhesive film is crosslinked with UV radiation.

UV-crosslinkable 100% acrylic systems. Since these are 100% solid adhesives, it is easy to coat heavy depositions at a good speed. Viscosity can be modified within certain limits by changing added photoreactive diluents.

The UV dose can be controlled by adjusting the power of the lamps and the speed at which the substrate is passed under the lamps in the production plant (Fig. 9) [10]:

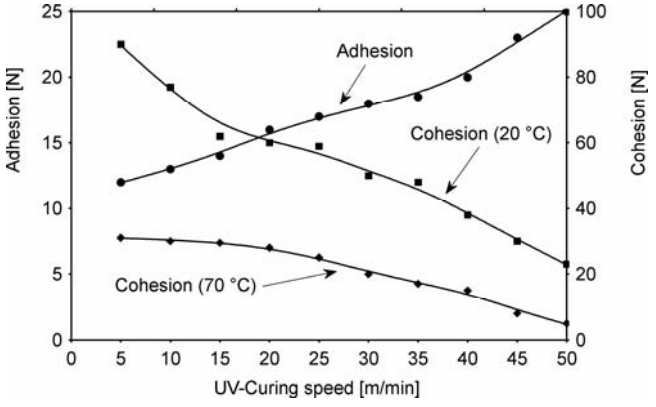

Figure 10. Adhesion and cohesion forces of coated 100% acrylic PSA systems vs. UV-curing speed

2.2. PSA silicones

Silicone pressure-sensitive adhesives are high-performance adhesives that can be utilized over a wide range of temperatures, from –40 to 300 ºC. They bond to both low energy and high-energy surfaces. Silicone polymers based on gum contain dimethylsiloxy and diphenylsiloxy groups

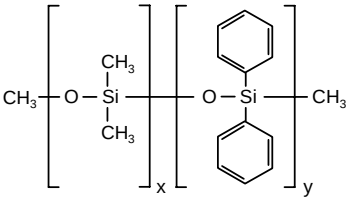

The molecular weights of solvent-borne silicones are preferably in the range from 500 000 to 1 500 000 Daltons [12]. The crosslinking of silicone PSAs containing methyl or/and phenyl groups can be achieved thermally between 120 and 150 °C using organic peroxide.

2.3. PSA polyurethanes

The extraordinarily diverse chemistry of polyurethanes has also contributed to the development of efficient adhesives. This applies only to a limited degree to pressure-sensitive adhesives, however, for which the number of patent publications is astonishingly small. Ready for coating, solvent free 2-K PSAs on the basis of polyether polyols and isocyanates are not available on the market

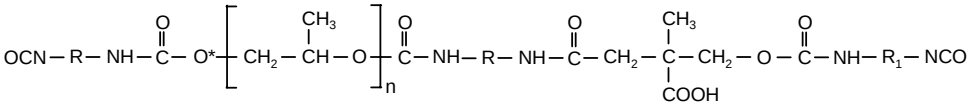

2.4. PSA polyesters

Previous studies have shown [13] that excellent adhesion can be obtained with aliphatic polyesters with molecular weights ranging from 10 000 to 50 000 Da [14] and glass transition temperatures T_g between –25 and –47 ºC.

A typical example of this approach is the acrylation of polyester PSAs containing end hydroxyl groups. In practice, the introduction of an unsaturated architecture can also be achieved through the reaction of the OH-groups of a polyester polymer chain with the corresponding acrylic or unsaturated isocyanate compounds [15].

3. Conclusion

The ever-changing high performance pressure-sensitive adhesive market continues to expand and to present new challenges. To date, the industry has seen a strong growth in traditional applications and the emergence of new applications. The chemistry of polymers with self-adhesive properties has taken on an additional dimension with the introduction of various raw materials, polymerisation techniques, and crosslinking methods. This expansion of the technology ensures that future performance and environmental requirements will be met.

References

[1] *Pressure-Sensitive Industry*, Yearbook (2004), 28.

[2] CZECH Z., *Crosslinking of PSA based on acrylics*, Press House Politechnika Szczecińska, Szczecin, 1999, ISBN: 83-87423-18-1.

[3] MILKER R., CZECH Z., Adhäsion, 33 (1989), 20.
[4] CZECH Z., Ekoplast, 23–24 (2003), 31.
[5] CZECH Z., Polimery, 41 (1996), 22.
[6] MILKER R., CZECH Z., J. Appl. Polymer Sci., 87 (2003), 1354.
[7] BROCKMANN W., MEYER-ROSCHER B., *Relation of Pressure-Sensitive properties and UV crosslinking technology*, TAPPI Hot Melt Symposium, Atlanta, USA, 1998, 174.
[8] CZECH Z., URBALA M., MARTYSZ D., Polymer Adv. Techn., 15 (2004), 387.
[9] CZECH Z., Kautschuk Gummi Kunststoffe, 55 (2002), 492.
[10] CZECH Z, MILKER R., J. Appl. Polymer Sci., 87 (2003), 182.
[11] GADDAM N., US Pat. 5,346,980 (1993).
[12] MAZUREK M., US Pat. 5,314,748 (1993).
[13] ACEVADO M., HUBER H., Proceedings RadTech Europe, Lyon (1997), p. 181.
[14] ACEVADO M., HUBER H., 23. Münchener Klebstoff- und Veredelungsseminar (1998), p. 128.
[15] RAMHARACK R., US Pat. 5,391,406 (1995).

Received 23 September 2004
Revised 1 March 2005

Materials Science-Poland, Vol. 23, No. 4, 2005

Some implications of the nonlinear properties of SASD crystals

I. E. LIPIŃSKI*, J. KURIATA

Institute of Physics, Szczecin University of Technology, al. Piastów 17, 70-310 Szczecin, Poland

The paper deals with the results of optical and EPR measurements performed on single-crystalline- and powdered samples of sodium ammonium sulphate dihydrate (SASD) and sodium ammonium selenate dihydrate (SASeD) doped with Cr^{3+} and irradiated with X-rays. It is shown that for samples doped with Cr^{3+} one detects in the optical spectrum, apart from the existence of two broad transmission bands, yet another narrow band, corresponding to the ${}^4A_{2g}(F) \rightarrow {}^4T_{1g}(F)$ transition, which suggests that such samples can potentially exhibit laser action. The EPR spectra of X-ray irradiated pure samples of SASD crystals indicate that a variety of paramagnetic centres (NH_4^- , SO_4^{-n}) are easily induced by irradiation. The concentrations of these centres are in close relation with the dose of irradiation. The observed relation can be used for dosimetry purposes.

Key words: *SASD crystas; optical spectrum; EPR; irradiation induced paramagnetic centre*

1. Introduction

Sodium ammonium sulphate dihydrate (SASD) and sodium ammonium selenate dihydrate (SASeD) belong to the same class of crystallographically isomorphous systems with the space group $P2_12_12_1$ in the paraelectric phase and $P2_1$ in the ferroelectric phase. Details of the structures of these crystals can be found in the literature [1, 2]. For pure (undoped) crystals, the transition temperature is 101 K for SASD and 180 K for SASeD. The introduction of Cr^{3+} (also Mn^{2+} or Fe^{3+}) ions as dopants substituting Na^+ ions can reduce T_C by a few degrees, even at as low concentrations as 0,01 mol % [3].

Over the last few years we have investigated physical properties of the crystals under discussion by using many different experimental and theoretical methods. These include: EPR (e.g. [4]), neutron inelastic scattering [5], optical [6], and hydro-

*Corresponding author, e-mail: Eryk.Lipinski@ps.pl

static stress [7] methods. The main results of these investigations were: description of the crystal lattice dynamics, the detection of new anomalies yet not reported in literature, and the discovery of the existence of a new "glassy" phase of SASD in the temperature range from 190 to 140 K [8].

A theory explaining the nature of the phase transitions in these crystals and the origin of the newly discovered anomalies was subsequently developed by us on the basis of the modified two-sublattice Mitsui model (e.g. [8–10]). Although the applied methods were meant to shed new light on the still controversial problem of the physical principles ruling the phase transition and newly detected anomalies, we found that some of the results we obtained can have practical value. These results will be discussed in more detail below.

2. Experimental

Large and good quality single crystals of SASD were grown by the evaporation of equimolar water solutions of $(NH_4)_2SO_4$ and Na_2SO_4. During the crystal growth the temperature was lowered from 304 K to 299 K at a rate of 0.4 deg/24 h. An example of the obtained single crystal is shown in Figure 1.

Samples of SASeD doped with Cr^{3+} were kindly supplied by Prof. Z. Czapla from the University of Wrocław. They were grown using the same technique as described above, and Cr^{3+} ions were introduced to the crystal lattice by adding $Cr_2(SO_4)_2 \cdot 18H_2O$ to the saturated solution of $NaNH_4SeO_4 \cdot 2H_2O$ in a molecular ratio of 1:0.02. The obtained single crystals have a light-green colour; a sample is shown in Figure 2.

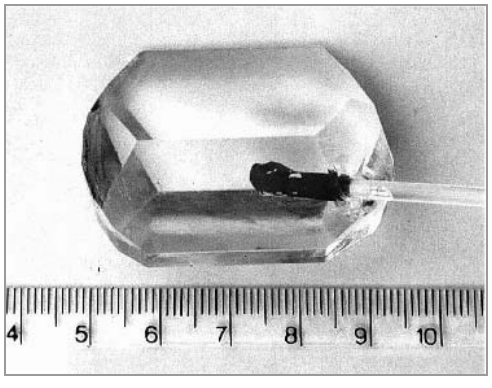

Fig. 1. A photograph of a grown $NaNH_4SO_4 \cdot 2H_2O$ single crystal

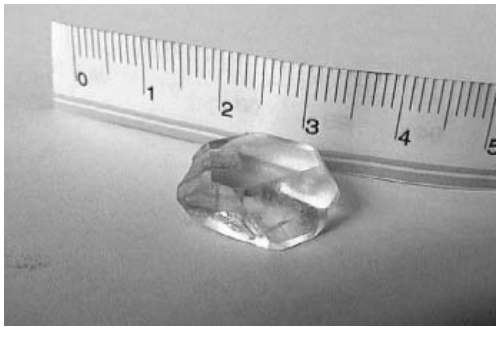

Fig. 2. A photograph of a grown $NaNH_4SeO_4 \cdot 2H_2O$ single crystal doped with Cr^{3+}

Optical measurements were done with a SPECORD UV VIS spectrometer working in the UV range of 50 000–28 000 cm^{-1} and VIS range 30 500–12 500 cm^{-1}. The experimental error was 20 cm^{-1}.

X-ray irradiation was carried out using an X-ray Dron-2.0 diffractometer. A wolfram tube was used as the source of X-rays. The applied cathode voltage was 30 kV, with a current of 20 mA. EPR measurements were performed with a standard X-band spectrometer working with a 100 kHz magnetic field modulation.

3. Results

In Figure 3, the optical spectrum of Cr^{3+} ions in SASeD is presented. As indicated by the arrows, three absorption bands are clearly seen. Two of them are very broad, which is usually observed for transition metal ions subject to the action of a crystal field. These bands were identified to belong to the ${}^4A_{2g}(F) \rightarrow {}^4T_{1g}(F)$ and ${}^4A_{2g}(F) \rightarrow {}^4T_{2g}(F)$ transitions, and the respective maxima (of absorption) are observed at 14 300(50) and 16 300(13) cm^{-1}. There exists yet another very narrow transition at 23 700(13) cm^{-1}, identified to correspond to the ${}^4A_{2g}(F) \rightarrow {}^4T_{1g}(F)$ transition. The Racah parameter B was estimated to be 774.05 cm^{-1}, while the Dq parameter (obtained from the energy diagram) was 1630 cm^{-1}.

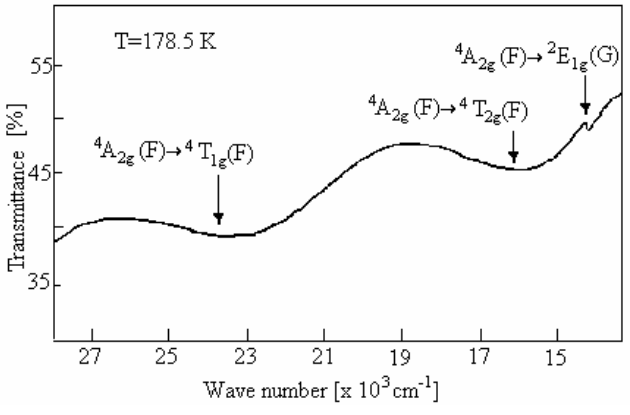

Fig. 3. The optical spectrum of SASeD doped with Cr^{3+}

The narrow band corresponding to the ${}^4A_{2g}(F) \rightarrow {}^4T_{1g}(F)$ transition, although of rather low quantum efficiency, indicates that relaxation times for this transition are much larger than for the remaining two transitions, and therefore the system investigated here can potentially exhibit laser action.

The EPR spectrum of the X-ray irradiated single crystal, taken at room temperature and with $\vec{B}$ parallel to one of the principal directions, is shown in Figure 4. The analysis of the angular dependence of the spectrum indicated that the it is due to a superposition of a variety of paramagnetic centres induced by the irradiation. Some of the identified centres are: SO_4^{-n} (central part of the spectrum), NH_3^-, and NH radicals.

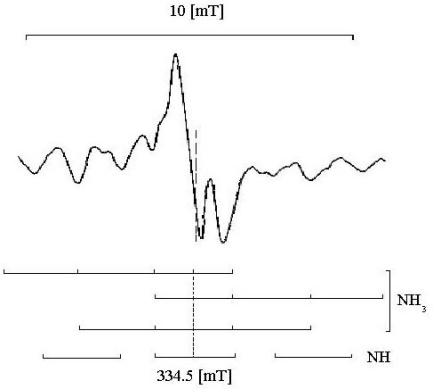

Fig. 4. The EPR spectrum of an X-ray irradiated SASD crystal (above) and the best fit of a "stick-like" spectrum for NH_3^- and NH radicals (below)

The spectra were analysed as a function of the irradiation dose, which was proportional to the time of irradiation. For this purpose, in order to avoid any influence of crystal sample misorientations on the EPR line intensity, the samples were powdered. An example of a powder EPR spectrum is shown in Figure 5.

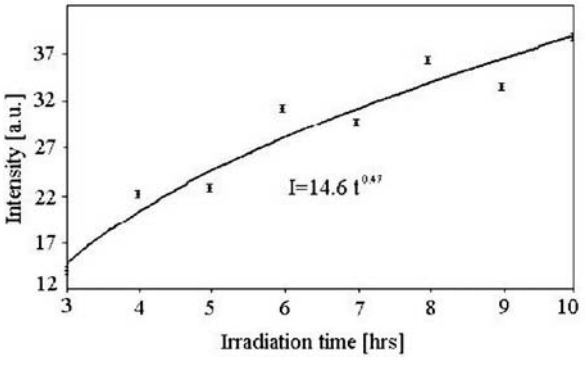

Fig. 5. The intensity of the central line vs. the time of irradiation

Two facts were found. The first is rather obvious – the intensity of the EPR lines is in strict relation with the dose of irradiation. This relation is shown in Figure 5. The experimental error seen in this figure is mainly caused by the error of measuring the exact mass of small powder samples. This can be improved by introducing a more careful procedure. The second fact is that the induced radicals are very stable, at least over a period of one month, which means that SASD and SASeD crystals can be efficiently used for dosimetric purposes.

References

[1] CORAZZA E., SABELLI C., GIUSEPPETTI G., Acta Crystallogr., 22 (1967), 683.
[2] ALEKSANDROV K.S., ALEKSANDROVA I.P., SHABANOV V.F., YUZVAK V.I., NOZIK Y.Z., FIKIN L.I., Phys. Stat. Sol. (a), 45 (1978), 53.

[3] BODZIONY T., LIPIŃSKI I.E., KURIATA J., BEDNARSKI W., Physica B, 299 (2001), 70.
[4] BAKER J.M., COOK M.I., TRONCONI A.L., KURIATA J., SADŁOWSKI L., J. Phys. Condens. Matter, 5 (1993), 459.
[5] LIPIŃSKI I.E., KURIATA J., NATKANIEC I., PAWLUKOJĆ A., Phys. Stat. Sol. (b), 227 (2001), 477.
[6] LIPIŃSKI I.E., N.A KORYNEVSKII., KURIATA J., Ferroelectrics, 303 (2004), 217.
[7] LIPIŃSKI I.E., KRUPSKI M., KURIATA J., SADŁOWSKI L., Phys. Stat. Sol. (B), R19 (1999), 214.
[8] LIPIŃSKI I.E., KURIATA J., KORYNEVSKII N.A., Condens. Matter Phys., 6 (2003), 245.
[9] KURIATA J., LIPIŃSKI I.E., KORYNEVSKII N.A., BODZIONY T., Physica B, 307 (2001), 203.
[10] LIPIŃSKI I.E., KORYNEVSKII N.A., KURIATA J., PASTUSIAK W., Physica B, 327 (2003), 116.

Received 12 October 2004
Revised 19 April 2005

Materials Science-Poland, Vol. 23, No. 4, 2005

Photoacoustic study of a new neodymium(III) hydrazone complex

N. GUSKOS[1, 2*], D.G. PASCHALIDIS[3], J. MAJSZCZYK[2], J. TYPEK[2], M. MARYNIAK[2]

[1]Solid State Section, Department of Physics, University of Athens, Panepistimiopolis, 15 784 Zografos, Athens, Greece

[2]Instytute of Physics, Szczecin University of Technology, al. Piastów 17, 70-310 Szczecin, Poland

[3]Department of Chemistry, Aristotle University, Thessaloniki, 54124, Greece

The neodymium(III) hydrazone complex $[Nd(DBH)_2(NO_3)_3]$ has been synthesized and characterized using microanalysis and IR spectroscopy. High-resolution photoacoustic spectrometry has been applied for studying the complex. The obtained photoacoustic spectrum has been analysed and compared to a similar $[Nd(PicBH)_2(NO_3)_2]NO_3$ complex. The intensities of the f–f transitions in the photoacoustic spectrum of $Nd(DBH)_2(NO_3)_3$ were two times greater than for the $[Nd(PicBH)_2(NO_3)_2]NO_3$ complex.

Key words: *photoacoustic spectroscopy; neodymium complex*

1. Introduction

Complexes of hydrazones with paramagnetic lanthanide metal ions have attracted close attention as a new class of potential magnetic resonance imaging contrast agents [1]. A number of hydrazone rare earth(III) complexes have gained wide interest, because they show a broad spectrum of biological and pharmaceutical activities, such as antimicrobial, antitumor, antituberculostatic, and anticancer actions [2–8]. Previously we have reported the structural characterization of lanthanide(III) –hydrazone complexes of higher coordination numbers [9–11]. Recently, rare earth(III) complexes of hydrazones have been studied with a high-resolution photoacoustic (PA) spectrometer [12]. The $\pi \rightarrow \pi^*$, $n \rightarrow \pi^*$, and f–f electron transitions with different intensities have been recorded. The PA absorptions of the f–f transitions in the yellow light region have been observed and it has been suggested that they could play a very important role in living matter [13].

The aim of this report is to present the results of PA spectroscopy study of a new kind of coordination compound – the neodymium(III) complex of hydrazone $[Nd(DBH)_2(NO_3)_3]$. Special attention will be paid to the intensities of the PA absorptions due to f–f transitions. A comparison will be made with a similar neodymium(III) complex – $[Nd(NO_3)_2(PicBH)_2]NO_3$ studied previously [12].

2. Experimental

All manipulations were performed in a dry box. The solutions were prepared in a glove box purged with dried nitrogen gas. The complex was prepared by the following general procedure: a methanol solution (10 cm^3) of DBH (4 mmol) was added to a methanolic solution (10 cm^3) of hydrated neodymium nitrate (2 mmol). The solution was stirred for 1 h. A fine microcrystalline product was obtained, filtered off, washed with small amounts of methanol, and dried in vacuum over anhydrous calcium chloride.

All chemicals were purchased from Aldrich Chemicals and used without further purification. All solvents were dried and distilled prior to use. Di-2-pyridylketone benzoylhydrazone was prepared by refluxing a methanolic solution (500 cm^3) of benzoic hydrazide (6.80 g, 50 mmol) and di-2-pyridylketone (9.21 g, 50 mmol) for 24 h. After 24 h of slowly cooling the reaction mixture at room temperature, a crude white product was filtered off, washed with methanol, and recrystallised from methanol. Microanalyses (C, H, N) were taken with a Perkin-Elmer analyzer model 2400. The metal contents of the complexes were determined by titration with the EDTA volumetric method, using xylenol orange as indicator [14]. Melting points were determined with a Büchi silicon oil bath apparatus and are uncorrected. Molar conductivities were measured on a WTW model LF 530 Conductivity Bridge, employing a calibrated immersion type cell, with the cell constant of 0.998 cm^{-1} (mean value calibrated at 25 °C with potassium chloride solution). Temperatures were controlled with an accuracy of ±0.1 °C using a Haake thermoelectric circulating system of water. IR spectra were recorded in the 4000–250 cm^{-1} region with a Perkin-Elmer 1650 FT–IR spectrophotometer using KBr pellets. Frequency readings were calibrated with polystyrene film.

The PA spectra of polycrystalline powder samples were obtained by using a modified PAS (photoacoustic spectroscopy) method initially proposed by Papadopoulos and Mair [15]. A Xenon arc lamp with 1 kW power and a ¼ m ORIEL monochromator were used as the light sources, with a band pass width of 5 nm (at 500 nm). The light, whose intensity was modulated with a chopper at 10 Hz, was directed into a photoacoustic cell equipped with a TREVI EM27 microphone. A dual SR830 lock-in amplifier measured the amplitude and phase of the PA signal detected on the microphone. Data acquisition ensured that each value was an average of 20 runs at the same wavelength of the incident light. Carbon black was used as the standard to recalibrate the final spectrum. The PA spectra of all complexes were recorded at room temperature in the range of 300–700 nm.

3. Results and discussion

3.1. Sample preparation and characterization

The analytical data of the complex (with the yield of 88%, m.p. 201 °C; elemental analyses found (calc.): C – 46.37 (46.25), H – 3.00 (3.02), N – 16.52 (16.48) and Nd – 15.60 (15.43)) indicate a 1:2 metal to ligand stoichiometry, corresponding to the molecular formula $NdC_{36}H_{28}N_{11}O_{11}$. The complex is an air–stable crystalline solid, soluble in methanol, ethanol, acetonitrile, DMF, DMSO, but insoluble in chloroform, dichloromethane and ether. The molar conductances of 0.001 M acetonitrile, methanol, DMF, and DMSO solutions of the neodymium(III) complex lie below 10 $S \cdot cm^2 \cdot mol^{-1}$ (CH_3CN – 4 $S \cdot cm^2 \cdot mol^{-1}$, CH_3OH – 3 $S \cdot cm^2 \cdot mol^{-1}$, DMF – 4 $S \cdot cm^2 \cdot mol^{-1}$, DMSO – 4 $S \cdot cm^2 \cdot mol^{-1}$), indicating its non-electrolytic nature. Infrared spectral data give evidence for the coordination of the neutral form of the hydrazone to the neodymium ion via azomethinic nitrogen, pyridine nitrogen and carbonylic oxygen. Infrared spectra also demonstrate the presence of only bidentate coordinated nitrate anions. Thereupon, the formula of the complex becomes $[Nd(DBH)_2(NO_3)_3]$ (Fig. 1).

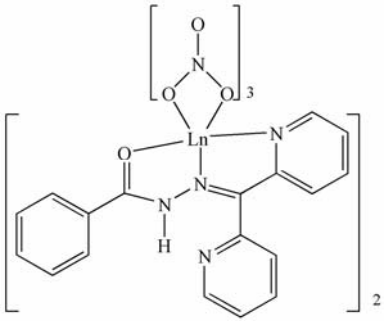

Fig. 1. Schematic structure of the $[Nd(DBH)_2(NO_3)_3]$ complex (Ln = Nd)

3.2. IR measurements

The relevant infrared vibration bands are given in Table 1. Assignments were made by comparing the spectra of the complex with those of the free DBH ligand. The broad absorption band at 3415 cm^{-1} was assigned to the ν(N–H) frequency in the spectra of the ligand and its complex. The strong IR bands due to ν(C=O) (1670 cm^{-1}) in the spectra of the complex are the evidence of the coordination of the hydrazone with the metal via carbonyl oxygen [16]. The band due to ν(C=N) (1576 cm^{-1}) indicates that azomethine nitrogen is coordinated to the metal. Low energy in-plane and out-of-plane vibrations of the pyridine ring were observed in the spectrum of the ligand at 615 and 410 cm^{-1}, respectively, but the corresponding bands for the complexes are shifted to higher frequencies – 622 and 428 cm^{-1}, respectively, indicating

a coordination of heterocyclic nitrogen [17–20]. The spectrum demonstrates the presence of coordinated nitrates. Two strong bands are observed at 1472 and 1300 cm^{-1} and are assigned to the ν_4 and ν_1 vibrations modes of the nitrate group, respectively (C_{2V} symmetry, coordinated nitrate group). The magnitude of splitting in the complex (ν_4–ν_1) is 172 cm^{-1}, typical of bidentate bonding of nitrates [21].

Table 1. Characteristic IR bands (cm^{-1}) of the ligand DBH and the neodymium(III)–hydrazone complex $Nd(DBH)_2(NO_3)_3$

Compound	ν(N–H)	ν(C=O)	ν(C=N)	$\nu_4(NO_3)$ (C_{2v})	$\nu_3(NO_3)$ (D_{3h})	$\nu_1(NO_3)$ (C_{2v})	Low-energy pyridine ring vibrations	
							In plane	Out-of -plane
DBH	3473	1684	1577	–	–	–	615	410
$Nd(DBH)_2(NO_3)_3$	3415	1640	1576	1472	–	1300	622	428

3.3. PA spectra

Figure 2 presents the PA spectra of the new neodymium(III) hydrazone–complex, $[Nd((DBH)_2(NO_3)_3$ and a similar neodymium(III)-hydrazone complex studied previously, $[Nd(PicBH)_2(NO_3)_2]NO_3$ [12]. The PA spectra correspond to three kinds of electron transitions: $\pi \rightarrow \pi^*$, $n \rightarrow \pi^*$, and f–f. For shorter wavelengths the first two types of transitions dominate and are more intense, whereas in the visible region the less intense f–f transitions appear. The f wavefunctions are mainly localized on rare earth(III) ions, and the position of the PA line for f–f transitions is only very weakly dependent on the kind of matrix. On the other hand, the opposite is true for d–d transitions, because the d wavefunctions are extended over the molecule [22, 23]. The transitions $\pi \rightarrow \pi^*$ and $n \rightarrow \pi^*$ strongly depend on the kind of matrix, because the first one takes part in the bonding processes, and the second could play an important role in the thermodynamic balance of living matter [24]. The intensity of the PA spectrum of f–f transitions is markedly different for the two complexes of neodymium(III) (Fig. 2). Intensity is one of the most important parameters in the photoacoustic spectroscopy of coordination compounds, especially if they are active in biological systems. This is connected to the intermolecular transfer energy as well as to relaxation processes between the exited and the ground states.

The PA spectrum is obtained by detecting the heat generated through non-radiative relaxation, released by a sample absorbing modulated incident light. The PA spectrum intensity, *I*, could be given by the following relation [25]:

$$I = k A_{abs} \gamma$$

where A_{abs} is the absorbance of the sample, γ is the probability of a non-radiative transition after excitation, and k is a coefficient determined by the thermal properties of the sample and the spectrometer. In our case, it can be supposed that k and A_{abs} are similar for both samples. The main contribution arises from γ and is connected to non-radiative transitions.

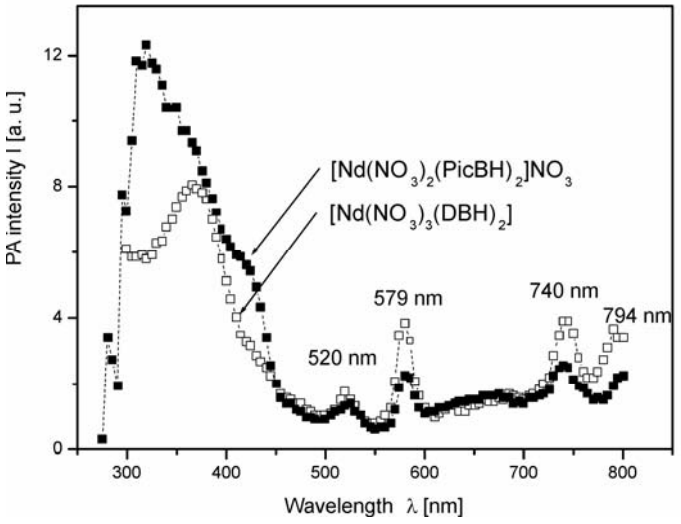

Fig. 2 Photoacoustic spectra of $[Nd(DBH)_2(NO_3)_3]$ and, for comparison, $[Nd(PicBH)_2(NO_3)_2]NO_3$

The PA band at shorter wavelengths is shifted to lower energies in both complexes than those observed for the other rare earth(III) organic complexes [26]. It is suggested that the bonds related to $\pi \rightarrow \pi^*$ transitions are weaker in our complexes. The f–f transitions for neodymium complexes are almost at the same positions, but significant differences are observed in the intensities of the PA spectra [26]. More intense PA spectra for the f–f transitions are recorded for the $[Nd(NO_3)_3(DBH)_2]$ complex than for the analogous $[Nd(NO_3)_2(PicBH)_2]NO_3$ [12] complex (Fig. 2). This is easily seen by comparing the PAS lines at 520 nm ($^4G_{9/2}$+$^2D_{7/2}$), 579 nm ($^4G_{5/2}$+$^2G_{7/2}$), 740 nm ($^4S_{3/2}$), and 794 nm ($^4F_{5/2}$). The integrated intensity of all f–f transitions is twice greater for the $Nd(DBH)_2(NO_3)_3$ complex.

In conclusion, a new neodymium(III) hydrazone complex has been prepared, characterized by microanalysis and IR measurements, and its PA spectrum recorded at room temperature. Intense lines in the PA spectrum due to $\pi \rightarrow \pi^*$ and $n \rightarrow \pi^*$ transitions have been observed to be shifted to lower energies, which suggests that in some parts of the molecule bonding processes are different than in other rare-earth complexes. The integral intensity of f–f transitions in the PA spectrum for the new complex is about two times larger than for an analogous neodymium(III)–hydrazone complex, and thus its intermolecular transfer energy is more robust.

References

[1] ZHANGA S., SHERRYA D., J. Solid State Chem., 171 (2003), 38.
[2] AINSCOUGH W., BRODIE A., RANFORD J., WATERS J., Inorg. Chim. Acta, 236 (1995), 83.
[3] KOH L., KONB O., LOH K., LONG Y., RANFORD J., TAN A., TJAN Y., J. Inorg. Biochem., 72 (1998), 155.
[4] BOTTARI B., MACCARI R., MONFORTE F., OTTANA R., ROTONDO E., VIGORITA M., Bioorg. Med. Chem. Lett., 10 (2000), 657.
[5] AINSCOUGH W., BRODIE A., DENNY W., FINLAY G., GOTHE S., RANFORD J., J. Inorg. Biochem., 77 (1999), 125.
[6] KAYMAKCIOGLOU B., ROLLAS S., Farmaco, 57 (2002), 595.
[7] KÜÇÜKGÜZEL S., ROLLAS S., KÜÇÜKGÜZEL I., KIRAZ M., Eur. J. Med. Chem., 34 (1999), 1093.
[8] SRIDHAR S., SARAVANAN M., RAMESH A., Eur. J. Med. Chem., 36 (2001), 615.
[9] CHRISTIDIS P., TOSSIDIS I., PASCHALIDIS D., Acta Cryst., C 55 (1999), 707.
[10] PASCHALIDIS D., TOSSIDIS I., GDANIEC M., Polyhedron, 19 (2000), 2629.
[11] PASCHALIDIS D., Syn. React. Inorg. Metal., 8 (2004**),** 1401.
[12] GUSKOS N., PAPADOPOULOS G.J., MAJSZCZYK J., TYPEK J., WABIA M., LIKODIMOS V., PASCHALIDIS D.G., TOSSIDIS I.A., AIDINIS K., Acta Phys. Pol. A, 103 (2003), 301.
[13] GUSKOS N., TYPEK J., PAPADOPOULOS G.J., WABIA M., MAJSZCZYK J., ANAGNOSTAKIS E.A., MARYNIAK M., Mol. Phys. Rep., 39 (2004), 66.
[14] LYLE S., RAHMAN M., Talanta, 10 (1963), 1177.
[15] PAPADOPOULOS G.J., MAIR G.L.R., J. Phys. D: Appl. Phys., 25 (1992), 722.
[16] SAKAMOTO M., Inorg. Chim. Acta, 131 (1987), 139.
[17] CLARK R., WILLIAMS CH., Inorg. Chem., 4 (1965), 350.
[18] KHALIL T., LABIB L., ISKANDER M., REFAAT L., Polyhedron, 13 (1994), 2569.
[19] VARGAS G., MILLA M., HIDALGO DE CISNERAS L., RODRIGUEZ B., Spectrochim. Acta, A 43 (1987), 355.
[20] PAOLUCCI G., MARANGONI G., BANDOLI G., CLEMENTE D., J. Chem. Soc. Dalton, (1980), 1304.
[21] CURTIS N., CURTIS Y., Inorg. Chem., 4 (1965), 804.
[22] GUSKOS N., PAPADOPOULOS G.P., LIKODIMOS V., MAIR G.L.R., MAJSZCZYK J., TYPEK J., WABIA M., GRECH E., DZIEMBOWSKA T., PERKOWSKA T.A., J. Phys.: Appl. Phys., 33 (2000), 1.
[23] GUSKOS N., PAPADOPOULOS G.P., LIKODIMOS V., MAJSZCZYK J., TYPEK J., WABIA M., GRECH E., DZIEMBOWSKA T., PERKOWSKA T.A., J. Appl. Phys., 90 (2001), 1436.
[24] GUSKOS N., TYPEK J., PASCHALIDIS D.G., MARYNIAK M., submitted for publication in Mat. Chem. Phys.
[25] ADAMS M.J., HIGHFIELD J.G., KIRKBRIGHT G.F., Anal. Chem., 52 (1980), 1260.
[26] YUETAO Y., SHUYI Z., J. Mol. Struct., 646 (2003), 103.

Received 23 September 2004
Revised 4 December 2005

Materials Science-Poland, Vol. 23, No. 4, 2005

EPR study of chromium centres in CrAPO-5 molecular sieves

B. PADLYAK[1, 3*], J. KORNATOWSKI[4], G. ZADROŻNA[4], K. FABISIAK[1, 2], A. GUTSZE[2]

[1]Department of Physics, Kazimierz Wielki University of Bydgoszcz, pl. Weyssenhoffa 11, 85-072 Bydgoszcz, Poland

[2]Department of Biophysics, Ludwik Rydygier Collegium Medicum of the Nicolaus Copernicus University, ul. Jagiellońska 13, 85-067 Bydgoszcz, Poland

[3]Institute of Physical Optics, Dragomanova Str. 23, 79-005 L'viv, Ukraine

[4]Institute of Chemical Technology II, University of Technology, 85747 München, Germany

The X-band EPR spectra of CrAPO-5 molecular sieves exhibiting high or low sorption capacities for nitrogen and benzene, signed HS and LS samples, respectively, were studied at 300 and 77 K. The EPR spectra of the as-synthesized HS and LS samples consist of a broad intense signal ($g_{\text{eff}} = 1.971 \pm 0.001$, $\Delta H_{pp} \cong 500$ G) with a positive lobe at $g_{\text{eff}} = 5.15 \pm 0.01$, assigned to Cr^{3+} ($3d^3$, $^4F_{3/2}$) ions with a rhombic distorted octahedral coordination. Calcined samples show an additional narrow EPR signal of axial symmetry with $g_{||} = 1.971 \pm 0.001$ and $g_{\perp} = 1.959 \pm 0.001$, also assigned to Cr^{5+} ($3d^1$, $^2D_{3/2}$) ions in an octahedral coordination. HS samples heated under vacuum exhibit a decrease in the intensity of the Cr^{3+} lines as well as several new signals. Two of them are characterized by an axially symmetric *g* factor and belong to Cr^{5+} centres in square pyramidal and tetrahedral coordination. The third signal may be assigned to Cr^{+} ($3d^5$, $^6S_{5/2}$) ions. The EPR spectra of LS samples heated under vacuum show a strong decrease in the intensity of Cr^{3+} lines and only the two signals of Cr^{5+} centres in the same coordination. Their *g* factors are similar to those in the HS samples. Thermal treatment under oxidative (O_2) and reductive (H_2) atmospheres reveal the reproducible redox properties of Cr^{5+} ions and a high stability of Cr^{3+} ions, especially in the HS samples.

Key words: *CrAPO-5; chromium centres; EPR; g factor; redox properties*

1. Introduction

The incorporation of transition metals into the framework sites of aluminophosphate molecular sieves by isomorphous substitution for Al^{3+} or P^{5+} is a useful method

*Corresponding author, e-mail: fizbp@ab.edu.pl

for modifying the properties of such materials. Transition metals, however, which can easily form ions of various valences and coordination states, e.g. V, Cr, Mo, W, etc., have generally supplied substantial difficulties for such incorporation. Chromium belongs to the group of catalytically interesting metals. For example, $AlPO_4$-5 containing Cr has been used as a recyclable catalyst for the auto-oxidation of hydrocarbons, polymerisation of ethylene, etc. Therefore there have been many efforts to incorporate chromium into the frameworks of aluminophosphates in order to create isolated redox centres.

A possible introduction of Cr into silicates was reported more often than into aluminophosphate molecular sieves, and some authors have postulated an isomorphous substitution of Cr into the framework positions of silicate zeolites. Weckhuysen and Schoonheydt [1, 2] reported on extensive spectroscopic (EPR and diffuse reflectance spectroscopy) studies of Cr in $AlPO_4$-5 and in various silicates. They concluded that Cr cannot be substituted into the framework positions but that it is anchored at the surface, which is mainly due to a strong preference of the Cr^{3+} ions for octahedral coordination. Sheldon et al. [3–6] postulated a framework substitution of both Cr^{3+} and Cr^{6+} ions in octahedral and tetrahedral coordination on the basis of catalytic behaviour, in spite of the fact that Cr^{6+} species can easily be washed out from their calcined materials. Radaev et al. [7, 8] investigated large crystals of CrAPO-5 synthesized via the fluoride method and concluded that Cr occurs as an extra-framework species. A spectroscopic study of Cr-containing SAPO-5 showed pseudo-octahedrally coordinated Cr^{3+} ions [9]. From EPR, electron spin echo modulation, and UV-Vis spectroscopy investigations of CrAPSO-11, Kevan et al. [10] postulated that Cr^{3+} can be incorporated in small amounts in the initial as-prepared materials, but that after calcination it is transformed into Cr^{5+} located at P^{5+} framework sites. The same authors maintained to provide evidence for the framework substitution of small amounts of Cr^{3+} and Cr^{5+} ions in CrAPSO-5 from similar EPR and electron spin echo modulation spectroscopy investigations [11].

Our method of synthesis [12] has for the first time allowed stable substitution of larger amounts of Cr^{3+} for Al^{3+} in the framework of $AlPO_4$-5, i.e. producing CrAPO-5 material with high sorption (HS samples) properties typical of AFI structures. Other synthesis procedures similar to those reported in the above cited literature have regularly yielded materials with low or very low sorption (LS samples) properties, though most of the other features were similar for both groups [12]. Though the applied characterisation methods [12], especially UV-Vis spectroscopy, seemed to indicate explicitly the framework incorporation of chromium, the final determination of the valence state and geometry of the local environment of Cr ions in both types of CrAPO-5 has appeared to be difficult. Therefore, we performed detailed EPR examinations in order to study the features, local symmetry, and stability of chromium in $AlPO_4$-5, as well as the behaviour of incorporated Cr ions during thermal treatment under oxidizing (O_2) and reducing (H_2) atmospheres. The results of these investigations were first presented in [13]. Some results obtained by EPR spectroscopy are presented in this paper.

2. Experimental

The CrAPO-5 samples were synthesised following the general procedure for growing large crystals given in [14–16] and modified as described elsewhere [12, 13]. The obtained crystals had dimensions within the range 20–80 μm and morphologies of single hexagonal prisms typical of the AFI structure type [12]. All the prepared CrAPO-5 samples had an intense green colour after synthesis. The obtained samples were calcined under a slow stream of air at 773 K for at least 48 h. After calcination and template removal, the samples synthesised from pseudoboehmite Al compound were coloured green-yellow (samples 1 and 2) and the others (from amorphous Al compounds) greenish-grey or dirty grey (samples 3 and 4). The green-yellow colour of samples 1 and 2 could change to violet and reversibly to green-yellow depending on the state of hydration, while the grey colour of samples 3 and 4 was stable and independent of any treatment.

The synthesised samples differed distinctly in their sorption properties. The green -yellow samples showed an adsorption capacity for water typical of the AFI structure type and a high sorption capacity for benzene and nitrogen (HS samples 1 and 2) [12, 13]. The grey samples adsorbed hardly any nitrogen or benzene, and their sorption of water was also somewhat reduced (LS samples 3 and 4) [12, 13]. This behaviour indicates a normal open state of the channels in the HS materials and clogged channels in the LS materials.

The redox processes of the samples were carried out in special tubes from Varian using the Balzers–Pfeifer vacuum system, high purity oxygen and hydrogen, and an automatic electric furnace controlled by a computer. The oxidation (reduction) process of the CrAPO-5 samples included heating them to 773 K and exposing to an oxygen (hydrogen) atmosphere (P = 10 mbar) for 12 h at 773 K.

X-band EPR measurements of the CrAPO-5 samples were carried out at room and liquid nitrogen temperatures using a computer controlled RADIOPAN SE/X-2544 spectrometer with RCX 660 cylindrical TM_{110} cavity, operating in the high-frequency (100 kHz) magnetic field modulation mode. The EPR spectra of the CrAPO-5 polycrystalline samples were recorded in closed high-pure quartz tubes from Varian in air and vacuum. The g values of EPR lines were determined from experimental spectra using the resonance relationships and BRUKER computer simulation program „SimFonia". The microwave frequency in each specific case was determined by means of a polycrystalline diphenylpicrylhydrazyl (DPPH) frequency marker (g = 2.0036 ± 0.0001) and the EPR line of the coke radicals (g = 2.0032 ± 0.0001).

3. Results and discussion

3.1. EPR spectra of as-synthesised and calcined CrAPO-5 samples

Typical X-band EPR spectra measured at 300 K for the as-synthesised HS (Fig. 1, spectrum 1) and LS samples (spectrum 3) are similar. The spectra recorded at liquid

nitrogen temperature were similar as well and consisted of a broad line, A (g_{eff} = 1.971 ± 0.001, $\Delta H_{pp} \cong$ 500 G), of Lorenz shape and a positive lobe, B (g_{eff} = 5.15 ± 0.01). The intensities of A and B vary strongly between the samples (Fig. 1). Similar EPR spectra have been observed earlier for Cr in alumina [17], silica [18], chromosilicate [19], molecular sieves of the AEL [10, 20] and AFI [11] types, and a number of other compounds with a disordered structure, particularly in Cr-doped glasses of different compositions [21–23]. Both observed signals have been assigned to Cr^{3+} ($3d^3$, $^4F_{3/2}$) ions.

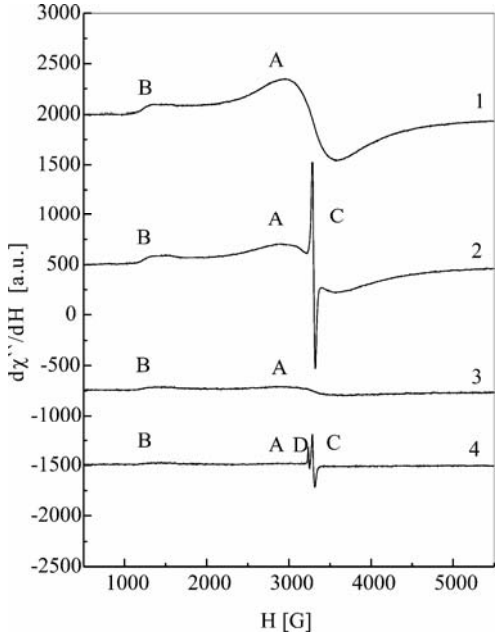

Fig. 1. Typical complete EPR spectra of HS (1, 2) and LS (3, 4) CrAPO-5 samples: 1, 3 – as-synthesised, 2, 4 – calcined samples (recorded at 300 K)

The A and B lines of Cr^{3+} ions were originally interpreted [18] by an analysis of the spin Hamiltonian:

$$H = \beta\, HgS + D[S_z^2 - 1/3S(S+1)] + E(S_x^2 - S_y^2) \qquad (1)$$

where D and E are the axial and orthorhombic crystal field terms, respectively, and β is the Bohr magneton. Such an interpretation of the EPR spectra of the Cr^{3+} ions in disordered systems has been confirmed in several studies [11, 20–23] and supported for CrAPSO-5 based on of computer simulation [11]. In particular, the best fit has been obtained for the following parameters of the spin Hamiltonian: $g_\perp$ = 1.98, $g_\parallel$ = 1.80, D = 0.50 cm^{-1}, E/D = 1/3, and a peak-to-peak derivative linewidth of ΔH_{pp} = 300 G. The simulated EPR spectrum of the Cr^{3+} ions showed a weak line at g_3 = 0.98 in addition to the two well-known lines at g_1 = 5.20 and g_2 = 2.00. This weak line has been found in the experimental spectra of CrAPSO-5 [11], whereas in the EPR spectra of our CrAPO-5 samples this line was not observed.

A significant broadening of the EPR lines of Cr^{3+} in CrAPO-5 samples ($\Delta H_{pp} \cong 500$ G) with respect to the same lines for CrAPSO-5 materials with very low contents of Cr ($\Delta H_{pp} = 300$ G) [11] can be related to a dipolar interaction of the Cr^{3+} ions [23–25]. We observed similar EPR spectra of isolated and dipolar-coupled Cr^{3+} ions in Cr/Al_2O_3 samples, which were used as a simple model system in our investigations.

Comparing our experimental data with those reported in [17–23], the observed EPR spectra of the as-synthesised HS and LS samples can be assigned to Cr^{3+} ions at sites with strongly (maximum) rhombic distorted ($|E/D| = 1/3$) octahedral coordination. Therefore, we may assume that chromium ions occur in the CrAPO-5 framework mainly as $CrO^{-}_{4/2}$ units complemented by two H_2O molecules from the pores, thus achieving a distorted octahedral coordination. This coordination gives the intense green colour to the species, which replace $AlO^{-}_{4/2}$ tetrahedra in the framework [12, 13]. The EPR lines of Cr^{3+} are much more intense (over 10 times) for the HS than for the LS samples (Fig. 1), despite much smaller differences in Cr content. The differences in the intensities suggest that some of the chromium may be retained during synthesis as ions with higher valence that may also be attached to the framework. This result correlates with UV-Vis spectroscopy, which shows that LS samples have a higher content of Cr^{6+}/Cr^{5+} and a lower content of Cr^{3+} centres than the HS samples [13]. One can notice that the concentration of the Cr^{5+} centres in the as-synthesised HS and LS samples is negligible and that their EPR spectra were not observed. Therefore, in the as-synthesised CrAPO-5 samples the Cr^{6+} ions, in general, are attached to the framework.

The EPR spectra of calcined HS and LS samples show a new narrow signal of chromium (denoted as C in spectra 2 and 4 of Fig. 1). The C signal is identical in all calcined HS and LS samples and consists of two weakly resolved lines (Fig. 2, spectra 1–4), which were not better resolved at liquid nitrogen temperature. The spectra of the calcined LS samples, however, show an additional isotropic symmetrical line, D, with $g = 2.0032 \pm 0.0001$ and $\Delta H_{pp} = (7.5 \pm 1.0)$ G (Fig. 1, spectrum 4 and Fig. 2, spectra 3–4). This D line was observed exclusively in the LS samples and was assigned to coke radicals [26], which formed in the channels from organic template molecules during the calcination process. A small amount of coke in the LS samples could provide an internal reference for determining the g values.

The parameters obtained from the experimental spectra have offered the possibility of simulating the C signal observed in calcined samples (Fig. 2, spectra 1–4). The computer simulation was performed using standard methods for disordered (polycrystalline or powdered) samples. The best fit of the simulated spectra to the experimental ones was obtained assuming a Lorenz line shape, with $\Delta H_{pp} = (16.5 \pm 1.0)$ G. The corresponding g factor values are given in Table 1. The g factors obtained for the C signals (Table 1) are similar to those of the octahedrally-coordinated Cr^{5+} ions in silica–alumina and alumina [17, 27–30]. It should be noted that the EPR spectra of Cr^{5+} in silica-alumina with low Al_2O_3 content (3 wt. %) are characterised by an anisotropic g factor and linewidth similar to that of Cr/SiO_2 ($g_\perp = 1.98$, $g_\parallel = 1.90$, $\Delta H_{pp} = 15$ G).

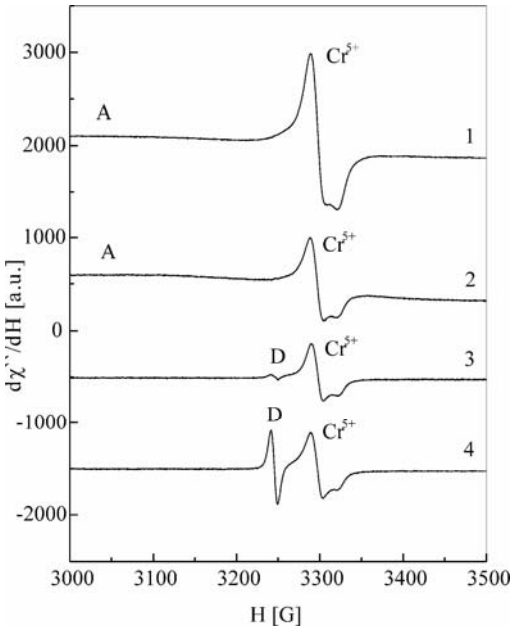

Fig. 2. Central region of the EPR spectra recorded at 300 K for the HS (1, 2) and LS (3, 4) CrAPO-5 samples calcined at 773 K. EPR signal C is attributed to Cr^{5+} ions

An increase of the Al_2O_3 content to 10 wt. % leads to a change in the spectral parameters of Cr^{5+} ($g_\perp = 1.97$, $g_{||} = 1.95$, $\Delta H_{pp} = 20$ G). In result, the Cr/Al_2O_3 system is characterised by an isotropic symmetric line with $g_0 = 1.96$ and $\Delta H_{pp} = 44$ G. An isotropic symmetric EPR line of Cr^{5+} ions with $g_0 = 1.972 \pm 0.001$ and $\Delta H_{pp} = 47.0 \pm 1.0$ G has also been observed by us in the model system Cr/Al_2O_3 calcined in air at 700 K. These changes in the EPR spectra are caused by the transformation of the coordination of Cr^{5+} from tetrahedral (local symmetry – T_d) in SiO_2 to square pyramidal with a short chromyl bond (local symmetry – C_{4v}) in Al_2O_3 [27, 30]. The adsorption of H_2O results in the transformation of the tetrahedral and square pyramidal coordinations of Cr^{5+} to an octahedral one in Cr/SiO_2, Cr/SiO_2–Al_2O_3, and Cr/Al_2O_3 systems and leads to an increase of the $g_{||}$ value from 1.90 to 1.95, i.e., to a "symmetrization" of the EPR spectra [31, 32].

Table 1. The g factors for the C signals of the calcined CrAPO-5 samples, obtained as the best fit of the spectra recorded at 300 K and simulated EPR spectra

Cr ion	g factor	HS samples		LS samples		Notes
		1	2	3	4	
Cr^{5+}	g_{xx}	1.970±0.001	1.971±0.001	1.972±0.001	1.972±0.001	$g_{xx} = g_{yy} = g_\perp$
	g_{yy}	1.970±0.001	1.971±0.001	1.972±0.001	1.972±0.001	
	g_{zz}	1.959±0.001	1.959±0.001	1.959±0.001	1.959±0.001	$g_{zz} = g_{||}$

Similar anisotropic EPR signals, with $g_\perp = 1.97$ and $g_{||} = 1.95$, for octahedrally-coordinated Cr^{5+} ions have been observed in hydrated zeolites of the ZSM-5 type

[33, 34]. During the oxidation process, Cr^{5+} ions are stabilised in the channels of ZSM-5 as CrO_2^+ particles with part of the non-framework O^{2-} ligands [33, 34]. These isolated ions in the zeolite structure may be considered to be coordinatively non-saturated surface ions, which define the catalytic activity of the material [34].

Therefore, signal C has been identified to correspond to isolated Cr^{5+} ions at axially-distorted octahedral sites. This signal appears during calcination and indicates that a certain part of the Cr^{3+} ions are oxidized to Cr^{5+} at sites with a more symmetric octahedral coordination.

3.2. EPR spectra of CrAPO-5 samples under vacuum heat treatment

Heat treatment at 773 K under vacuum (2.4×10^{-7} mbar) for 12 h led to the dehydratation of the calcined HS samples and lowered the coordination of the Cr ions. In result, the lines of Cr^{3+} (A and B lines in Fig. 1) and Cr^{5+} (C line in Fig. 2) vanished and several new EPR signals of Cr appeared (Fig. 3). Instead of the former Cr^{3+} signals, an extremely broad ($\Delta H_{pp} \cong 2500$ G) and intense signal appeared, with $g = 2.55 \pm 0.01$, attributed to Cr^{3+} as well and described in [13].

New narrow signals were three EPR signals originating from Cr^{5+} centres for the dehydrated HS (1) sample as well as two signals of Cr^{5+} and two signals of Cr^+ centres for the dehydrated HS (2) sample (Fig. 3, spectra 1 and 2). The identification of the new Cr centres was made on the basis of literature data for other Cr-containing oxide compounds, such as silica, silica–alumina, and alumina [10, 11, 27–34]. The assignments, *g* factors, and possible coordinations for Cr centres in all investigated samples after such treatment are presented in Table 2.

Table 2. Assignments and g factors of the experimental EPR signals, obtained at 300 K, for chromium ions in CrAPO-5 samples after heating at 773 K under vacuum (2×10^{-7} mbar) for 12 h, and the corresponding coordination of the Cr centres

Cr ion	*g* factor	HS samples		LS samples		Coordination
		1	2	3	4	
Cr^{5+} (1)	$g_{\|}$	1.962±0.001	1.960±0.001	1.962±0.002	1.961±0.002	Square
	$g_{\perp}$	1.974±0.001	1.969±0.001	1.975±0.002	1.974±0.002	pyramidal
Cr^{5+} (2)	$g_{\|}$	1.943±0.002	1.951±0.002	1.930±0.002	1.930±0.002	tetrahedral
	$g_{\perp}$	1.990±0.002	1.982±0.002	1.991±0.002	1.991±0.002	
Cr^{5+} (3)	$g_{\|}$	1.951±0.002	not observed	not observed	not observed	tetrahedral
	$g_{\perp}$	1.999±0.002				
Cr^+ (1)	g_{iso}	not observed	2.005±0.001	not observed	not observed	near to P^{5+} ion
Cr^+ (2)	g_{iso}	not observed	2.005±0.001	not observed	not observed	unknown

The EPR signals of Cr^{5+} ($3d^1$, $^2D_{3/2}$) ions in the dehydrated HS (1) sample are characterised by axially symmetric *g* factors and belong to centres in square pyramidal (Cr^{5+} (1) lines) and tetrahedral (Cr^{5+} (2) and Cr^{5+} (3) lines) coordinations. The

axially symmetric EPR signals of the HS (2) sample similarly belong to Cr^{5+} (1) and Cr^{5+} (2) centres in square-pyramidal and tetrahedral coordinations, respectively. The EPR signal of Cr^{+} ($3d^5$, $^6S_{5/2}$) ions, consisting of a single narrow ($\Delta H_{pp} \cong 9$ G) line (for Cr^{+} (2) centres) and two symmetric satellites (for Cr^{+} (1) centres) is characterised by an isotropic g factor ($g_{iso} = 2.005 \pm 0.001$). In our opinion, the two satellite lines are caused by the superhyperfine (SHF) interaction (the isotropic SHF constant $a_{iso} \cong 21$ G) of Cr^{+} (1) centres with one nucleus of the ^{31}P isotope (nuclear spin being $I = 1/2$, and natural abundance 100%).

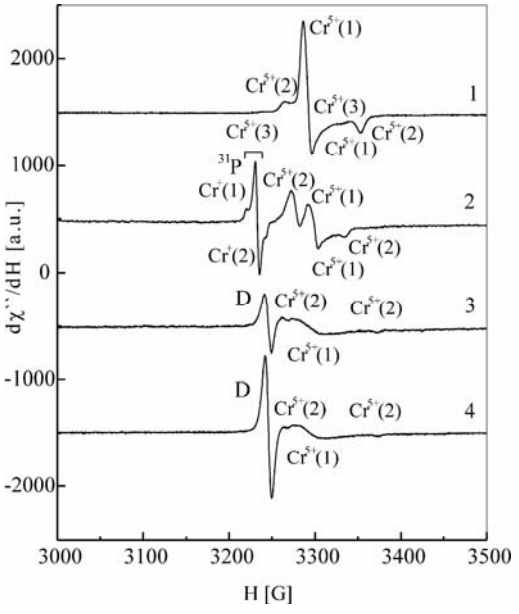

Fig. 3. Central region of the EPR spectra, recorded at 300 K, of HS (1 and 2) and LS (3 and 4) CrAPO-5 samples after heating at 773 K under vacuum (2×10^{-7} mbar) for 12 h

Vacuum heat treatment of the calcined LS samples under the same conditions as for HS samples led to a strong decrease of the Cr^{3+} lines (A and B in Fig. 1) and to a full disappearance of the octahedral Cr^{5+} centres (signal C in Fig. 2). Instead of the former Cr^{5+} signals, two new EPR signals appeared, which were attributed to Cr^{5+} (1) and Cr^{5+} (2) centres with square-pyramidal and tetrahedral coordinations, respectively (Fig. 3, spectra 3 and 4), and with g factors similar to those of the HS samples (Table 2). In the LS samples after vacuum heat treatment, only traces of the A and B Cr^{3+} signals (Fig. 1, spectra 3 and 4) were observed, whereas the characteristic of HS samples broad Cr^{3+} signal, with $g = 2.55 \pm 0.01$, was not observed. Together with a grey colour, these spectral features indicated that only a small amount of Cr^{3+} ions could be substituted into the framework positions of the LS samples.

The observed new forms of Cr^{5+} and Cr^{+} centres may be created from the extra-framework (or surface) Cr^{6+} and Cr^{2+} ions, respectively, under vacuum heat treatment. Some type of disproportionation reaction of Cr^{5+} or/and Cr^{3+} ions may also be imagined.

3.3. Redox behaviour of CrAPO-5 samples

The stability of the observed Cr^{+}, Cr^{3+}, and Cr^{5+} ions in CrAPO-5 was studied by applying redox processes to the calcined HS and LS samples, pre-treated in vacuum. Heat treatment in oxidative and reductive atmospheres did not considerably affect Cr^{3+} ions in either the HS or LS materials, but strongly influenced Cr^{+} and Cr^{5+} centres.

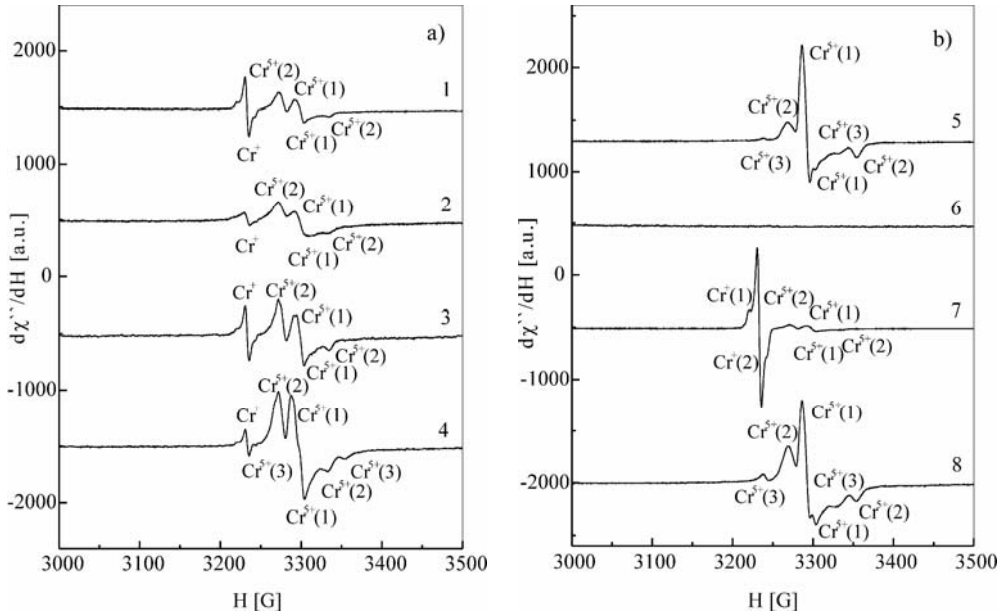

Fig. 4. Central region of the EPR spectra, recorded at 300 K, of the calcined HS (2) sample after the following treatments: a) heating at 773 K under vacuum (2×10^{-7} mbar) for 12 h (1), exposure to air (10 mbar) at 300 K for 85 h (2), adsorption of O_2 (10 mbar) at 300 K and evacuation (3), heating at 573 K under vacuum (8.9×10^{-6} mbar) for 1 h (4); b) heating at 773 K in O_2 (10 mbar) for 12 h and evacuation (5), heating at 773 K in H_2 (10 mbar) for 12 h and evacuation (6), exposure to air (10 mbar) for 4 h (7), heating at 773 K in O_2 (10 mbar) for 12 h and evacuation (8)

Changes in the EPR spectra of sample HS (2) after various oxidative and reductive treatments are show in Fig. 4. It should be noted that the spectrum of Cr^{+} centres was unstable and that its intensity decreased strongly after exposition to air at room temperature, whereas the intensities of the Cr^{5+} (1) and Cr^{5+} (2) spectra were only slightly reduced under the same conditions (Fig. 4a, spectra 1, 2). The adsorption of O_2 at 300 K with further evacuation of residual gas led to an increase of the intensity of Cr^{+} lines and to an improvement in the resolution of the Cr^{5+} (1) and Cr^{5+} (2) lines (Fig. 4a, spectrum 3). The observed differences between exposure to air and pure O_2 at room temperature may be connected to the adsorption of water from air, i.e. the hydration of sample. Heat treatment at 573 K in vacuum led to a decrease in the intensity of the Cr^{+} signal and to an increase in the intensity of the Cr^{5+} (1) and Cr^{5+} (2) EPR signals. This heat treatment also led to an appearance of an additional signal of

Cr^{5+} (3) (Fig. 4a, spectrum 4), with g factors ($g_{||}$ = 1.951±0.002 and $g_{\perp}$ = 1.999±0.002) similar to those of the Cr^{5+} (3) signal for the vacuum pre-treated HS (1) sample (Table 2). Oxidation of the HS (2) sample in an O_2 atmosphere at 773 K led to a full disappearance of the Cr^{+} EPR lines and to the appearance of a complex spectrum (Fig. 4b, spectrum 5) similar to that for the HS (1) sample pre-treated in vacuum (Fig. 3, spectrum 1). This complex spectrum belongs to the Cr^{5+} (1) and Cr^{5+} (2) centres, which are characterised by axially-symmetric g factors similar to those for the same Cr^{5+} centres in the HS (1) sample (Table 2). The reduction of the HS (2) sample with hydrogen at 773 K led to the full disappearance of all EPR lines (Fig. 4b, spectrum 6). Exposure to air at 300 K restored the initial Cr^{+} and Cr^{5+} EPR spectra (Fig. 4b, spectrum 7). Reoxidation in an O_2 atmosphere at 773 K led to the full disappearance of Cr^{+} spectra and restored the well-resolved complex EPR spectrum (Fig. 4b, spectrum 8) similar to that of the HS (1) sample (Fig. 3, spectrum 1) and the HS (2) sample after the first oxidation (Fig. 4b, spectrum 5).

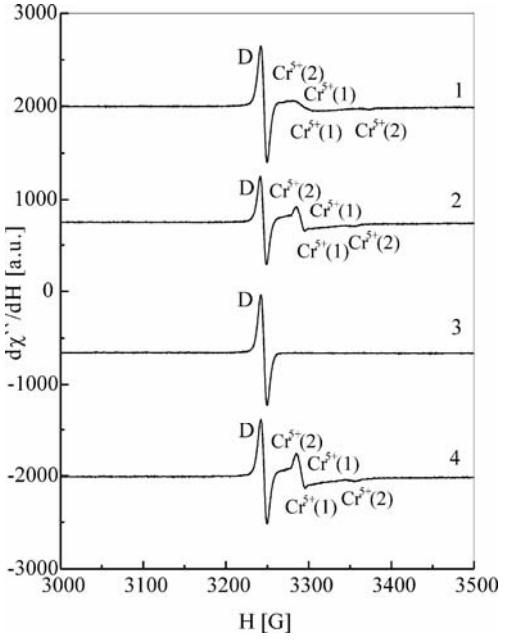

Fig. 5. Central region of the EPR spectra, recorded at 300 K, of the calcined LS (4) sample after heating at 773 K for 12 h: 1 – under vacuum (2×10^{-7} mbar), 2, 4 – in oxidising atmosphere (O_2, 10 mbar), 3 – in a reducing atmosphere (H_2, 10 mbar)

The CrAPO-5 LS samples revealed redox properties similar to those of the HS samples. Figure 5 shows the changes in the EPR spectra of the LS (4) sample calcined and pre-treated in vacuum (spectrum 1), after oxidation in oxygen (spectra 2, 4) and after reduction in hydrogen (spectrum 3). The oxidation of the LS (4) sample led to an insignificant change in the linewidth of the Cr^{5+} (1) centres and in the $g_{||}$ value of the Cr^{5+} (2) centres (Fig. 5, spectrum 2). Hydrogen reduction of the LS (4) sample led to the full disappearance of Cr^{5+} (1) and Cr^{5+} (2) lines (Fig. 5, spectrum 3). Reoxidation in oxygen gave the same EPR spectra of Cr^{5+} (1) and Cr^{5+} (2) centres as after the first oxidation (Fig. 5, spectrum 4). A decrease in the linewidth of Cr^{5+} (1) centres and

anisotropy of the *g* factor for Cr^{5+} (2) centres in the LS (4) sample after oxidation may suggest partial healing of the structure under oxidative treatment [35], in the sense Cr incorporating into CrAPO-5 framework positions. The almost constant line intensity of coke radicals (Fig. 5, line D) observed for the LS (4) sample during redox, however, indicated that a considerable part of chromium still remained as an extra-framework species in the channels. This part made the complete removal of organic carbonaceous residuals impossible.

4. Conclusions

Cr occurs in the HS samples mostly as Cr^{3+} in the octahedral form $[CrO_{4/2}L_2]^-$, as a framework species. A certain amount of Cr^{6+} and/or Cr^{5+}, seen with UV-Vis and/or EPR spectroscopy, seems to be either a framework species substituted for P or, more likely, a type of surface species anchored to the framework and not hindering diffusion and sorption in channels. In LS samples, Cr^{6+} and/or Cr^{5+} share to a distinctly higher extent, which most likely results in the clogging of pores.

In vacuum pre-treated calcined HS materials, Cr remains mostly as Cr^{3+} and two forms of Cr^{5+} appear: square pyramidal (five coordinated) chromyl groups and tetrahedrally coordinated Cr^{5+} centres. The latter may be an extra-framework species. In vacuum pre-treated calcined LS materials mainly tetrahedral extra-framework Cr^{5+} species occur, and Cr^{3+} exists in small amounts only. The LS samples also show a strong signal from carbon, which is extremely resistant against oxidation. Thus, the vacuum heat treatment of the calcined samples confirms the occurrence of Cr^{3+} in strongly prevailing amounts in the HS materials and indicates that only small amounts of Cr^{3+} exist in the LS materials. The formation of a small amount of Cr^{5+}, which does not hinder adsorption in the HS samples, may suggest that these ions can be substituted for P.

Oxidative and reductive treatments reveal reproducible redox properties of Cr^{5+} centres in square-pyramidal and tetrahedral coordinations in both HS and the LS calcined CrAPO-5 samples pre-treated in vacuum. These treatments do not considerably influence the EPR spectra of the Cr^{3+} ions in the samples. Results reveal a high stability of the Cr^{3+} ions, especially in HS CrAPO-5 materials, which can be justified only by framework incorporation.

Acknowledgements

This work was partially supported by the Deutsche Forschungsgemeinschaft, and by the Polish Committee for Scientific Research (KBN) within the Grant No. 3T09A04714.

References

[1] WECKHUYSEN B.M., SCHOONHEYDT R.A., Zeolites, 14 (1994), 360.
[2] WECKHUYSEN B.M., SCHOONHEYDT R.A., Stud. Surf. Sci. Catal., 84 (1994), 965.

[3] SHELDON R.A., CHEN J.D., DAKKA J., NEELMAN E., Stud. Surf. Sci. Catal., 83 (1994), 407.
[4] CHEN J.D., HAANEPEN M.J., VAN HOOF J.H.C., SHELDON R.A., Stud. Surf. Sci. Catal., 84 (1994), 973.
[5] LEMPERS E.B., CHEN J.D., SHELDON R.A., Stud. Surf. Sci. Catal., 94 (1995), 705.
[6] LEMPERS H.E.B., SHELDON R.A., Stud. Surf. Sci. Catal., 105 (1997), 1061.
[7] RADAEV S.F., JOSWIG W., BAUR W.H., J. Mater. Chem., 6 (1996), 1413.
[8] TRIELE S., HOFFMANN K., VETTER R., MARLOW F., RADAEV S., Zeolites, 19 (1997), 190.
[9] DEMUTH D., UNGER K.K., SCHÜTH F., SRDANOV V.I., STUCKY G.D., J. Phys. Chem., 99 (1995), 479.
[10] ZHU Z., WASOWICZ T., KEVAN L., J. Phys. Chem., B 101 (1997), 10763.
[11] ZHU Z., KEVAN L., Phys. Chem. Chem. Phys., 1 (1999), 199.
[12] KORNATOWSKI J., ZADROZNA G., [in:] Proc. of the 12th IZC, Baltimore, USA, 1998; M.M.J. Treacy, B.K. Marcus, M.E. Bisher, J.B. Higgins (Eds.), Materials Research Society, Warrendale, 1999, vol. III, p. 1577.
[13] PADLYAK B.V., KORNATOWSKI J., ZADROŻNA G., ROZWADOWSKI M., GUTSZE A., J. Phys. Chem. A., 104, (2000), 11837.
[14] KORNATOWSKI J., FINGER G., Bull. Soc. Chem. Belg., 99 (1990), 857.
[15] FINGER G., RICHTER-MENDAU J., BÜLOW M., KORNATOWSKI J., Zeolites, 11 (1991), 443.
[16] KORNATOWSKI J., ROZWADOWSKI M., FINGER G., Pol. Pats. PL 166147, 166149, 166162, 166505 (all 1995).
[17] O'REILLY D.E., MACLVER D.S., J. Phys. Chem., 66 (1962), 276.
[18] CORNET D., BURWELL R.L., J. Am. Chem. Soc., 90 (1968), 2489.
[19] PRZHEVALSKAYA L.K., SHVETS V.A., KAZANSKII V.B., Kinet. Catal. (USSR), 11 (1970), 1085.
[20] WECKHUYSEN B.M., SCHOONHEYDT R.A., MABBS F.E., COLLISON D., J. Chem. Soc., Faraday Trans., 92 (1996), 2431.
[21] ZAKHAROV V.K., YUDIN D.M., Sov. Phys. Solid State, 7 (1965), 1267.
[22] PADLYAK B.V. GUTSZE A., Appl. Magn. Reson., 14 (1998), 59.
[23] LANDRY R.J., FOURNIER J.T., YOUNG C.G., J. Chem. Phys., 46 (1967), 1285.
[24] TROUNSON E.P., BLEIL D.F., WAGNESS R.K., MAXWELL R.L., Phys. Rev., 79 (1950), 542.
[25] FOURNIER, J.T., LANDRY, R.J., J. Chem. Phys. 55 (1971) 2522.
[26] LANGE J.-P., GUTSZE A., KARGE H.G., J. Catal., 114 (1988), 136.
[27] VAN REIJEN L.L., COSSEE P., HAREN H.J., J. Chem. Phys., 38 (1963), 572.
[28] PECHERSKAYA YU. N., KAZANSKII VB., *Kompleksoobrazovanie v katalize* (*Formation of Complexes in Catalysis*), Nauka, Moscow, 1968.
[29] BORESKOV G.K., BUKANAEVA F.M., DZISKO V.A., Kinet. Catal. (USSR), 5 (1964), 434.
[30] VAN REIJEN L.L., COSSEE P., Disc. Faraday Soc., 41 (1966), 277.
[31] KAZANSKII V.B., PECHERSKAYA YU.N., Kinet. Catal. (USSR), 4 (1963), 244.
[32] KUCHEROV A.V., SLINKIN A.A., Zeolites, 7 (1987), 38, 43.
[33] KUCHEROV A.V., SLINKIN A.A., Kinet. Catal. (USSR), 27 (1986), 1199.
[34] SLINKIN A.A., KUCHEROV A.V., GORYASHCHENKO S.S., ALESHIN E.G., SLOVETSKAYA K.I., Kinet. Catal., 30 (1986), 184.
[35] BRÜCKNER A., LOHSE U., MEHNER H., [in:] *Magnetic Resonance and Related Phenomena*, Vol. II, Extended Abstracts of the Joint 29th AMPERE, 13th ISMAR Intern. Conf., Eds. D. Ziessow, W. Lubitz, F. Lendzian, Techn. Univ. Berlin, Berlin, 1998, p. 1053.

Received 10 November 2004
Revised 18 March 2005

Materials Science-Poland, Vol. 23, No. 4, 2005

Magnetic resonance study of $SbVO_5$ thermal decomposition products

J. TYPEK[1*], E. FILIPEK[2], M. MARYNIAK[1], N. GUSKOS[1, 3]

[1]Institute of Physics, Szczecin University of Technology, al. Piastów 17, 70-310 Szczecin, Poland

[2]Department of Inorganic and Analytical Chemistry, Szczecin University of Technology, al. Piastów 42, 71-065 Szczecin, Poland

[3]Solid State Section, Department of Physics, University of Athens, Panepistimiopolis, 15 784 Zografos, Athens, Greece

A new $SbVO_5$ compound, which can be synthesized from an equimolar mixture of Sb_2O_3/V_2O_5 or α-Sb_2O_4/V_2O_5 oxides by heating in air to temperatures below 650 °C, is stable in air up to 710 °C and in argon atmosphere up to ~645 °C. At higher temperatures it decomposes into a phase with a rutile-type structure. Using electron spin resonance (ESR) we have studied the magnetic properties of the thermal decomposition products of $SbVO_5$ in air (sample 1D) and in argon atmosphere (sample 2D), as well as two phases of the of the rutile-type structure (samples 3S and 4S) synthesized at conditions similar to the previous two samples. The ESR spectra of all four samples consisted mostly of two types of lines: a narrow line (designated as the N component) and a very broad line (designated as the VB component). Close inspection of the ESR parameters for these components allowed the samples to be grouped according to the environment they were annealed in (air or oxygen-free argon). The origin of these lines and the implications concerning the phase composition of the decomposition products are discussed. ESR results confirm that the solid decomposition product of $SbVO_5$ in air is a non-stoichiometric compound with a rutile structure and formula $Sb^{5+}_{0.9}V^{3+}_{0.1}V^{4+}_{0.8}\square_{0.2}O_4$ and in argon a near -stoichiometric $V^{4+}Sb^{5+}O_{4.5}$.

Key words: *electron spin resonance; vanadate compounds*

1. Introduction

Acrylonitrile (ACN), with a worldwide annual production of well over 5 million tons, is produced, among others, by the ammoxidation of propylene, using catalysts from the Bi-Fe-Mo-O or USb_3O_{10}–Sb_2O_4 (SOHIO process) systems [1, 2]. In the last decade, for economic reasons (the price of propylene is about six times higher than

* Corresponding author, e-mail: typjan@ps.pl

that of propane), investigations of new catalytic materials for the direct synthesis of acrylonitrile from propane have been carried out, which would reduce the price of ACN by ~20 % [3–6]. As the catalysts synthesized from a mixture of antimony and vanadium oxides and/or containing compounds formed in the Sb–V–O system reveal a good activity and high selectivity in the direct ammoxidation of propane to acrylonitrile, they have been the subjects of an intense research [4, 7–10].

Knowledge of the exact number of phases formed in the Sb–V–O system and of their chemical and physical properties is crucial for the formation of a new class of catalysts. According to rich literature on the possible phases formed in the Sb–V–O system, the most important two factors during synthesis are the type of starting oxides and the gaseous atmosphere used [11–14]. It has been established that the annealing of an equimolar mixture of Sb_2O_3/V_2O_5 or α-Sb_2O_4/V_2O_5 oxides in air at 800 °C leads to the formation of a non-stoichiometric compound with a rutile structure, described by the formula $Sb^{5+}_{0.92}V^{3+}_{0.28}V^{4+}_{0.64}\square_{0.16}O_4$ where the square denotes a cation vacancy [11–13]. Canovas et al. have synthesized vanadium antimonate from Sb_2O_3/V_2O_5 in an atmosphere with a variable O_2/N_2 ratio and obtained the first continuous series of non-stoichiometric rutile-type $Sb_{0.9}V_{0.9+x}\square_{0.2-x}O_4$ ($0 < x < 0.2$) phases containing variable proportions of V^{3+} and V^{4+} ions, ranging from $Sb^{5+}_{0.9}V^{3+}_{0.1}V^{4+}_{0.8}\square_{0.2}O_4$ ($x = 0$ in O_2) to $Sb^{5+}_{0.9}V^{3+}_{0.9}V^{4+}_{0.2}\square_{0.0}O_4$ ($x = 0.2$ in N_2) [12]. For the second series, synthesized at reducing conditions, the authors described the phases as $Sb_{0.9-y}V_{1.1+y}O_4$, where $0 < y < 0.7$. In compounds of this type, antimony – similarly as in the previous series – is in the 5+ oxidation state and vanadium in both the 3+ and 4+ oxidation states. This series of phases was recognized as a solid solution spreading between $Sb_{0.9}V_{1.1}O_4$ and VO_2 [12]. Birchal and Sleight [13], as well as Berry et al. [14], have synthesized vanadium antimonate from Sb_2O_3/V_2O_5 in closed containers at 800 °C and obtained $Sb_{0.95}V_{1.05}O_4$ and $VSb_{1-y}O_{4-2y}$ ($0 < y < 0.1$), respectively. Berry et al. have provided evidence that in an atmosphere of oxygen-free nitrogen the obtained compound could be described by the formula $VSb_{1-y}O_{4-3/2y}$ [14]. The opinion of the majority of researchers in this field is that antimony in these phases is in the 5+ oxidation state, while vanadium in 4+ one. A small number of researches claim that the stoichiometric $Sb^{3+}V^{5+}O_4$ could be synthesized from an equimolar mixture of antimony(III) oxide with vanadate(V) oxide in argon atmosphere [15–17]. Furthermore, near stoichiometric antimony vanadate, with the formula $V^{4+}Sb^{5+}O_{4.5}$, could be synthesized using a novel peroxide-based sol-gel synthesis procedure [18].

Our investigations have shown that annealing an equimolar mixture of Sb_2O_3/V_2O_5 or α-Sb_2O_4/V_2O_5 oxides at temperatures not higher than 650 °C leads to the formation of the $SbVO_5$ compound in air [19], and the $SbVO_{4.5}$ ($Sb_2V_2O_9$) compound has been synthesized from α-Sb_2O_4/V_2O_5 oxides in an atmosphere of oxygen-free argon [20].

$SbVO_5$ differs from currently known compounds in many ways: its XRD, IR, and thermal properties are different, not to mention its colour. It is very probable that in this compound the Sb and V ions are in the 5+ oxidation state [21]. $SbVO_5$ is stable in

air up to 710 °C, and in oxygen-free argon up to ~645 °C, where it decomposes in the solid state into one phase with a rutile-type structure [19].

Electron spin resonance (ESR) studies of the $SbVO_5$ compound have already been erformed in the 3.6–300 K temperature range [21]. At room temperature only a weak ESR signal was detected, corroborating the absence of bulk V(IV) ions in the structure. Below 100 K, a well resolved hyperfine structure typical of isolated vanadium ions in axial symmetry, present as VO^{2+} species, and a broad line attributed to electron hopping along V^{4+}–O–V^{5+} bonds, can be seen. At 3.65 K, a spectrum typical for a triplet state, indicating the presence of two interacting VO^{2+} species, was recorded.

In this paper, the results of ESR investigations of both decomposition products of $SbVO_5$ (in air and in argon) and of the rutile-type phases, synthesized in conditions similar to the decomposition conditions, have been carried out. The aim of this study is to gain knowledge on the decomposition products of $SbVO_5$ and to resolve the problem of the oxidation state of vanadium ions (+3 or +4) in these phases. The question of the oxidation states of metal ions in non-stoichiometric rutile-type compounds has been the subject of some controversy and is of great importance for the interpretation of catalytic mechanisms.

2. Experimental

$SbVO_5$ was prepared by heating an equimolar mixture of V_2O_5 (p.a. product, POCh, Gliwice, Poland) with α-Sb_2O_4 (obtained by heating in air pure Sb_2O_3, Merck, Germany, in air) by the method described in Ref. [19]. Two samples of the obtained $SbVO_5$ powder were subject to the following thermal treatment: the first sample (designated as 1D) was heated in air at 735 °C for 24 h, the second (designated as 2D) was heated in oxygen-free argon for 24 h at 660 °C. The heating temperatures were selected so as to fall into the temperature range between the onset and maximum temperatures of the endothermic effect recorded in the DTA curves of $SbVO_5$. These decomposition changes were accompanied by a mass loss of ~ 3.5 wt. % in air and 3.2 wt. % in argon, as evidenced by TG curves.

Two additional samples (designated as 3S and 4S) were obtained by heating an equimolar mixture of α-Sb_2O_4 and V_2O_5 oxides at temperatures close to that at which $SbVO_5$ decomposes. Sample 3S is a product of the synthesis of these oxides in air at 735 °C, lasting 36 h (2 times by 18 h). Sample 4S was synthesized in an oxygen-free argon atmosphere at 650 °C for 24 h. The diffractograms of all four samples were very similar and contained the same set of diffraction lines. The only difference was that the respectable interplane distances were slightly greater for samples synthesized in air. The indexation of a selected diffractogram showed that the investigated phases had a rutile-type structure [20].

ESR measurements were carried out on a standard X band spectrometer (Bruker E 500) at room temperature. The spectrometer was equipped with a TE_{102} cavity and 100 kHz field modulation. The investigated samples were in powder forms and were

placed into 4 mm diameter quartz tubes. The masses of samples 1D, 2D, 3S, and 4S were 30.7, 26.6, 56.0, and 47.0 mg, respectively. ESR detects the power P absorbed by the sample from the transverse magnetic microwave field as a function of the static magnetic field. The signal-to-noise ratio is improved by recording the derivative d*P*/d*H*, using the lock-in technique with field modulation. For the estimation of the number of spins participating in the resonance, a standard sample of polycrystalline $VOSO_4 \cdot 5\ H_2O$ was used.

3. Results and discussion

Vanadium ions exhibit a wide range of stable oxidation states, among them being the often-encountered V(III), V(IV), and V(V) states. Vanadium(V), with a $3d^0$ configuration, is diamagnetic and thus ESR inactive. Vanadium(III) is not a Kramer's ion, possessing two unpaired electrons, and as such is not likely to give an ESR signal in the experimental condition of the present study. In many biological and materials science systems the majority of vanadium exists in paramagnetic oxovanadium(IV) VO^{2+} ions complexed in some form. Various V(IV) species could be detected by the ESR technique. Vanadium (IV) clusters give rise to a broad signal owing to significant dipolar interactions, whereas isolated V(IV) species exhibit a hyperfine structure derived from the interaction of free electrons ($3d^1$) with the magnetic nuclear moment of ^{51}V (I = 7/2). In this case, the ESR signal splits eightfold. In solids, the hyperfine structure can be substantially suppressed or even disappear due to various interactions of electron spins with their surroundings. For example, in conducting vanadate glasses (V_2O_5–TeO_2) such interaction occurs via the so-called super-exchange of electrons, i.e. the hopping of a mobile electron along V^{4+}–O–V^{5+} bonds [22].

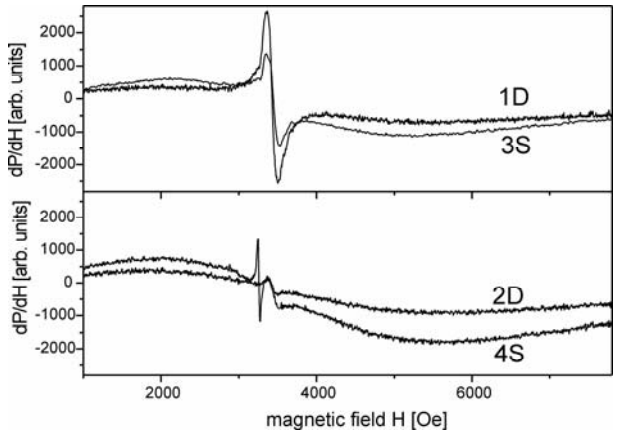

Fig. 1. ESR spectra of the four investigated samples:
samples 1D and 3S – upper panel, samples 2D and 4S – lower panel.
The sample masses are different, hence
the spectral intensities are not directly comparable

The experimental ESR spectra, taken at room temperature, of all four investigated samples are shown in Fig. 1. All recorded spectra show the same features: the presence of one very broad (designated as VB) and one relatively narrow (designated as N) resonance line. Additionally, the spectrum of sample 4S contains a very narrow component (designated as VN). The values of the ESR parameters for all these lines, i.e. the peak-to-peak linewidth ΔH_{pp}, effective g-factor, and relative intensity I_r, were found by fitting the experimental spectra and are presented in Table 1. As the linewidth of the VB component is of the same order of magnitude as the resonance field H_{res}, both circular components of the exciting linearly polarized microwave field have to be taken into account in calculations. Therefore, the resonance at the reversed magnetic field, $-H_{res}$, was included into the fit (using a Lorentzian-type line) for the VB component [23]. The relative intensity I_r was calculated by numerical integration of the absorption spectra of the four investigated samples and refers to a unit mass of the sample. The most intensive VB component in the ESR spectrum of sample 4S was taken as the unit of the relative intensity.

Table 1. ESR parameters for various spectral components of the four investigated samples

Sample	Spectrum component	Peak-to-peak linewidth [Oe]	Effective g-factor	Relative intensity [a. u.]
1D	VB	4160	1.880	0.59
	N	142	1.957	$30 \cdot 10^{-4}$
2D	VB	4650	1.868	0.92
	N	130	1.967	$4 \cdot 10^{-4}$
3S	VB	3780	1.912	0.47
	N	149	1.961	$30 \cdot 10^{-4}$
4S	VB	4480	1.877	1.00
	N	144	1.965	$7 \cdot 10^{-4}$
	VN	27	2.074	$0.7 \cdot 10^{-4}$

None of the observed lines displays the hyperfine structure expected for V^{4+} paramagnetic ions with nuclear spins. Usually, this absence is explained by the exchange interaction between neighbouring ions and by the delocalisation of the $3d^1$ electrons of V^{4+}, particularly in the conducting state of the material. It follows that in our samples there are no V^{4+} ions that are not subject to magnetic interactions. Thus the observed paramagnetic centres must be close enough ($d < 0.7$ nm) to allow spin–spin interactions. For the VB component, the interaction between V^{4+} ions is particularly strong, leading to the formation of bulk clusters. A similar broad line was observed in variable oxygen stoichiometry materials such as $La_2NiO_{4+\delta}$and $(V_{1-x}Mo_x)_{2-\delta}O_3$ [23].

The relative intensity of the VB component in the four investigated samples (Table 1) allow them to be divided into two groups: those processed in oxygen-free argon and with larger intensity (samples 4S and 2D), and the second group processed in air

and exhibiting the ESR signal roughly twice as weak (samples 1D and 3S). Also, the linewidths and *g*-factors of the VB component correlate well with this division: samples processed in air are on average 595 Oe narrower than those processed in oxygen-free argon, and their *g*-factors are larger by 0.024.

Although the ESR intensity of the N component is about three orders of magnitude smaller than that of the VB line, the same grouping of samples is observed if the ESR intensity of the N spectral component is considered. This time, though, samples 1D and 3S display a larger intensity, and their integral intensity is about six times stronger than that of samples 2D and 4S. The linewidth (130–149 Oe) and *g*-factor (1.957–1.967) for this line seem to be independent of the type of sample. The VN component observed only in the spectrum of sample 4S is the weakest of all lines, about one order of magnitude less intensive than the weakest N component line. Its linewidth is small and its *g*-factor greater than 2 – it may arise from an unwanted paramagnetic contamination and will not be discussed further.

A comparison of the ESR intensities of the four samples with the intensity of a standard allows the absolute number of paramagnetic centres in the investigated compounds to be determined. Taking into account the uncertainties in determining the masses and areas under the ESR absorption curves, the accuracy of this number was estimated to be about 30%. Within this limit, it was calculated that almost all vanadium ions present in the samples contributed to the recorded ESR spectra, i.e. were in the 4+ oxidation state. It is known that the spectra of vanadium(IV) ions, located in a perfect oxygen octahedron, are characterized by a short spin-lattice relaxation time [24]. As a result, the ESR spectra of V(IV) ions in the substitution positions of rutile are observed only at low temperatures. In contrast, in the case of V(IV) ions in a pressed octahedron, and at the interstitial positions, ESR spectra are observed at room temperature.

Taking into account all the discussed ESR features of the investigated samples, it is proposed that the VB component lines arise from vanadium(IV) clusters present inside the micrograins forming the powder samples, while the B component arises from vanadium(IV) ions located on the surface of these grains. The relative ESR intensity of the VB and B components ($\sim 10^{-3}$) reflects the relative number of these centres and also the volume fraction of the sample they occupy. This value seems reasonable taking into account the mean grain diameter. As in the $SbVO_5$ compound, the bulk of the vanadium is in the 5+ valence state and thus unobservable in ESR spectrum, and the heating of this sample causes the conversion of V(V) to V(IV) and loss of oxygen. As the electrons needed for vanadium conversion originate from released oxygen, the bigger the oxygen loss the stronger the intensity of the ESR signal. This is indeed what is being observed: oxygen loss is bigger for samples heated in an argon atmosphere and the VB component in the ESR spectra of these samples is more intense. A slightly greater linewidth of the argon-processed samples might be evidence of a larger spread of the ESR parameters of the involved paramagnetic centres, which in turn could be interpreted as the result of a more defective environment.

As far as the B component of the ESR spectra is concerned, it is proposed that it originates from V(IV) ions located at or near the surfaces of the grains. There are relatively more such vanadium(IV) ions in oxygen-processed samples, as the availability of valence conversion electrons is greater in these samples. The mobility of such electrons might be significantly reduced due to the abundance of defects in this layer, leading to long relaxations and narrow ESR lines.

Similarly, the ESR spectra of samples 1D and 3S (both air-processed) allow the assumption that the solid decomposition product of $SbVO_5$ in air is a non-stoichiometric compound with a rutile structure and the formula $Sb^{5+}_{0.9}V^{3+}_{0.1}V^{4+}_{0.8}\square_{0.2}O_4$ [12]. This assumption is further corroborated by comparing the theoretical (3.52 wt. %) and experimental (3.5 wt. %) oxygen mass loss during the decomposition stage:

$$9SbVO_5 = 10Sb_{0.9}V^{3+}_{0.1}V^{4+}_{0.8}O_4 + 5/2O_2$$

Oxygen released during that process increases the partial pressure of the gas in air, which stimulates the increase of the number of cation vacancies in the crystal lattice. An investigation of the electrical properties of the decomposition product has showed that it is a p-type semiconductor [25]. Slight differences between the ESR spectra of samples 1D and 3S may be related to a lower concentration of cation vacancies in sample 3S. According to literature data, the formula for the 3S compound is $Sb^{5+}_{0.92}V^{3+}_{0.28}V^{4+}_{0.64}\square_{0.16}O_4$. Thus the V^{4+}/V^{3+} ratio for the sample 1D should be significantly greater than that for 3S. This is indeed what can be observed for the ESR intensity of the VB component in these samples.

The solid decomposition product of $SbVO_5$ in oxygen-free argon is probably the near stoichiometric compound $Sb^{5+}V^{4+}O_{4.5}$. Its formation is favoured by a lower temperature of decomposition and a lower oxygen partial pressure, which results in the lack of that gas at the solid/gas interface. Thus the decomposition process could be summarized by the equation

$$SbVO_5 = Sb^{5+}V^{4+}O_{4.5} + 1/4O_2$$

Mass loss calculated from this equation (3.17 wt. %) compares favourably with the value observed using thermogravimetric methods (3.2 wt. %).

4. Conclusion

Two decomposed samples of $SbVO_5$ and two synthesized samples aimed at obtaining the same compounds were investigated by room temperature ESR. The obtained spectra were similar, proving that decomposition and synthesis leads to the same results. The oxidation state of the majority of vanadium ions has been determined as 4+. The ESR spectra of two types of vanadium paramagnetic centres have been identified in the investigated samples and connected with the surface and interior of the grains.

ESR results confirm that the solid decomposition product of $SbVO_5$ in air is a non-stoichiometric compound with a rutile structure and formula $Sb^{5+}_{0.9}V^{3+}_{0.1}V^{4+}_{0.8}\square_{0.2}O_4$, and in argon the near stoichiometric $V^{4+}Sb^{5+}O_{4.5}$. An investigation of the temperature dependence of the ESR spectra may shed more light on the origin and dynamics of the paramagnetic centres and is planned for the future.

References

[1] BETTARHAR M.M., COSTENTIN G., SAVARY L., LAVALLEY J.C., Appl. Catal., A 145 (1996), 1.
[2] NILSSON R., LINDBLAD T., ANDERSSON A., Catal. Lett., 29 (1994), 409.
[3] NILSSON J., LANDA-CANOVAS A., HANSEN S., ANDERSSON A., J. Catal., 160 (1996), 244.
[4] CENTI G., PERATHONER S., TRIFIRO F., Appl. Catal. A, 157 (1997), 143.
[5] GRASSELLI R.K., Catal. Today, 49 (1999), 141.
[6] GUERRERO- PEREZ M.O., FIERRO J.L.G., BANARES M.A., Catal. Today, 78 (2003), 387.
[7] ALBONETTI S., BLANCHARD G., BURATTIN P., CASSIDY T.J., MASETTI S., TRIFIRO F., Catal. Lett., 45 (1997), 119.
[8] NILSSON J., LANDA-CANOVAS A., HANSEN S., ANDERSSON A., Catal. Today, 33 (1997), 97.
[9] CHIANG H.B., LEE M.D., Appl. Catal. A,154 (1997), 55.
[10] CENTI G., MAZZOLI P., Catal. Today, 28 (1996), 351.
[11] HANSEN S., STAHL K., NILSSON R., ANDERSSON A., J. Solid State Chem.,102 (1993), 340.
[12] LANDA-CANOVAS A., NILSSON J., HANSEN S., STAHL K., ANDERSSON A., J. Solid State Chem., 116 (1995), 369.
[13] BIRCHALL T., SLEIGHT A.W., Inorg. Chem., 15 (1976), 868.
[14] BERRY F.J., M.E.BRETT M.E., PATTERSON W.R., J. Chem. Soc., Dalton Trans. (1983), 9.
[15] VERNON L.A., MILLIGAN W.O., Tex. J. Sci., 1 (1951), 82.
[16] RENAUD R., Rev. Chem. Miner., 8 (1971), 633.
[17] ROTH R.S., WARING J.L., Am. Mineral., 48 (1963), 1348.
[18] BRAZDIL J.F., TOFT M.A, BARTEK J.P., TELLER R.G., CYNGIER R.M., Chem. Mater., 10 (1998), 4100.
[19] FILIPEK E., J. Therm. Anal. Cal., 56 (1999), 159.
[20] FILIPEK E., RAKOWSKA K., Proc. VIIth European Conference on Solid State Chemistry, ECSSC' 99, Madrid (Spain), 1999, Book of Abstracts, Vol. I, P-32.
[21] TYPEK J., GUSKOS N., BUCHOWSKI D., WABIA M., FILIPEK E., Rad. Effect. Def. Solids, 157 (2002), 1093.
[22] GUPTA S., KHANIJO N., MANSINGH A., J. Non-Cryst. Solids, 181 (1995), 58.
[23] TENAILLEAU C., KASSIBA A., LACORRE P., J. Phys. Chem. Solids, 65 (2004), 1809.
[24] KOSOVA N.V., VOSEL S.V., ANUFRIENKO V.F., VASENIN N.T., DEVYATKINA E.T., J. Solid State Chem. 160 (2001), 444
[25] GRON T., FILIPEK E., KUKULA Z., KRAJEWSKI A., DUDS H., Proc. European Congress on Advanced Materials and Processes, Lausanne, Switzerland, Abstracts, P-21390

Received 23 September 2004
Revised 3 February 2005

Materials Science-Poland, Vol. 23, No. 4, 2005

Temperature dependence of the FMR spectra of Fe_3O_4 and Fe_3C nanoparticle magnetic systems in copolymer matrices

T. BODZIONY[1*], N. GUSKOS[1, 2], J. TYPEK[1], Z. ROSLANIEC[3], U. NARKIEWICZ[4], M. KWIATKOWSKA[3], M. MARYNIAK[1]

[1]Institute of Physics, Szczecin University of Technology, al. Piastów 17, 70-310 Szczecin, Poland

[2]Solid State Section, Department of Physics, University of Athens, Panepistimiopolis, 15 784, Greece

[3]Institute of Material Engineering, Szczecin University of Technology, al. Piastów 17, 70-310 Szczecin, Poland

[4]Department of Chemical Engineering, Szczecin University of Technology, al. Piastów 17, 70-310 Szczecin, Poland.

A binary magnetic nanoparticle system, consisting of Fe_3O_4 (35 wt. %), Fe_3C (29 wt. %), and C (36 wt. %) filling in a PTMO–block–PET polymer at low concentration (0.3 %), has been synthesized. X-ray and SEM analyses have been carried out. The temperature dependence of the FMR spectrum of this system has been investigated. At higher temperatures resonance from Fe_3O_4 nanoparticles dominates the FMR spectrum, while at lower temperatures a more intense line from Fe_3C is recorded. The temperature dependence of the FMR spectrum confirms that the nanoparticles of Fe_3O_4 reach the ordered state faster than Fe_3C nanoparticles. In both cases, the spin-glass state is observed below 50 K.

Key words: *magnetite; iron carbide; magnetic resonance*

1. Introduction

Although magnetite (Fe_3O_4) has been well known since an early period of human civilization, its magnetic and electrical properties are still intensively studied at different scales, from macro- to nanoscopic [1–6]. After the discovery of magnetic resonance, magnetite was one of the first materials studied by the magnetic resonance technique [7]. Iron carbide (Fe_3C) is one of the most important components used in

* Corresponding author, e-mail: Tomasz.Bodziony@ps.pl

metallurgy. The ferromagnetic resonance (FMR) spectra of iron carbide nanoparticle agglomerates in a carbon matrix have been shown to exhibit very interesting behaviour [6, 8, 9]. The resonance absorption signal arises from agglomerates of iron carbide with strong magnetic interactions and is significantly influenced by the concentration of magnetic nanoparticles in a non-magnetic matrix. Polymers traditionally have been considered as excellent host matrices for composite materials. Several advanced polymer nanocomposites with magnetic particles dispersed in organic or inorganic matrices are of great interest due to their various applications [10]. Nano-size magnetic materials have attracted the attention of many researchers, because magnetic nanoparticles exhibit such unusual chemical and physical properties as superparamagnetism and quantum tunnelling of magnetization [11]. Therefore it would be very interesting to study the binary magnetic system of iron carbide and iron oxide in a non-magnetic matrix. Moreover, magnetite exhibits extraordinary behaviour near T_c = 125 K (the Verway transition) [2], and this temperature decreases with a diminishing size of the magnetic particles.

The aim of this work is to report the preparation of a binary system of Fe_3O_4 and Fe_3C magnetic nanoparticles dispersed at low concentration (0.3 wt. %) in a PTMO–block–PET polymer, its characterization (by XRD and SEM), and a study of the temperature dependence of its FMR spectra.

2. Experimental

The fusion of magnetite with small amounts of Al_2O_3 and CaO (3 wt.%) was first used in the preparation of the sample. The material obtained after the fusion was cooled to room temperature, crushed and sieved (the 1.2–1.5 mm fraction was taken), and reduced in hydrogen at temperatures in the range of 620–770 K. Nanocrystalline iron was obtained after reduction, while the promoter oxides remained in the oxidized state and their role was to stabilize a well-developed nanocrystalline iron structure. To avoid oxidation after reduction, the sample was passivated with nitrogen containing traces of water vapour. The mean size of iron crystallites was determined by using the XRD method; the size was estimated to be about 17 nm. The sample of nanocrystalline iron was carburised with a CO–CO_2 mixture (98 vol. % CO) at 720 K in a glass flow reactor. The carburising gas mixture was obtained via the Boudouard process ($C + CO_2 = 2CO$), passing carbon dioxide through the bed of active carbon at 1370 K. The analysis of the gas at the inlet and outlet of the carburisation reactor was performed using gas chromatography (Hewlett Packard, 4890D). 5 A molecular sieves of were used as a column filling. After carburisation the samples were characterised using XRD (Philips X Pert, $CoK_{\alpha 1}$), TOC (total carbon, Multi N/C, equipped with an Eltra HFT-540 oven, Analytik Jena), and SEM (DSM-962, LEO, Zeiss Jena) methods. The specific surface area and pore distribution were measured using low temperature nitrogen adsorption (Micromeritics, ASAP).

The composite used in our experiments consisted of a PTMO–block–PET polymer filled at low concentration (0.3 %) with the nanoparticle mixture: Fe_3O_4 (35 wt. %), Fe_3C (29 wt. %) and C (36 wt. %). The composite was carefully mixed manually, poured out into the mould and hardened thermally.

The nanocomposite samples were obtained by introducing the filler into the reaction mixture and synthesizing multiblock poly(ether–ester) copolymers based on polyoxytetramethylene and poly(ethylene terephtalate) (PET). An appropriate amount of filler was dispersed in 1,4-ethanediol by ultrasonication in a Sonoplus-Homogenisator HD2200. The synthesis of the multiblock copoly(ether–ester) was a two-stage process, carried out in an acid-resistant steel reactor. The transesterification of dimethyl terephthalate (DMT) with ED was the first stage process. The reaction was carried out at temperatures between 420 and 460 K, under atmospheric pressure, until the 90% conversion was measured by the amount of distilled methanol with respect to the theoretical amount. In the next stage, the transesterification of di(2-hydroxytetramethylene) terephthalate with α, ω-dihydroxy-polyoxytetramethylene (PTMEG) was performed. Polycondensation was carried out at 460–500 K, with the pressure decreasing step by step down to 0.1 hPa. The progress of the reaction was determined on the basis of the amount of distilled ED and the increase in the torque of the stirrer. The polymer was extruded from the reactor using compressed nitrogen.

Magnetic resonance absorption measurements were carried out with a conventional X-band (ν = 9.43 GHz) Bruker E 500 spectrometer and 100 kHz magnetic field modulation. The samples, each containing around 20 mg of the material, were placed in quartz tubes 4 mm in diameter. Prior to measurements, the samples were magnetized by a steady 1.6 T magnetic field in order to saturate any domain structure. The measurements were performed in the range from room to helium temperature, with $\Delta T = \pm 1.0$ K stability, using an Oxford cryogenic system.

3. Results and discussion

The sample was characterized using XRD and SEM. Figure 1 presents an XRD pattern for a binary system of magnetic nanoparticles in carbon. According to the XRD and TOC methods, after carburisation and before polymerisation the sample contained: Fe_3O_4 (35 wt. %), Fe_3C (29 wt. %), and C (36 wt. %). A SEM micrograph (Fig. 2) shows that the grains of the magnetic binary system in carbon are distributed almost homogeneously in the PTMO–block – PET polymer matrix. The two magnetic phases are contained in one grain, with carbon being the environment. Over 95% of all grains had a radius below 100 nm.

Figure 3 presents an FMR spectrum of the investigated sample at various temperatures. At higher temperatures, an intense, slightly asymmetric resonance line centred at $g_{\text{eff}} = 2.204(1)$ is observed. With decreasing temperature, the intensity of the FMR spectrum strongly decreases, the linewidth increases, and the resonance field shifts towards lower magnetic fields (Fig. 3).

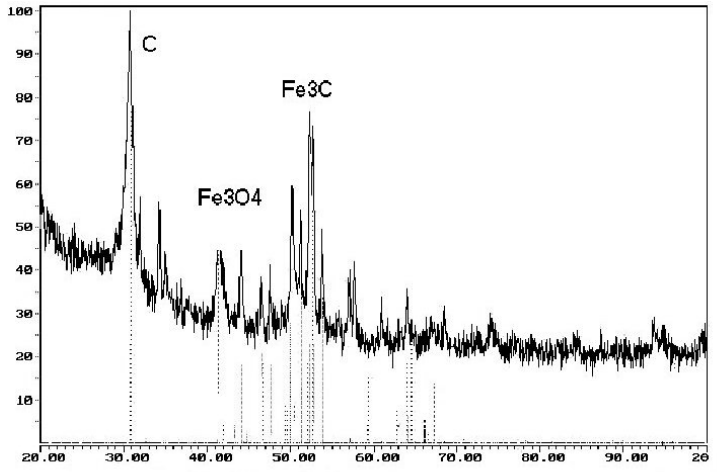

Fig. 1. The XRD pattern for a binary system of magnetic nanoparticles in carbon

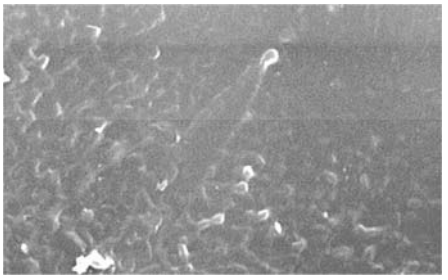

Fig. 2. The SEM micrograph of a magnetic binary system in carbon in a polymer matrix

The FMR study of the Fe_3O_4 + Fe_3C magnetic nanoparticle system dispersed in epoxy resin has revealed a resonance line that could be fitted by two separate Lorentzian functions [12]. A similar procedure has been successfully used for the present sample. The line shape asymmetry observed at higher temperatures can be explained assuming the spectrum is a superposition of two separate Lorentzian-shaped lines, including the tail of the resonance absorption at negative fields due to the linearly polarized radio frequency radiation.

Figure 4 presents, as an example, the FMR spectra registered at two temperatures, 33.1 K and 263.1 K, together with the fitted Lorenztian curves. The dotted line and the dashed line show the first (narrow) and second (broad) component Lorentzian lines, respectively. The solid line shows the best fit of the resonance spectrum by assuming a superposition of two Lorenztian lines. The FMR spectrum at room temperature (T = 295 K) consists of two lines with the following g-factors and peak-to-peak linewidths: g = 2.250(1) and ΔH_{pp} = 142 mT for the first component, and the second being centred near zero resonance magnetic field with the linewidth of ΔH_{pp} = 365 mT. On the basis of our earlier studies of a Fe_3O_4 + Fe_3C magnetic nanoparticle system dispersed in epoxy resin and PTMO–block–PET polymer at a higher concen-

tration (0.5 %) [13], we were able to make the assumption that the narrow and more intense component observed in the FMR spectrum at higher temperatures arises from the magnetite, while the broader line is due to iron carbide.

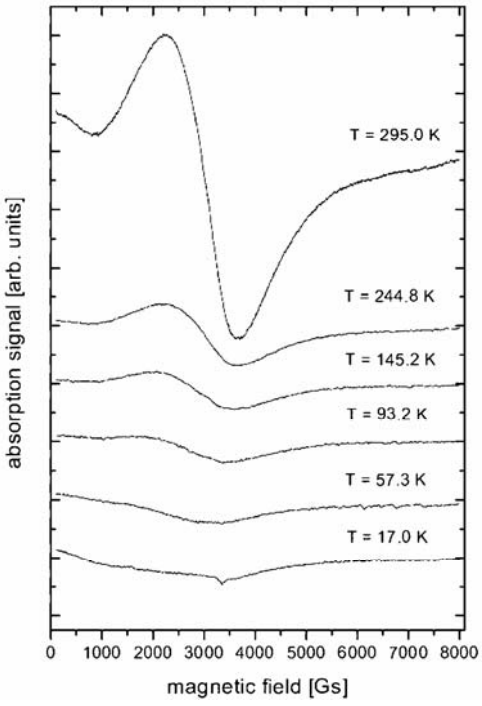

Fig. 3. An example of an FMR spectrum for 0.3% (Fe_3O_4 + Fe_3C)/C in a polymer matrix at different temperatures

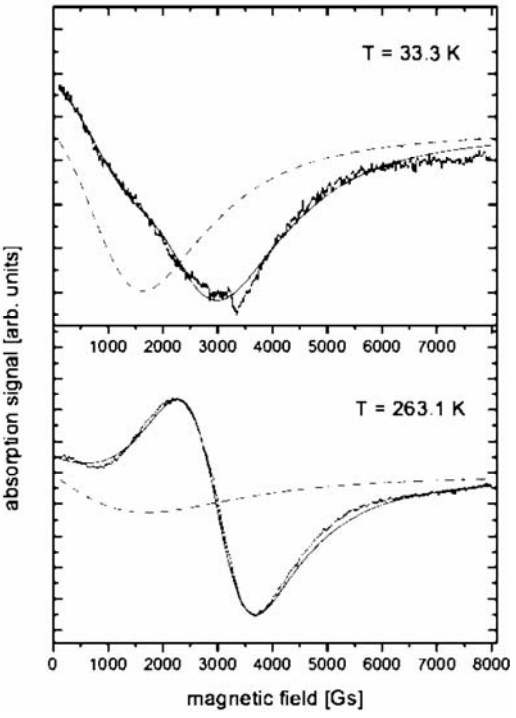

Fig. 4. An example of an FMR spectrum for T = 33.1 K and T = 263.1 K. The solid line shows the best fit of the resonance spectrum using two Lorenztian lines. The dotted and dashed line show the first (narrow) and second (broad) Lorentzian lines originating from magnetite and iron carbide, respectively

Figures 5 and 6 present the temperature dependences of the resonance field H_r, peak-to-peak linewidth ΔH_{pp}, and integrated intensity I arising from magnetite (Fig. 5) and iron carbide (Fig. 6). At high temperatures (55 K < T < 300 K), this type of temperature dependence has been frequently observed in the FMR spectra of iron oxide nanoparticles and suggests the presence of superparamagnetic phenomena [14–17]. The gradual suppression of the averaging effect of thermal fluctuations and interparticle interaction or the emergence of spin-glass like freezing with decreasing temperature for magnetite nanoparticles could essentially influence the FMR spectrum at higher temperatures, at which it is dominated by the signal from magnetite.

Figure 7 shows the temperature dependence of the g parameter from room temperature to about 20 K, computed from the best fit of the resonance spectra for the

broader Lorentzian line (Fig. 7a), and for the narrower component (Fig. 7b), originating from iron carbide and magnetite, respectively. The FMR line from iron carbide displays an abrupt change in its g parameter at temperatures between 93.2 K and 118.5 K (Fig.7a). This effect should be expected in the behaviour of a Lorentzian line arising from magnetite, which undergoes a structural phase transition at T_c = 125 K for bulk material, known in literature as the Verwey transition [2]. The temperature dependence of the *g* parameter for the narrower component (arising from magnetite) at temperatures from 57.3 K to room temperature was fitted with a Curie–Weiss curve (Fig. 8).

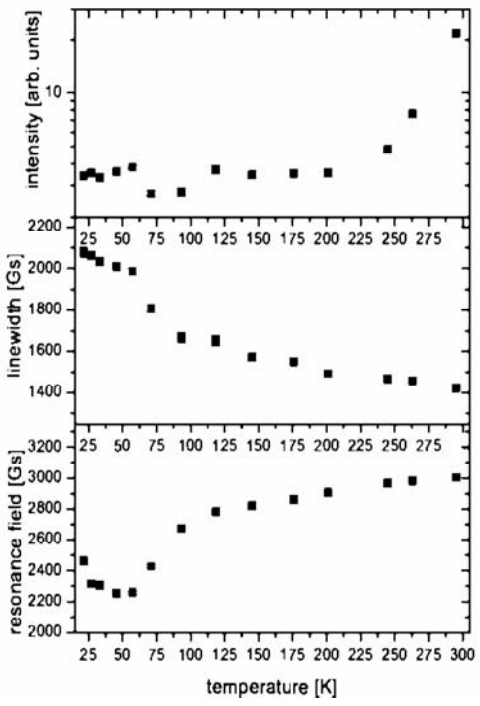

Fig. 5. Temperature dependence of FMR intensity, peak-to-peak linewidth, and resonance field for the narrow component originating from magnetite

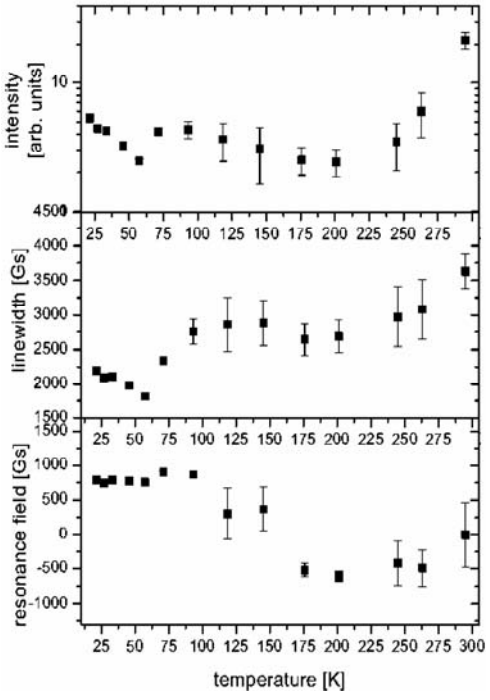

Fig. 6. Temperature dependence of FMR intensity, peak-to-peak linewidth, and resonance field for the broad component originating from iron carbide

Figure 9 shows the temperature dependence of the integrated intensity ratio of the lines, $I_{\text{iron carbide}}/I_{\text{magnetite}}$, expressed in %. The temperature dependence of this ratio varies between 60% and about 160%.

In order to understand the behaviour of the FMR spectrum of a binary magnetic system, we have to remember that the internal magnetic field acting on a mono-domain nanometer-size ferromagnetic particle can be formed by the following components [8]:

$$B_{\text{tot}} = B_{\text{dem}} + B_{\text{app}} + B_{\text{dip}} + B'_{\text{dip}} \tag{1}$$

where B_{dem} is the demagnetisation field, B_{app} is the applied external magnetic field, B_{dip} is the dipole field from the neighbouring nanoparticles, and B'_{dip} is the dipole –dipole interaction between aggregates. The collective spins of aggregates or agglomerates could recognize an additional magnetic field, and this could broaden the FMR spectrum and shift it towards lower magnetic fields.

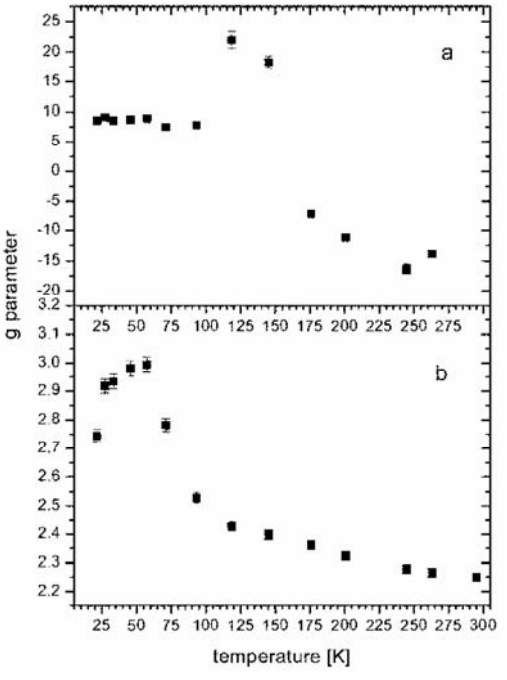

Fig. 7. Temperature dependence of the *g* parameter computed from the best fit to the resonance spectrum for the broad Lorentzian line (a), and for the narrow Lorentzian line (b), originating from iron carbide and magnetite, respectively

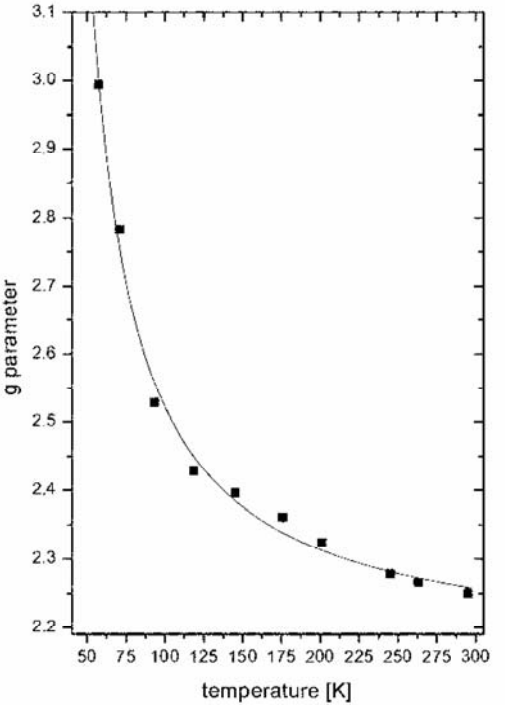

Fig. 8. A fragment of temperature the dependence of the *g* parameter for the narrow Lorentzian line originating from magnetite, and a fitted Curie–Weiss curve

The magnetic nanoparticles are distributed in the PTMO–block–PET polymer matrix almost homogenously, as evidenced by the SEM micrograph (Fig. 2), so only the exchange interaction of the neighbouring magnetic nanoparticles must be taken into account, while the interaction between agglomerates (or aggregates) can be neglected. The influence of neighbouring magnetic nanoparticles on the FMR spectrum could be observed by a closer inspection of the temperature dependence. The same binary magnetic system but in greater concentration in the epoxy resin matrix showed a resonance line significantly broader than in the polymer matrix [12]. The behaviour of the peak-to-peak linewidth and integrated intensity (Figs. 5 and 6) suggests that in the

case of a Fe_3O_4 + Fe_3C binary magnetic system dispersed at low concentration (0.3 %) in the PTMO–block–PET polymer, the magnetic field B_{dip} – the dipole field from neighbouring nanoparticles – can be small or even negligible. This may be the consequence of a low concentration of magnetic nanoparticles in a non-magnetic matrix and of a situation in which particular nanoparticles are rather isolated from their neighbours.

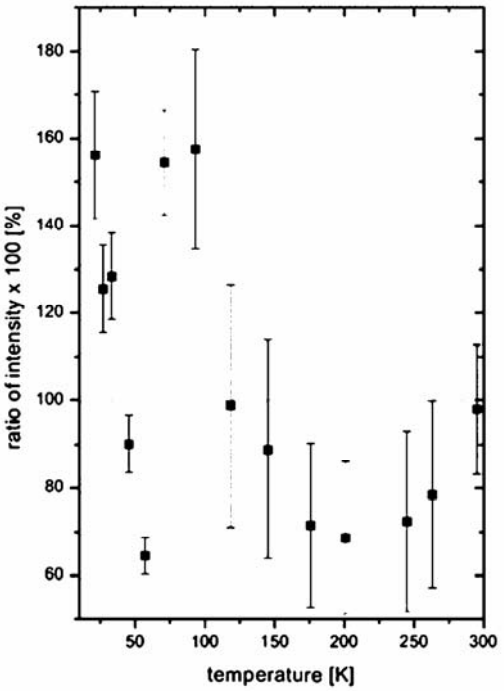

Fig 9. Temperature dependence of the ratio of FMR intensity of the broad Lorentzian component to that of the narrow Lorentzian component

The behaviour of the *g* parameter for lines originating from magnetite and iron carbide is rather interesting. In the case of the *g* parameter for iron carbide, an abrupt change in the temperature range between 93.2 K and 118.5 K can be seen. Such an effect should be expected in the behaviour of this line due to the Verwey transition. It might be supposed that the inner layer of a nanoparticle is made of iron carbide and surrounded by magnetite, and that the outer layer is formed by carbon [13]. An anomaly in the FMR spectra recorded below 50 K could suggest some parts of the sample may be in the spin-glass state.

4. Conclusions

The binary magnetic system of (Fe_3O_4 + Fe_3C)/C in a non-magnetic matrix of PTMO–block–PET polymer has been prepared. FMR measurements have shown that the spectrum at higher temperatures is dominated by a magnetite signal, while at

lower temperatures it transforms into the FMR spectrum of iron carbide. The complex structure of nanoparticles in these binary magnetic systems could consist of an inner layer made of iron carbide surrounded by magnetite, and an outer layer made of carbon. Below 50 K, the spin-glass state may be formed.

Acknowledgements

This work was partially supported by the grant PBZ-KBN-095/TO8/2003.

References

[1] CHAINANI A., YOKOYA T., MORIMOTO T., TAKAHASHI T., TODO S., Phys. Rev., B51 (1995), 17976.
[2] WALZ F., J. Phys.: Condens. Matter, 14 (2002), R285.
[3] OWENS F.J., J. Phys. Chem. Solids, 64 (2003), 2289.
[4] HIRANO S., YOGO T., SAKAMOTO W., YAMADA S., NAKAMURA T., YAMAMMTO T., UKAI H., BANNO K., NAKAFUKU T., ANDO Y., J. Sol-Gel Sci. Technol., 26 (2003), 35.
[5] ZHANG X.Y., CHEN Y.J., J. Magn. Magn. Mat., 271 (2004), 184.
[6] GUSKOS N., TYPEK J., NARKIEWICZ U., MARYNIAK M., AIDINIS K., Rev. Adv. Mater. Sci., 8 (2004) 34.
[7] BICKFORD L.R., Phys. Rev., 78 (1950), 449.
[8] NARKIEWICZ U., GUSKOS N., ARABCZYK W., TYPEK J., BODZIONY T., KONICKI W., GASIOREK G., KUCHAREWICZ I., ANAGNOSTAKIS E.A., Carbon, 42 (2004), 1127.
[9] GUSKOS N., ANAGNOSTAKIS E.A., GASIOREK G., TYPEK J., BODZIONY T., NARKIEWICZ U., ARABCZYK W., KONICKI W., Mol. Phys. Rep., 39 (2004), 58.
[10] XIAOTUN Y., LINGGE X., CHOON N.S., HARDY C.S.O., Nanotechnology, 14 (2003), 624.
[11] TANGO T., HATSUTA T., MIYAJIMA K., KISHADA M., TASHIRO S., WAKABAYASHI K., J. Am. Ceram. Soc., 85 (2002), 2188.
[12] GUSKOS N., ANAGNOSTAKIS E.A., LIKODIMOS V., BODZIONY T., TYPEK J., MARYNIAK M., NARKIEWICZ U., KUCHAREWICZ I., WAPLAK S., J. Appl. Phys., 97 (2005), 024304
[13] BODZIONY T., GUSKOS N., TYPEK J., ROSLANIEC Z., NARKIEWICZ., KWIATKOWSKA M., MARYNIAK M., Rev. Adv. Mater. Sci., 8 (2004), 86
[14] GAZEAU F., SHILOV V., BACRI J.C., DUBOIS E., GENDRON F., PERZYNSKI R., RAIKHER YU.L., STEPANOV V.I., J. Magn. Magn. Mater., 202 (1999), 535.
[15] BERGER R., CLIAVA J., BISSEY J.C., BAIETTO V., J.Appl. Phys., 87 (2000), 7389.
[16] BERGER R., BISSEY J.C., CLIAVA J., DAUBRIC H., ESTOURNES C., J. Magn. Magn. Mater., 234 (2001), 535.
[17] KOSKAROV YU.A., PANKRATOV D.A., GUBIN S.P., KOSOBUDSKY I.D., BELTRAN M., KHODORKOVSKY Y., TISHIN A.M., J. Appl. Phys., 89 (2001), 2293.

Received 12 November 2004
Revised 17 March 2005